Universidade do Minho
Escola de Engenharia

André Paulo Galvão de Castro

DEVELOPMENT OF A BIOMIMETIC FINITE ELEMENT MODEL OF THE INTERVERTEBRAL DISC DISEASES AND REGENERATION

DEVELOPMENT OF A BIOMIMETIC FINITE ELEMENT MODEL
OF THE INTERVERTEBRAL DISC DISEASES AND REGENERATION
André Paulo Galvão de Castro

UMinho | 2013

Novembro de 2013

Universidade do Minho
Escola de Engenharia

André Paulo Galvão de Castro

DEVELOPMENT OF A BIOMIMETIC FINITE ELEMENT MODEL OF THE INTERVERTEBRAL DISC DISEASES AND REGENERATION

Tese de Doutoramento
Programa Doutoral em Engenharia Biomédica

Trabalho efectuado sob a orientação de
Professor Doutor José Luís Carvalho Martins Alves

e co-orientação de:
Professor Doutor João Paulo Flores Fernandes
Professor Doutor António Manuel Godinho Completo

Novembro de 2013

DECLARAÇÃO

Nome: André Paulo Galvão de Castro

Endereço electrónico: andrepgcastro@gmail.com Telefone: 965153925

Número do Bilhete de Identidade: 12972512

Título tese:

Development of a Biomimetic Finite Element Model of the Intervertebral Disc Diseases and Regeneration

Orientador:

Professor Doutor José Luís Carvalho Martins Alves

E co-orientação de:

Professor Doutor João Paulo Flores Fernandes

Professor Doutor António Manuel Godinho Completo

Ano de conclusão:2013

Designação do Ramo de Conhecimento do Doutoramento:

Programa Doutoral em Engenharia Biomédica

Nos exemplares das teses de doutoramento ou de mestrado ou de outros trabalhos entregues para prestação de provas públicas nas universidades ou outros estabelecimentos de ensino, e dos quais é obrigatoriamente enviado um exemplar para depósito legal na Biblioteca Nacional e, pelo menos outro para a biblioteca da universidade respectiva, deve constar uma das seguintes declarações:

É AUTORIZADA A REPRODUÇÃO PARCIAL DESTA TESE (indicar, caso tal seja necessário, nº máximo de páginas, ilustrações, gráficos, etc.), APENAS PARA EFEITOS DE INVESTIGAÇÃO, MEDIANTE DECLARAÇÃO ESCRITA DO INTERESSADO, QUE A TAL SE COMPROMETE

Universidade do Minho, ____/____/_____

Assinatura: _____

To all those people who have always been there,
and also to everyone who has arrived and stayed...

ACKNOWLEDGMENTS

This is supposed to be a short section, but I would easily make it too long.

First, I want to acknowledge my supervisor, Professor José Luís Alves, for all the guidance and advice. I would definitely not be here if he was not so passionate about working on research and development. I also want to acknowledge my co-supervisors, Professor Paulo Flores and Professor António Completo, for helping me everything I needed.

Professor Jacques Huyghe, from the Eindhoven University of Technology, was not formally my supervisor, but his contribution for this work was outstanding. I must also acknowledge Professor Keita Ito, Wouter Wilson and all those people who received me so well in my two visits to Eindhoven.

From the University of Minho, special thanks for all the people that have crossed my way on the CT2M Researchers' Room along these four years. You know how hard might be working in this field. Good luck for all of you!

My friends know how important they are for me, and I would not name them. They have been there for me for a long time, and I hope that they can still be for much longer.

My family also knows what they mean to me, particularly my parents, Rosa and Paulo, and my sister Ana. They never missed my call whenever I needed them and they motivated me all along my academic track.

Finally, I want to thank Sílvia for her support, caring and patience. You know how stubborn I am, but you always pushed me forward!

For everyone, **thank you very much**. I wish you all my best!

ABSTRACT

Degenerative Disc Disease is one of the largest health problems faced worldwide, based on lost working time and associated costs. This is the driving force for the development of a biomimetic Finite Element (FE) model of the Intervertebral Disc (IVD), which is a multiphasic and highly inhomogeneous structure. A great amount of experimental and numerical works have studied the IVD and proven that it presents osmo-poro-hyper-visco-elastic behavior, with high influence of the anisotropic behavior of collagen fibers.

Poroelastic models of the IVD are mostly implemented in commercial FE-packages, which means that the accessibility to the source algorithm is often circumscribed. In order to approach to the biomechanical behavior of the IVD in the Human spine with higher flexibility and accuracy, an innovative poroelastic formulation implemented on a home-developed open-source FE solver is addressed and validated throughout this work.

Numerical simulations were mostly devoted to the analysis of the non-degenerated Human IVD time-dependent behavior, using a geometrically accurate FE model of a full motion segment (MS), constructed with quadratic 27 nodes hexaedral elements. The results of the tests performed for creep assessment were inside the scope of the experimental and numerical literature data, with remarkable improvements of the numerical accuracy when compared with some previously published results obtained with the commercial FE-package ABAQUS®. Previously unpublished experimental data from the research partners at VUmc (Amsterdam, The Netherlands) were also analyzed and compared with the MS FE model, which proved to reproduce satisfactorily to the physiological and non-physiological conditions of those experimental tests.

The IVD biomechanical behavioral is complex and dependent on multiple factors. The numerical simulations with the present MS FE model, using the home-developed open-source FE solver, demonstrated potential to biomimitize the IVD and thus contribute to the advance of the knowledge on its biomechanics.

RESUMO

A Doença Degenerativa dos Discos é um dos maiores problemas de saúde enfrentados a nível mundial, a nível de tempo de trabalho perdido e custos associados. Esta é a motivação para o desenvolvimento de um modelo biomimético de Elementos Finitos (EF) do Disco Intervertebral (DIV), que é uma estrutura multifásica e altamente heterogénea. Um grande número de trabalhos, experimentais e numéricos, estudou o DIV e provou que este apresenta comportamento osmo-poro-hiper-visco-elástico, com influência significativa do comportamento anisotrópico das fibras de colagénio.

Os modelos poroelásticos do DIV têm sido frequentemente implementados em programas comerciais de EF, o que significa que o acesso ao algoritmo-fonte é circunscrito. Para obter uma aproximação mais flexível e rigorosa ao comportamento biomecânico do DIV, uma formulação poroelástica inovadora foi implementada num programa de EF de acesso livre, desenvolvido internamente. Esta formulação é descrita e validada ao longo do presente trabalho.

As simulações numéricas foram quase totalmente dedicadas à análise do comportamento do DIV Humano não-degenerado, que se sabe ser fortemente dependente do factor tempo. Para esse feito, foi utilizado um modelo de EF geométrico correcto de um segmento móvel (SM) completo, construído com elementos quadráticos hexaédricos de 27 nós. Os resultados dos testes levados a cabo para análise do comportamento do DIV em termos de fluência ficaram dentro do espectro dos resultados experimentais e numéricos disponíveis na literatura. Foram, inclusivé, registadas melhorias notáveis em relação a alguns trabalhos que utilizaram ABAQUS®, um programa de EF comericalmente disponível. Foram também analisados dados experimentais não publicados dos parceiros de investigação da VUmc (Amesterdão, Holanda). A comparação com o modelo EF do SM demonstrou que este modelo reproduz satisfactoriamente as condições dos testes experimentais, sejam elas condições fisiológicas ou não-fisiológicas.

O comportamento biomecânico do DIV é complexo e dependente de múltiplos factores. As simulações numéricas levadas a cabo com o modelo EF do SM, utilizando o programa de EF de acesso livre desenvolvido internamente, demonstraram potencial para biomimetizar o DIV e assim contribuir para o avanço do conhecimento da sua biomecânica.

"Facts are the air of scientists. Without them you can never fly."

Linus Pauling

INDEX

Acknowledgments	iv
Abstract	v
Resumo	vi
Index	vii
List of Figures	xii
List of Tables	xix
List of Acronyms	xx
Nomenclature	xxii

1. Introduction

1.1. Motivation	1.1
1.2. Objectives	1.4
1.2.1. Contributions	1.5
1.3. Thesis Structure	1.7
1.4. References	1.9

2. The Intervertebral Discs

2.1. Anatomy and Physiology	2.1
2.1.1. Nucleus Pulposus	2.5
2.1.2. Annulus Fibrosus	2.6
2.1.3. Cartilage Endplate	2.7
2.1.4. Cellular Level	2.8
2.2. Biomechanics	2.10
2.2.1. Loads	2.12
2.2.2. Mechanical Responses	2.13
2.3. Degeneration	2.15
2.3.1. Associated Diseases	2.20
2.3.2. Treatments	2.21
2.4. Numerical Modeling	2.23
2.4.1. Multiphasic Media	2.25
2.4.2. Finite Element Models	2.27
2.4.3. Summary	2.46
2.5. References	2.47

3. Finite Element Modeling

3.1. Mechanical Modeling	3.1
3.1.1. Basic Kinematics	3.2
3.1.2. Constitutive Modeling	3.4
3.1.3. Boundary Value Problem	3.7
3.1.4. Variational Principle	3.8

3.1.5. Finite Element Implementation 3.11
3.1.6. Innovative Biphasic Modeling 3.14
3.1.7. Osmotic Swelling Behavior 3.16
3.1.8. Viscoelastic Behavior 3.17
3.1.9. Innovative Annulus Fibrosus Modeling 3.19
3.1.10. Summary 3.20
3.2. Finite Element Model 3.21
3.3. Mesh Convergence Study 3.26
3.4. References 3.28

4. Validation

4.1. Terzaghi's 1D Test 4.1
4.2. Swelling Periods 4.6
4.2.1. Comparison of swelling simulation methods 4.10
4.2.2. Summary 4.14
4.3. Short Creep Validation 4.15
4.3.1. 500N, 15mins 4.15
4.3.2. Convergence study outcomes 4.17
4.3.3. Increasing loads, 15mins 4.21
4.3.4. Other configurations 4.24
4.3.5. Summary 4.27
4.4. References 4.28

5. Results and Discussion

5.1. Short Creep	5.1
5.1.1. 800N, 20mins	5.2
5.1.2. 2000N, at 1N/s	5.7
5.1.3. Summary	5.12
5.2. Long Creep	5.13
5.2.1. 200-500N	5.13
5.2.2. 200-600N	5.15
5.2.3. 250-600N	5.17
5.2.4. Comparison #1	5.18
5.2.5. 250-700N	5.21
5.2.6. 250-850N	5.22
5.2.7. 250-1000N	5.24
5.2.8. Comparison #2	5.25
5.2.9. 350-1000N	5.28
5.2.10. 500-1000N	5.31
5.2.11. Comparison #3	5.33
5.2.12. Summary	5.36
5.3. Bioreactor Data Analysis	5.37
5.3.1. Comparison with the MS FE model	5.45
5.3.2. Summary	5.53
5.4. References	5.54

6. Conclusions

6.1. Concluding Remarks	6.1
6.2. Future Work	6.5
6.3. References	6.6

7. Annexes

7.1. 500N, 15mins, altered osmotic properties	7.1
7.2. Detailed analysis of Overloaded LDCS Data	7.3
7.3. General aspect of the open-source FE solver	7.6
7.3.1. Input Files	7.6
7.3.2. Output Files	7.9
7.4. Publications and Communications	7.13

LIST OF FIGURES

Figure 1.1. Typical schematic axial representation of the IVD (excluding the CEP). Adapted from Adams and Roughley (2006).	1.1
Figure 1.2. The details of the Human spine studied by Da Vinci. Adapted from Sanan and Rengachary (1996).	1.3
Figure 2.1. The complete Human spine, in both sagittal and frontal views. Adapted from Noailly (2009).	2.2
Figure 2.2. The Human IVD: a) Ex vivo photography of a healthy Human lumbar IVD, with the VB also visible (mid sagittal cut, anterior-posterior direction). Adapted from Adams et al. (2009); b) Schematic representation of a mid sagittal cut of the IVD, posterior-anterior direction. Adapted from Noailly (2009).	2.3
Figure 2.3. Anatomy of a MS, with emphasis on the IVD dimensions. Adapted from Raj (2008).	2.4
Figure 2.4. Nutrition pathways of the IVD. Adapted from Raj (2008).	2.8
Figure 2.5. Schematic representation of the pressure distribution inside the IVD, under a typical axial compressive load. Adapted from Noailly (2009).	2.12
Figure 2.6. Comparison between healthy (left) and degenerated IVDs (right): a) Axial cut. Adapted from Urban & Roberts (2003); b) Sagittal cut. Adapted from Adams et al. (2009).	2.16
Figure 2.7. Multiple pathways for IVD degeneration. Adapted from Hadjipavlou et al. (2008).	2.17
Figure 2.8. Metabolic changes in discs subjected to abnormal loads. Adapted from Colombini et al. (2008).	2.18
Figure 2.9. L3-L4 MS FE model developed by Goel and Kim (1989).	2.30
Figure 2.10. Lumbar MS FE model developed by Wu and Chen (1996).	2.31
Figure 2.11. Schematic representation of the 8 fiber layers of the L2-L3 MS FE model developed by Argoubi and Shirazi-Adl (1996).	2.31
Figure 2.12. Cross-sectional view of the degenerated AF FE model developed by (Eberlein	2.33

et al., 2004).

Figure 2.13. Lumbar IVD FE model developed by Ferguson and co-workers. 2.33

Figure 2.14. L4-L5 MS FE model developed by Natarajan et al. (2008). 2.34

Figure 2.15. Schematic representation of the under-dimensioned implants modeled by Joshi et al. (2009). a) Under-height implant ("NP Implant 1"); b) Under-diameter implant ("NP Implant 2"). 2.35

Figure 2.16. Healthy IVD (without CEP) FE model developed by (Little, 2004). 2.36

Figure 2.17. L3-S1 FE model developed by Goel et al. (2005). The Charité® disc implant was also modeled and included in this study, at the L5-S1 level. 2.37

Figure 2.18. L4-L5 MS FE model developed by Ehlers et al. (2009). 2.39

Figure 2.19. L3-L5 FE model developed by Noailly et al. (2012). 2.39

Figure 2.20. L3-L4 MS FE models developed by Rohlmann et al. (2006). a) Native MS model, with normal IVD height; b) Severely degenerated MS model, with highly reduced IVD height. 2.40

Figure 2.21. L4-L5 IVD FE model developed by Schmidt et al. (2011). The authors have chosen to model the CEP on the full diameter of the IVD and distinguished between the NP-covering CEP and the AF-covering CEP. 2.42

Figure 2.22. AF FE model developed by Malandrino et al. (2013), with regional variation. 2.44

Figure 2.23. Native L4-L5 IVD model developed by Strange et al. (2010). 2.45

Figure 3.1. Decomposition of deformation gradient tensor into volumetric and isochoric parts. From the left to the right, the sequence of the image is reference and current configurations. 3.3

Figure 3.2. Boundary value problem configuration. 3.8

Figure 3.3. Schematic representation of the adopted rheological model, i.e., a generalized Maxwell model, where up to 5 Maxwell elements can be assembled in parallel with a non-linear spring. Adapted from (Jimenez Rios et al., 2007). 3.18

Figure 3.4. Schematic representation of the AF differentiation. "V" stands for "ventral" and "D" stands for "dorsal". In addition, "e" stands for exterior and "i" stands for "interior", in relation to the position of the IVD in the spine. Adapted from Elliott and Setton (2000) and Holzapfel et al. (2005). 3.19

Figure 3.5. Sagittal cut of the original Human L4 VB FE model from Smit (1996). 3.21

Figure 3.6. Sagittal cuts of the original FE models: a) The model developed by Smit 3.23

(1996), with one VB and two IVDs; b) The first stage of the full MS model, with the two facets and its respective facet cartilage layers.

Figure 3.7. Sagittal cut of the L3-L4 FE model. 3.23

Figure 3.8. The geometrical MS model (a)) derived in six different FE models. b) and c) are the non-refined models, while d) and e) ate the refined ones. b) and d) were built with 27-node hexahedrons. As only the vertex nodes are shown, the visualization of 4-node and 10-node tetrahedra is the same (c) and e)). 3.26

Figure 4.1. Testing scheme for Terzaghi's test, for the 27-node hexahedral mesh. The same scheme was adopted for the 4 and 10-node meshes. Only the vertex nodes are shown. 4.3

Figure 4.2. Comparison between the results of Relative Pressure vs. Relative Depth predicted by the analytical solution of Terzaghi's model and the results obtained with different types of elements, namely the linear 4-node tetrahedron enriched with a bubble function at the center of the element (Tet4), the quadratic 10-node tetrahedron (Tet10) and the quadratic 27-node hexahedra (Hex27). The Relative Consolidation Time varied between four values: a) $T_T = 0.0105$; b) $T_T = 0.0901$; c) $T_T = 0.540$; d) $T_T = 1.112$. 4.5

Figure 4.3. Comparison between the DHV results of the four possibilities for the initial swelling period, along the 8h of the present (Free Pre-Swelling, 200N, 250N and 350N). 4.7

Figure 4.4. Pressure results of the four possibilities for the initial swelling period: a) Free Pre-Swelling; b) 200N; c) 250N and d) 350N. NP AveP, IDP and OsmP were assessed and compared between each other, along the 8h of the test. 4.9

Figure 4.5. Comparison between the present model and Galbusera and co-workers model: a) DHV; b) IDP; c) NP volume variation and d) AF volume variation. 4.13

Figure 4.6. Comparison between the evolution of IDP and OsmP of the BS models from the present work and the work of Galbusera et al. (2011). 4.13

Figure 4.7. Results of a 15min creep test at 500N of compression: a) DHV; b) NP AveP. The three options for the swelling behavior of the numerical model are compared with the experimental work of Heuer et al. (2007). 4.16

Figure 4.8. Comparison between the experimental results of Heuer et al. (2007) and the numerical results obtained with different types of elements, for the non-refined meshes ("NR"): a) DHV; b) NP AveP. 4.18

Figure 4.9. Comparison between the experimental results of Heuer et al. (2007) and the numerical results obtained with different types of elements, for the refined meshes ("R"): a) DHV; b) NP AveP. 4.19

Figure 4.10. Comparison between the non-refined ("NR") and the refined ("R") models: a) DHV; b) NP AveP. 4.20

Figure 4.11. Simulated creep test during 15min at different load magnitudes of uniaxial compression, namely 500, 1000, 1500 and 2000N: a) DHV; b) NP AveP. 4.22

Figure 4.12. Simulated creep test during 15min at 500N of uniaxial compression. The FE model was configured with three different sets of material properties (standard parameters, permeability parameters from Argoubi and Shirazi-Adl (1996) and material parameters from Schmidt et al. (2013)) and the outcomes were compared with the experimental results of Heuer et al. (2007) and also with the numerical results of Schroeder et al. (2010). Assessed outcomes: a) DHV; b) NP AveP. 4.26

Figure 5.1. Curves of SHR versus time: a) Comparison of the literature data (Tyrrell et al. (1985) and Williams et al. (2007)) with the numerical results of the three pre-conditioning options, applying the original protocol; b) Comparison of the literature data with the numerical results of the three pre-conditioning options, applying the adapted protocol with reduced load of 200N. 5.3

Figure 5.2. Comparison between the outcomes of the six numerical simulations: a) SHR; b) NP AveP; c) OsmP. 5.4

Figure 5.3. Comparison between the pressure variables (NP AveP and OsmP) of the numerical simulations: a) Free Pre-Swelling; b) Pre-Load 200N; c) Pre-Load 400N. 5.6

Figure 5.4. Sagittal cut of the MS FE model, with the visualization of the (average) pressure distribution correspondent to the "Free Pre-Swelling (2)" loading profile: a) After the first stage; b) At the end of the test. The scale is presented on the images, and the pressure unit is MPa. 5.7

Figure 5.5. Three stages loading test, involving: i) a pre-conditioning period, ii) a loading period of 2000N at 1 N/s and, finally, iii) a creep stage. The following parameters were assessed, considering the full length of the test: a) DHV versus loading scheme; b) NP AveP and Osmotic Pressure of the NP (OsmP); c) Volume variation of the three IVD components (NP, AF and CEP); d) Relative distribution of AF fibers by its stretch, at the end of the test. The distinction between the compression and traction zones is signaled. 5.10

Figure 5.6. Sagittal cuts of the MS FE model, at the end of each one of the three stages: a) After the pre-conditioning; b) After the ramp loading; c) At the end of the test, after the creep phase. The average pressure distribution inside the model is shown. The scale is presented on the images, and the pressure unit is MPa. 5.11

Figure 5.7. Results of the 200-500N loading profile, along 48h: a) DHV vs. Load; c) Pressure variables (IDP, OsmP and NP AveP); c) Volume variation. The comparison with the work of Galbusera et al. (2011) is held between 24 and 48h, for the DHV, IDP and OsmP variables. 5.15

Figure 5.8. Results of the 200-600N loading profile, along 48h: a) DHV vs. Load; c) Pressure variables (IDP, OsmP and NP AveP); c) Volume variation. 5.17

Figure 5.9. Results of the 250-600N loading profile, along 48h: a) DHV vs. Load; c) 5.18

Pressure variables (IDP, OsmP and NP AveP); c) Volume variation.

Figure 5.10. Comparison between the three low activity daily cycles, namely 200-500N, 200-600N and 250-600N loadcases. a) DHV; b) IDP; c) OsmP; d) NP AveP. 5.20

Figure 5.11. Results of the 250-700N loading profile, along 48h: a) DHV vs. Load; c) Pressure variables (IDP, OsmP and NP AveP); c) Volume variation. 5.22

Figure 5.12. Results of the 250-850N loading profile, along 48h: a) DHV vs. Load; c) Pressure variables (IDP, OsmP and NP AveP); c) Volume variation. 5.23

Figure 5.13. Results of the 250-1000N loading profile, along 48h: a) DHV vs. Load; c) Pressure variables (IDP, OsmP and NP AveP); c) Volume variation. 5.25

Figure 5.14. Comparison between the four moderate to harsh activity daily cycles, namely 250-{600, 700, 850, 1000}N loadcases. a) DHV; b) IDP; c) OsmP; d) NP AveP. 5.26

Figure 5.15. Results of the 350-1000N loading profile, along 48h: a) DHV vs. Load; c) Pressure variables (IDP, OsmP and NP AveP); c) Volume variation. 5.29

Figure 5.16. Comparison between the numerical outcomes of the MS FE model and the analogous outcomes of the work of Schmidt et al. (2010): a) DHV; b) Pressure (IDP and NP AveP). The first situation (Schmidt et al., 2010 (1)) considered the permeability parameters from Ferguson et al. (2004) and the second situation (Schmidt et al., 2010 (2)) considered a hybrid set of parameters. 5.31

Figure 5.17. Results of the 500-1000N loading profile, along 48h: a) DHV vs. Load; c) Pressure variables (IDP, OsmP and NP AveP); c) Volume variation. The comparison with the work of Galbusera et al. (2011) is held between 24 and 48h, for the DHV, IDP and OsmP variables. 5.32

Figure 5.18. Comparison between the three loadcases with the top activity load, namely {250, 350, 500}-1000N loadcases. a) DHV; b) IDP; c) OsmP; d) NP AveP. 5.35

Figure 5.19. Schematic representation of the LCDS. Adapted from (Paul et al., 2012). 5.37

Figure 5.20. Comparison of the overall displacement outcomes of the LDCS test-groups, for 16 days. a) DHV of the native IVDs, from test-groups 1 and 2; b) DHV of the injected IVDs, from test-groups 1 and 2 and overloaded IVD from test-group 3. 5.39

Figure 5.21. Comparison of the DHV outcomes within each test-group, for 16 days. a) Test-group 1; b) Test-group 2. 5.40

Figure 5.22. DHV evolution over the first two days of the LDCS experiment. a) First test-group; b) Second test-group. Two native and two injected IVDs are considered in each test-group. 5.43

Figure 5.23. DHV outcomes of the five numerical approaches to the experimental data, namely “Native”, “Low OsmP 1”, “Low OsmP 2”, “No Swelling” and “Overload” models. 5.47

Figure 5.24. Native and non-physiological DHV outcomes of the experimental and numerical tests, for two daily cycles. a) The four native IVDs compared with the native numerical model; b) The four injected IVDs compared with the two reduced OsmP models. 5.49

Figure 5.25. Non-physiological DHV outcomes of the experimental and numerical tests, for two daily cycles. a) The injected IVDs from goats 1 and 3 compared with the two reduced OsmP and the "No Swelling" models; b) The injected IVDs from goats 2 and 4 compared with the two reduced OsmP and the "No Swelling" models. 5.51

Figure 5.26. DHV outcomes from the five non-physiological goat IVDs compared with the overloaded model. 5.52

Figure 7.1. Simulated creep test during 15min at 500N of uniaxial compression. The FE model was configured with four different sets of osmotic swelling material properties, namely "No Swelling", "Pre-Swelling" (standard parameters), "Low OsmP 1" and "Low OsmP 2". Assessed outcomes: a) DHV; b) NP AveP. 7.2

Figure 7.2. Comparison between the experimental displacement outcomes ("Exp") during the activity periods, for the overloaded IVD. The presented outcomes are from days 1, 2, 8 and 16. 7.3

Figure 7.3. Comparison between the adjusted exponential curves ("Adj") related to the displacement outcomes of the activity periods, for the overloaded IVD. The presented outcomes are from days 1, 2, 8 and 16. 7.4

Figure 7.4. Comparison between the exponential and the experimental curves. The presented DHV curves are from days 1 and 16. 7.5

Figure 7.5. Example of an input file for the assignment of the boundary conditions. The FE solver has the capacity of reading sequential boundary conditions files. a) First input file (".bio"); b) Second input file (".bio1"). 7.7

Figure 7.6. Example of a section of an input file for the identification of each degree-of-freedom where the boundary conditions will be assigned. ".bcid" stand for "Boundary Conditions Identification". 7.8

Figure 7.7. Example of an input file for the assignment of the constitutive parameters of a given material. This example refers to the standard NP. 7.8

Figure 7.8. Example of the generic output file, which contains the evolution of the simulation. This information is also visualized in real time through command line environment. a) First section of the file, containing the generic information from the mesh, from the simulation and also from the materials; b) Continuation, with the information from the other materials and also with the numerical characteristics of the first time step of the simulation. 7.10

Figure 7.9. Example of a section of an output file containing force and displacement 7.11

information, along the duration of the simulation. This file is divided per each "bcid". It also provides additional information on whether force or displacement boundary conditions were applied to that "bcid".

Figure 7.10. Example of a section of an output file containing the results for average pressure, divided per material, for each time step of the simulation. 7.11

Figure 7.11. Example of a section of an output file containing the results of the fiber stretch, along the simulation. 7.12

Figure 7.12. Example of a section of an output file containing the information on the volume variation of the each one of the materials, along the simulation. 7.12

LIST OF TABLES

Table 2.1. Morphological classification of IVD degeneration grades. Adapted from Thompson et al. (1990). 2.19

Table 2.2. Imaging classification of IVD degeneration grades. Adapted from Pfirrmann et al. (2001). 2.19

Table 3.1. Material properties of the MS components. Multiple data sources were assessed, as stated on each entry of the table. Numerical optimization was also performed throughout the choice of these parameters. 3.12

Table 3.2. List of characteristics of each 3D FE MS model. 3.14

Table 4.1. Pressure and displacement measurements over time, for the free swelling test. 4.10

Table 4.2. Displacement measurements for the different load magnitudes of uniaxial compression, namely 500N, 1000N, 1500N and 2000N. 4.23

Table 4.3. NP AveP measurements for the different load magnitudes of uniaxial compression, namely 500N, 1000N, 1500N and 2000N. 4.23

Table 4.4. Alternative material configurations. 4.25

Table 5.1. Maximum values of DHV and IDP, for the four moderate to harsh activity daily cycles, namely 250-{600, 700, 850, 1000}N loadcases. 5.27

Table 5.2. Relative displacement measurements of the nine IVDs, from the five goats. 5.41

Table 5.3. Osmotic swelling material properties of the native FE model and reduced OsmP models. 5.46

Table 5.4. Summary of the DHV values of the four injected IVDs and the reduced OsmP models, after each activity and recovery period, obtained by numerical simulation. 5.51

Table 7.1. Characteristic parameters of the exponential curve adjustment, for days 1, 2, 8 and 16. 7.5

LIST OF ACRONYMS

Intervertebral Disc	IVD
Vertebral Bodies	VB
Nucleus Pulposus	NP
Annulus Fibrosus	AF
Cartilage Endplate	CEP
Degenerative Disc Disease	DDD
Finite Element Method	FEM
Finite Element Analysis	FEA
Finite Element	FE
VU University Medical Center	VUmc
Motion Segment	MS
Vertebral Endplate	VEP
Trabecular Bone	TB
Cortical Bone	CB
Computational Tomography	CT
Magnetic Resonance Imaging	MRI
Multibody Systems	MBS
Intradiscal Pressure	IDP
Extracellular Matrix	ECM
Whole Body Vibration	WBV
Volumetric	vol
Isochoric	isoc

Linear 8 Nodes Hexahedron	Hex8
Quadratic 27 Nodes Hexahedron	Hex27
Linear 4 Nodes Tetrahedron	Tet4
Quadratic 10 Nodes Tetrahedron	Tet10
Disc Height Variation	DHV
Average Pressure	AveP
Osmotic Pressure	OsmP
Biphasic Swelling	BS
Fixed Osmotic Pressure	FOP
Initial Disc Height	DHi
Spine Height Reduction	SHR
Relative Disc Height Variation	RDHV
Relative Pressure Variation	RPV
Loaded Disc Culture System	LDCS
Chondroitinase ABC	CABC
Final Disc Height Variation	DHVf

NOMENCLATURE

Second Piola-Kirchhoff Stress Tensor	$\mathbf{\Pi}$
Reference Configuration of an Arbitrary Body of Interest	Ω_0
Current configuration of an arbitrary body of interest	Ω
Position Vector of a given Material Point on the Reference Configuration	$\mathbf{X}$
Position Vector of a given Material Point on the Current Configuration	$\mathbf{x}$
Deformation Gradient Tensor	$\mathbf{F}$
Displacement Field	$\mathbf{u}$
Second Order Unit Tensor	$\mathbf{I}$
Jacobian of the Deformation Gradient Tensor	J
Isochoric Contribution of the Deformation Gradient Tensor	$\overline{\mathbf{F}}$
Right Cauchy-Green Strain Tensor	$\mathbf{C}$
Green-Lagrange Strain Tensor	$\mathbf{E}$
Strain Energy Function	$W(\mathbf{C})$
Isotropy-related Invariants of the Right Cauchy-Green Strain Tensor	I_1, I_2, I_3
Unit Vector Fields	$\mathbf{a}_1$, $\mathbf{a}_2$
Anisotropy- related Invariants of the Right Cauchy-Green Strain Tensor	I_4, ..., I_9

Isochoric Contribution of the Invariants $I_1,...,I_9$	$\bar{I}_1,$ ..., $\bar{I}_9$
Isochoric Contribution of the Right Cauchy-Green Strain Tensor	$\overline{\mathbf{C}}$
Penalty Parameter playing the Role of a Bulk Modulus	λ_k
Pressure Interpolated from the (Unknown) Pressure Field	$\tilde{p}$ (or simply p)
Pressure Computed from the (Unknown) Displacement Fields	$\bar{p}$
Volumetric Strain Energy Function	$\overline{W}_H(J)$
Shear Modulus	G
Material Parameters from the Mooney-Rivlin's Model	C_{10}, C_{01}
Bulk Modulus	K
Material Parameters from the Holzapfel's Model	k_1, k_2
Body Boundary in the Reference Configuration	$\partial\Omega_0$
Body Boundary where Surface Tractions	$\partial\Omega_{0,N}$
Prescribed Surface Tractions	$\underline{\mathbf{t}}_0$
Body Boundary where Displacements are prescribed	$\partial\Omega_{0,D}$
Prescribed Displacements	$\underline{\mathbf{u}}_0$
Solution Space where $\mathbf{u}=\underline{\mathbf{u}}_0$	U
Prescribed Body Forces	$\mathbf{f}_0$
Exterior Unit Normal Vector	$\mathbf{N}$
Notation for Prescribed Functions on the Boundaries	$\underline{(\bullet)}$

Total Potential Energy	$\Phi(\mathbf{u})$
Arbitrary Virtual Displacement Field	$\delta\mathbf{u}$
Function Space where $\delta\mathbf{u}=\mathbf{0}$	U_0
Strain Energy Function Term, which is Function of both Displacements and the Separately and Independently Interpolated Pressure	$Q^0(J)$
Additional Pressure Field	P
First Variational of the Green-Lagrange Strain Tensor with Respect to the Displacement Field	$\delta\mathbf{E}$
Isoparametric Shape Functions	N_A, G_A
Vector of Natural Coordinates	$\boldsymbol{\xi}$
Nodal Coordinates	$\mathbf{x}^A$
Nodal Pressure	p^A
Nodal Point Forces (Vector of the External Forces) corresponding to a given Time	$\mathbf{R}$
Time	t
Linearization Operator	$\Delta(\bullet)$
Vector containing Nodal Increments in $\mathbf{u}$	$\Delta\mathbf{u}$
Vector containing Nodal Increments in p	$\Delta\mathbf{p}$
Internal Forces Vector	$\begin{bmatrix}\mathbf{F_U}\\ \mathbf{F_P}\end{bmatrix}$
Displacements Variations of the Internal Forces Vector	$\mathbf{F_U}$
Pressure Variations of the Internal Forces Vector	$\mathbf{F_P}$
4th Order Constitutive Tensor that derives from the chosen Isotropic and/or Anisotropic Constitutive Models and Volumetric Strain Function	$\overline{C}_{klrs}$
Stiffness Matrix Displacement and Pressure Parts	$\mathbf{K_{UU}}$, $\mathbf{K_{UP}}$, $\mathbf{K_{PU}}$, $\mathbf{K_{PP}}$

Fluid	f
Solid	s
Flux of the Fluid Relative to the Solid Matrix	$\mathbf{w}$
Current Fluid Fraction	n_f
Relative Velocity	$\mathbf{v}$
Hydraulic Permeability	$\mathbf{K}^*$
Strain-Dependent Permeability	$K^*(J)$
Second Order Unity Tensor	$\mathbf{I}$
Gradient of the Pore (or Fluid) Pressure	∇p^f
Material Parameter of the Strain-Dependent Permeability Van der Voet's Model	M
Total Cauchy Stress	$\boldsymbol{\sigma}_{tot}$
Effective Solid Phase Stress Tensor	$\boldsymbol{\sigma}_s$
Water Chemical Potential	μ^f
Osmotic Pressure Gradient	$\Delta\pi$
Temperature	T
External Salt Concentration	c_{ext}
Osmotic Coefficients	ϕ_{int}, ϕ_{ext}
Fixed Charge Density	c_F
Time Relaxation Function	$G(t)$
Damper Characteristic Time	τ_n
Nonlinear Spring introduced by the Maxwell Element	a_n
Absolute Fiber Angle	φ
Polar Angle associated with the Circumferential Position of a given Material Point	α
Relative Pressure	P_T

Relative Depth	Z_T
Relative Consolidation Time	T_T
Cumulative for Terzaghi's Model	M_T
Consolidation Depth	z
Layer's Thickness	h
Compressive Modulus	H
Initially Applied Pressure	$\tilde{p}_0$

"It is the weight, not numbers of experiments that is to be regarded."

Isaac Newton

1. INTRODUCTION

The present work is devoted to the development of a biomimetic finite element model of the Human intervertebral disc, with the aim of creating a framework to understand the diseases that affect this highly complex structure, along with evaluating possible pathways to promote its rehabilitation and regeneration. This chapter intends to describe the motivation for this work, as well as to enumerate its major objectives and relevant contributions.

Finally, the structure of this thesis will be detailed.

1.1. Motivation

The intervertebral discs (IVDs) are fibro-cartilaginous cushions serving as shock absorbing system of the spine, which protect the vertebral bodies (VB), brain, and other structures, providing both flexibility and load support. They are considered as chondroid tissues and are composed by three major components: the nucleus pulposus (NP), the annulus fibrosus (AF) and the cartilage endplate (CEP). Healthy IVDs are highly hydrated and essential for human well-being, because their functions are of upmost importance for the spine (Adams et al., 2009; Raj, 2008). Figure 1.1 shows one of the most typical representations of the IVD.

The motivation for this work comes directly from the fact that degeneration of the IVD is strictly associated with spine problems, which are a major cause of disability on western societies (Whatley and Wen, 2012).

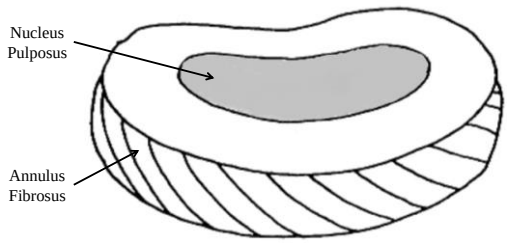

Figure 1.1. Typical schematic axial representation of the IVD (although the CEP is not visible). Adapted from Adams and Roughley (2006).

In fact, work absenteeism and decrease of productivity placed these diseases into the category of economic and social priorities. Over the last eighty years, a considerable amount of studies developed efforts to found the causes and possible treatment strategies for Degenerative Disc Disease (DDD) and other spine problems (Gamradt and Wang, 2005). Experimental[i] and computational[ii] studies were held, covering the fields of anatomy, physiology and biomechanics, for both native and degenerated conditions of the IVD. The most important works on this field[iii] will be referred later on this document, as well as the most important facts on IVD biomechanics.

The first record of a spinal biomechanical study goes back to an Egyptian papyrus, which was endorsed to the 17th century BC. Later on, the outstanding work of Leonard da Vinci started a new era for the study of the biomechanics of the Human body, with the well-known "Vitruvian Man". Da Vinci was probably the first one trying to describe the problematic of spinal stability, and produced the first detailed analysis of the constitution of the Human spine, with the correct curvatures and number of MS, as shown in Figure 1.2. On the 17th century, Giovanni Borelli's studies lead to merge of mechanisms with anatomy and physiology, creating a discipline that he called "iatromechanics", which preceded biomechanics. Borelli described the IVD as a viscoelastic substance, since he found that the spinal musculature was not able to support all the loading efforts. Therefore, the IVD should be a spring in-between the VBs, cushioning and protecting the bone, which corresponds to nowadays knowledge's about the load-sharing ability of the Human spine components (Sanan and Rengachary, 1996).

Despite of the advances of the 20th century, the knowledge on this subject is still incomplete. On the one hand, experimental studies are not able to explain all the specificities of

[i] Experimental studies include *in vivo*, *ex vivo* and *in vitro* studies. *In vitro* studies are performed with IVDs that can be kept alive after extraction or tested *post-mortem*.

[ii] The computational studies may also be denominated as *in silico* studies.

[iii] The main focus is on the computational studies.

the IVD and its interactions with the adjacent structures (Bron et al., 2009). On the other hand, computational models still have a way to go until the biological and biomechanical phenomena are accurately reproduced, despite of the great amount of computational spine and IVD studies published in the last forty years (Schmidt et al., 2013). Therefore, the pursuit of a more complete and reliable IVD model is the driving force for this work. To reach this innovation, the Finite Element Method (FEM) is here adopted.

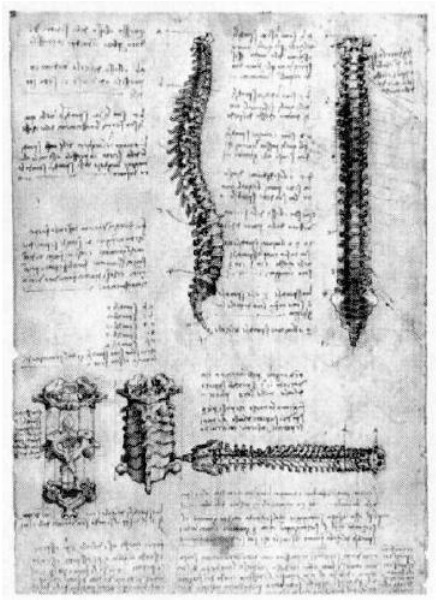

Figure 1.2. The details of the Human spine studied by Da Vinci. Adapted from Sanan and Rengachary (1996).

This work is divided into two branches: geometrical and functional. Firstly, a finite element (FE) model of the IVD is required. Such model shall include the relevant anatomical and geometrical features of the Human IVD. Secondly, the soft-tissues that compose the IVD must be identified and modeled in order to carry out the numerical simulations. These *in silico* studies shall allow the identification of the biomechanical functionality of the native human IVD and the pathways for its degeneration. Literature data and bioreactor experimental tests[IV] from research partners[V] are the benchmark for the evaluation of the numerical results obtained with the biomechanical model of the IVD to be developed under the present work.

[IV] The bioreactor experimental tests are *in vitro* compression studies performed with animal IVDs that are kept alive after extraction, between one to three weeks. Human IVDs are not used on these experiments, due to ethical issues, so the outcomes from animal IVDs are extrapolated to Human models.

[V] Department of Orthopedic Surgery, VU University Medical Center (VUmc, Amsterdam, The Netherlands).

1.2. Objectives

The present work is oriented to the development of a computational framework to study the specificities of IVD. In detail, this works involves updating a home-developed open-source FE solver and the development of a complete 3D FE model of an IVD.

The applied methodology starts with a literature review, in order to understand all the issues related with the Human IVD and its degeneration, as well as the state-of-the-art concerning the numerical modeling and numerical simulation of the Human spine. Additionally, this first stage will contribute for the definition of the situations to be numerically simulated and analyzed.

The developed FE model shall produce valuable information for the study of IVD degeneration and regeneration. Finally, the results from the Finite Element Analysis (FEA) will be compared with *in vitro/in vivo* tests, in order to validate the developed model and the implemented algorithms.

In addition, the present work runs in parallel with the European project NPmimetic[vi], which has the purpose of developing a biomimetic nano-polymer based gel for minimally invasive IVD regeneration treatment. The developments achieved in this work may also contribute for the progress of this project.

Therefore, four major objectives may be defined for this work:

1) Development of an accurate 3D FE model of a human IVD and its major adjacent structures;
2) Modeling and implementation of the time-dependent behavior of the IVD, using a home-developed open source FE solver. The most important features are:
    a. Hyper-viscoelasticity, i.e., rheological behavior of the IVD;
    b. Osmo-poroelasticity, i.e., multiphasic behavior of the soft-tissues that constitute the IVD, including the osmotic swelling pressure gradient;
3) Identification of the mechanical loads and mechanical properties of the healthy IVD, in order to establish an IVD characteristics framework. This objective will be completed with

[vi] For further information on this project, please visit www.npmimetic.com

the analysis of several groups of results, namely:

a. Short creep tests, i.e., computational tests with duration inferior to 3h, associated with short-term activities;
b. Long creep tests, i.e., computational tests with the duration of 48h, related to the Human daily activities;
c. Analysis of bioreactor data from VUmc, including comparison with analogous numerical simulations;

4) Contribute to the definition of a set of design specifications of the IVD functionality. The quantification of the mechanical properties is a key factor to the success and definition of treatment strategies of degenerated IVDs. The most relevant topics are:

a. The quantification of the appropriate mechanical loads to maintain the viability of the Human IVD, i.e., the determination of the limits for the healthy levels of loading;
b. The definition of the osmo-poro-hyper-viscoelastic characteristic of the native and degenerated IVD, i.e., the identification of the behavioral differences between what is a healthy IVD and what is a non-healthy one.

1.2.1. Contributions

The first contribution from the present work is the development of a full 3D FE model of a Human lumbar motion segment (MS), which includes one IVD and the two adjacent VBs. This model shall be geometrically and constitutively accurate, i.e., the FE model shall be able to reproduce the *in-vivo* behavior of the Human IVD, and such aim can only be achieved if the geometrical and constitutive features are correctly modeled. In addition, this model shall be also capable of accounting for the multiple degeneration-related behavioral changes that occur on the Human spine, in order to establish a framework for the biomechanical differences between native and degenerated conditions of the IVD, as much as possible.

Such model can only be developed and explored with the proper set of computational tools. This work deals with the update of a home-developed open-source FE solver, oriented to the IVD biomechanical features and implemented in FORTRAN language. This software was already oriented to the modeling and simulation of soft-tissues, as it included their almost

incompressibility, the most relevant constitutive models and viscoelastic effects, as presented by (Alves et al., 2010). However, it was limited to monophasic problems. As the IVD was previously identified as a multiphasic soft-tissue, an innovative biphasic formulation is here developed and implemented. This formulation is the second major contribution of the present work.

The third major contribution of this work is related with the validation of the first two key contributions, i.e., the validation of both MS model and FE solver. An integrated computational framework for the analysis of bioreactor data from the partners at VUmc is developed, combining custom-made FORTRAN data filters and numerical simulation through the open-source FE solver. Even if the validation task is first performed through comparison with well-known literature data, the analysis of the tests performed with the VUmc bioreactor is the paramount methodology for the evaluation of the *in vivo* behavior of the IVD, due to the nature of these tests[VII]. This group already published bioreactor-related works (Paul et al., 2013, 2012)[VIII], but a systematic tool for the analysis of the bioreactor outcomes was needed, as well as the comparison of the experimental outcomes with analogous numerical predictions, in order to achieve a better understanding over the complex IVD behavior. Simultaneously, such procedure also completes the validation of the numerical work.

[VII] As previously described, the bioreactor environment allows the maintenance of the IVD viability up to three weeks, under compression tests.

[VIII] Additional references on the analysis of the IVD behavior from this group may be considered: (Bron et al., 2009; Detiger et al., 2013; Smit, 2002; van der Veen, 2009).

1.3. Thesis Structure

The present thesis is globally structured in six chapters: "Introduction", "The Intervertebral Discs", "State-of-the-art", "Finite Element Modeling", "Results and Discussion" and "Conclusions". These chapters are briefly described below.

The first (and present) chapter, "Introduction", reveals the motivation and objectives for this work, under the framework of the FE modeling of the IVD.

The second chapter, "The Intervertebral Discs", is a comprehensive description of the particularities of the IVD, covering the grounds of anatomy, physiology, functionality, biomechanics and degeneration. In addition, this chapter also deals with the biomechanics of the IVD in the constitutive and numerical points of view, i.e., it includes a literature review of the constitutive modeling of incompressible soft-tissues (oriented to the IVD) and a description of the most significant IVD FE models available in the literature.

The third chapter, "Finite Element Modeling", presents the mechanical modeling, the development of the constitutive equations and the generation and optimization of the FE mesh. The fundamental tool for this work is an open-source home-developed FE solver, whose functioning and modeling features are described. This solver already comprised several relevant features of biomechanics, namely the almost incompressibility of soft-tissues, viscoelastic effects and the relevant isotropic and anisotropic hyperelastic laws. In addition, an innovative biphasic poroelastic formulation (coupled with osmotic swelling) is implemented and detailed. The IVD FE model is also fully described, from the geometrical features to the material properties.

The fourth chapter, "Validation", deals with the validation of the innovative biphasic poroelastic formulation. This task starts with the generic Terzaghi's 1D consolidation test. Afterwards, the validation task is performed using the IVD FE model, through comparison with literature data and also through a mesh convergence study.

The fifth chapter, "Results and Discussion", comprises a complete numerical study of the IVD, using FEM. The main purpose is to characterize the biomechanical behavior and functionality of the IVD (and the adjacent structures in the Human spine), both in healthy and pathological conditions. Several numerical tests are held and its results are compared with

available literature data and experimental tests from research partners. The results are analyzed and discussed at the light of the current knowledge on IVD FE modeling.

The sixth (and last) chapter, "Conclusions", is the comprehensive description of the outcomes of the present work. Therefore, a critical review of the whole work is presented. In addition, suggestions for possible future work are addressed.

This thesis also includes four annexes, including the exploration of one numerical case that was out of scope of the "Results and Discussion", the detailed analysis of a very particular experimental test from the research partners, the example of a set of input and output files of the open-source FE solver and, finally, the list of publications and communications related to the present work.

1.4. References

Adams, M.A., Dolan, P., McNally, D.S., 2009. The internal mechanical functioning of intervertebral discs and articular cartilage, and its relevance to matrix biology. Matrix Biol. 28, 384–9.

Adams, M.A., Roughley, P.J., 2006. What is intervertebral disc degeneration, and what causes it? Spine (Phila. Pa. 1976). 31, 2151–61.

Alves, J.L., Yamamura, N., Oda, T., Teodosiu, C., 2010. Numerical simulation of musculo-skeletal systems by V-Biomech. In: CMBBE2010.

Bron, J.L., Helder, M.N., Meisel, H.-J., Van Royen, B.J., Smit, T.H., 2009. Repair, regenerative and supportive therapies of the annulus fibrosus: achievements and challenges. Eur. Spine J. 18, 301–13.

Detiger, S.E.L., Hoogendoorn, R.J.W., van der Veen, A.J., van Royen, B.J., Helder, M.N., Koenderink, G.H., Smit, T.H., 2013. Biomechanical and rheological characterization of mild intervertebral disc degeneration in a large animal model. J. Orthop. Res. 31, 703–9.

Gamradt, S.C., Wang, J.C., 2005. Lumbar disc arthroplasty. Spine J. 5, 95–103.

Paul, C., Schoorl, T., Zuiderbaan, H., Zandieh Doulabi, B., van der Veen, A., van de Ven, P., Smit, T., van Royen, B., Helder, M., Mullender, M., 2013. Dynamic and Static Overloading Induce Early Degenerative Processes in Caprine Lumbar Intervertebral Discs. PLoS One 8, e62411.

Paul, C., Zuiderbaan, Zandieh Doulabi, B., van der Veen, A.J., van de Ven, P.M., Smit, T.H., Helder, M.N., van Royen, B.J., Mullender, M.G., 2012. Simulated-physiological loading conditions preserve biological and mechanical properties of caprine lumbar intervertebral discs in ex vivo culture. PLoS One 7, e33147.

Raj, P., 2008. Intervertebral Disc: Anatomy Physiology Pathophysiology Treatment. Pain Pract. 8, 18–44.

Sanan, A., Rengachary, S., 1996. The history of spinal biomechanics. Neurosurgery 39, 657–669.

Schmidt, H., Galbusera, F., Rohlmann, A., Shirazi-Adl, A., 2013. What have we learned from finite element model studies of lumbar intervertebral discs in the past four decades? J. Biomech. 46, 2342–55.

Smit, T.H., 2002. The use of a quadruped as an in vivo model for the study of the spine - biomechanical considerations. Eur. Spine J. 11, 137–44.

Van der Veen, A., 2009. Mechanical behaviour of the intervertebral disc under sustained compressive loading.

Whatley, B.R., Wen, X., 2012. Intervertebral disc (IVD): Structure, degeneration, repair and regeneration. Mater. Sci. Eng. C 32, 61–77.

2. THE INTERVERTEBRAL DISCS

The present chapter is a comprehensive description of the particularities of the IVD, covering the grounds of anatomy, physiology, functionality, biomechanics and degeneration. In addition, the IVD-oriented constitutive modeling and state-of-the-art on the IVD FE models are revised and detailed, with focus on the most relevant works published to date. In other words, this chapter deals with the review of the literature associated with the IVD, being divided in four sections, namely "Anatomy and Physiology", "Biomechanics", "Degeneration" and "Numerical Modeling".

2.1. Anatomy and Physiology

The Human spine is a complex system, anchored on an advanced neuromuscular control and consisting of 4 major zones: the neck with the cervical VBs (C1 to C7), the thoracic VBs (T1 to T12), the lumbar VBs (L1 to L5) and the sacral VB (S1). Figure 2.1 shows a representation of the complete Human spine, which is also denominated as vertebral column or backbone[1].

This is a stable structure, even if highly mobile. Furthermore, none of the components of the spine can be considered as self-sufficient, because they are mutually dependent (Ebraheim et al., 2004; Grumme and Bittl, 1998; Niosi and Oxland, 2004). The major functions of the spine are weight bearing, allowing motion between upper torso and pelvis and protection of the spinal cord and nerve roots (Dolan and Adams, 2001; Niosi and Oxland, 2004).

The functional unit of the spine is the MS, also denominated as functional spinal unit (FSU or simply SU) (Frei et al., 2002; Gamradt and Wang, 2005). There are 24 MS on the Human spine and each one of these load-sharing units is composed of 2 VBs linked by one IVD. Figure

[1] Sagittal (or lateral) and axial (or transverse) planes are the most frequent choice for spine and IVD representation, and are usually presented from the anterior (or ventral) position to the posterior (or ventral) position, or vice versa. Visualization of the frontal (or coronal) plane is less usual.

2.2 shows a picture of a sagittal cut of a healthy Human lumbar IVD (a)) and a schematic representation on the same perspective (b)). There are a total of 23 IVDs in the entire length of the spinal cord. It must be highlighted that there is no IVD between the C1 and C2 VBs (Raj, 2008).

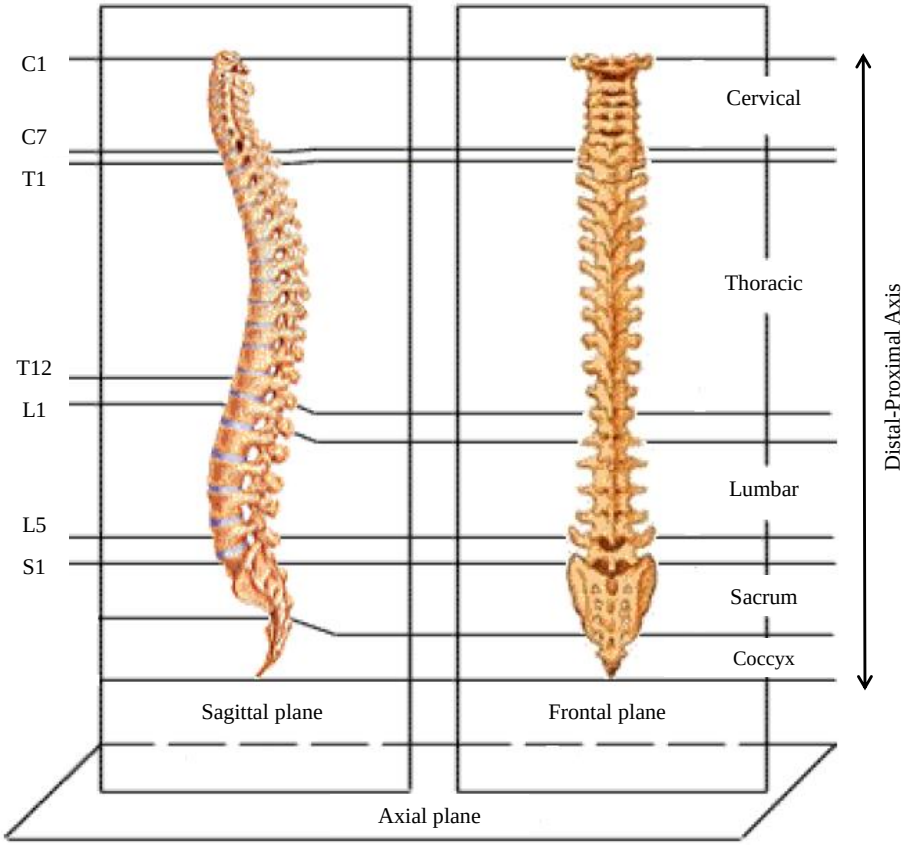

Figure 2.1. The complete Human spine, in both sagittal and frontal views. Adapted from Noailly (2009).

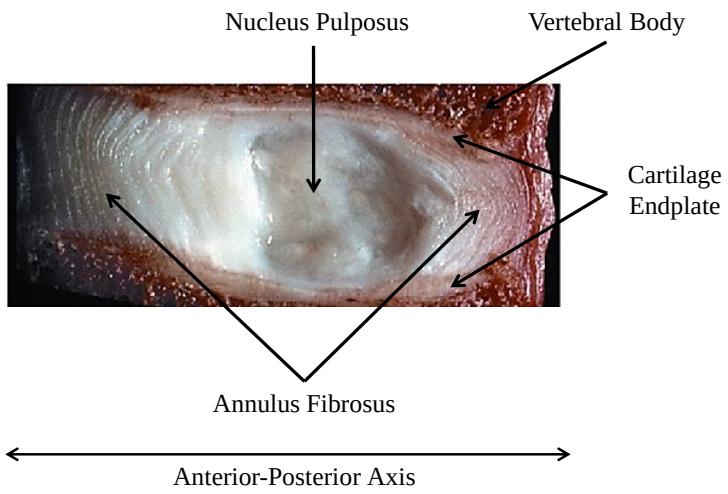

a)

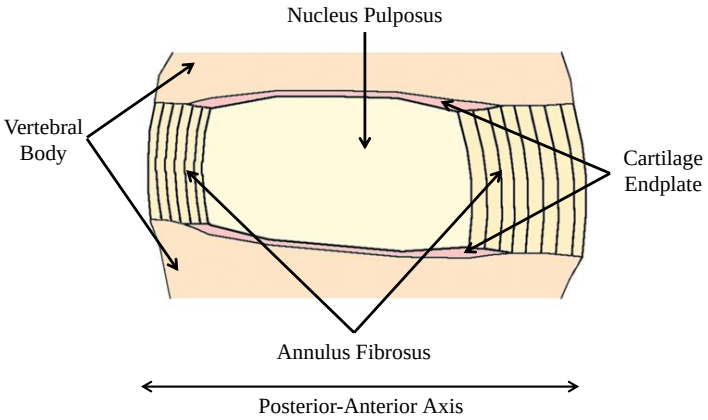

b)

Figure 2.2. The Human IVD: a) Ex vivo photography of a healthy Human lumbar IVD, with the VB also visible (mid sagittal cut, anterior-posterior direction). Adapted from Adams et al. (2009); b) Schematic representation of a mid sagittal cut of the IVD, posterior-anterior direction. Adapted from Noailly (2009).

The spine is exposed to different types of loads and stresses, namely dynamic and static loads, tensile stresses, torsional loads, shear stresses and a combination of tensile, compressive and shear stresses. The importance of the IVD for the spine is to maintain flexibility and motion, preserving the proper anatomic spatial orientation (Adams et al., 2009; Nixon, 1986; Riches et al., 2002). Nevertheless, the stability and dynamics of the Human spine is also dependent on other structures, namely the facet joints and several ligaments (Ebraheim et al., 2004).

The IVD is a highly inhomogeneous porous structure, which contains solid and fluid materials. It is, in its majority, avascular (Raj, 2008; Shankar et al., 2009). The central structures of the disc (NP and AF) are quite different in both constitution and function, but are paired structures, vertically limited by the CEPs and vertebral endplates (VEPs). The NP presents a gelly-structure with embedded fibers and occupies the core of the IVD. Surrounding it, emerge an amount of concentrically arranged fibers supported on a porous matrix, which is the AF (Shankar et al., 2009; Urban et al., 2000; Wagner and Lotz, 2004). The CEP is a layer of hyaline cartilage that is responsible for most of the nutrients exchange with the VB. Each IVD has approximately 7-13mm in height and 35-55mm in diameter (axial plane). If one considers the 23 IVDs stacked, this construct would comprise approximately one-fourth to one-third of the total height of the vertebral column (Ebraheim et al., 2004; Raj, 2008; Whatley and Wen, 2012). Figure 2.3 shows an example of a MS, with the IVD anatomy highlighted.

The VB is substantially stiffer than the IVD. It is a highly porous and vascularized portion of bone tissue, containing two distinct layers of bony material, as happens with other bony structures. The inner layer is the trabecular bone (TB), which can be roughly distinguished by the lower density, in comparison with the cortical bone (CB) (Fields et al., 2010). This last one forms the outside layer, which is in direct contact (proximal-distal axis of the spine) with the IVD through the VEP. The discrimination between the VEP and the CEP is not always clear, as some authors only refer to the "endplate" and do not separate these two structures (Swider et al., 2012). However, the CEP only covers the internal one-third of the extension of the AF, which means that this IVD component is also in direct contact with the VB. Therefore, even considering that a continuum medium is being discretized, the VEP is the existent and perceptible border between the IVD and the remaining VB (Adams et al., 2009; Ebraheim et al., 2004; Mirza and White, 1995; Raj, 2008).

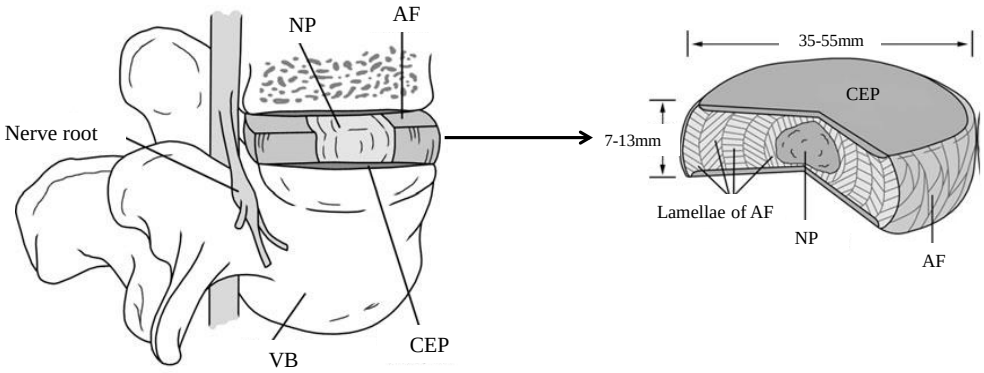

Figure 2.3. Anatomy of a MS, with emphasis on the IVD dimensions. Adapted from Raj (2008).

In what concerns to the boundaries between the three IVD components, these are to a certain extent visible, but the transition from one component to another is smooth. Therefore, detaching one from another is demanding, both on *ex vivo* experiments and computational imaging techniques (McNally et al., 2000). The discussion on the correct definition of the IVD internal boundaries may be correlated with the discussion of what is the better imaging technique to investigate the IVD structure and when should a certain technique be applied. Presently, discography, X-Rays, Computational Tomography (CT), Magnetic Resonance Imaging (MRI) and myelography are used (Grumme and Bittl, 1998; Li and Wang, 2006; Taher et al., 2012). CT images have proved to be a good tool for the segmentation of hard tissue like the bony structures, but turned out to be less efficient than MRI images in the detection of soft tissues,

such as the IVD components. However, more important than the imaging technique, the obtained images should have good resolution, in order to allow the identification of the IVD components and its healthiness.

The IVDs are positioned in one of the most sensible locations of the Human body, next to the spinal canals. Consequently, *in vivo* studies are quite challenging to perform (Nachemson and Morris, 1964). As a matter of fact, the work of Wilke et al. (1999) proved that those studies could be performed, but they are highly dependent on the availability of volunteers and the experiment can be excessively painful and intrusive. Therefore, the major part of the information about the IVD behavior still comes from *in vitro* studies. These studies are usually performed *ex vivo*, but some up-to-date techniques allow the IVD to be kept alive[II] after the sacrifice of the animal. The works of (Chan et al., 2013; Gantenbein et al., 2006; Korecki et al., 2007; Paul et al., 2013, 2012) described bioreactors capable of providing nutrition and mechanical stimulation to the extracted IVD between one to three weeks. This kind of procedures can become the next benchmark for IVD experimental studies. Allied to these remarkable developments, numerical studies through the FEM[III] are benefiting from the improvements on the computational power to become more exhaustive and wide-ranging every day (Schmidt, Galbusera, et al., 2013).

2.1.1. Nucleus Pulposus

The NP has high water content, through a highly hydrated gel. Embedded on this gel are fibers of collagen and elastin. In detail, the NP consists of two major regions: the solidified porous center and the surrounding gel-like area. Type II collagen and radially organized elastin fibers provide consistence to the central region and hold the less dense surrounding area, which contains proteoglycan molecules, with preponderance of aggrecan. The presence of hydrophilic glycoaminoglycans (mainly chondroitin and keratin sulfate) creates strong water-bonds and also contributes to the global consistency of the NP (Iatridis et al., 1996; Shankar et al., 2009; Urban et al., 2000).

The NP is osmo-poro-visco-hyperelastic, mostly isotropic and almost incompressible. It is neither exclusively a solid nor a fluid, thus it is considered a biphasic tissue (Iatridis et al., 1997,

[II] The artificial nutrition and the loading stimuli are the most important factors for the survival of the IVDs.
[III] Simulations through Multibody Systems (MBS) are also frequent for the study of spine macromechanics.

1996). However, it must be highlighted that young NP show tendency for a fluid-like behavior, which progressively turns into a solid-like behavior with ageing, as the hydration decreases.

Such characteristics tailor the NP into a structure that sustains the stress gradients *in vivo*, mainly compressive and shear stresses. The volumetric changes along the daily activities are almost exclusively due to the fluid exchanges with the adjacent structures (CEP and AF), which are regulated by the osmotic swelling pressure[iv]. Consequently, these internal pressure gradients rule the stress and strain profiles of the NP (Nerurkar et al., 2010; Schroeder et al., 2010; Schultz et al., 2009; Skrzypiec et al., 2007).

The complex biochemical composition is probably the key for the mechanical behavior of the NP, together with the spatial confinement between the AF and the CEP. Modeling approaches to the NP must consider the influence of both porous and fluid parts (multiphasic approaches), as well as the interaction between them (Huyghe et al., 2003; Schmidt, Bashkuev, et al., 2013; Schmidt, Galbusera, et al., 2013; Schroeder et al., 2010).

2.1.2. Annulus Fibrosus

The AF is stiffer than the NP. This higher stiffness is due to a porous matrix with high density of fibrous composite tissue. Its biochemical composition is mainly grounded on collagen fibers, but elastin fibers and proteoglycans can also be found. The biomechanical functions of the AF are containing intradiscal pressure (IDP)[v] and guiding the intervertebral motion (Adams and Green, 1993; Iatridis et al., 1999; Wagner and Lotz, 2004).

The architecture of the AF is highly stratified, with intricate angle relations (cross-angle) between several layers of fibers, which are denominated as lamellae. Marchand and Ahmed (1990) reported a range of 15 to 26 AF fiber layers, and it is frequent to see references to an average number of 20 layers (Iatridis et al., 2013; Noailly et al., 2005). Each one of these layers works to bear up the harsh mechanical conditions of the spine, in thigh association with spine ligaments. The AF fibers are inhomogeneous (region-dependent), thus the AF is typically divided into inner and outer regions. In fact, fibers present radial and circumferential differentiation, in terms of mechanical properties and cross-angle (Holzapfel et al., 2005; Malandrino et al., 2013).

[iv] The concept of "osmotic swelling pressure" will be detailed in the following section.
[v] The AF acts as vessel wall, in order to intradiscal fluid.

The outermost fibers of the AF are well organized and more resistant to tensile forces, i.e., after flexion or extension efforts, the elastin fibers are essential to the return of the whole IVD structure to its pre-movement position. Therefore, these fiber layers are responsible for the characteristic bulging effect of the AF, as a response to the NP pressure gradient.

The organization and concentration of the collagen fibers decreases from the outside into inside, which means that the innermost AF is less stiff. A thin band of tissue makes the transition from the AF to the NP (Adams and Green, 1993; Eberlein et al., 2001; Holzapfel et al., 2005). This structural organization leads to a tissue that is anisotropic and osmo-poro-visco-hyperelastic (Eberlein et al., 2001; Holzapfel et al., 2005). FE models of the AF commonly use hyperelastic constitutive laws with tension-only reinforcing elements to model the collagen fibers (Little et al., 2010; Noailly et al., 2005).

2.1.3. Cartilage Endplate

The CEP is a thin layer of hyaline cartilage, composed by proteoglycan, collagen and water. Such composition is quite close to the composition of articular cartilage, but the water content of the articular cartilage is superior (Wilson et al., 2007). It is a non-uniform structure, with an average thickness of 0,6mm. The highest cell density is registered in its center, but the center is also the thinnest region of the CEP (Hamilton et al., 2006; Moore, 2006, 2000; Roberts et al., 1989).

Nevertheless, Thompson's morphological classification of IVD degeneration[VI] originally considered the irregularity of the CEP as a degeneration mark (Thompson et al., 1990). It acts as an anchoring structure, covering the whole extension of the NP and about one-third of the AF, but it includes some points of contact with the marrow as well (Moore, 2006, 2000).

Given these features, the CEP is the main responsible for the exchange of nutrients with the adjacent VB, as already indicated (Swider et al., 2012). Figure 2.4 shows the nutrition pathways of the IVD. Since the healthy IVD is avascular for adult Humans, the greater part of its nutrition goes by diffusion, as the capillary network of the CEP take the nutrients to the inner parts of the IVD, by osmotic regulation of the proteoglycan content (Hamilton et al., 2006; Jackson et al., 2011; Roberts et al., 1989).

[VI] This classification will be detailed in the third section of the present chapter.

Subsequently, most of the known problems affecting the IVD tend to start or to involve CEP-related issues. When the CEP is calcified (by ageing effect, for example), it becomes gradually impermeable, so the flow of nutrients is interrupted. Later on, this effect may promote the appearing of cracks, which will increase again the permeability, but the fluid flow is then hardly regulated. In addition, an incomplete or injured endplate will be less able to withstand the pressure from the NP. Fractures may cause this kind of damage too. Pathological conditions of the CEP may also lead to the appearance of protuberant structures on the adjacent VB, denominated as Schmorl's nodes. These nodes are probably a root for disc degeneration (Adams and Dolan, 2012; Iatridis et al., 2013; Moore, 2006).

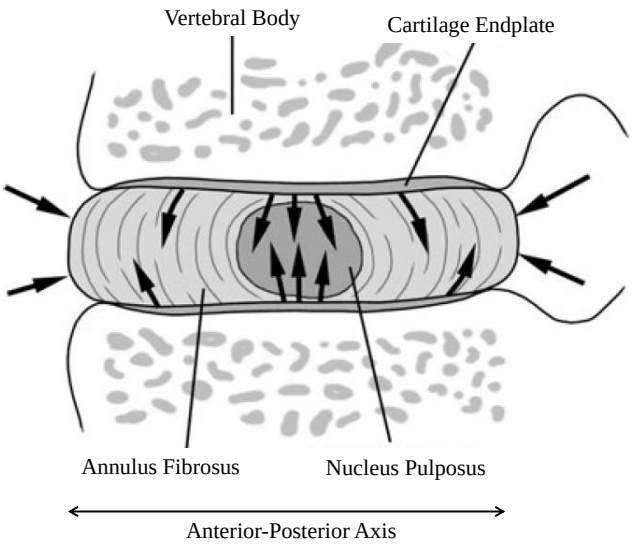

Figure 2.4. Nutrition pathways of the IVD. Adapted from Raj (2008).

2.1.4. Cellular Level

The extracellular matrix (ECM) of the IVD cells has a "cartilage-like" behavior, which may explain most of the characteristics of the IVD components. The major issue concerning the current knowledge about the mechanobiology of IVD cells is the source of the data, given that *in vitro* or *in vivo* animal experiments are not able to mimic the response of the Human cells (Beckstein et al., 2008; Schmidt and Reitmaier, 2013). The *in vitro* tests are performed with isolated cells or separated group of cells, instead of a proper continuum environment. The *in vivo* animal experiments can be useful to understand the live phenomena, but they are (at most) comparable

to the Human cells[VII]. Therefore, the mechanisms of mechanotransduction of the Human IVD are not quite understood yet, even if there is evidence that the ECM determines the non-uniform intercellular mechanical environment of the IVD (Choi, 2009; Guilak et al., 1999; Hsieh and Twomey, 2010; Song et al., 2008).

Today there is recognition that the IVD has a low metabolic rate. Moreover, the NP cell population changes drastically since immaturity to adulthood: from chordocytes and chordoblasts to chondricytic cells. The exact behavior of the immature NP cells is one of the major questions that remains to be answered in this field of knowledge, even if the mechanical properties follow the natural changes related with ageing: from predominantly swelling properties to elastic properties. Therefore, NP cells are usually subjected to compression and shear stresses, combined with the tendency of the tissue to swell (Neidlinger-Wilke et al., 2013). However, relative cell homogeneity is maintained, opposite to the AF inhomogeneous cell population. This inhomogeneity corresponds to the layered structure of the AF and contributes to its complex mechanical behavior. The AF cells are typically subjected to tensile and shear strains, which may occur between the lamellae or even within the lamellae (Adams and Green, 1993; Hsieh and Twomey, 2010; Neidlinger-Wilke et al., 2013). Given that the nutrients supply is provided by the CEP, the cells from this component are determinant for the maintenance of synthesis and integrity of the ECM (Cao et al., 2011; Choi, 2009; Shirazi-Adl et al., 2010; Song et al., 2008).

[VII] Alini et al. (2008) reported that the absence of notochordal cells in adult cow and sheep NP resembles the organization of Human adult NP, which does not occur with other animals, such as mouse, dog or pig.

2.2. Biomechanics

The major role of the IVD is mechanical, as it constantly transmits loads arising from body weight and muscle activity through the spinal column, starting on the head into the upper extremities and beginning on the torso into the lower extremities. Each IVD provide six degrees of freedom to the correspondent spinal MS, serving as a central axial structure for cushioning loads. Moreover, it must be highlighted that the IVD has a rate-dependent behavior, based on viscoelasticity (short periods, under 1min) and poroelastic effects (longer periods, from minutes to hours) (Ebraheim et al., 2004; Galbusera, Schmidt, Noailly, et al., 2011; Raj, 2008; Schroeder et al., 2010; Shankar et al., 2009).

Diverse mechanical solicitations on the spine take place all day long, even during rest or sleep. The response of each MS is clearly influenced by the IVD behavior and by the interaction with the adjacent structures, namely ligaments and musculoskeletal system. In addition, the distribution and transfer of loads is dependent on the type of solicitation. For example, the MS is stiffer in extension than in flexion, even if the IVD internal pressure is higher on flexion movements (Jayson et al., 1973; Martinez et al., 1997; Riches et al., 2002; Williams et al., 2007). During activities as frequent as level walking, the peak compressive forces can rise to more than three times of the value of body weight, increasing to at least five times of the value of body weight for vigorous forms of activity or at the extremes of motion, with trunk flexion or load carriage. However, concerns must be particularly addressed to the first hours of the day, due to an effect of bending stiffness that is declared to occur during the first three active hours of the day (after the rise up). During bending and lifting tasks, the peak bending moment resisted by the lumbar spine is twice as great in the early morning compared to later in the day, on healthy people with no IVD degeneration (Dolan and Adams, 2001; Rohlmann et al., 2006; Snook et al., 2002; van der Veen, 2009)

The healthy IVDs are very similar along the different spinal levels, in both composition and function. Mostly size and shape vary from the cervical level into the lumbar region (Ebraheim et al., 2004). Given these geometrical differences, the stress and strain fields are different. The lumbar spine is the most studied section, since it concentrates most of the circadian deformation, and thus most of the injuries. Spinal instability, disc degeneration, posture, loading

history and muscle fatigue were proved to significantly change the stress distribution, inside the IVD (Moore, 2006; Niosi and Oxland, 2004; Panjabi, 2003). On the one hand, the IVD is an anisotropic structure, dependent on the fiber directions, mainly those from the AF (Adams and Green, 1993; Tsuji et al., 1993). On the other hand, the loading equilibrium is provided by the osmotic swelling pressure. The osmotic swelling pressure is the regulatory mechanism of the solute exchange through permeable membranes, i.e., the minimum pressure to nullify osmosis. In simple terms, the healthy IVD permanently presents a given positive internal pressure that ensures the integrity and responsiveness of the system[VIII], mostly due to the NP swelling properties[IX] (Lanir, 2012; Sivan et al., 2006; Whatley and Wen, 2012). The IVD osmotic swelling behavior is more noticeable on the height recovery during rest periods (Adams et al., 2009; Galbusera, Schmidt, Noailly, et al., 2011; Zander et al., 2010). The conjunction of these features (anisotropy and osmotic swelling pressure) with the viscoelasticity of the tissues (matrixes and fibers) allows the IVD to deal with a great complexity of efforts.

The NP is responsible for sustaining the axial compressive loads, while the tensile stresses are held by the AF, which is always in a pre-stressed condition. In detail, under loading conditions, the pressure goes from the NP to the surrounding structures, i.e., a radial flow occurs from the NP into the inner layers of the AF and a vertical flow is noticed from the NP into the CEPs (Neidlinger-Wilke et al., 2013; Raj, 2008). Figure 2.5 shows a schematic representation of this pressure distribution inside the IVD.

These phenomena may occur dynamically at multiple time scale and convert the compressive loading from the NP into tension within the AF, while reducing the loads on the adjacent VB. However, different loading profiles may disarrange this organization. For example, sustained compression efforts decrease the NP pressure and increase the compressive stress in the AF and neural arch (Adams and Dolan, 2012; Iatridis et al., 2013; Nixon, 1986).

The CEP is not really able to handle with compressive loads, but has also the function of absorbing some of the pressure that originally comes from the NP. Therefore, this component acts as a physical barrier, establishing the major part of the IVD-VB interactions (Hadjipavlou et al., 2008; Moore, 2006; Roberts et al., 1989; Shankar et al., 2009).

[VIII] This is extremely relevant for the maintenance of healthy IDP levels (Adams et al., 2009).

[IX] The native NP osmotic swelling pressure is around 0.20MPa, while the equivalent pressure for the AF is around 0.05MPa (Galbusera, Schmidt, Noailly, et al., 2011).

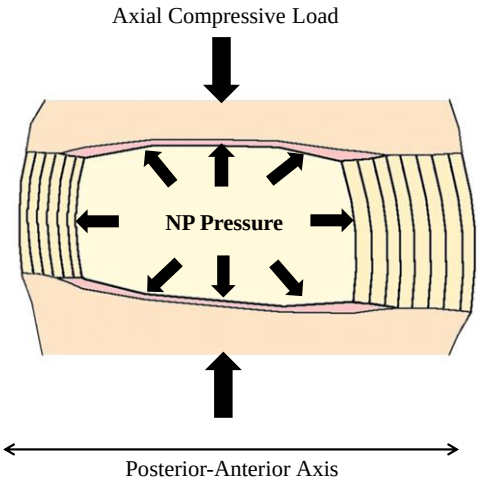

Figure 2.5. Schematic representation of the pressure distribution inside the IVD, under a typical axial compressive load. Adapted from Noailly (2009).

2.2.1. Loads

The spine system experiences the most demanding mechanical solicitations of the whole Human body. Day by day, on an infinite diversity of environments, the spine is being subjected to different kinds of loading profiles, in slow or rapid movements. In simple terms, there are compressive and shear loads and a complex combination of compressive and shear forces as well (Bazrgari, Shirazi-Adl, and Kasra, 2008; Frei et al., 2002; Niosi and Oxland, 2004; Schultz et al., 1982). The lumbar spine transmits loads between each intervertebral level through the IVD and the facet joints. Under compression, the load is transmitted primarily through the anterior spine. For that reason, the IVD is able to support large loads within the spine.

The dominant features for load-bearing are the maintenance of the internal pressure within the NP[x] and the associated bulging effect on the AF and on the CEP. Nevertheless, some authors have suggested that the proportion of load transmission shifts to the posterior elements of the spine with advancing degeneration (Bazrgari, Shirazi-Adl, and Kasra, 2008; Natarajan et al., 2004; Niosi and Oxland, 2004; Rohlmann et al., 2006). This means that whenever the portion of load transmitted through the anterior spine is decreased, degeneration is probably occurring or has occurred. Under shear loads, it was found that the healthy IVD transfers load peripherally through the AF. Unfortunately, there is a lack of studies concerning the biomechanics of load

[x] NP internal pressure is mostly based on the osmotic swelling pressure gradient.

transfer in shear or in combined loading (Bazrgari, Shirazi-Adl, and Larivière, 2009; Bazrgari, Shirazi-Adl, and Kasra, 2008; Iatridis et al., 1999; Yang and King, 1984).

The regular daily loads[xi] are averagely 200N during rest[xii] and between 600 to 800N during activity. For the present discussion, the magnitude of the loads is considered as independent from the type of solicitation, i.e., all the described activities are equaled to a compressive load. Nevertheless, this is only an oversimplification, since angular movements[xiii] are of topmost importance for the spine. Typical moments on the spine for pure flexion and extension movements are averagely 4 to 10 Nm[xiv]. These moments correspond, for example, to position changes (Guan et al., 2007; Rohlmann et al., 2012). In what concerns the daily periods, moderate activities such as level walking, sitting or carrying light objects are considered for the typical loading profiles (Adams et al., 1987; Sato et al., 1999; Wilke et al., 1999). Harsher activities, such as lifting and carrying heavy objects, may be represented through 1500 or even 2000N loads (Pollintine et al., 2010; Wilke et al., 1999).

2.2.2. Mechanical Responses

The velocity of a given movement is one of the factors influencing the mechanical response of the spine, i.e., if the movement is faster, the effect for the structures of the spine is more severe. Such effect is more noticed on the IVD, regardless of the type of movement or carried/lifted load. The acceleration of the movement also determines the response of the spinal structures, because muscle activation-reaction mechanism is more difficult when a given movement begins suddenly. The muscles, as well as the ligaments, may not accomplish the task required by that sudden movement, so the spine will be exposed to excessive loadings and the probability of injury is larger (Bazrgari et al., 2008a; Colombini et al., 2008; Dolan and Adams, 2001; Niosi and Oxland, 2004).

The posture of the subject is determinant for the response of the Human spine, particularly on the magnitude of the beard load and percentage of load transferred through the spinal

[xi] For the present discussion, the magnitude of the loads is considered as independent from the type of solicitation, i.e., all the described activities are equaled to a compressive load.

[xii] The rest period is associated with lying prone.

[xiii] Angular movements: rotation, flexion and extension.

[xiv] Moments from 1 to 20Nm are reported in the literature (Guan et al., 2007; Moramarco et al., 2010; Rohlmann et al., 2012; Schmidt et al., 2009).

structures. Subjects who work constantly with flexed postures probably have higher risk of developing spine diseases, as the consequences of the loading effects become less sustainable and the condition of the IVD is increasingly degraded (Gunning et al., 2001; Holzapfel et al., 2005; Nerurkar et al., 2010; Rohlmann et al., 2012). To prove this point, one may mention the concept of Whole Body Vibration (WBV), i.e., the exposition of the body to vibratory environment. Such conditions influence the response of the Human tissues and the spine is not an exception (Dupuis and Zerlett, 1987). People are not only exposed to WBV in harsh working environments (truck drivers or construction workers, for example), but even in their leisure time. Indeed, some authors defend that WBV is a proper training method for better performances in work and sport (Prisby et al., 2008), while others have found that it is a risk factor for spinal injuries (Dupuis and Zerlett, 1987; Guo et al., 2011; Wilder and Pope, 1996).

The works of Bazrgari and co-workers (2008 to 2009[xv]) reported that the probability of occurrence of DDD may be increased by long exposure to vibration, augmenting the consequences of IVD degeneration, especially if linked with genetic predisposition. The assessment of WBV may help to understand, macroscopically, the degree of mechanical solicitations on the spine and, subsequently, on the IVD. They also investigated the effects of musculoskeletal excitation on the spine and concluded that near-resonance frequencies are associated to heavier loads.

[xv] Full references: Bazrgari, Shirazi-Adl, and Kasra (2008); Bazrgari, Shirazi-Adl, and Larivière (2009); Bazrgari, Shirazi-Adl, and Parnianpour (2009); Bazrgari, Shirazi-Adl, Trottier, et al. (2008).

2.3. Degeneration

The degeneration of the IVD is firmly associated with the diseases of the spine, particularly low back pain. For many years, a considerable amount of studies have developed efforts to trace the causes and possible solutions for such issue, given that spine problems are a major cause of disability on western societies. Recent reports from the European Commission (and associated agencies) clearly show that the frequency of these diseases tends to augment every year (European Agency for Safety and Health at Work, 2008; European Comission, 2007; Hadjipavlou et al., 2008; Taher et al., 2012).

The mechanical structure, and consequently the mechanical behavior of the three main components of the IVD are altered by degeneration. Figure 2.6 shows different snapshots on the comparison between healthy and degenerated IVDs. The beginning of adulthood has been described as the age for the first symptoms of IVD degeneration to appear: an effect of conversion of tensile stresses in compressive stresses is stated to occur, meaning weakened mechanical conditions of the AF and CEP (Adams et al., 2009; Holm et al., 2004).

Afterwards, the NP will be affected, as the fluid exudation is insufficient and the aggrecan content is degraded. Overall, the mechanical performance stress distribution is altered, as the load-support function is progressively transferred from the NP to the AF. The IVD starts to suffer from increasing height reduction, the hydration level is also lower and herniation may occur. These events may be correlated with pathologic quantity and distribution changes on the collagen fibers (Choi, 2009; Hadjipavlou et al., 2008; Iatridis et al., 2013; Shankar et al., 2009; Urban and Roberts, 2003). On the one hand, it should be highlighted that none of these events occur separately, as all the components of the IVD are mutually-dependent. On the other hand, the timeline is not linear, as the described complications may be happening simultaneously or not.

The causes for IVD degeneration are not yet fully understood, and the complaints from the patients are also miscellaneous. An assortment of pathways for degeneration may be numbered: it may start with a fracture (or other damage) on the CEP, as a result of abnormal loading or calcification (Colombini et al., 2008). Proteoglycan loss, first on the CEP and then on the NP, may precipitate degeneration as well (Massey et al., 2012). Moreover, it must be highlighted that

CEP failure is one of the most important triggers for DDD, as nutrition can be interrupted and so the viability of the IVD cells is compromised. The nutrients flow can still be ensured through the outer AF, but this pathway is not enough to maintain the integrity of the whole IVD[XVI] (Adams and Roughley, 2006; Galbusera et al., 2013; Hadjipavlou et al., 2008).

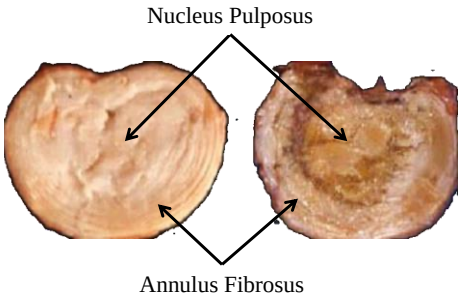

a)

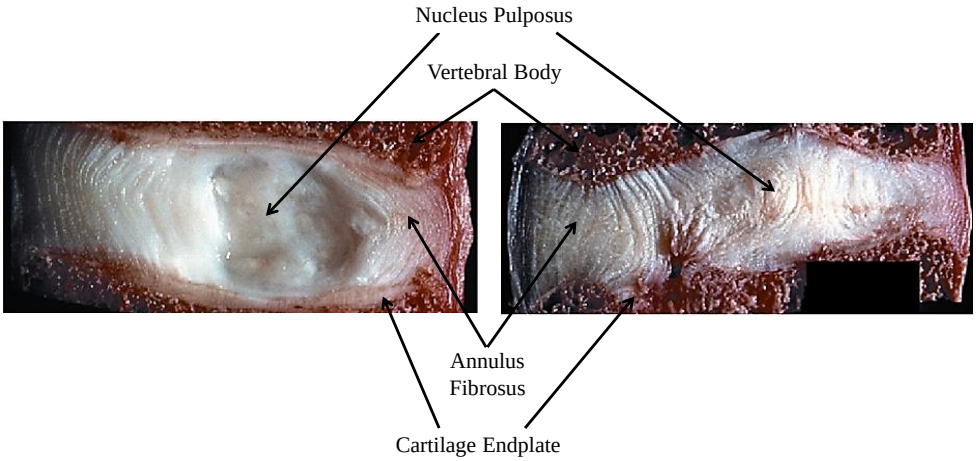

b)

Figure 2.6. Comparison between healthy (left) and degenerated IVDs (right): a) Axial cut. Adapted from Urban & Roberts (2003); b) Sagittal cut. Adapted from Adams et al. (2009).

The individual environmental conditions are also important to understand this problem, namely vibratory[XVII] environments or other demanding work postures (Dupuis and Zerlett, 1987; Niosi and Oxland, 2004; Stokes and Iatridis, 2004). Consequently, the etiology of IVD degeneration must be described as multifactorial, considering the range of factors that may cause it: genetic factors (the group of genes corresponding to the various components of the

[XVI] The pathways for IVD nutrition were already described in the previous sections of the present chapter.
[XVII] The effects of vibration on the Human spine were described in the previous section.

ECM are strongly related to the risk factors for degeneration), metabolic disorders, neurogenic inflammation, autoimmune issues, low-grade infection, toxicity, nutrition issues, ageing and mechanical factors (Beattie, 2008; Hadjipavlou et al., 2008; Kalichman and Hunter, 2008). Again, these factors may occur simultaneously, with direct or indirect links, contributing for the pathologic state of the IVD, as shown in Figure 2.7. One must also take into account that IVD degeneration may be considered as an expression of the state of the IVD, and not so much as a diagnostic for a disease (Kalichman and Hunter, 2008).

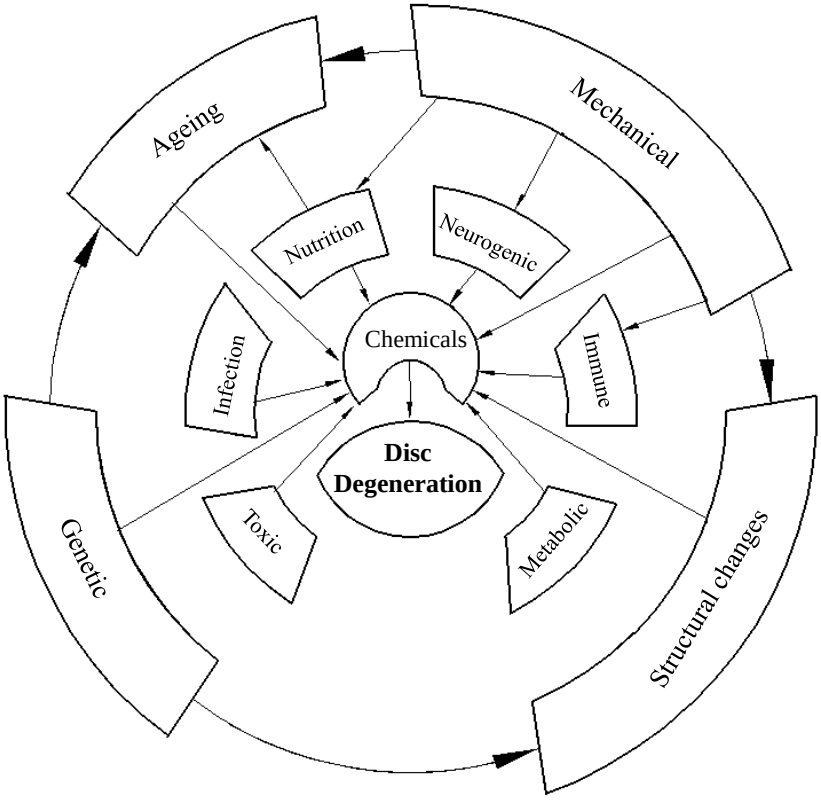

Figure 2.7. Multiple pathways for IVD degeneration. Adapted from Hadjipavlou et al. (2008).

Ageing is one of the most reported factors for IVD degeneration, even if some complications are not age-related, such as disc narrowing. IVD herniation, for example, is related with senescence of disc cells. Blood irrigation of the IVD is also a collateral effect of ageing, as the IVD is not vascularized (Hadjipavlou et al., 2008; Shankar et al., 2009; Song et al., 2008; Urban and Roberts, 2003). Nowadays, it is also widely accepted that mechanical stress and inflammatory response are directly connected. At the cellular level, abnormal events (as chronic loading or severe acute efforts) trigger metabolic reactions (which begin on lower nutrients

supply) that lead to loss of extracellular matrix integrity, and consequently, losses on disc functions (Colombini et al., 2008). Figure 2.8 gives a perspective on the detailed sequence of events that lead to IVD degeneration after abnormal chronic load.

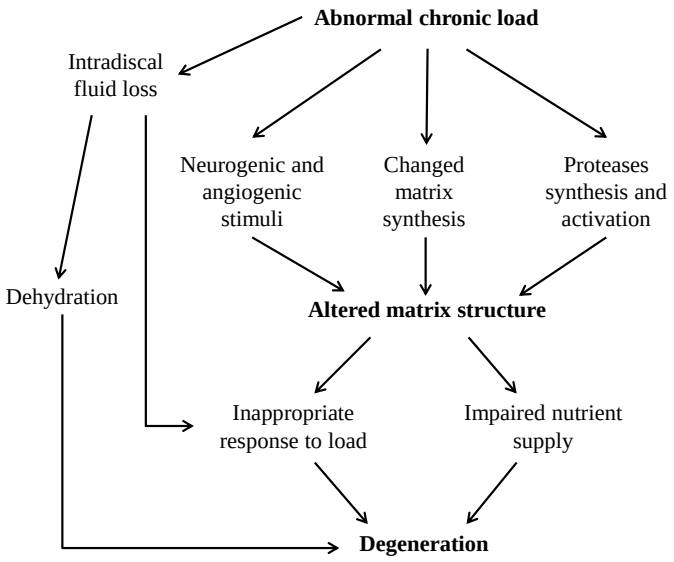

Figure 2.8. Metabolic changes in discs subjected to abnormal loads. Adapted from Colombini et al. (2008).

Furthermore, the pathway for IVD degeneration may depend on the time of the day: it is recognized that early hours of the day are more suitable to spine injuries, so IVDs become more vulnerable to degeneration if subjected recurrently to efforts during that time. Accumulation of repetitive efforts or, in other words, fatigue, has also an important role on promoting the degeneration, due to the low metabolic rate presented by the IVD (Dolan and Adams, 2001; Martin et al., 2002; Niosi and Oxland, 2004).

Along the years, several classifications of IVD degeneration have been proposed. The first benchmark was the Thompson scale (Table 2.1), primarily based on *ex vivo* morphological analysis over the mid-sagittal plane of the MS (Thompson et al., 1990). The Pfirrmann scale (Table 2.2) benefited from the advances of the imaging techniques and provided an *in vivo* classification through MRI (Pfirrmann et al., 2001). Both scales consider five grades, from minor to severe degeneration. The primary *ex vivo* analysis is clearly useful for the *in situ* evaluation of the tissues, so these two classifications are complementary. Given the intricate nature of this problem, some particular cases may not be fully diagnosed through imaging methods, i.e., if the images do not match the patient complaints, the diagnostic will rely mostly on the experience of

the examiner and also on the cooperation of that patient. Some authors even defended that the existing classifications were not detailed enough and proposed modifications. In detail, the modified Pfirrmann scale elaborated by Griffith and co-workers has 8 grades, including meticulous evaluation of the IVD height decrease, for the more severe cases (Griffith et al., 2007). Nevertheless, most of the authors agree that the IVD is a very specific tissue and shows unique rates of degradation, in comparison with other connective tissues (Adams and Roughley, 2006; Gamradt and Wang, 2005; Griffith et al., 2007; Pfirrmann et al., 2001; Roughley, 2004). At worst, disc prolapse (or even rupture) may occur, as a combination of degradation effects, formation of fissures and severe loading (Wognum et al., 2006).

Table 2.1. Morphological classification of IVD degeneration grades. Adapted from Thompson et al. (1990).

Grade	NP	AF	CEP	VB
I	Bulging gel	Discrete fibrous lamellae	Hyaline cartilage with uniform thickness	Margins rounded
II	White fibrous tissue peripherally	Mucinous material between the lamellae	Thickness irregularities	Margins pointed
III	Consolidated fibrous tissue	Extensive mucinous infiltration and loss of distinction between the NP and the AF	Focal defects	Early chondrophytes or osteophytes at margins
IV	Horizontal clefts, parallel to the CEP	Focal disruptions	Fibrocartilage extending from subchondral bone, which suffers from focal sclerosis and irregularity	Osteophytes smaller than 2mm
V	Clefts extend through NP and AF Lost		Diffuse sclerosis	Osteophytes larger than 2mm

Table 2.2. Imaging classification of IVD degeneration grades. Adapted from Pfirrmann et al. (2001).

Grade	Structure	Distinction between NP and AF	Signal intensity	Height of the IVD
I	Homogeneous, bright white	Clear	Hyperintense, isointense to cerebrospinal fluid	Normal
II	Inhomogeneous, with or without horizontal bands	Clear	Hyperintense, isointense to cerebrospinal fluid	Normal
III	Inhomogeneous, gray	Unclear	Intermediate	Normal to slightly decreased
IV	Inhomogeneous, gray to black	Lost	Intermediate to hypointense	Normal to moderately decreased
V	Inhomogeneous, black	Lost	Hypointense	Collapsed disc space

2.3.1. Associated Diseases

The DDD, also known as spondylosis, is a condition expressed by degenerated IVD. Patients may suffer from disc herniation, spinal stenosis or a combination of both, since the symptoms for these diseases tend to overlap and one may provoke the other. Other spine diseases, as rheumatoid arthritis[XVIII] , may (indirectly) contribute to the deterioration of the condition of a patient with DDD (Roughley, 2004; Shankar et al., 2009).

DDD involves an accelerated pathology, mostly initiated by a small protrusion that presses the posterior longitudinal ligament. Subsequently, this protrusion starts to increase and causes back pain, followed by large protrusion that herniates through the posterior ligament. At this stage, the integrity of the nerve roots is compromised and the pain is acute. Progressive degeneration of the IVD leads to osteoarthritis, including angiogenesis and cytokine release in the area that can spread to the posterior intervertebral joints as well as to the central joints (Panjabi, 2003; Ruberté et al., 2009; Urban and Roberts, 2003).

Furthermore, spinal instability, disc narrowing or injuries caused by mechanical loads[XIX] can lead to DDD, or at least improve the chances of this disease to appear. After some years studying this subject, Panjabi (2003) resumed clinical spinal instability as the condition of inability of the spine to maintain the proper kinematic performance under normal physiological conditions.

Mechanical instability is a slightly different concept, as it is characterized by loss of the ability to handle spinal loads. To sum up, this lack of stability produces abnormal intervertebral motions, which accelerate the degenerative process. However, the opposite may also be true: degenerated discs may produce abnormal kinematic patterns (Colombini et al., 2008; Grumme and Bittl, 1998; Panjabi, 2003).

Disc herniation is normally triggered by weakening or tearing of the AF, caused by excessive stress or even by an accident. Ageing also plays an important role, considering the senescence of the IVD cells. It provokes abnormal compression of the spinal cord and nerve roots and, consequently, inflammation of these structures. Herniation may occur as bulging, protusion, extrusion or a free fragment (Adams and Roughley, 2006; Buy and Gangi, 2010;

[XVIII] Rheumatoid arthritis is a progressive inflammatory condition which is characteristic of synovial joints.

[XIX] Injuries caused by mechanical loads may be acute (e.g., whiplash) or resultant from abnormal chronic loads (e.g., wrong working postures).

Michalek et al., 2012). Spinal stenosis has almost the same consequences, and can be triggered by a previous degenerated state, osteoporosis or a tumor. The narrowing of the lumbar spine canal exposes the nervous components to acute damage (Fritz et al., 1998; Pollintine et al., 2010).

2.3.2. Treatments

The intricate etiology of the DDD leads to several approaches for its treatment, from disc arthroplasty to gene therapy (Andreula et al., 2004; Iatridis et al., 2013; Martin et al., 2002; Van den Broek et al., 2012). Native and degenerated IVD properties have been studied in Human and animal models, as well as new treatment strategies. Goat and sheep models are the most frequent, as they show similar properties to Human IVD. However, here again some doubts still exist about the validity of those studies for the development of solutions for Human DDD[xx]. Other treatments, such as ozone therapy or NP replacement through hydrogel injection are less invasive and tend to present better results, in case of light to moderate degenerative stages.

Nevertheless, one shall consider first the non-surgical treatments, such as pain relief medication and physiotherapy methods. This first option may produce effective results, if the disease is in its preliminary stages (Strange et al., 2010; Wilke et al., 1999). The surgical options shall only be considered after the failure of the conservative rehabilitation procedures.

Most of the established surgical treatments of DDD show reasonable results on pain reduction, particularly in short-term. Spinal fusion, chemonucleolysis, microdiscectomy or disc arthroplasty[xxi] are the most applied techniques. However, they are mostly invasive[xxii] and they are also not totally satisfactory in terms of restoring the capability of normal motion to the patients (Andreula et al., 2004; Gamradt and Wang, 2005). Therefore, surgeons seek new spinal technologies, which must be minimally invasive to reduce pain and preserve motion. In addition, such strategies shall ensure long-term or permanent cure. Potential biological strategies that have been studied include protein injection, gene transfer, and cell therapy. Although short-term

[xx] Alini et al. (2008) reported the similarities between Human and goat (or cow) IVD cells (as described in the first section of this chapter), while Smit (2002) analyzed (and supported) the use of quadruped animals for Human-related IVD studies, in terms of biomechanics.

[xxi] Disc arthroplasty may include total or partial substitution of the IVD.

[xxii] Tissue disruption may be pointed out as the major disadvantage of the massively invasive techniques.

satisfactory outcomes have been reported following intradiscal injection of growth factors, this method faces several limitations. Gene therapy may be more effective, but similar doubts as with protein administration arise. The safety of gene transfer into IVD cells needs to be further investigated as well, since the science of IVD cell transplantation is still in its early stages. Advancements in nanotechnology based tissue regeneration techniques may offer the possibility of repairing damaged discs, but such techniques are also not satisfactorily developed yet (Ruan et al., 2007; Taher et al., 2012; Yoon, 2005).

Ozone therapy is a minimally invasive technique that consists on the injection of a medical mixture based on oxygen and ozone (Oder et al., 2008). The surgeon guides the insertion of the needle into the NP recurring to live image feed (X-Ray). For patients under 50 years old, this may be the best answer, if they are suffering from an early stage of DDD. Older patients or those suffering from an advanced stage of DDD are not eligible for this kind of therapy (Andreula et al., 2003; Muto et al., 2004). Even if this technique has been motivating significant debates, most of the studies proved its safety and reliability (Re et al., 2008; Steppan et al., 2010). It has three major advantages, namely i) being minimally invasive, ii) the patient may leave the hospital a few hours after the treatment and iii) no tissue is removed, as this technique is solely based on the injection of a compound.

If the patient is suffering from moderate to severe DDD, the current treatment trend is NP replacement techniques through hydrogel injection. This technique is being constantly improved and can even become to be the best strategy to preserve normal spine biomechanics and tissue integrity, as much as possible. Since only that damaged portion of tissue is removed, this procedure can still be considered as minimally invasive. The procedure consists on the injection of a two-function needle, which means that the removal of the degenerated NP tissue and the injection of the compound is done through the same channel, i.e., the needle (Reitmaier et al., 2012; Silva-Correia et al., 2011; Van den Broek et al., 2012).

2.4. Numerical Modeling

Soft tissues in general and the IVD constituents in particular are known to be highly complex and very much dependent on the characteristics of each individual, as well as on its biomechanical function.

The IVD is a very good example of a highly specific soft tissue, because it is a heterogeneous mixture of a highly hydrated core (the NP) with a dense structure of fibers (on the AF) and cartilage (CEP), i.e., in short, the IVD consists on a solid porous matrix filled with a fluid (Raj, 2008). Thus, one may sustain that IVD numerical modeling can only be accurate enough if poroelasticity[XXIII], viscoelasticity and fiber anisotropy are considered (Schmidt, Galbusera, et al., 2013). Fibers resist to tension and aqueous solutions characteristically resist to compression (Huyghe et al., 2003), so the osmotic swelling pressure shall also be considered, as it rules the IVD pressure under the typical compressive loadings[XXIV] (Neidlinger-Wilke et al., 2013).

Stress and strain fields within an IVD are mostly time-dependent. Creep and stress-relaxation phenomena[XXV] have been exhaustively described in the literature, as the IVD (mainly through the NP and the AF) has a rate-dependent behavior, grounded not only on poroelastic behavior, but also on hiper-viscoelasticity (Schroeder et al., 2010). Maxwell, Kelvin-Voigt or Zener[XXVI] rheological models have been widely applied, but the generalized Maxwell model[XXVII] was described as the best suited for IVD modeling (Ehlers et al., 2009, 2003; Liu and Ovaert, 2011).

Nonetheless, while viscoelasticity is more important to model fast events (a few seconds), poroelasticity is far more important to describe long-term phenomena like creep and/or stress relaxation, i.e., to model the long-term behavior (minutes to hours). AF fibers are the other focus of attention on IVD modeling. The works of Eberlein et al. (2001),

[XXIII] Biphasic, triphasic or quadriphasic theories may be applied to model this category of tissues.

[XXIV] A brief overview on the multiphasic media, focused on the IVD modeling, is going to be held in the next sub-section.

[XXV] Creep behavior corresponds to the ability of a given tissue or structure to deform permanently under the action of constant mechanical stress, while stress relaxation effects correspond to the analogous mechanism of deformation under the action of constant strain (Athanasiou and Natoli, 2008; Pierce et al., 2013).

[XXVI] The Zener rheological model, also known as Standard Linear Solid model, is a combination of Maxwell and Kelvin-Voigt models (Casula and Carcione, 1992).

[XXVII] This model will be detailed in the next chapter, on the "Formulation" section.

Holzapfel et al. (2005), Malandrino et al. (2013) and Noailly et al. (2011) described the strict relationship between the local fibers orientation and the global morphology of the MS[xxviii]. AF Fibers are modeled with regional differentiation of crossing angle and mechanical properties. Traditional approaches considered an average of ±30 degrees of crossing angle (Jensen, 1980), but Holzapfel et al. (2005) described a variation between 23 to 46 degrees (approximated values) from the ventral to the dorsal regions, through a linear regression model. Eberlein and co-workers (2001) proved that the mechanical properties, such as the stiffness of the fibers, varied both radially and circumferentially. This detailed description of the fibers properties is essential to the global behavior of the MS, particularly on rotation and flexion/extension movements (Noailly et al., 2011).

In what concerns to the FE modeling solutions, the commercial FE-package ABAQUS® (Simulia, USA) is probably the most applied, as will be shown in the "Finite Element Models" sub-section. The commercial FE-package ANSYS® (Ansys Inc., USA) is also frequently mentioned, but mostly for the pre-processing tasks, even if this software is capable of performing the simulations as well (Dennison et al., 2008). The other commercial FE solver to be mentioned is Marc MSC® (MSC Software, USA), which was chosen by Noailly et al. (2011) or Swider et al. (2010), for example. These (and other) software are able to deal with multiphasic problems and with the major part of the particularities of the soft tissues. In addition, when a given feature is not available on the FE-package, the researcher may program (and integrate) user-defined subroutines[xxix].

However, the adoption of a fully home-developed FE solver offers major advantages over programming in commercial FE-packages, because the drawbacks associated with the rigidity of a proprietary commercial code hamper the freedom of the researcher, when the complexity of the model increases. Firstly, as the researcher has direct view on the source code, the verifiability of the software is taken to a higher level and the bridging between the relevant features of constitutive modeling is much more flexible. Secondly, the dissemination of models and their implementation is not limited, as well as the discussion of the outcomes. The present work is based on the development of a home-developed open-source FE solver, based on the need of crafting solutions for the very specific

[xxviii] Other works regarding the modeling of AF fibers may be considered, namely Elliott and Setton (2001), Hollingsworth and Wagner (2011) or Klisch and Lotz (1999).

[xxix] These subroutines are usually programmed in FORTRAN or C++ languages.

demands of biomechanical (and soft tissue) modeling. Other open-source packages are available, and the most relevant of them for multiphasic soft tissue modeling is FEBio (The University of Utah, USA), which may be shortly described as a nonlinear implicit FE framework, designed specifically for analysis in computational solid biomechanics and written in C++. This package is freely available and may also include pre- and post-processing tools, which are denominated PREVIEW and POSTVIEW, respectively (Maas et al., 2012). Besides the access to the source and the possibilities of modifying and recompiling the code, another great advantage of FEBio is the dissemination, as the developing team distributes the details of their FE implementation is peer-reviewed publications (Ateshian et al., 2012, 2011, 2010; Maas et al., 2012). This dissemination usually does not occur with commercial packages, i.e., the common researcher does not have access to the implementation details and not even to the source formulation while working with ANSYS® or ABAQUS®. In addition, other groups are already testing (and validating) the performance of FEBio in their works (Galbusera et al., 2012).

The researcher shall be aware of the advantages and disadvantages of using commercial or open-source FE packages. On the one hand, the FEBio team may claim to have developed the first FE implementation of solute transport across contact interfaces in deformable porous media (Ateshian et al., 2012), but they also reckon that still need problem-specific verification and validation to ensure that the outcomes obtained with FEBio are accurate enough for a specific problem (Henninger et al., 2010; Maas et al., 2012). To achieve this, the FEBio user-community must grow. On the other hand, the commercial solvers are presented as powerful tools, with high verifiability and validation levels, provided by a large community of users.

2.4.1. Multiphasic Media

Terzaghi was probably the first author analyzing the multiphasic problems, in 1925. He devoted his work to the understanding of soil consolidation, establishing the consolidation experiments and theoretical soil mechanics in general, through “Terzaghi's theory of one-dimensional consolidation” (Terzaghi, 1943, 1925). This theory is based on the principle of effective stress, which undertakes that a porous matrix and the water filling those pores fully carry the portions of the total material stress. The other historic reference in this field

is the work of Biot, who developed the theory which is now referred as "Biot theory of poroelasticity". In a few words, the previously described Terzaghi's Principle was transformed by Biot in order to be valid for more complex three-dimensional (3D) situations (Biot, 1972, 1941).

Detournay and Cheng (1993) provided an extensive review about poroelasticity. Accordingly to these authors, if both Terzaghi and Biot works are taken into consideration, one may simply describe poroelasticity as the study of the behavior of porous media, which consists of a porous solid elastic matrix enclosing interconnected fluid-saturated pores. The presence of the fluid not only increases the stiffness of the whole material, but also results in fluid flow driven by the pressure gradients between the different material regions.

Most of the poroelastic IVD FE studies[xxx] were performed using biphasic formulations. These formulations are an effective choice, as they mean smaller number of constitutive parameters and thus lower complexity of the constitutive modeling (Frijns et al., 1997; Pierce et al., 2013). In depth, biphasic approaches only consider the influence of solid and fluid parts, while triphasic and quadriphasic theories also include the influence of the ionic fluxes. Therefore, biphasic modeling may be considered as a simplification of the more complete quadriphasic models. In order to achieve such simplification, the ionic flux is considered to be infinitely fast and is, subsequently, dismissed (Snijders et al., 1995; van Loon et al., 2003; Wilson, van Donkelaar, van Rietbergen, et al., 2005). In addition, biphasic approaches showed good commitment between the accuracy of the results and the requested computational time, in comparison with more complex models (Iatridis et al., 2003; Wilson, van Donkelaar, and Huyghe, 2005; Wu and Chen, 1996).

One of the major references in multiphasic modeling applied to soft tissues is the work of Huyghe and co-workers (Eindhoven University of Technology, The Netherlands). This group developed a FE implementation of a biphasic model (Huyghe, 1986) that tries to describe solid-fluid interactions with high accuracy. The evolution of this model, through mechano-electrochemical theories, led to state-of-the-art triphasic and quadriphasic formulations (Huyghe et al., 2003; van Loon et al., 2003). The connection with experimental work was essential to the establishment of parameters and boundaries. The primary field of application of the bioporomechanical theory was the cardiovascular tissue,

[xxx] To be detailed in the "Finite Element Models" sub-section.

but this model became appropriate to describe articular cartilage and IVD components (Huyghe, 1986; Oomens et al., 1987; Schroeder et al., 2010; Snijders et al., 1995).

This group typically uses ABAQUS® FE-package, in which they integrate home-developed material laws[xxxi]. One good example is their implementation of the state-of-the-art biphasic swelling theory[xxxii], which was first published by Wilson, van Donkelaar and Huyghe (2005), and derived from the work of Lanir (1987). The osmotic swelling behavior describes the tendency of a given soft tissue to swell due to the fluid flow. Such flow is related to the osmosis-driven positive gradient of pressure, which allows the fluid to enter in the porous matrix of that soft tissue, i.e., the fiber network of the tissue functions under tensile pre-stressing and the fluid saturating the extrafibrillar space is under pressure. ABAQUS® did not have the solution to model poroelastic materials with swelling properties, so Wilson and co-workers developed an UMAT user-subroutine to include osmotic swelling behavior on their ABAQUS-based cartilage poroelastic FE model (Wilson et al., 2007; Wilson, van Donkelaar, and Huyghe, 2005), which was later applied to their IVD model (Schroeder et al., 2010, 2006).

2.4.2. Finite Element Models

Simulations through FEA contributed for some of the most important advances in biomechanical science, namely on knee, hip or spine studies (Oomens et al., 2009). The benefits of using FE models in biomechanical studies are mostly related with the possibility of controlling all the parameters of a given simulation, from boundary conditions to material properties. In addition, some biological structures are not easy to study *in vivo* or even to obtain for *ex vivo* studies, so the predictions obtained through computational models and their correspondent numerical simulations are essential. The IVD is a good example of one of these structures (Schmidt, Galbusera, et al., 2013).

Around the world, several research groups have applied FEA to study the biomechanics of the IVD, since 1974 (Belytschko et al., 1974). In fact, it is being shown across this work that one

[xxxi] The home-developed material laws are usually known as user-defined subroutines, as previously mentioned.

[xxxii] One may also consider the work of Broberg (1993) as an approach for the IVD osmotic swelling behavior.

of the major issues on IVD studies is the fact that they are hardly accessible for *in vivo* studies. *In vitro* studies are a valid and recurrent option for experimental tests, but they mostly use cadaveric IVDs (Goins et al., 2005). As already mentioned, the most advanced culture systems allow the survival of the IVDs for a given period of time, usually no more than three weeks after extraction (Paul et al., 2013). Even if this is an important technological advance, it is still time-constrained, due to the senescence of the IVDs after those three weeks.

Consequently, FEA is the most appropriate answer for "unlimited" studies involving the biomechanical behavior of the Spine and the IVDs. However, it must be highlighted that the best option is to combine FEM with experimental studies, in order to obtain a general overview of the problematic and also to get retro-feedback between the experimental outputs and the numerical inputs[xxxiii], as performed on the studies of Joshi et al. (2009) or Wang et al. (2012). In fact, one of the major challenges in the numerical simulation is the extrapolation of experimental data to a set of parameters to feed the simulations.

This section intends to describe the state-of-the-art on the evolution of the IVD FE modeling. Knowledge has evolved from the pioneer 2D studies to the more realistic 3D simulations, with the help of fast progress of computing science. Several topics have been covered, from the effects of different boundary conditions to new treatment strategies. On the one hand, the most up-to-date studies apply multiphasic poroelastic formulations coupled with osmotic pressure gradient, in order to account for the fluid exchanges and activity/recovery cycles (Hussain et al., 2012; Massey et al., 2012; Schmidt, Bashkuev, et al., 2013; Schroeder et al., 2010; van den Broek et al., 2012). On the other hand, modeling of the highly non-linear AF fibers also deserved the attention of several works (Eberlein et al., 2004; Holzapfel et al., 2005).

Belytschko et al. (1974) developed the first known FE model of an IVD, in 2D. They studied the effects of different magnitudes of axial loading in stress distribution and IDP. Even if the technology was limited at the time, this group could conclude that the AF is stiffer than was initially supposed by direct measurements and that the decrease on the elastic properties has no significant influence on IDP.

Lin et al. (1978) were the firsts to create a complete 3D FE model of an IVD. They coupled experimental work, FE modeling and optimization in the same study, creating a complete framework to study the biomechanical behavior of the lumbar IVD. The objective was to identify

[xxxiii] Hybrid simulation, combining FEM and MBS, may also be considered.

the material properties of the IVD, starting with axial compression experiments. After the FE simulation and subsequent parameters optimization, they have shown the uniformity of the discs within the lumbar section of the spine, and confirmed that the orthotropic elastic moduli decrease directly with the advance of IVD degeneration.

Simon et al. (1985) developed the first published approach to the study of IVD poroelastic biomechanical behavior. They analyzed factors as strain fields, fluid flow, fluid pressure and stress fields, in order to evaluate the creep response of the IVD. The major outcome of this work was the description of the association between the increase of permeability and disc degeneration. It was shown that the daily cycles, including both loading and recovery phases, are highly dependent of the poroelastic phenomena. The healthy IVD depends on the flow of nutrients from the adjacent spine components, so degeneration may occur if such flow is altered.

Shirazi-Adl and co-workers (1986-1987)[xxxiv] developed a L2-L3 nonlinear 3D FE model to investigate the effects of various loading conditions in this lumbar motion segment, as sagittal plane moments, axial torque alone and axial torque combined with compression. They concluded, amongst other facts, that the stiffness of the motion segment is dependent on the sagittal plane moments and that the most vulnerable element of the segment in torque is the posterior bony structure. In addition, they also found correlation between large extension/flexion loads and disc degeneration. These works may be considered as pioneers on the study of the IVD macromechanics and were indeed the firsts to consider the facet joints all together.

Goel and Kim (1989) developed a FE model of the L3-L4 MS, which is shown in Figure 2.9. This model was presented with a coarse mesh, due to the computing limitations, but its geometric features were accurate enough. The goal for this work was to study the effects of two surgical procedures to heal injuries of the lumbar spine. Total denucleation and bilateral total discectomy were simulated, and both of them included NP removal. At the biomechanical point of view, these two surgical procedures are almost similar. They found that the loading through the facets was increased and the disc bulge in posterior region decreased, for both of the facets have an important role in protecting injured IVD, as the total stresses in the two VBs were not significantly increased after the injury. These conclusions led to important developments in terms of the NP replacement or regeneration procedures

[xxxiv] Complete references: (Shirazi-Adl and Drouin, 1987; Shirazi-Adl et al., 1986a, 1986b).

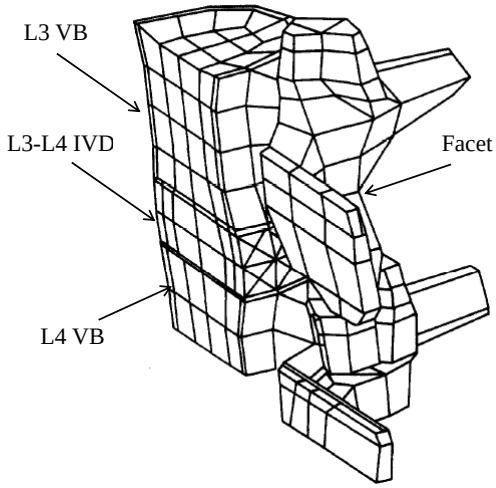

Figure 2.9. L3-L4 MS FE model developed by Goel and Kim (1989).

Natarajan et al. (1994) developed FE models of the L3-L4 MS, on intact and damaged conditions. This study intended to determine the pathways for IVD degeneration (and failure), and became an important reference in this subject. Their analyses showed that degeneration mainly started with problems in the CEP, which was pointed out as the weak link of each MS. In what concerns the applied loads, they demonstrated that pure compressive load is not enough to produce real damage on the AF[xxxv], i.e., the biomechanical behavior (and degeneration) of this IVD component is more influenced by the formation of peripheral tears. In addition, flexion efforts are more likely to cause damage than equivalent extension efforts. This group would later continue their IVD FE studies.

Wu and Chen (1996) developed a 3D poroelastic FE model of a lumbar MS (Figure 2.10), using and defining the mechanical modeling of a mixed FE formulation. This work is one of the pioneer studies on long term creep response of the IVD using poroelasticity. The FE model was constructed based on CT imaging information, including one VB and one IVD, as well as adjacent structures, such as the facet joints and ligaments. They came to the conclusion that this model was able to give correct clinical information about the behavior of the Human spine. The implemented 3D FE mixed formulation was essential to this accuracy on the results, since it was developed in such way that the imposition and derivation of the pore fluid pressure can be obtained on FE nodes. Thus, the total stress is calculated correctly on the poroelastic structure, which was not possible with the existing FE implementations on porous media.

[xxxv] Later on, it was shown that this finding was not correct.

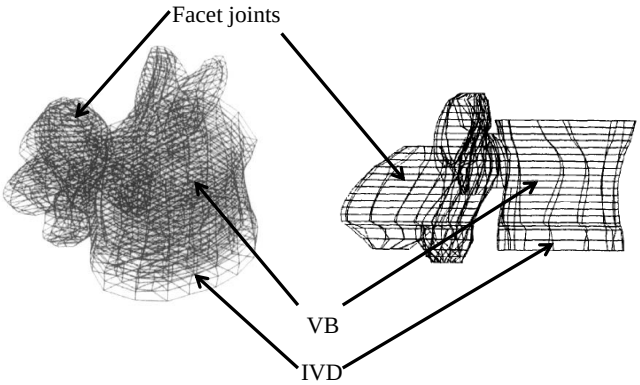

Figure 2.10. Lumbar MS FE model developed by Wu and Chen (1996).

Argoubi and Shirazi-Adl (1996) developed a poroelastic FE model of the L2-L3 MS, in order to analyze the creep response of the MS under different loading profiles and pathological conditions. This study continued (in some extent) the works of Shirazi-Adl and co-workers, which were previously mentioned. They developed a stratified AF model, with 8 layers of fibers embedded in an AF-matrix bulk (Figure 2.11) and also introduced an approach for simulating the osmotic pressure gradient, by applying a positive pressure along the MS free boundaries. However, the major novelty of this work was the implementation of strain-dependent permeability for the MS components, based on articular cartilage studies. This characteristic proved to be essential for the validity of long-term compression studies, for both native and pathological conditions. The strain-dependent permeability formulation and the material parameters determined on this work are still one of the benchmark for poroelastic IVD studies, along with the works of (van der Voet, 1997) and (Ferguson et al., 2004).

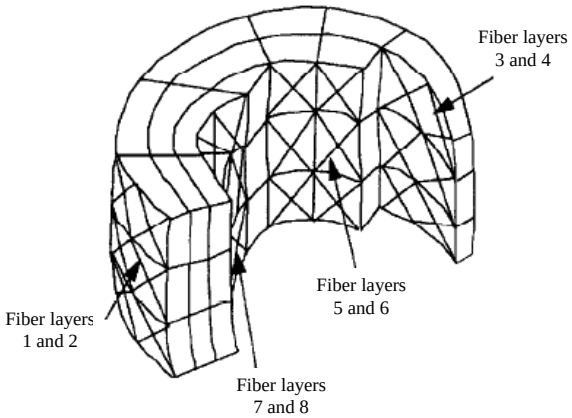

Figure 2.11. Schematic representation of the 8 fiber layers of the L2-L3 MS FE model developed by Argoubi and Shirazi-Adl (1996).

Kong et al. (1996-1998)[xxxvi] combined FEM and numerical optimization to measure several biomechanical parameters on the L3-L4 MS, during the simulation of lifting tasks. They analyzed the evolution of deformation, IDP, strains, stresses, and load transfer paths. Their results showed general evidence that muscles stabilize the spine, particularly when the spine is being subjected to high loads or large flexed postures. Consequently, muscular malfunctioning will cause overload on the IVDs and ligament. They also concluded that the posterolateral regions of the IVD are more subjected to higher stresses than the other regions.

Kim (2000) presented a comparison between young and old adults, by developing FE models of the L3-L4 MS that simulated each one of those stages. Their main goal was to study the process of formation of peripheral tears in the anterior outer AF over the years. The AF was modeled with 16 layers of fibers and 6 different materials, depending on the region. The results allow concluding that, in the early years of life, the strain levels are significantly high and may cause layer failure in that region of the AF. This proves that the biomechanical properties of the AF are influenced by ageing.

Eberlein and co-workers (2001-2004)[xxxvii] developed FE models of Human lumbar spine (isolated L2-L3 and also more complete L2-S1), firstly in healthy condition. They focused their study on the development of an innovative constitutive model for the description of the heterogeneity and nonlinear anisotropic response of the AF collagen fiber network, starting with stress-strain experiments of healthy single AF lamellae. Their approach included regional variation of the AF properties, both on dorsal-ventral regions and internal-external regions, which resulted in four different regions with specific material properties[xxxviii] and variable fiber angle, calculated through a linear regression[xxxix]. They defined the AF as a fiber-reinforced material, with specific stiffening behavior, which was not possible in standard ABAQUS®. Therefore, they developed and implemented an user-subroutine to include their constitutive model on that FE-package. Afterwards, they developed a comparable degenerated model. This degenerated AF has less material density, modeled through the removal of the central elements, as shown in Figure 2.12. Overall, these works provided reasonable approximations to the experimental data for flexion and lateral bending and extension and axial moments. The major difficulty found by the authors was the imprecise knowledge about the local degree of hard and soft tissue degeneration in the whole

[xxxvi] Complete references: (Kong et al., 1998, 1996)
[xxxvii] Complete references: (Eberlein et al., 2004, 2001).
[xxxviii] Dorsal-internal, dorsal-external, ventral-internal and ventral-external.
[xxxix] Dependent on the angular region.

Human spine. However, the new constitutive model showed potential to be applied on the development of spinal implants, as it described the physiological strain behavior of AF fibers. In addition, the achieved regional differentiation rates of the AF tissue are one of the current benchmarks on AF FE modeling.

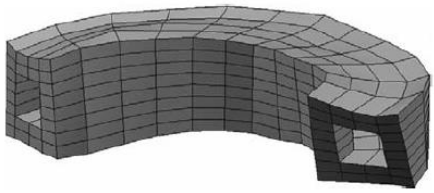

Figure 2.12. Cross-sectional view of the degenerated AF FE model developed by (Eberlein et al., 2004).

Ferguson et al. (2004) studied the transport of solutes within a lumbar IVD. They considered strain-dependent permeability and osmotic swelling pressure through fixed boundary pore pressure[XL]. In addition, their FE model (which is shown in Figure 2.13) is highly refined, in order to eliminate possible mesh-related issues on the fluid flow simulation. They analyzed the fluid flow through diffusion and convection during 24h simulations, i.e., they simulated a diurnal loading cycle, consisting of 8h of resting period[XLI] and 16h of constant compressive load[XLII].

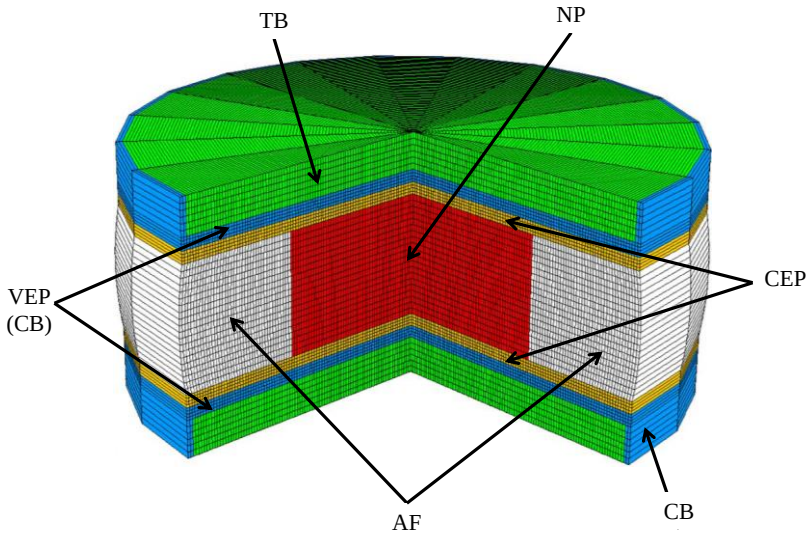

Figure 2.13. Lumbar IVD FE model developed by Ferguson and co-workers.

[XL] 0.2MPa boundary pore pressure at the VEP and outer AF.
[XLI] This resting period was based on the action of the osmotic pressure.
[XLII] The applied load was equivalent to 0.5MPa average mechanical stress.

The key conclusion from this work is that the convective transport of solutes during resting periods is substantial. Such phenomenon is strictly associated with the proper functioning of the CEP, so this model proved that the obstruction of this channel shall acelerate disc degeneration. Nevertheless, while the transport of low-weight solutes was accurately predicted, the influence of larger solutes on IVD physiology stood not well understood. As previously mentioned, the material parameters correspondent to the strain-dependent permeability formulation determined on this work are one of the benchmark for poroelastic IVD studies.

Natarajan and co-workers (2004-2008)[XLIII] developed a 3D poroelastic FE model from a serial computed axial CT scan of L4-L5 MS. The commercially available ADINA FE-package was the selected FE solver, and the FE model is shown in Figure 2.14. They considered osmotic swelling pressure[XLIV] and regional strain-dependent permeability[XLV], even if such parameters were obtained from discrepant sources in the literature. Their models simulated grades I and IV of Thomson's scale. The severely degenerated model was modeled with reduced permeability and porosity, along with increased stiffness. They concluded that asymmetric manual lifting (in three different activities) causes large translational and rotational motion, injuring the IVD, starting with local yield failure in the AF and CEP. Fluid exchange between the IVD and surrounding tissues was described as essential to the healthiness of the spine. Restriction of the fluid exchange process may increase IDP, leading to higher IVD bulge and, ultimately, causing back pain.

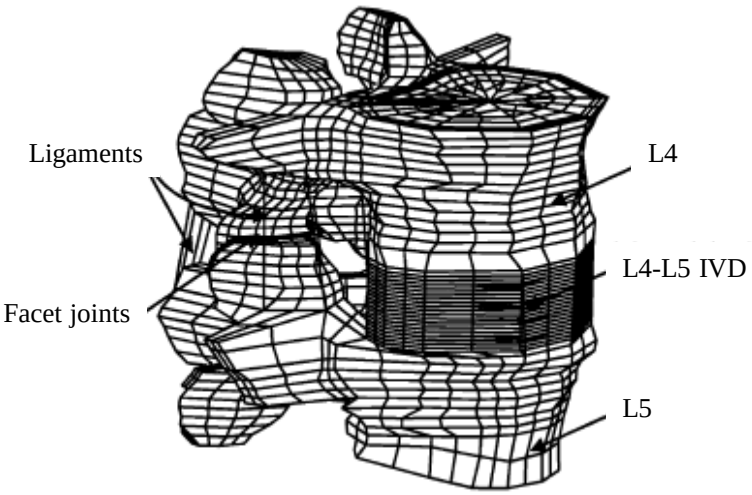

Figure 2.14. L4-L5 MS FE model developed by Natarajan et al. (2008).

[XLIII] Full references: (Natarajan et al., 2008, 2007, 2006, 2004).

[XLIV] The osmotic swelling behavior approach used in this work derived from the work of Broberg (1993).

[XLV] The approach presented by (Iatridis et al., 1998) was considered in this study for the implementation of the strain-dependent permeability.

Joshi and co-workers (2004-2009)[XLVI] used ABAQUS® to study four conditions of the IVD: intact, bone in plug, denucleated and implanted (with an NP-hydrogel replacement). In what concerns this last condition, they tested precise filling of the NP cavity (after 80% denucleation), as well as under- and over-dimensioned implants, in terms of height and diameter. Figure 2.15a) shows "NP Implant 1", which is under-height, while Figure 2.15b) shows "NP Implant 2", which is under-diameter. The objective was to evaluate the performance of NP-hydrogel replacement.

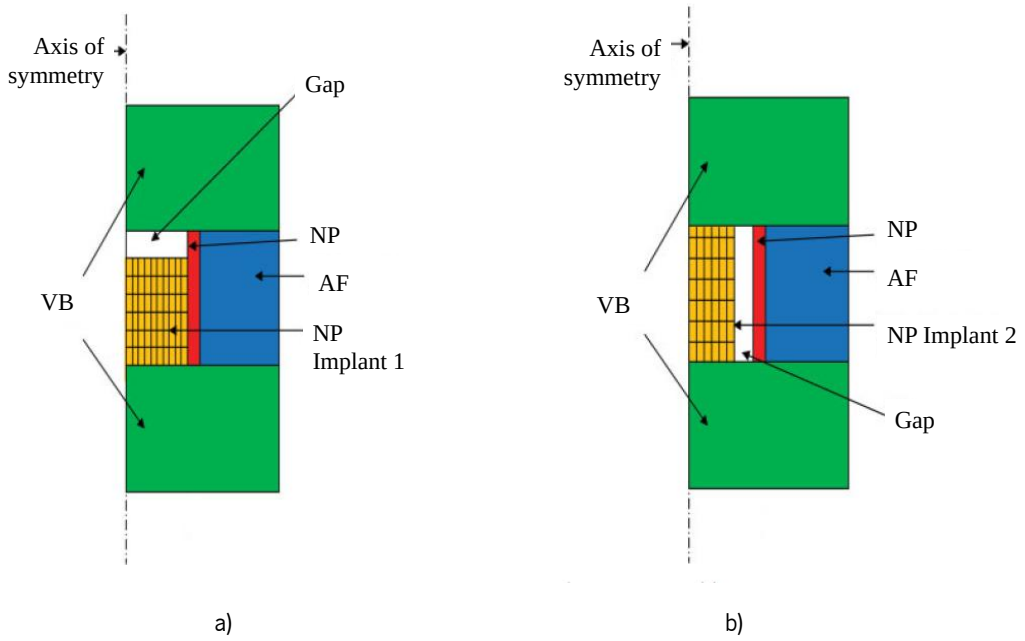

Figure 2.15. Schematic representation of the under-dimensioned implants modeled by Joshi et al. (2009). a) Under-height implant ("NP Implant 1"); b) Under-diameter implant ("NP Implant 2").

The results showed good approximation to the intact IVD, for the situations of correct or exaggerated filling of the NP cavity. In fact, for these cases, the abnormal stresses caused by previous implants were reduced and the load transfer from the NP to the AF was inside the scope of the conditions registered for healthy IVD. The behavior of the under-dimensioned implants was not satisfactory. These works contributed to the optimization of forthcoming IVD implants, through the definition of thresholds for several biomechanical parameters of the implant, such as volume or material stiffness. However, the constitutive modeling was limited, as the IVD components were only modeled as hyperelastic materials, i.e., no osmo-poro-viscoelasticity behavior was considered.

[XLVI] Complete references: (Joshi, 2004; Joshi et al., 2009).

Little and co-workers (2004-2010)[XLVII] developed FE models of the healthy and degenerated L4-L5 in order to identify critical aspects of IVD degeneration, using ABAQUS®. Figure 2.16 shows the healthy IVD FE model, with so-called "fluid elements" defining the NP. They modeled the AF matrix as a reinforced-ground matrix, accounting for the interactions in-between the fibers and between the fibers and the solid matrix[XLVIII]. Osmo-poro-viscoelasticity was not explicitly included in this work, which means that the model could be more accurate, but the hydrostatic pressure of the NP was considered. They applied kinematic boundary conditions for the loading of their models, namely 500N axial compression for simulation of relaxed standing[XLIX] and also several rotation profiles to simulate the motion limits of the IVD. Such boundary conditions intended to simulate the action of muscles and ligaments of the spine. After the definition of the healthy condition, this group found that the lesions[L] on the AF are less significant for the IVD biomechanics than the loss of NP hydrostatic pressure, i.e., the removal of the NP hydrostatic pressure provoked reduced IVD stiffness and innervated the surrounding tissues, increasing back pain. Thus, the great importance of the NP internal pressure for the IVD biomechanics (and degeneration triggering) is the key outcome of this work.

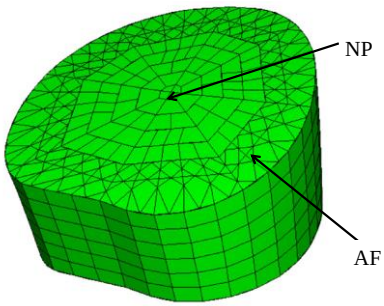

Figure 2.16. Healthy IVD (without CEP) FE model developed by (Little, 2004).

Goel et al. (2005) developed intact and implanted geometrical models of L3-S1, in order to study the influence of the implantation of a Charite® (DePuy Spine, USA) artificial disc model at the L5-S1 level. This implanted model is shown in Figure 2.17. Axial compression and pure flexion/extension simulations were performed with ABAQUS®. This group also validated the FE models with load-controlled experimental tests on cadaveric Human lumbar spines. In what

[XLVII] Complete references: (Little and Adam, 2010; Little, 2004; Little et al., 2008, 2007).

[XLVIII] This part of the study was supported by experimental work, using sheep IVDs, as described on (Little et al., 2010) and also partially described on (Little, 2004; Little et al., 2007).

[XLIX] This loading profile also served for validation purposes.

[L] Rim, radial and circumferential lesions.

concerns to the major conclusions, they found that the major effects of this implant are registered at the upper CEP. The differences in IDP and shear stresses between intact and implanted models were minor, but this study was limited to this particular implant model. The other limitation that can be addressed to this study was the application of linear elastic materials for all the components, instead of the more accurate non-linear formulations, which were proved as particularly important for the IVD tissues.

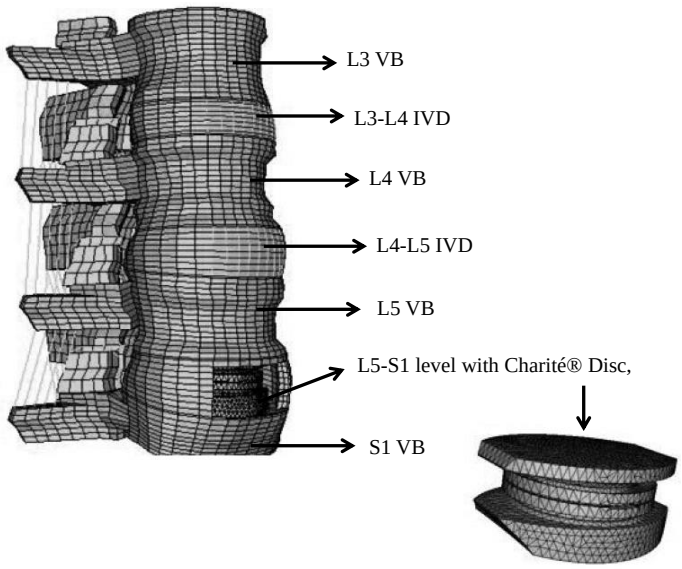

Figure 2.17. L3-S1 FE model developed by Goel et al. (2005). The Charité® disc implant was also modeled and included in this study, at the L5-S1 level.

Lodygowski et al. (2005) proposed, developed and validated a simplified L4-L5 MS model based on medical images. This group previously developed a more complete lumbar 3-D MS model, but with this study they intended to prove that it was possible to generate valuable simplified model. This model was proved as worthy for numerical simulation of surgery and analysis of spine behavior, namely for compression, bending and torsion. However, it must be highlighted that this model was validated for whole spine deformations (macromechanics), i.e., the simplification approach may not be reasonable for more focused studies.

Silva et al. (2005) developed an axisymmetric nonlinear poroelastic FE model with strain-dependent permeability[u] of an IVD hydrogel prosthesis, using ABAQUS®. No osmotic swelling

[u] The Argoubi and Shirazi-Adl model (1996) was chosen for the implementation of the strain-dependent permeability.

behavior was considered, but the free draining of the model was ensured by the condition of zero pore pressure on the free external boundaries. They also tested their hydrogel replacement experimentally, in order to perform a numerical-experimental comparison of axial deformation and predicted fluid loss, during creep loading. The outcomes of the numerical model indicated that fluid loss of the prosthetic IVD is similar to that of native IVDs, i.e., the NP lost more water content than the AF, which was in agreement with the experimental results. The obtained stress distribution pattern revealed that this IVD replacement technique allowed the maintenance of the native IVD stress patterns, namely in what concerns the fluid and stress transferences from the NP to the AF. They identified shortages on the consolidation model available on ABAQUS®, as this model was not capable of predicting material creep that is not related with fluid loss. Nevertheless, the good correlation between this IVD hydrogel prosthesis and the available data on native IVDs was interesting for the evaluation of this IVD replacement technique.

Ehlers et al. (2005-2009)[LII] developed a simplified L4-L5 MS FE model as an example to prove that is was possible to reproduce accurately the fundamental mechanical and electro-chemical responses of hydrated soft tissues. This model, which is shown in Figure 2.18, only included three components, namely the NP, the AF and the VB. Therefore, no distinction was made on the VB layers and the CEP was also not considered. They used quadratic 20-nodes Taylor-Hood elements. However, the constitutive modeling included all the relevant features of the IVD biomechanics, which means that this work was the pioneer on the comprehensive numerical modeling of the IVD. The NP was modeled as isotropic, viscoelastic and charged material. The AF was treated as anisotropic and charged material, with regional variation of the properties of the fibers. The isotropic solid matrixes were modeled with the Neo-Hookean model, the anisotropic part of the AF was modeled with polyconvex Ogden-type law and the generalized Maxwell model was selected for the viscoelastic modeling. Their fitting for the viscoelastic material parameters is one of the major references in the field. Nevertheless, the main emphasis was on the application of the Theory of Porous Media, which was proposed to the description of the charged hydrated tissues, along with strain-dependent permeability and osmotic swelling behavior[LIII]. Overall, the validation performed by the authors, through swelling experiments[LIV], allowed them to conclude that this was a thermodynamically consistent biphasic model and could be used for IVD degeneration and replacements studies.

[LII] Full references: (Ehlers et al., 2009, 2006)
[LIII] The approach for the IVD osmotic swelling behavior was based on a simplification of Lanir's model (1987).
[LIV] Without mechanical loading, i.e., consolidation tests.

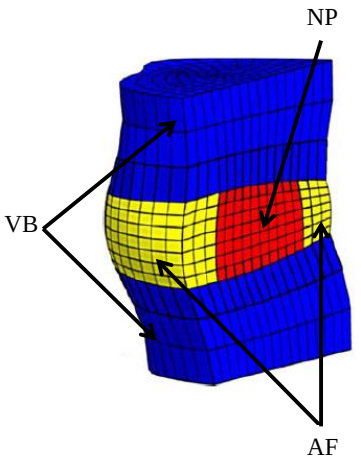

Figure 2.18. L4-L5 MS FE model developed by Ehlers et al. (2009).

Noailly and co-workers (2005-2012)[LV] developed a L3-L5 FE model, which is shown in Figure 2.19, to understand the relative biomechanical roles of the different spinal tissues. They included the facets and the ligaments, which were carefully modeled with a hyperelastic law. In addition, the distinction between the CEP and the VEP was also considered. They found evidence that the geometrical characteristics of tissues affect the stress distribution, especially when accurate non-linear behavior laws are applied on the FE models. Several loading profiles were tested, with particular emphasis on flexion/extension and rotation movements.

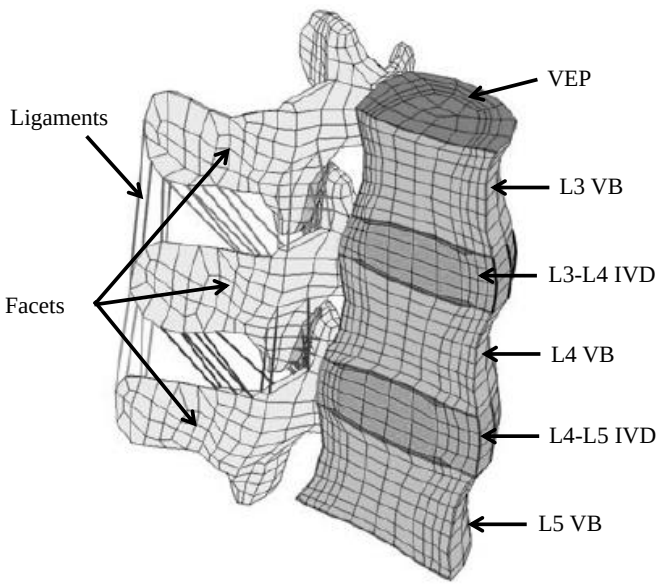

Figure 2.19. L3-L5 FE model developed by Noailly et al. (2012).

[LV] Complete references: (Noailly, 2009; Noailly et al., 2012, 2011, 2007, 2005).

Later on, they used this model to work on the development of new IVD replacement strategies. This work reveals the limitations of previous FE studies of IVD, namely on the reproduction of the proper biomechanical kinematic parameters of the Human spine. Nevertheless, it was determined that the interactions within the IVD and between the IVD and its adjacent structures are influenced by soft tissue structural organization, tissue material properties and boundary conditions. Therefore, important findings were achieved for the next generation of biomechanical studies of the IVD, namely on the importance of the criss-cross angle of the AF collagen fibers. However, the major drawback of this study was the absence of osmo-poroelasticity.

Rohlmann et al. (2006) developed FE models of the L3-L4 MS to investigate the influence of different grades of IVD degeneration on the mechanical behavior of the Human spine[LVI]. For that purpose, normal and reduced height IVD models were developed. Figure 2.20a) shows the native MS model, while Figure 2.20b) shows the severely degenerated model. Variations on the bulk modulus of the NP were also considered. Some simplifications were assumed, as the neglecting of muscle forces and fluid transfer within the IVD. One may consider that such simplifications would reduce the accuracy of the model, but the authors found good correlation with *in vitro* data on the outcomes of intersegmental rotation and IDP. The advanced DDD condition, i.e., the IVD with severely reduced height, provoked a decrease on intersegmental and axial rotation, through the increase of AF stiffness. A buckling effect on the ligaments was also noticed, as the length of the ligaments remained unaltered.

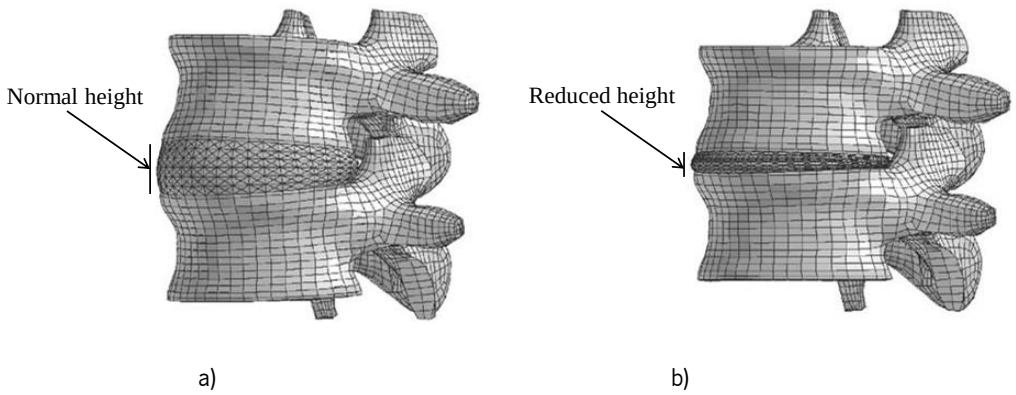

Figure 2.20. L3-L4 MS FE models developed by Rohlmann et al. (2006). a) Native MS model, with normal IVD height; b) Severely degenerated MS model, with highly reduced IVD height.

[LVI] This team was also responsible for several studies on spinal loadings, with or without IVD instrumentation, as summarized on (Rohlmann et al., 2012).

Schroeder and co-workers (2006-2010)[LVII] developed a simplified[LVIII] lumbar IVD FE model based on the geometry of Human L4-L5 IVD. They modeled their IVD[LIX] with osmo-poro-visco-hyper-elasticity[LX], which they denominate as "OVED model", because they reckoned that some internal mechanical conditions of the IVD could not be directly measured as a function of experimentally assessable biophysical characteristics. They modeled the non-fibrilar NP and AF matrixes with the same modified Neo-Hookean law, while the AF fibers were modeled through the Zener model. The osmotic swelling behavior model was the one from Wilson et al. (2005), accounting for the presence of intra- and extra-fibrillar water, which was a distinguishing novelty[LXI]. Such features were not included on ABAQUS®, which was the selected FE-package for this work, so they were included through user-defined materials. Therefore, the guiding lines of this model are the IVD tissues biochemical composition, organization and specific constituent properties. Their approach was firstly to model and simulate isolated samples of tissue, in order to obtain the constituent properties of both NP and AF. The parameter values were compiled for the construction of the full IVD model[LXII] and its behavior was validated against *in vitro* creep experiments that used Human lumbar IVDs (500N of uniaxial compression, as performed by (Heuer et al., 2007)). The selected outcomes for this validation were the radial bulge, axial creep displacement and IDP. One may argue that the validation presented in this work is not sufficiently accurate, in comparison with the experimental work of Heuer et al. (2007), but this "OVED model" was very important for the next generation of IVD FE studies. In fact, this model was the pioneer on the description the possibility of accurately determining the internal mechanical conditions of the IVD as a function of assessable biophysical characteristics, through the FE modeling of the IVD osmo-poro-hiper-viscoelasticity (with primary and secondary fibers network).

Schmidt and co-workers (2006-2013)[LXIII] developed a L1-L5 FE model, in order to simulate IVD degeneration and then to evaluate a NP substitute, using ABAQUS®. However, they focused their analyses on the L4-L5 MS. The L4-L5 IVD FE model is shown in Figure 2.21. First, they simulated three different stages of IVD degeneration, namely mild, moderate, and severe

[LVII] Full references: (Schroeder et al., 2010, 2008, 2007, 2006).

[LVIII] This group has chosen to work with a model which represents ¼ of the full IVD.

[LIX] Despite being denominated as "IVD model", this model only included the NP and the AF, i.e., the CEP was not considered.

[LX] Including small fibrillar structures.

[LXI] The implemented law for the osmotic swelling behavior was dependent on the intra-fibrillar water, based on the work of (Urban and McMullin, 1988).

[LXII] This approach is denominated as "composition-based model".

[LXIII] Full references: (Schmidt and Reitmaier, 2013; Schmidt et al., 2011, 2010, 2007, 2006; Schmidt, Bashkuev, et al., 2013).

degeneration. In comparison with the healthy condition, the IVD height was reduced by 16.5%, 49.5% and 82.5% for each case, respectively. The stiffness of the NP was also increased, in direct proportion to the advance of the degeneration, while the AF remained unaltered. Their goal was to identify the loading properties of the AF in each one of these situations. For the simulations with the full lumbar spine model, they included a connecting element between the four IVDs to act as a "load follower". Their results allowed concluding that circumferential tears, one of the major precursors of degeneration, could occur since early stages. In addition, both shear and tensile strain on the AF decrease with advanced degeneration. Afterwards, they studied the relation between time of the day and loading on the spine, through the evaluation of fluid pressure. At this point, they included the strain-dependent permeability and simulated 48h of axial compression cycles, considering activity (1000N) and recovery periods (350N), i.e., considering the regular circadian variations. Partial saturation for the IVD to avoid having negative pore pressures on unloading/recovery phases was applied, as well as an external pressure gradient, playing the role of an osmotic pressure gradient.

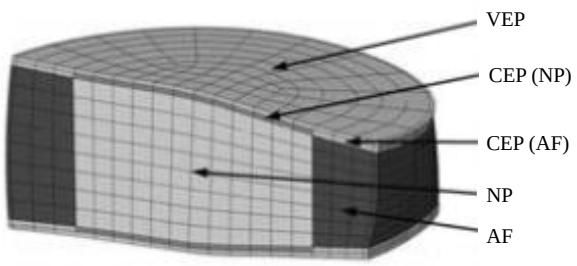

Figure 2.21. L4-L5 IVD FE model developed by Schmidt et al. (2011). The authors have chosen to model the CEP on the full diameter of the IVD and distinguished between the NP-covering CEP and the AF-covering CEP.

The results showed that the permeability of the IVD tissues[LXIV] and the resting periods play a major role on the mechanical behavior of the spine, given that these tissues present greater resistance to fluid outflow than inflow, which is an essential feature to the equilibrium in the recovering phases. Finally, in order to evaluate the behavior of a NP substitute, they considered osmotic swelling behavior[LXV] on their model. They found that under-sized implants are not capable of mimicking the behavior of the native IVD. Overall, this group improved their work throughout

[LXIV] They compared the strain-dependent permeability parameters of Argoubi and Shirazi-Adl (1996) and Ferguson (2004), using the model of Argoubi and Shirazi-Adl (1996).

[LXV] The adopted osmotic swelling behavior model was the one from Wilson et al. (2005).

the years, from a non-poroleastic model to an osmo-poro-hyperelastic IVD model, including seventeen criss-cross fiber layers on the AF. The behavior of this model was validated with experimental data and proved to be a good approach to the Human IVD.

Teo et al. (2007) devoted their work to the creation of a tool for surgical training. They developed a FE model of the Human spine, based on medical images. Their challenge was to determine the effects of heterogeneous meshing for complex anatomic structures. In the end, they found that using different types of elements can be helpful for better accuracy (and lower computational time) on biomechanical studies.

Monteiro (2009) presented a hybrid method (MBS and FEM) to study the effects of interbody fusion on IVD. In what concerns the FE model, the multilevel L3-L5 model was validated with experimental data. Simulations were performed for compression and flexion. Co-simulation studies are interesting, as they cover the grounds of the different numerical methods. In fact, the MBS method was useful to complement the macromechanical analysis. The outcomes of this work allowed concluding that not only the fused IVD is biomechanically altered, as higher stresses were measured on the adjacent IVDs, which would probably lead to multilevel IVD degeneration.

Massey and co-workers (2009-2012)[LXVI] developed an axisymmetric MS FE model to study the degeneration of IVD and the influence of a hydrogel NP replacement. Poroelasticity and osmotic swelling were considered in order to produce accurate predictions of the physiological and biomechanical changes on the IVD behavior during the diurnal cycle. This investigation eventually leads to the detection of earlier intervention points in spine treatments. It also exposed the association between the loss of proteoglycan content and the stress increase, which are directly related to IVD degeneration.

Malandrino and co-workers (2009-2013)[LXVII] presented a L4-L5 IVD FE model with a poro-hyperlastic matrix, based on the Neo-Hookean model and also on the strain-dependent permeability model of Argoubi and Shirazi-Adl (1996). The main focus of this work was on the AF modeling, namely on the description of the significance of the AF fiber angle for the mechanical behavior of the whole IVD. Their AF model, which is shown in Figure 2.22, included four

[LXVI] Complete references: (Massey, 2009; Massey et al., 2012).
[LXVII] Complete references: (Malandrino et al., 2013, 2009).

mechanically different regions[LXVIII], and the orientation of the fibers was calibrated for each one of those regions, using a direction-dependent strain energy density term, reproducing the well-known criss-cross pattern. Nevertheless, they simplified their model by considering that all the hyperelastic and fluid-phase material parameters remained unchanged throughout the AF. They validated their model by comparing it with the experimental results of Heuer et al. (2007), and the results showed that fiber patterns and stiffness variations can determine a realistic approximation to the IVD biomechanics, depending on the AF criss-cross fiber patterns.

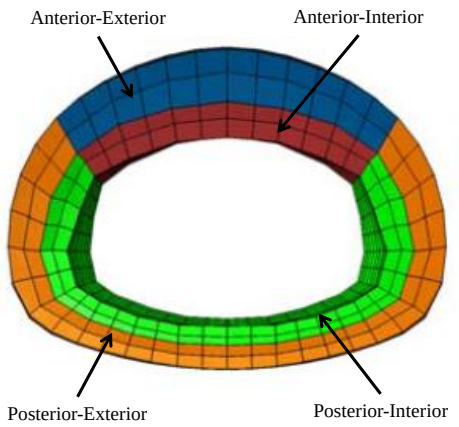

Figure 2.22. AF FE model developed by Malandrino et al. (2013), with regional variation.

Shirazi-Adl et al. (2010) developed FE models of a uniaxial cell culture[LXIX] and a complete axisymmetric IVD, in order to study the IVD cells and the effects of CEP permeability. They found numerical evidence that reinforced the previous knowledge on the extreme importance of the CEP for the IVD survival. The periphery of the AF still transports nutrients, even when the CEP is calcified or damaged, but this is not enough to maintain the viability of the whole disc. The IVD ECM is determinant for the global behavior of the IVD, so the knowledge about material and cellular properties must become deeper, even if this is a very particular field of the IVD FE studies.

Swider et al. (2010) applied the substructuring technique[LXX] to simplify a poroelastic FE model of L5-S1 MS. They proved that this technique is useful to reduce the computational time and improve the detection of local effects, on behalf of the time-dependent response of biological

[LXVIII] Anterior-interior, Anterior-exterior, Posterior-interior and Posterior-exterior.
[LXIX] This cell culture was necessarily performed i*n vitro.*
[LXX] Reducing the structure's initial domain to several subset domains.

tissue. This substructured model was validated with results from complete models, also with non-linear behavior. Three different loading profiles were selected, namely compression and torsion, which proved the accuracy and usability of this technique.

Strange et al. (2010) developed a L4-L5 IVD model in both native and degenerated conditions, in order to evaluate the biomechanical behavior of an elastomeric NP replacement, which can be implanted via minimally invasive surgery. The NP and the AF were solely hyperelastic, through Mooney-Rivlin law, which means that neither viscoelasticity nor poroelasticity were considered. However, regional variation of the AF properties was taken into account and the internal fiber angle was ± 30 degrees. Figure 2.23 shows that the CEP was not included in the model, but it also shows that the FE mesh is reasonably refined. For the evaluation of the NP substitute, the compressive stiffness, radial AF bulge and stress distribution patterns were measured under displacement-controlled loading. They tested several conditions, namely the native IVD, complete nucleotomy, partial nucleotomy, partial implant and complete implant. The results were satisfactory and comparable with literature data, despite of the limitations of the model. Nevertheless, this study seems to demonstrate that the elastomeric NP replacement implant can restore the axial compressive mechanical properties of the native IVD.

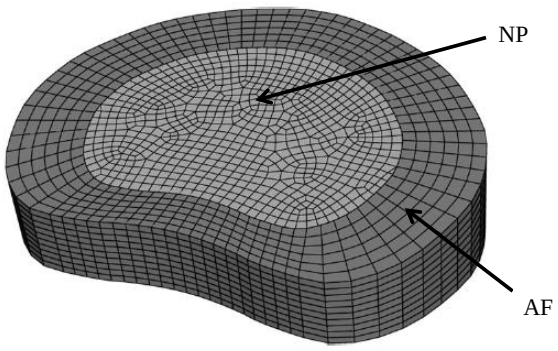

Figure 2.23. Native L4-L5 IVD model developed by Strange et al. (2010).

Galbusera and co-workers (2011)[LXXI] analyzed different approaches for simulating the swelling behavior of the IVD, through the daily cycles. For this purpose, they developed and tested a L4-L5 MS FE model, using ABAQUS®, coupled with user-subroutines when needed. They compared the biphasic swelling theory derived from the works of Lanir

[LXXI] Complete references: (Galbusera, Schmidt, Neidlinger-Wilke, et al., 2011; Galbusera, Schmidt, Noailly, et al., 2011)

(1987) and Wilson et al. (2005) with a phenomenological swelling approach based on the poroelastic consolidation theory (fixed swelling pressure). They also included hyperelasticity of the solid matrixes through Neo-Hookean model and strain-dependent permeability through Argoubi and Shirazi-Adl model. This work led them to the conclusion that IVD behavior is highly dependent on reliable material properties, with focus on the parameters for permeability. The osmotic swelling behavior parameters applied on this work are the reference for the IVD FE studies which include such behavior. They concluded that the swelling behavior due to the strain-dependent osmotic pressure is a realistic approach to IVD macro-biomechanics. Afterwards, they analyzed the degenerative morphological changes of the IVD, through the simulation of several degenerative conditions: reduced disc height, endplate sclerosis, reduced water content, reduced IVD permeability and reduced osmotic swelling pressure. Their simulations first included a pre-conditioning free-swelling period, which was not time-limited, i.e., they allowed the model to swell until consolidation was reached. Then, they simulated the daily cycle, through axial compression loadings, namely 200N for 8h (recovery period) and 500N for 16h (activity period). Most of these conditions are related with changes on IVD porosity and permeability, which demonstrated the influence directly and indirectly all the mechanisms of the IVD behavior. The reduction of IVD height, water content and osmotic swelling pressure were proved to be the most relevant features on the degeneration process.

2.4.3. Summary

The state-of-the-art IVD FE modeling reflects that the global behavior of the IVD is assumed to be osmo-hyper-poro-visco-elastic, with high influence of the anisotropy of AF fibers (Schmidt, Galbusera, et al., 2013). The most complete models use all these features, even if some studies still neglect the impact of poroelasticity. Nonetheless, when this feature is considered, the osmotic swelling behavior is either neglected or implemented through the addition of an extra pressure or through fixed boundary pressure, which is also not realistic for the reproduction of the complex fluid flow biomechanisms.

2.5. References

Adams, M.A., Dolan, P., 2012. Intervertebral disc degeneration: evidence for two distinct phenotypes. J. Anat. 221, 497–506.

Adams, M.A., Dolan, P., Hutton, W.C., 1987. Diurnal variations in the stresses on the lumbar spine. Spine (Phila. Pa. 1976). 12, 130–7.

Adams, M.A., Dolan, P., McNally, D.S., 2009. The internal mechanical functioning of intervertebral discs and articular cartilage, and its relevance to matrix biology. Matrix Biol. 28, 384–9.

Adams, M.A., Green, T.P., 1993. Tensile properties of the annulus fibrosus. Eur. Spine J. 203–208.

Adams, M.A., Roughley, P.J., 2006. What is intervertebral disc degeneration, and what causes it? Spine (Phila. Pa. 1976). 31, 2151–61.

Alini, M., Eisenstein, S.M., Ito, K., Little, C., Kettler, A.A., Masuda, K., Melrose, J., Ralphs, J., Stokes, I., Wilke, H.-J., 2008. Are animal models useful for studying Human disc disorders/degeneration? Eur. Spine J. 17, 2–19.

Andreula, C., Muto, M., Leonardi, M., 2004. Interventional spinal procedures. Eur. J. Radiol. 50, 112–9.

Andreula, C.F., Simonetti, L., De Santis, F., Agati, R., Ricci, R., Leonardi, M., 2003. Minimally invasive oxygen-ozone therapy for lumbar disk herniation. AJNR. Am. J. Neuroradiol. 24, 996–1000.

Argoubi, M., Shirazi-Adl, A., 1996. Poroelastic creep response analysis of a lumbar motion segment in compression. J. Biomech. 29, 1331–9.

Ateshian, G.A., Albro, M.B., Maas, S., Weiss, J.A., 2011. Finite element implementation of mechanochemical phenomena in neutral deformable porous media under finite deformation. J. Biomech. Eng. 133, 081005.

Ateshian, G.A., Maas, S., Weiss, J.A., 2010. Finite element algorithm for frictionless contact of porous permeable media under finite deformation and sliding. J. Biomech. Eng. 132, 061006.

Ateshian, G.A., Maas, S., Weiss, J.A., 2012. Solute transport across a contact interface in deformable porous media. J. Biomech. 45, 1023–7.

Athanasiou, K.A., Natoli, R.M., 2008. Introduction to Continuum Biomechanics. Synth. Lect. Biomed. Eng. 3, 1–206.

Bazrgari, B., Shirazi-Adl, A., Kasra, M., 2008. Seated whole body vibrations with high-magnitude accelerations–relative roles of inertia and muscle forces. J. Biomech. 41, 2639–46.

Bazrgari, B., Shirazi-Adl, A., Larivière, C., 2009. Trunk response analysis under sudden forward perturbations using a kinematics-driven model. J. Biomech. 42, 1193–200.

Bazrgari, B., Shirazi-Adl, A., Parnianpour, M., 2009. Transient analysis of trunk response in sudden release loading using kinematics-driven finite element model. Clin. Biomech. (Bristol, Avon) 24, 341–7.

Bazrgari, B., Shirazi-Adl, A., Trottier, M., Mathieu, P., 2008. Computation of trunk equilibrium and stability in free flexion-extension movements at different velocities. J. Biomech. 41, 412–21.

Beattie, P.F., 2008. Current understanding of lumbar intervertebral disc degeneration: a review with emphasis upon etiology, pathophysiology, and lumbar magnetic resonance imaging findings. J. Orthop. Sports Phys. Ther. 38, 329–40.

Beckstein, J.C., Sen, S., Schaer, T.P., Vresilovic, E.J., Elliott, D.M., 2008. Comparison of animal discs used in disc research to Human lumbar disc: axial compression mechanics and glycosaminoglycan content. Spine (Phila. Pa. 1976). 33, E166–73.

Belytschko, T., Kulak, R.F., Schultz, a B., Galante, J.O., 1974. Finite element stress analysis of an intervertebral disc. J. Biomech. 7, 277–85.

Biot, M., 1941. General theory of three-dimensional consolidation. J. Appl. Phys. 12, 155–164.

Biot, M., 1972. Theory of finite deformations of porous solids. Indiana Univ. Math. J. 21, 597–620.

Broberg, K.B., 1993. Slow deformation of intervertebral discs. J. Biomech. 26, 501–512.

Buy, X., Gangi, A., 2010. Percutaneous treatment of intervertebral disc herniation. Semin. Intervent. Radiol. 27, 148–59.

Cao, L., Guilak, F., Setton, L., 2011. Three-dimensional finite element modeling of pericellular matrix and cell mechanics in the nucleus pulposus of the intervertebral disk based on in situ morphology. Biomech. Model. Mechanobiol. 10, 1–10.

Casula, G., Carcione, J.M., 1992. Generalized mechanical model analogies of linear viscoelastic behaviour. Boll. di Geofis. Teor. e Appl. 34.

Chan, S.C.W., Walser, J., Käppeli, P., Shamsollahi, M.J., Ferguson, S., Gantenbein-Ritter, B., 2013. Region specific response of intervertebral disc cells to complex dynamic loading: an organ culture study using a dynamic torsion-compression bioreactor. PLoS One 8, e72489.

Choi, Y.-S., 2009. Pathophysiology of degenerative disc disease. Asian Spine J. 3, 39–44.

Colombini, A., Lombardi, G., Corsi, M.M., Banfi, G., 2008. Pathophysiology of the Human intervertebral disc. Int. J. Biochem. Cell Biol. 40, 837–42.

Dennison, C.R., Wild, P.M., Wilson, D.R., Cripton, P. a, 2008. A minimally invasive in-fiber Bragg grating sensor for intervertebral disc pressure measurements. Meas. Sci. Technol. 19, 085201.

Detournay, E., Cheng, A., 1993. Fundamentals of Poroelasticity II, 113–171.

Dolan, P., Adams, M.A., 2001. Recent advances in lumbar spinal mechanics and their significance for modelling. Clin. Biomech. 1, 8–16.

Dupuis, H., Zerlett, G., 1987. Whole-body vibration and disorders of the spine. Int. Arch. Occup. Environ. Health 59, 323–36.

Eberlein, R., Holzapfel, G.A., Frolich, M., 2004. Multi-segment FEA of the Human lumbar spine including the heterogeneity of the annulus fibrosus. Comput. Mech. 34, 147–163.

Eberlein, R., Holzapfel, G.A., Schulze-Bauer, C.A.J., 2001. An Anisotropic Model for Annulus Tissue and Enhanced Finite Element Analyses of Intact Lumbar Disc Bodies. Comput. Methods Biomech. Biomed. Engin. 4, 209–229.

Ebraheim, N., Hassan, A., Lee, M., Xu, R., 2004. Functional anatomy of the lumbar spine. Semin. Pain Med. 2, 131–137.

Ehlers, W., Karajan, N., Markert, B., 2009. An extended biphasic model for charged hydrated tissues with application to the intervertebral disc. Biomech. Model. Mechanobiol. 8, 233–51.

Ehlers, W., Markert, B., Acartürk, A., 2003. Large strain viscoelastic swelling of charged hydrated porous media.

Ehlers, W., Markert, B., Karajan, N., Acartürk, A., 2006. A coupled FE analysis of the intervertebral disc based on a multiphasic TPM formulation. In: Holzapfel, G.A., Ogden, R.W. (Eds.), Mechanics of Biological Tissue. pp. 405–419.

Elliott, D., Setton, L., 2001. Anisotropic and Inhomogeneous Tensile Behavior of the Human Anulus Fibrosus: Experimental Measurement and Material Model Predictions. J. Biomech. Eng. 123, 256.

European Agency for Safety and Health at Work, 2008. Work-related musculoskeletal disorders: Prevention report.

European Comission, 2007. Special Eurobarometer: Health in the European Union.

Ferguson, S.J., Ito, K., Nolte, L.-P., 2004. Fluid flow and convective transport of solutes within the intervertebral disc. J. Biomech. 37, 213–221.

Fields, A.J., Lee, G.L., Keaveny, T.M., 2010. Mechanisms of initial endplate failure in the Human vertebral body. J. Biomech. 43, 3126–31.

Frei, H., Oxland, T.R., Nolte, L.P., 2002. Thoracolumbar spine mechanics contrasted under compression and shear loading. J. Orthop. Res. 20, 1333–8.

Frijns, A.J.H., Huyghe, J.M., Janssen, J.D., 1997. A validation of the quadriphasic mixture theory for intervertebral disc tissue. Int. J. Eng. Sci. 35, 1419–1429.

Fritz, J.M., Delitto, A., Welch, W.C., Erhard, R.E., 1998. Lumbar spinal stenosis: a review of current concepts in evaluation, management, and outcome measurements. Arch. Phys. Med. Rehabil. 79, 700–8.

Galbusera, F., Bashkuev, M., Wilke, H.-J., Shirazi-Adl, A., Schmidt, H., 2012. Comparison of various contact algorithms for poroelastic tissues. Comput. Methods Biomech. Biomed. Engin. 37–41.

Galbusera, F., Bellini, C.M., Raimondi, M.T., Fornari, M., Assietti, R., 2008. Cervical spine biomechanics following implantation of a disc prosthesis. Med. Eng. Phys. 30, 1127–33.

Galbusera, F., Mietsch, A., Schmidt, H., Wilke, H., 2013. Effect of intervertebral disc degeneration on disc cell viability: a numerical investigation. Comput. Methods Biomech. Biomed. Engin. 37–41.

Galbusera, F., Schmidt, H., Neidlinger-Wilke, C., Wilke, H.-J., 2011. The effect of degenerative morphological changes of the intervertebral disc on the lumbar spine biomechanics: a poroelastic finite element investigation. Comput. Methods Biomech. Biomed. Engin. 14, 729–39.

Galbusera, F., Schmidt, H., Noailly, J., Malandrino, A., Lacroix, D., Wilke, H.-J., Shirazi-Adl, A., 2011. Comparison of four methods to simulate swelling in poroelastic finite element models of intervertebral discs. J. Mech. Behav. Biomed. Mater. 4, 1234–41.

Gamradt, S.C., Wang, J.C., 2005. Lumbar disc arthroplasty. Spine J. 5, 95–103.

Gantenbein, B., Grünhagen, T., Lee, C.R., van Donkelaar, C.C., Alini, M., Ito, K., 2006. An in vitro organ culturing system for intervertebral disc explants with vertebral endplates: a feasibility study with ovine caudal discs. Spine (Phila. Pa. 1976). 31, 2665–73.

Goel, V.K., Grauer, J.N., Patel, T.C., Biyani, A., Sairyo, K., Vishnubhotla, S., Matyas, A., Cowgill, I., Shaw, M., Long, R., Dick, D., Panjabi, M.M., Serhan, H., 2005. Effects of charité artificial disc on the implanted and adjacent spinal segments mechanics using a hybrid testing protocol. Spine (Phila. Pa. 1976). 30, 2755–64.

Goel, V.K., Kim, Y.E., 1989. Effects of injury on the spinal motion segment mechanics in the axial compression mode. Clin. Biomech. 4, 161–167.

Goins, M.L., Wimberley, D.W., Yuan, P.S., Fitzhenry, L.N., Vaccaro, A.R., 2005. Nucleus pulposus replacement: an emerging technology. Spine J. 5, 317S–324S.

Griffith, J.F., Wang, Y.-X.J., Antonio, G.E., Choi, K.C., Yu, A., Ahuja, A.T., Leung, P.C., 2007. Modified Pfirrmann grading system for lumbar intervertebral disc degeneration. Spine (Phila. Pa. 1976). 32, E708–12.

Grumme, T., Bittl, M., 1998. Imaging and therapy of degenerative spine diseases–a neurosurgeon's view. Eur. J. Radiol. 27, 235–40.

Guan, Y., Yoganandan, N., Moore, J., Pintar, F., Zhang, J., Maiman, D.J., Laud, P., 2007. Moment-rotation responses of the Human lumbosacral spinal column. J. Biomech. 40, 1975–80.

Guilak, F., Ting-Beall, H.P., Baer, A., Trickey, W.R., Erickson, G.R., Setton, L. a, 1999. Viscoelastic properties of intervertebral disc cells. Identification of two biomechanically distinct cell populations. Spine (Phila. Pa. 1976). 24, 2475–83.

Gunning, J.L., Callaghan, J.P., McGill, S.M., 2001. Spinal posture and prior loading history modulate compressive strength and type of failure in the spine: a biomechanical study using a porcine cervical spine model. Clin. Biomech. (Bristol, Avon) 16, 471–80.

Guo, L.-X., Zhang, Y.-M., Zhang, M., 2011. Finite element modeling and modal analysis of the Human spine vibration configuration. IEEE Trans. Biomed. Eng. 58, 2987–90.

Hadjipavlou, A., Tzermiadianos, M.N., Bogduk, N., Zindrick, M.R., 2008. The pathophysiology of disc degeneration: a critical review. J. Bone Joint Surg. Br. 90, 1261–70.

Hamilton, D.J., Séguin, C. a, Wang, J., Pilliar, R.M., Kandel, R. a, 2006. Formation of a nucleus pulposus-cartilage endplate construct in vitro. Biomaterials 27, 397–405.

Henninger, H.B., Reese, S.P., Anderson, A.E., Weiss, J.A., 2010. Validation of computational models in biomechanics. Proc. Inst. Mech. Eng. Part H J. Eng. Med. 224, 801–812.

Heuer, F., Schmitt, H., Schmidt, H., Claes, L., Wilke, H.-J., 2007. Creep associated changes in intervertebral disc bulging obtained with a laser scanning device. Clin. Biomech. (Bristol, Avon) 22, 737–44.

Hollingsworth, N.T., Wagner, D.R., 2011. Modeling shear behavior of the annulus fibrosus. J. Mech. Behav. Biomed. Mater. 4, 1103–14.

Holm, S., Holm, A.K., Ekström, L., Karladani, A., Hansson, T., 2004. Experimental disc degeneration due to endplate injury. J. Spinal Disord. Tech. 17, 64–71.

Holzapfel, G.A., Schulze-Bauer, C.A.J., Feigl, G., Regitnig, P., 2005. Single lamellar mechanics of the Human lumbar anulus fibrosus. Biomech. Model. Mechanobiol. 3, 125–40.

Hsieh, A.H., Twomey, J.D., 2010. Cellular mechanobiology of the intervertebral disc: new directions and approaches. J. Biomech. 43, 137–45.

Hussain, M., Natarajan, R.N., An, H.S., Andersson, G.B.J., 2012. Progressive disc degeneration at C5-C6 segment affects the mechanics between disc heights and posterior facets above and below the degenerated segment: A flexion-extension investigation using a poroelastic C3-T1 finite element model. Med. Eng. Phys. 34, 552–8.

Huyghe, J.M., 1986. Non-linear finite element models for the beating left ventricle and the intramyocardial coronary circulation.

Huyghe, J.M., Houben, G.B., Drost, M.R., van Donkelaar, C.C., 2003. An ionised/non-ionised dual porosity model of intervertebral disc tissue. Biomech. Model. Mechanobiol. 2, 3–19.

Iatridis, J., Kumar, S., Foster, R.J., Weidenbaum, M., Mow, V.C., 1999. Shear mechanical properties of Human lumbar annulus fibrosus. J. Orthop. Res. 17, 732–7.

Iatridis, J., Laible, J.P., Krag, M.H., 2003. Influence of fixed charge density magnitude and distribution on the intervertebral disc: applications of a poroelastic and chemical electric (PEACE) model. J. Biomech. Eng. 125, 12–24.

Iatridis, J., Nicoll, S.B., Michalek, A.J., Walter, B., Gupta, M.S., 2013. Role of biomechanics in intervertebral disc degeneration and regenerative therapies: what needs repairing in the disc and what are promising biomaterials for its repair? Spine J. 13, 243–62.

Iatridis, J., Setton, L., Foster, R.J., Rawlins, B., Weidenbaum, M., Mow, V.C., 1998. Degeneration affects the anisotropic and nonlinear behaviors of Human anulus fibrosus in compression. J. Biomech. 31, 535–44.

Iatridis, J., Setton, L., Weidenbaum, M., Mow, V., 1997. The viscoelastic behavior of the non-degenerate Human lumbar nucleus pulposus in shear. J. Biomech. 30, 1005–1013.

Iatridis, J., Weidenbaum, M., Setton, L., Mow, V., 1996. Is the nucleus pulposus a solid or a fluid? Mechanical behaviors of the nucleus pulposus of the Human intervertebral disc. Spine (Phila. Pa. 1976). 21, 1174–1184.

Jackson, A.R., Huang, C.-Y., Gu, W.Y., 2011. Effect of endplate calcification and mechanical deformation on the distribution of glucose in intervertebral disc: a 3D finite element study. Comput. Methods Biomech. Biomed. Engin. 14, 195–204.

Jayson, M.I., Herbert, C.M., Barks, J.S., 1973. Intervertebral discs: nuclear morphology and bursting pressures. Ann. Rheum. Dis. 32, 308–15.

Jensen, G.M., 1980. Biomechanics of the lumbar intervertebral disk: a review. Phys. Ther. 60, 765–73.

Joshi, A., 2004. Mechanical Behavior of the Human Lumbar Intervertebral Disc with Polymeric Hydrogel Nucleus Implant: An Experimental and Finite Element Study.

Joshi, A., Massey, C.J., Karduna, A., Vresilovic, E., Marcolongo, M., 2009. The effect of nucleus implant parameters on the compressive mechanics of the lumbar intervertebral disc: a finite element study. J. Biomed. Mater. Res. B. Appl. Biomater. 90, 596–607.

Kalichman, L., Hunter, D.J., 2008. The genetics of intervertebral disc degeneration. Associated genes. Joint. Bone. Spine 75, 388–96.

Kim, Y., 2000. Prediction of peripheral tears in the anulus of the intervertebral disc. Spine (Phila. Pa. 1976). 25, 1771–4.

Klisch, S.M., Lotz, J.C., 1999. Application of a fiber-reinforced continuum theory to multiple deformations of the annulus fibrosus. J. Biomech. 32, 1027–36.

Kong, W.Z., Goel, V.K., Gilbertson, L.G., 1998. Prediction of biomechanical parameters in the lumbar spine during static sagittal plane lifting. J. Biomech. Eng.

Kong, W.Z., Goel, V.K., Gilbertson, L.G., Weinstein, J.N., 1996. Effects of muscle dysfunction on lumbar spine mechanics. A finite element study based on a two motion segments model. Spine (Phila. Pa. 1976). 21, 2197–206; discussion 2206–7.

Korecki, C.L., MacLean, J.J., Iatridis, J.C., 2007. Characterization of an in vitro intervertebral disc organ culture system. Eur. Spine J. 16, 1029–37.

Lanir, Y., 1987. Biorheology and fluid flux in swelling tissues. I.Bicom- ponent theory for small deformations, including concentration effects. Biorheology 24, 173–187.

Lanir, Y., 2012. Osmotic swelling and residual stress in cardiovascular tissues. J. Biomech. 45, 780–9.

Li, H., Wang, Z., 2006. Intervertebral disc biomechanical analysis using the finite element modeling based on medical images. Comput. Med. imaging Graph. 30, 363–70.

Lin, H.S., Liu, Y.K., Ray, G., Nikravesh, P., 1978. Systems identification for material properties of the intervertebral joint. J. Biomech. 11, 1–14.

Little, J., Adam, C.J., 2010. Development of a computer simulation tool for application in adolescent spinal deformity surgery. Biomed. Simul. 90–97.

Little, J.P., 2004. Finite Element Modelling of Anular Lesions in the Lumbar Intervertebral Disc.

Little, J.P., Adam, C.J., Evans, J.H., Pettet, G.J., Pearcy, M.J., 2007. Nonlinear finite element analysis of anular lesions in the L4/5 intervertebral disc. J. Biomech. 40, 2744–51.

Little, J.P., De Visser, H., Pearcy, M.J., Adam, C.J., 2008. Are coupled rotations in the lumbar spine largely due to the osseo-ligamentous anatomy?—A modeling study. Comput. Methods Biomech. Biomed. Engin. 11, 95–103.

Little, J.P., Pearcy, M.J., Tevelen, G., Evans, J.H., Pettet, G., Adam, C.J., 2010. The mechanical response of the ovine lumbar anulus fibrosus to uniaxial, biaxial and shear loads. J. Mech. Behav. Biomed. Mater. 3, 146–57.

Liu, K., Ovaert, T.C., 2011. Poro-viscoelastic constitutive modeling of unconfined creep of hydrogels using finite element analysis with integrated optimization method. J. Mech. Behav. Biomed. Mater. 4, 440–50.

Lodygowski, T., Witold, K., Wierszycki, M., 2005. Three-dimensional nonlinear finite element model of the Human lumbar spine segment. Acta Bioeng. Biomech. 7, 17–28.

Maas, S., Ellis, B.J., Ateshian, G.A., Weiss, J.A., 2012. FEBio: finite elements for biomechanics. J. Biomech. Eng. 134, 011005.

Malandrino, A., Noailly, J., Lacroix, D., 2013. Regional annulus fibre orientations used as a tool for the calibration of lumbar intervertebral disc finite element models. Comput. Methods Biomech. Biomed. Engin. 16, 923–928.

Malandrino, A., Planell, J., Lacroix, D., 2009. Statistical factorial analysis on the poroelastic material properties sensitivity of the lumbar intervertebral disc under compression, flexion and axial rotation. J. Biomech. 42, 2780–8.

Martin, M.D., Boxell, C.M., Malone, D.G., 2002. Pathophysiology of lumbar disc degeneration: a review of the literature. Neurosurg. Focus 13, E1.

Martinez, J.B., Oloyede, V.O., Broom, N.D., 1997. Biomechanics of load-bearing of the intervertebral disc: an experimental and finite element model. Med. Eng. Phys. 19, 145–56.

Massey, C.J., 2009. Finite Element Analysis and Materials Characterization of Changes Due to Aging and Degeneration of the Human Intervertebral Disc.

Massey, C.J., van Donkelaar, C.C., Vresilovic, E., Zavaliangos, A., Marcolongo, M., 2012. Effects of aging and degeneration on the Human intervertebral disc during the diurnal cycle: a finite element study. J. Orthop. Res. 30, 122–8.

McNally, D., Naish, C., Halliwell, M., 2000. Intervertebral disc structure: observation by a novel use of ultrasound imaging. Ultrasound Med. Biol. 26, 751–758.

Michalek, A., Gardner-Morse, M.G., Iatridis, J., 2012. Large residual strains are present in the intervertebral disc annulus fibrosus in the unloaded state. J. Biomech. 45, 1227–31.

Mirza, S.K., White, A.A., 1995. Anatomy of intervertebral disc and pathophysiology of herniated disc disease. J. Clin. Laser Med. Surg. 13, 131–42.

Monteiro, N., 2009. Analysis of the Intervertebral Discs Adjacent to Interbody Fusion using a Multibody and Finite Element Co-Simulation.

Moore, R.J., 2000. The vertebral end-plate: what do we know? Eur. Spine J. 9, 92–6.

Moore, R.J., 2006. The vertebral endplate: disc degeneration, disc regeneration. Eur. Spine J. 15 Suppl 3, S333–7.

Moramarco, V., Pérez del Palomar, A., Pappalettere, C., Doblaré, M., 2010. An accurate validation of a computational model of a Human lumbosacral segment. J. Biomech. 43, 334–42.

Muto, M., Andreula, C., Leonardi, M., 2004. Treatment of herniated lumbar disc by intradiscal and intraforaminal oxygen-ozone (O 2-O 3) injection. j. Neuroradiol. 31, 183–189.

Nachemson, A., Morris, J.M., 1964. in Vivo Measurements of Intradiscal Pressure. Discometry, a Method for the Determination of Pressure in the Lower Lumbar Discs. J. Bone Joint Surg. Am. 46, 1077–92.

Natarajan, R.N., Ke, J.H., Andersson, G.B., 1994. A model to study the disc degeneration process. Spine (Phila. Pa. 1976).

Natarajan, R.N., Williams, J.R., Andersson, G.B.J., 2004. Recent advances in analytical modeling of lumbar disc degeneration. Spine (Phila. Pa. 1976). 29, 2733–41.

Natarajan, R.N., Williams, J.R., Andersson, G.B.J., 2006. Modeling changes in intervertebral disc mechanics with degeneration. J. Bone Joint Surg. Am. 88 Suppl 2, 36–40.

Natarajan, R.N., Williams, J.R., Lavender, S. a, An, H.S., Andersson, G.B., 2008. Relationship between disc injury and manual lifting: a poroelastic finite element model study. Proc. Inst. Mech. Eng. Part H J. Eng. Med. 222, 195–207.

Natarajan, R.N., Williams, J.R., Lavender, S. a., Andersson, G.B.J., 2007. Poro-elastic finite element model to predict the failure progression in a lumbar disc due to cyclic loading. Comput. Struct. 85, 1142–1151.

Neidlinger-Wilke, C., Galbusera, F., Pratsinis, H., Mavrogonatou, E., Mietsch, A., Kletsas, D., Wilke, H.-J., 2013. Mechanical loading of the intervertebral disc: from the macroscopic to the cellular level. Eur. Spine J.

Nerurkar, N.L., Elliott, D.M., Mauck, R.L., 2010. Mechanical design criteria for intervertebral disc tissue engineering. J. Biomech. 43, 1017–30.

Niosi, C., Oxland, T., 2004. Degenerative mechanics of the lumbar spine. Spine J. 4, 202S–208S.

Nixon, J., 1986. Intervertebral disc mechanics: a review. J. R. Soc. Med. 79, 100–4.

Noailly, J., 2009. Model developments for in silico studies of the lumbar spine biomechanics.

Noailly, J., Ambrosio, L., Elizabeth Tanner, K., Planell, J., Lacroix, D., 2012. In silico evaluation of a new composite disc substitute with a L3-L5 lumbar spine finite element model. Eur. Spine J. 21 Suppl 5, S675–87.

Noailly, J., Lacroix, D., Planell, J., 2005. Finite element study of a novel intervertebral disc substitute. Spine (Phila. Pa. 1976). 30, 2257–64.

Noailly, J., Planell, J., Lacroix, D., 2011. On the collagen criss-cross angles in the annuli fibrosi of lumbar spine finite element models. Biomech. Model. Mechanobiol. 10, 203–19.

Noailly, J., Wilke, H.-J., Planell, J., Lacroix, D., 2007. How does the geometry affect the internal biomechanics of a lumbar spine bi-segment finite element model? Consequences on the validation process. J. Biomech. 40, 2414–25.

Oder, B., Loewe, M., Reisegger, M., Lang, W., Ilias, W., Thurnher, S., 2008. CT-guided ozone/steroid therapy for the treatment of degenerative spinal disease–effect of age, gender, disc pathology and multi-segmental changes. Neuroradiology 50, 777–85.

Oomens, C., Brekelmans, M., Baaijens, F., 2009. Biomechanics: concepts and computation.

Oomens, C., van Campen, D.H., Grootenboer, H.J., 1987. A mixture approach to the mechanics of skin. J. Biomech. 20, 877–885.

Panjabi, M.M., 2003. Clinical spinal instability and low back pain. J. Electromyogr. Kinesiol. 13, 371–379.

Paul, C., Schoorl, T., Zuiderbaan, H., Zandieh Doulabi, B., van der Veen, A., van de Ven, P., Smit, T., van Royen, B., Helder, M., Mullender, M., 2013. Dynamic and Static Overloading Induce Early Degenerative Processes in Caprine Lumbar Intervertebral Discs. PLoS One 8, e62411.

Paul, C., Zuiderbaan, Zandieh Doulabi, B., van der Veen, A.J., van de Ven, P.M., Smit, T.H., Helder, M.N., van Royen, B.J., Mullender, M.G., 2012. Simulated-physiological loading conditions preserve biological and mechanical properties of caprine lumbar intervertebral discs in ex vivo culture. PLoS One 7, e33147.

Pfirrmann, C.W., Metzdorf, a, Zanetti, M., Hodler, J., Boos, N., 2001. Magnetic resonance classification of lumbar intervertebral disc degeneration. Spine (Phila. Pa. 1976). 26, 1873–8.

Pierce, D.M., Ricken, T., Holzapfel, G. a, 2013. A hyperelastic biphasic fibre-reinforced model of articular cartilage considering distributed collagen fibre orientations: continuum basis, computational aspects and applications. Comput. Methods Biomech. Biomed. Engin. 16, 1344–61.

Pollintine, P., van Tunen, M., Luo, J., Brown, M., Dolan, P., Adams, M.A., 2010. Time-dependent compressive deformation of the ageing spine: relevance to spinal stenosis. Spine (Phila. Pa. 1976). 35, 386–94.

Prisby, R.D., Lafage-Proust, M.-H., Malaval, L., Belli, A., Vico, L., 2008. Effects of whole body vibration on the skeleton and other organ systems in man and animal models: what we know and what we need to know. Ageing Res. Rev. 7, 319–29.

Raj, P., 2008. Intervertebral Disc: Anatomy Physiology Pathophysiology Treatment. Pain Pract. 8, 18–44.

Re, L., Mawsouf, M.N., Menéndez, S., León, O.S., Sánchez, G.M., Hernández, F., 2008. Ozone therapy: clinical and basic evidence of its therapeutic potential. Arch. Med. Res. 39, 17–26.

Reitmaier, S., Wolfram, U., Ignatius, A., Wilke, H.-J., Gloria, A., Martín-Martínez, J.M., Silva-Correia, J., Miguel Oliveira, J., Luís Reis, R., Schmidt, H., 2012. Hydrogels for nucleus replacement-Facing the biomechanical challenge. J. Mech. Behav. Biomed. Mater. 14, 67–77.

Riches, P.E., Dhillon, N., Lotz, J., Woods, a W., McNally, D.S., 2002. The internal mechanics of the intervertebral disc under cyclic loading. J. Biomech. 35, 1263–71.

Roberts, S., Menage, J., Urban, J., 1989. Biochemical and structural properties of the cartilage end-plate and its relation to the intervertebral disc. Spine (Phila. Pa. 1976). 14, 166–174.

Rohlmann, A., Petersen, R., Schwachmeyer, V., Graichen, F., Bergmann, G., 2012. Spinal loads during position changes. Clin. Biomech. (Bristol, Avon) 27, 754–8.

Rohlmann, A., Zander, T., Schmidt, H., Wilke, H.-J., Bergmann, G., 2006. Analysis of the influence of disc degeneration on the mechanical behaviour of a lumbar motion segment using the finite element method. J. Biomech. 39, 2484–90.

Roughley, P.J., 2004. Biology of intervertebral disc aging and degeneration: involvement of the extracellular matrix. Spine (Phila. Pa. 1976). 29, 2691–9.

Ruan, D., He, Q., Ding, Y., Hou, L., Li, J., Luk, K.D.K., 2007. Intervertebral disc transplantation in the treatment of degenerative spine disease: a preliminary study. Lancet 369, 993–9.

Ruberté, L.M., Natarajan, R.N., Andersson, G.B., 2009. Influence of single-level lumbar degenerative disc disease on the behavior of the adjacent segments–a finite element model study. J. Biomech. 42, 341–8.

Sato, K., Kikuchi, S., Yonezawa, T., 1999. In vivo intradiscal pressure measurement in healthy individuals and in patients with ongoing back problems. Spine (Phila. Pa. 1976). 24, 2468–74.

Schmidt, H., Bashkuev, M., Galbusera, F., Wilke, H.-J., Shirazi-Adl, A., 2013. Finite element study of Human lumbar disc nucleus replacements. Comput. Methods Biomech. Biomed. Engin.

Schmidt, H., Galbusera, F., Rohlmann, A., Shirazi-Adl, A., 2013. What have we learned from finite element model studies of lumbar intervertebral discs in the past four decades? J. Biomech. 46, 2342–55.

Schmidt, H., Galbusera, F., Wilke, H.-J., Shirazi-Adl, A., 2011. Remedy for fictive negative pressures in biphasic finite element models of the intervertebral disc during unloading. Comput. Methods Biomech. Biomed. Engin. 14, 293–303.

Schmidt, H., Heuer, F., Simon, U., Kettler, A., Rohlmann, A., Claes, L., Wilke, H.-J., 2006. Application of a new calibration method for a three-dimensional finite element model of a Human lumbar annulus fibrosus. Clin. Biomech. (Bristol, Avon) 21, 337–44.

Schmidt, H., Heuer, F., Wilke, H.-J., 2009. Which axial and bending stiffnesses of posterior implants are required to design a flexible lumbar stabilization system? J. Biomech. 42, 48–54.

Schmidt, H., Kettler, A., Rohlmann, A., Claes, L., Wilke, H.-J., 2007. The risk of disc prolapses with complex loading in different degrees of disc degeneration - a finite element analysis. Clin. Biomech. (Bristol, Avon) 22, 988–98.

Schmidt, H., Reitmaier, S., 2013. Is the ovine intervertebral disc a small Human one? A finite element model study. J. Mech. Behav. Biomed. Mater. 17, 229–41.

Schmidt, H., Shirazi-Adl, A., Galbusera, F., Wilke, H.-J., 2010. Response analysis of the lumbar spine during regular daily activities–a finite element analysis. J. Biomech. 43, 1849–56.

Schroeder, Y., Elliott, D.M., Wilson, W., Baaijens, F.P.T., Huyghe, J.M., 2008. Experimental and model determination of Human intervertebral disc osmoviscoelasticity. J. Orthop. Res. 26, 1141–6.

Schroeder, Y., Huyghe, J.M., van Donkelaar, C.C., Ito, K., 2010. A biochemical/biophysical 3D FE intervertebral disc model. Biomech. Model. Mechanobiol. 9, 641–50.

Schroeder, Y., Sivan, S., Wilson, W., Merkher, Y., Huyghe, J.M., Maroudas, A., Baaijens, F.P.T., 2007. Are disc pressure, stress, and osmolarity affected by intra- and extrafibrillar fluid exchange? J. Orthop. Res. 25, 1317–24.

Schroeder, Y., Wilson, W., Huyghe, J.M., Baaijens, F.P.T., 2006. Osmoviscoelastic finite element model of the intervertebral disc. Eur. Spine J. 15 Suppl 3, S361–71.

Schultz, A., Andersson, G., Ortengren, R., Haderspeck, K., Nachemson, A., 1982. Loads on the lumbar spine. Validation of a biomechanical analysis by measurements of intradiscal pressures and myoelectric signals. J. Bone Joint Surg. Am. 64, 713–20.

Schultz, D.S., Rodriguez, A.G., Hansma, P.K., Lotz, J.C., 2009. Mechanical profiling of intervertebral discs. J. Biomech. 42, 1154–7.

Shankar, H., Scarlett, J., Abram, S.E., 2009. Anatomy and pathophysiology of intervertebral disc disease. Tech. Reg. Anesth. Pain Manag. 13, 67–75.

Shirazi-Adl, A., Ahmed, A.M., Shrivastava, S.C., 1986a. Mechanical response of a lumbar motion segment in axial torque alone and combined with compression. Spine (Phila. Pa. 1976). 11, 914–27.

Shirazi-Adl, A., Ahmed, A.M., Shrivastava, S.C., 1986b. A finite element study of a lumbar motion segment subjected to pure sagittal plane moments. J. Biomech. 19, 331–350.

Shirazi-Adl, A., Drouin, G., 1987. Load-bearing role of facets in a lumbar segment under sagittal plane loadings. J. Biomech. 20, 601–13.

Shirazi-Adl, A., Taheri, M., Urban, J.P.G., 2010. Analysis of cell viability in intervertebral disc: Effect of endplate permeability on cell population. J. Biomech. 43, 1330–6.

Silva, P., Crozier, S., Veidt, M., Pearcy, M.J., 2005. An experimental and finite element poroelastic creep response analysis of an intervertebral hydrogel disc model in axial compression. J. Mater. Sci. Mater. Med. 16, 663–9.

Silva-Correia, J., Oliveira, J.M., Caridade, S.G., Oliveira, J.T., Sousa, R.A., Mano, J.F., Reis, R.L., 2011. Gellan gum-based hydrogels for intervertebral disc tissue-engineering applications. J. Tissue Eng. Regen. Med. 5, e97–107.

Simon, B.R., Wu, J.S., Carlton, M.W., Evans, J.H., Kazarian, L.E., 1985. Structural models for Human spinal motion segments based on a poroelastic view of the intervertebral disk. J. Biomech. Eng. 107, 327–35.

Sivan, S., Neidlinger-Wilke, C., Würtz, K., Maroudas, A., Urban, J.P.G., 2006. Diurnal fluid expression and activity of intervertebral disc cells. Biorheology 43, 283–91.

Skrzypiec, D.M., Pollintine, P., Przybyla, A., Dolan, P., Adams, M.A., 2007. The internal mechanical properties of cervical intervertebral discs as revealed by stress profilometry. Eur. Spine J. 16, 1701–9.

Smit, T.H., 2002. The use of a quadruped as an in vivo model for the study of the spine - biomechanical considerations. Eur. Spine J. 11, 137–44.

Snijders, H., Huyghe, J.M., Janssen, J.D., 1995. Triphasic finite element model for swelling porous media. Int. J. Numer. Methods Fluids 20, 1039–1046.

Snook, S.H., Webster, B.S., McGorry, R.W., 2002. The reduction of chronic, nonspecific low back pain through the control of early morning lumbar flexion: 3-year follow-up. J. Occup. Rehabil. 12, 13–9.

Song, Y.-Q., Sham, P., Cheung, K.M.C., Chan, D., 2008. (iv) Genetics of disc degeneration. Curr. Orthop. 22, 259–266.

Steppan, J., Meaders, T., Muto, M., Murphy, K.J., 2010. A metaanalysis of the effectiveness and safety of ozone treatments for herniated lumbar discs. J. Vasc. Interv. Radiol. 21, 534–48.

Stokes, I., Iatridis, J., 2004. Mechanical conditions that accelerate intervertebral disc degeneration: overload versus immobilization. Spine (Phila. Pa. 1976). 29, 2724–32.

Strange, D.G.T., Fisher, S.T., Boughton, P.C., Kishen, T.J., Diwan, A.D., 2010. Restoration of compressive loading properties of lumbar discs with a nucleus implant-a finite element analysis study. Spine J. 10, 602–9.

Swider, P., Accadbled, F., Laffosse, J.M., Sales de Gauzy, J., 2012. Influence of fluid-flow direction on effective permeability of the vertebral end plate: an analytical model. Comput. Methods Biomech. Biomed. Engin. 15, 151–6.

Swider, P., Pédrono, A., Ambard, D., Accadbled, F., Sales de Gauzy, J., 2010. Substructuring and poroelastic modelling of the intervertebral disc. J. Biomech. 43, 1287–91.

Taher, F., Essig, D., Lebl, D.R., Hughes, A.P., Sama, A., Cammisa, F.P., Girardi, F.P., 2012. Lumbar degenerative disc disease: current and future concepts of diagnosis and management. Adv. Orthop. 2012.

Teo, J.C.M., Chui, C.K., Wang, Z.L., Ong, S.H., Yan, C.H., Wang, S.C., Wong, H.K., Teoh, S.H., 2007. Heterogeneous meshing and biomechanical modeling of Human spine. Med. Eng. Phys. 29, 277–90.

Terzaghi, K., 1925. Principle of soil mechanics. Liepzig: Eng. News Record.

Terzaghi, K., 1943. Theoretical soil mechanics. John Wiley & Sons.

Thompson, J., Pearce, R., Schechter, M., 1990. Preliminary evaluation of a scheme for grading the gross morphology of the Human intervertebral disc. Spine (Phila. Pa. 1976).

Tsuji, H., Hirano, N., Ohshima, H., Ishihara, H., Terahata, N., Motoe, T., 1993. Structural variation of the anterior and posterior anulus fibrosus in the development of Human lumbar intervertebral disc. Spine (Phila. Pa. 1976). 18, 204–210.

Urban, J., Roberts, S., 2003. Degeneration of the intervertebral disc. Arthritis Res. Ther. 5.

Urban, J., Roberts, S., Ralphs, J., 2000. The nucleus of the intervertebral disc from development to degeneration. Am. Zool. 40, 53–61.

Urban, J.P.G., McMullin, J.F., 1988. Swelling pressure of the lumbar intervertebral discs: influence of age, spinal level, composition, and degeneration. Spine (Phila. Pa. 1976). 13, 179–187.

Van den Broek, P.R., Huyghe, J.M., Ito, K., 2012. Biomechanical behavior of a biomimetic artificial intervertebral disc. Spine (Phila. Pa. 1976). 37, E367–73.

Van den Broek, P.R., Huyghe, J.M., Wilson, W., Ito, K., 2012. Design of next generation total disk replacements. J. Biomech. 45, 134–40.

Van der Veen, A., 2009. Mechanical behaviour of the intervertebral disc under sustained compressive loading.

Van der Voet, A., 1997. A comparison of finite element codes for the solution of biphasic poroelastic problems. Proc. Inst. Mech. Eng. H. 211, 209–11.

Van Loon, R., Huyghe, J.M., Wijlaars, M.W., Baaijens, F.P.T., 2003. 3D FE implementation of an incompressible quadriphasic mixture model. Int. J. Numer. Methods Eng. 57, 1243–1258.

Wagner, D.R., Lotz, J.C., 2004. Theoretical model and experimental results for the nonlinear elastic behavior of Human annulus fibrosus. J. Orthop. Res. 22, 901–9.

Wang, S., Park, W.M., Gadikota, H.R., Miao, J., Kim, Y.H., Wood, K.B., Li, G., 2012. A combined numerical and experimental technique for estimation of the forces and moments in the lumbar intervertebral disc. Comput. Methods Biomech. Biomed. Engin.

Whatley, B.R., Wen, X., 2012. Intervertebral disc (IVD): Structure, degeneration, repair and regeneration. Mater. Sci. Eng. C 32, 61–77.

Wilder, D.G., Pope, M.H., 1996. Epidemiological and aetiological aspects of low back pain in vibration environments - an update. Clin. Biomech. (Bristol, Avon) 11, 61–73.

Wilke, H.-J., Neef, P., Caimi, M., Hoogland, T., Claes, L.E., 1999. New in vivo measurements of pressures in the intervertebral disc in daily life. Spine (Phila. Pa. 1976). 24, 755–62.

Williams, J.R., Natarajan, R.N., Andersson, G.B.J., 2007. Inclusion of regional poroelastic material properties better predicts biomechanical behavior of lumbar discs subjected to dynamic loading. J. Biomech. 40, 1981–7.

Wilson, W., Huyghe, J.M., van Donkelaar, C.C., 2007. Depth-dependent compressive equilibrium properties of articular cartilage explained by its composition. Biomech. Model. Mechanobiol. 6, 43–53.

Wilson, W., van Donkelaar, C.C., Huyghe, J.M., 2005. A Comparison Between Mechano-Electrochemical and Biphasic Swelling Theories for Soft Hydrated Tissues. J. Biomech. Eng. 127, 158.

Wilson, W., van Donkelaar, C.C., van Rietbergen, B., Huiskes, R., 2005. A fibril-reinforced poroviscoelastic swelling model for articular cartilage. J. Biomech. 38, 1195–204.

Wognum, S., Huyghe, J.M., Baaijens, F.P.T., 2006. Influence of osmotic pressure changes on the opening of existing cracks in 2 intervertebral disc models. Spine (Phila. Pa. 1976). 31, 1783–8.

Wu, J.S., Chen, J.H., 1996. Clarification of the mechanical behaviour of spinal motion segments through a three-dimensional poroelastic mixed finite element model. Med. Eng. Phys. 18, 215–24.

Yang, K., King, A., 1984. Mechanism of facet load transmission as a hypothesis for low-back pain. Spine (Phila. Pa. 1976).

Yoon, S.T., 2005. Molecular therapy of the intervertebral disc. Spine J. 5, 280S–286S.

Zander, T., Krishnakanth, P., Bergmann, G., Rohlmann, A., 2010. Diurnal variations in intervertebral disc height affect spine flexibility, intradiscal pressure and contact compressive forces in the facet joints. Comput. Methods Biomech. Biomed. Engin. 13, 551–7.

3. FINITE ELEMENT MODELING

The mechanical modeling and finite element implementation of a novel poroelastic biphasic model is introduced and detailed, and the constitutive modeling briefly addressed. The FE implementation is carried out in a home-developed open-source FE solver. The chapter ends with the description of the building of an anatomically relevant FE mesh of a Human lumbar motion segment.

3.1. Mechanical Modeling

The continuum formulation (mechanical and constitutive modeling) suited for the FE implementation and simulation of the biomechanical behavior of an osmo-poro-hyper-viscoelastic MS FE model is described in what follows. A novel poroelastic formulation was developed and implemented in a home-developed FE solver, which already included the most relevant features for biomechanical modeling and simulation of soft-tissues, such as their almost incompressibility and viscoelastic effects.

The essential continuum mechanics background is presented, along with derivations of the second Piola-Kirchhoff stress tensor ($\mathbf{\Pi}$) and their FE implementation. Biological soft tissues such as the NP and the AF are subject to finite deformations and their mechanical behavior is highly nonlinear, anisotropic, inhomogeneous and incompressible in the physiological state.

To model the non-linear isotropic and/or anisotropic tissues' passive mechanical behavior, several phenomenological hyperelastic constitutive models are implemented and used. In particular, an anisotropic fiber-reinforced hyperelastic material which takes into account and incorporates the histological structure, i.e., an anatomically-based fibers distribution within the AF is accurately taken into account and a new algorithm detailed and described. The multiphasic

nature of the IVD, coupled with the Darcy's law and osmotic properties, are also a key feature of the IVD's tissues.

The implementation of these biomechanical phenomena into a FE formulation is based on a mixed two-field variational principle, i.e., displacement and pressure fields, with a total Lagrangian formulation and a fully implicit time integration scheme (Alves et al., 2010) in agreement with the pioneer work of (Sussman and Bathe, 1987). The name of mixed u/P formulation reflects the use of separate interpolations for the displacements and the Cauchy (hydrostatic) pressure. Although its primary application to almost incompressible media, it may also be applied to compressible analyses. Both u/P-c and u/P finite elements can be used, being the first ones the most appropriate for multiphasic applications, as they guarantee the required continuity of the pressure fields between adjacent elements[i]. The second ones are recommended for monophasic applications. In the following derivation, a general nonlinear framework is adopted, in which material and/or geometric nonlinearities and large deformations are considered.

3.1.1. Basic Kinematics

The description of the basic kinematics starts with the assumption that Ω_0 represents the configuration of an arbitrary body of interest and $\aleph : \Omega_0 \rightarrow \Omega$, $\aleph : \mathbf{X} \rightarrow \mathbf{x}$ be the non-linear deformation. $\aleph$ maps points $\mathbf{X} \in \Omega_0$ of the reference configuration (load free state) one to one and onto points $\mathbf{x} \in \Omega$ of the current configuration (loaded deformed state).

The deformation gradient tensor ($\mathbf{F}$) is defined as

$$\mathbf{F} = \frac{\partial \mathbf{x}}{\partial \mathbf{X}} = \mathbf{I} + \frac{\partial \mathbf{u}}{\partial \mathbf{X}}. \qquad 3.1$$

The displacement field is defined as $\mathbf{u} = \mathbf{x} - \mathbf{X}$, and $\mathbf{I}$ is the second order unit tensor. As described in Figure 3.1, $\mathbf{F}$ is a linear transformation that maps infinitesimal small vector $\mathrm{d}\mathbf{X}$ of the reference configuration onto infinitesimal small vector $\mathrm{d}\mathbf{x}$ of the current configuration,

[i] The discussion on the finite elements chosen for the lumbar MS model will be held on the second section of the present chapter.

$\mathrm{d}\mathbf{x} = \mathbf{F}\,\mathrm{d}\mathbf{X}$. The Jacobian $J = \det(\mathbf{F}) > 0$ is a measure of the local volume change. Adopting a decomposition of the total deformation gradient into volumetric $J^{1/3}\mathbf{I}$ and isochoric $\overline{\mathbf{F}}\left(= J^{-1/3}\mathbf{F}\right)$ parts, the total deformation gradient $\mathbf{F}$ can be rewritten as:

$$\mathbf{F} = \left(J^{+1/3}\mathbf{I}\right)\cdot\left(J^{-1/3}\mathbf{F}\right) = J^{+1/3}\,\overline{\mathbf{F}}\,, \qquad 3.2$$

With the isochoric deformation gradient defined as:

$$\overline{\mathbf{F}} = J^{-\frac{1}{3}}\mathbf{F}\,. \qquad 3.3$$

The right Cauchy-Green strain tensor $\mathbf{C}$ and the Green-Lagrange strain tensor $\mathbf{E}$ are two different measures of the continuum strain field, and are defined, respectively, by:

$$\mathbf{C} = \mathbf{F}^T\mathbf{F} \qquad 3.4$$

$$\mathbf{E} = \frac{1}{2}\left(\mathbf{C} - \mathbf{I}\right) \qquad 3.5$$

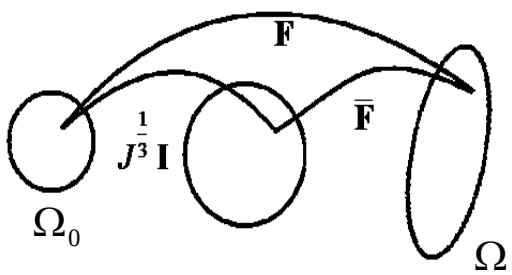

Figure 3.1. Decomposition of deformation gradient tensor $\mathbf{F}$ into volumetric $J^{1/3}\mathbf{I}$ and isochoric $\overline{\mathbf{F}}\left(= J^{-1/3}\mathbf{F}\right)$ parts. From the left to the right, the sequence of the image is reference and current configurations.

Observing Figure 3.1, and rather than dealing directly with $\mathbf{F}$, $\mathbf{C}$ and $\mathbf{E}$, one can apply the same multiplicative decomposition, in order to obtain strain measures of the isochoric deformation $\overline{\mathbf{F}}$,i.e.,:

$$\overline{\mathbf{C}} = \overline{\mathbf{F}}^T\overline{\mathbf{F}} = J^{-\frac{2}{3}}\mathbf{C} \qquad 3.6$$

$$\overline{\mathbf{E}} = \frac{1}{2}\left(\overline{\mathbf{C}} - \mathbf{I}\right) \qquad 3.7$$

The term $J^{\frac{1}{3}}\mathbf{I}$ is associated with volumetric deformations, while $\overline{\mathbf{F}}$ is related to the isochoric deformations of the material, i.e., volume preserving deformation.

3.1.2. Constitutive Modeling

Soft-tissues have shown to have a non-linear elastic constitutive behavior. In a hyperelastic framework, one needs to postulate the existence of strain energy function $W(\mathbf{C})$, defined per unit reference volume. The constitutive equations must fulfill two requirements, namely the principle of material frame indifference and the concept of material symmetry. If materials are homogeneous, the second Piola-Kirchhoff stress tensor, which is a totally material symmetric tensor that express the stress relative to the reference configuration (Bonet and Wood, 1997; Sussman and Bathe, 1987), is derived from the strain energy function $W(\mathbf{C})$, which plays the role of a stress potential, as follows:

$$\mathbf{\Pi} = 2\frac{\partial W(\mathbf{C})}{\partial \mathbf{C}} \qquad 3.8$$

From the representation theorem for invariants, isotropic hyperelastic materials can be expressed in terms of the principal invariants of $\mathbf{C}$. So, the following equality can be written:

$$W(\mathbf{C}) = W(I_1, I_2, I_3), \qquad 3.9$$

Where I_1, I_2, I_3 are the invariants of $\mathbf{C}$, defined as:

$$I_1 = \mathbf{C} : \mathbf{I} \qquad 3.10$$

$$I_2 = \frac{1}{2}\left(I_1^2 - \mathbf{C} : \mathbf{C}\right) \qquad 3.11$$

$$I_3 = \det(\mathbf{C}) \qquad 3.12$$

Moreover, a homogeneous hyperelastic material can evidence not only an isotropic behavior but also an anisotropic behavior. Considering that the anisotropic behavior can be associated with two families of fibers, characterized by two unit vector fields $\mathbf{a}_1$ and $\mathbf{a}_2$ in the reference configuration that describes the local fiber directions, the strain energy function $W(\mathbf{C})$ must be expressed as a function of these two unit vectors, in addition to their dependence of $\mathbf{C}$,

i.e., $W(\mathbf{C},\mathbf{a}_1,\mathbf{a}_2)$. Moreover, from the representation theorem for invariants, anisotropic hyperelastic material which is assumed to be reinforced by two family of fibers is represented by the nine invariants $I_i, i=1,9$ of the right Cauchy-Green strain tensor $\mathbf{C}$. Thus the strain energy function $W(\mathbf{C},\mathbf{a}_1,\mathbf{a}_2)$ can be rewritten as:

$$W(\mathbf{C},\mathbf{a}_1,\mathbf{a}_2)=W(I_1,I_2,I_3,I_4...,I_9) \qquad 3.13$$

The first three invariants of the right Cauchy-Green tensor (I_1,I_2,I_3) are related with isotropy. An anisotropic material which is reinforced by one family of fibers has a single preferred direction at each material point, motivating invariants I_4 and I_5, while an anisotropic material which is reinforced by two families of fibers has two preferred directions. Considering this last situation, the anisotropy-related invariants I_4 to I_9 are required. In summary, the mixed invariants of the right Cauchy-Green tensor are defined as:

$$I_4 = \mathbf{a}_1 \cdot \mathbf{C}\,\mathbf{a}_1 \qquad 3.14$$

$$I_5 = \mathbf{a}_1 \cdot \mathbf{C}^2\,\mathbf{a}_1 \qquad 3.15$$

$$I_6 = \mathbf{a}_2 \cdot \mathbf{C}\,\mathbf{a}_2 \qquad 3.16$$

$$I_7 = \mathbf{a}_2 \cdot \mathbf{C}^2\,\mathbf{a}_2 \qquad 3.17$$

$$I_8 = \mathbf{a}_1 \cdot \mathbf{C}\,\mathbf{a}_2 \qquad 3.18$$

$$I_9 = (\mathbf{a}_1 \cdot \mathbf{a}_2)^2 \qquad 3.19$$

Having the multiplicative decomposition of the deformation gradient $\mathbf{F}$, as written in equation 3.2, and considering that a material which keeps the volume constant throughout a motion is characterized by the incompressible constraint $J=1$, it is assumed that the strain energy function $W(\mathbf{C},\mathbf{a}_1,\mathbf{a}_2)$ for a slightly compressible anisotropic material reinforced by two families of fibers takes an uncoupled form, in which the volumetric ("vol") and isochoric ("isoc") components are such that:

$$W(\mathbf{C},\mathbf{a}_1,\mathbf{a}_2)=W_{vol}(J)+W_{isoc}(\bar{I}_1,...,\bar{I}_9)\,, \qquad 3.20$$

Where $\bar{I}_1,...,\bar{I}_9$ are the isochoric contribution of the invariants $I_1,...,I_9$, i.e., are the invariants of $\overline{\mathbf{C}}$. For the sake of simplicity $W_{vol}(J)$ and $W_{isoc}(\bar{I}_1,...,\bar{I}_9)$ will be hereafter rewritten as $\overline{W}_H(J)$ and $\overline{W}(\overline{\mathbf{C}},\mathbf{a}_1,\mathbf{a}_2)$, respectively, as referred by Holzapfel and Gasser (2001).

The strain energy function adopted in this work is in accordance with the work of Alves et al. (2010):

$$W(\mathbf{C},\mathbf{a}_1,\mathbf{a}_2)=\overline{W}(\overline{\mathbf{C}},\mathbf{a}_1,\mathbf{a}_2)+\overline{W}_H(J)+Q^0(J) \qquad 3.21$$

where the additional term Q^0 has the merit of coupling the mixed formulation, i.e., displacement and pressure fields (Alves et al., 2010; Sussman and Bathe, 1987). Besides, the total isochoric strain energy function $\overline{W}(\overline{\mathbf{C}},\mathbf{a}_1,\mathbf{a}_2)$ can be decomposed into isotropic and anisotropic parts. The 3 terms of $W(\mathbf{C},\mathbf{a}_1,\mathbf{a}_2)$ shown in equation 3.21 are given by:

$$\overline{W}(\overline{\mathbf{C}},\mathbf{a}_1,\mathbf{a}_2)=\overline{W}_{iso}(\overline{\mathbf{C}})+\overline{W}_{aniso}(\overline{\mathbf{C}},\mathbf{a}_1,\mathbf{a}_2) \qquad 3.22$$

$$\overline{W}_H(J)=+\frac{\lambda_k}{2}(J-1)^2 \qquad 3.23$$

$$Q^0(J)=-\frac{1}{2\lambda_k}(\overline{p}-\tilde{p})^2 \qquad 3.24$$

In equations 3.22 to 3.24, λ_k is a penalty parameter playing the role of a bulk modulus, $\tilde{p}$ is the pressure interpolated from the (unknown) pressure field and $\overline{p}$ is the pressure computed from the (unknown) displacement fields. The mathematical contribution of λ_k to the second Piola-Kirchhoff stress tensor can be clearly seen from the derivative the volumetric strain energy function $\overline{W}_H(J)$:

$$\frac{\partial W_H(J)}{\partial \mathbf{C}}=\frac{\partial \overline{W}_H(J)}{\partial J}\frac{\partial J}{\partial \mathbf{C}}, \qquad 3.25$$

Where $\overline{p}$ is given by (Sussman and Bathe, 1987):

$$\overline{p}=\frac{\partial \overline{W}_H(J)}{\partial J}=-\lambda_k(J-1) \ . \qquad 3.26$$

After some mathematical developments (Alves et al., 2010), it can be shown that $\bar{p}\ (=\tilde{p})$ is the hydrostatic pressure of the Cauchy stress tensor, and that the hydrostatic pressure results from the penalization of volume variation quantified by quantity $(J-1)$, i.e., the volume variation.

The contribution of the isochoric strain energy density arises from the adopted hyperelastic constitutive model. In what concerns the IVD modeling, the most used isotropic hyperelastic constitutive models are the compressible Neo-Hookean (equation 3.27) and incompressible Mooney-Rivlin (equation 3.28). The isotropic part comprises the matrixes of the NP and the AF, along with the CEP (Bonet and Wood, 1997; Schmidt et al., 2007). The Holzapfel model (equation 3.29) is applied for the anisotropic contribution of the AF fibers (Holzapfel et al., 2005).

$$\overline{W}_{NH}(\mathbf{C}) = \frac{G}{2}(I_1 - 3) - G(\ln J) - \frac{G}{3}(\ln J)^2 + \frac{K}{2}(\ln J)^2 \qquad 3.27$$

$$\overline{W}_{MR}(\overline{\mathbf{C}}) = C_{10}(\bar{I}_1 - 3) + C_{01}(\bar{I}_2 - 3) \qquad 3.28$$

$$\overline{W}_{Holzapfel}(\overline{\mathbf{C}}, \mathbf{a}_1, \mathbf{a}_2) = \frac{1}{2k_2}\left\{k_1\left[e^{k_2(\bar{I}_4 - 1)^2} - 1\right] + k_1\left[e^{k_2(\bar{I}_6 - 1)^2} - 1\right]\right\} \qquad 3.29$$

About equations 3.27 and 3.28, G is the shear modulus and C_{10} and C_{01} are material parameters ([MPa]). K is the bulk modulus of the (compressible) material. On equation 3.29, $k_1 > 0$ and $k_2 > 0$ are material parameters (k_1 [MPa], k_2 is dimensionless). It must be highlighted that these invariants depend on fibers' directions, as defined in equations 3.14 and 3.16, respectively.

3.1.3. Boundary Value Problem

The boundary value problem of a finite elastostatics problem consists in finding a displacement field $\mathbf{u} \in U$ such that the equations of equilibrium and the boundary conditions are satisfied:

$$\mathrm{Div}\mathbf{F}\boldsymbol{\Pi} + \mathbf{f}_0 = \mathbf{0} \qquad 3.30$$

$$\boldsymbol{\Pi} = \boldsymbol{\Pi}^T \qquad 3.31$$

$$\mathbf{u} = \underline{\mathbf{u}}_0 \quad (\text{on } \partial\Omega_{0,D}) \tag{3.32}$$

$$\underline{\mathbf{t}}_0 = \mathbf{F}\mathbf{\Pi} \cdot \mathbf{N} \quad (\text{on } \partial\Omega_{0,N}) \tag{3.33}$$

The second Piola-Kirchhoff stress tensor ($\mathbf{\Pi}$) is symmetric (equation 3.8) from the balance of angular momentum. Ω_0 and $\partial\Omega_0$ are the volume and surface of the body in the reference configuration, respectively. Boundary $\partial\Omega_0$ is partitioned into $\partial\Omega_{0,N}$ and $\partial\Omega_{0,D}$. $\partial\Omega_{0,N}$ is a boundary where surface tractions (i.e. first Piola-Kirchhoff traction vector) $\underline{\mathbf{t}}_0$ are prescribed, and $\partial\Omega_{0,D}$ is a boundary where displacements $\underline{\mathbf{u}}_0$ are prescribed. U is a solution space where $\mathbf{u} = \underline{\mathbf{u}}_0$ on $\partial\Omega_{0,D}$ and $\mathbf{f}_0$ denotes prescribed body forces. $\mathbf{N}$ is the exterior unit normal vector. The underbars $(\underline{\bullet})$ denote prescribed functions on the boundaries $\partial\Omega_{0,(\underline{\bullet})}$ of the continuum medium occupying the domain $\partial\Omega$ (Alves, 2003; Sussman and Bathe, 1987). A representation of this configuration is shown in Figure 3.2.

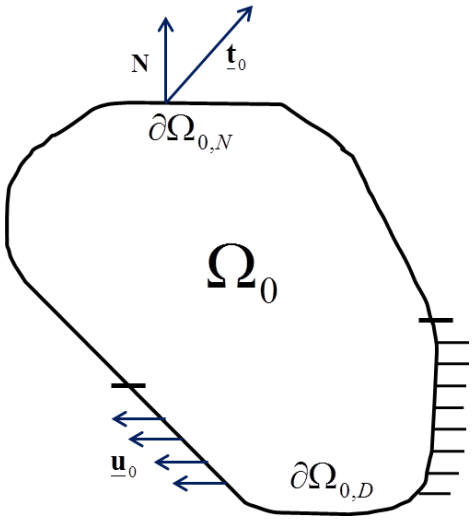

Figure 3.2. Boundary value problem configuration.

3.1.4. Variational Principle

Based on the variational principle, the weak form of the boundary value problem is derived in the material description. In the following, anisotropic hyperelastic materials which are reinforced by two families of fibers are considered.

The boundary value problem defined in equations 3.30 to 3.33 is equivalent to finding the minimization points $\mathbf{u}$ of the functional of the total potential energy $\Phi(\mathbf{u})$ over the set U. The functional of the total potential energy can be written as:

$$\Phi(\mathbf{u}) = \left(\int_{\Omega_0} W d\Omega_0 \right) + \Phi_{ext}(\mathbf{u}), \qquad 3.34$$

With the potential of external forces given by:

$$\Phi_{ext}(\mathbf{u}) = -\int_{\partial\Omega_{0,N}} \underline{\mathbf{t}}_0 \cdot \mathbf{u}\, dS_0 - \int_{\Omega_0} \mathbf{f}_0 \cdot \mathbf{u}\, d\Omega_0 \qquad 3.35$$

It must be reminded that $\mathbf{f}_0$ are prescribed body forces (like gravity forces), which will be neglected hereafter, and $\underline{\mathbf{t}}_0$ are prescribed external surface tractions, which will be assumed as not dependent on the deformation. To solve the minimization problem, the first variation of the functional $\Phi(\mathbf{u})$, with respect to the displacement field $\mathbf{u}$ vanishes, as:

$$D_{\mathbf{u}}\Phi(\mathbf{u}) \cdot \delta\mathbf{u} = 0 \qquad 3.36$$

For an arbitrary virtual displacement field, $\delta\mathbf{u} \in U_0$. U_0 is a function space where $\delta\mathbf{u} = \mathbf{0}$ on $\partial\Omega_{0,D}$ (Simo and Taylor, 1991). Equation 3.36 is called weak form of the boundary value problem formulated in equations 3.30 to 3.33. In other words, it means that the variation of the integrated 'internal stress' potential[ii] must equal the variation in the 'external loading' potential for any field of virtual displacements $\delta\mathbf{u} \in U_0$ compatible with boundary value problem.

However, it is worth noting that in a mixed formulation there are admissible independent variations of displacements and pressure. Therefore, the previous functional $\Phi(\mathbf{u})$ and minimization problem must be properly modified to include the independent variation of the pressure variable.

The inclusion in the strain energy function of the term $Q^0(J)$, which is a function of both displacements $\mathbf{u}$ and the separately and independently interpolated pressure $\tilde{p}$ (or simply p), allows to rewrite $\Phi(\mathbf{u})$ in such a way that, for independent variations of displacements and pressure variables, the following equality holds:

[ii] Due to variations in the displacements and pressure.

$$\Phi(\mathbf{u}, p) = \left(\int_{\Omega_0} W d\Omega_0 \right) + \Phi_{ext}(\mathbf{u}). \qquad 3.37$$

The new boundary value problem which is associated with constrained conditions such as almost incompressibility can now be applied to derive the mixed variational formulation. Besides the usual displacement field $\mathbf{u} \in U$, one additional pressure field $p \in P$ is incorporated and treated as independent variable. Therefore, the first variation of the new mixed functional $\Phi(\mathbf{u}, p)$ with respect to the displacement field $\mathbf{u}$ and pressure filed p shall vanish:

$$D_{\mathbf{u}}\Phi(\mathbf{u}, p) \cdot \delta\mathbf{u} = 0 \quad \wedge \quad D_p\Phi(\mathbf{u}, p) \cdot \delta p = 0 \qquad 3.38$$

This is valid for arbitrary functions $\delta\mathbf{u} \in U$ and $\delta p \in P$, respectively. After some mathematical developments, and by substituting equation 3.37 into equation 3.38, by the chain rule, the problem can be stated as: find solution $(\mathbf{u}, p) \in U \times P$ such that for all virtual solutions $(\delta\mathbf{u}, \delta p) \in U \times P$:

$$\int_{\Omega_0} \mathbf{\Pi} : \delta\mathbf{E} \, d\Omega_0 + \int_{\partial\Omega_{0,N}} \underline{\mathbf{t}}_0 \cdot \delta\mathbf{u} \, dS = 0 \quad \text{and} \qquad 3.39$$

$$\int_{\Omega_0} \frac{\partial Q^0(J)}{\partial p} : \delta p \, d\Omega_0 = 0, \qquad 3.40$$

Where $\delta\mathbf{E}$ is the first variational of $\mathbf{E}$ with respect to the displacement field $\mathbf{u}$. The second Piola-Kirchhoff stress tensor $\mathbf{\Pi}$ is given, by definition, as follows:

$$\mathbf{\Pi} = 2\frac{\partial W}{\partial \mathbf{C}} = 2\frac{\partial\left[\overline{W}(\overline{\mathbf{C}}) + \overline{W}_H(J) + Q^0(J)\right]}{\partial \mathbf{C}} = \mathbf{\Pi}_{isoc} + \mathbf{\Pi}_{vol}. \qquad 3.41$$

After some mathematical developments, it can be shown that:

$$\Pi_{kl} = 2\frac{\partial \overline{W}(\overline{\mathbf{C}})}{\partial C_{kl}} + \lambda_k \; J\,(J-1)\,C_{kl}^{-1} = 2\frac{\partial \overline{W}(\overline{\mathbf{C}})}{\partial C_{kl}} - \tilde{p}\; J\; C_{kl}^{-1} \qquad 3.42$$

Where the equality $\overline{p} = -\lambda_k(J-1)$ (equation 3.26) was considered. The first and second terms of the second Piola-Kirchhoff stress tensor are, respectively, the so-called isochoric and volumetric parts of the second Piola-Kirchhoff stress tensor. It is worth noting that $\overline{p}$ does not

play any role in equation 3.42. In addition, it can be established that $\tilde{p}$ corresponds to the hydrostatic pressure of the Cauchy stress tensor.

3.1.5. Finite Element Implementation

It is well known that displacement-based finite element methods are difficult to use in the analysis of incompressible or slightly compressible materials. These difficulties include ill-conditioning of stiffness matrix and volumetric locking of the mesh due to over-constraint of the displacement field, as the bulk modulus $K \to +\infty$ in case of total incompressibility. To incorporate the incompressibility constraint in a mixed formulation is a solution commonly followed to circumvent this problem, and almost incompressibility can be simply achieved if volumetric strains are conveniently penalized, i.e., λ_k shall be at least three orders of magnitude larger than the shear modulus. By invoking finite element approximation, displacements and pressure are interpolated independently,

$$\mathbf{x} = N_A(\xi)\,\mathbf{x}^A \qquad 3.43$$

$$\tilde{p} = G_A(\xi)\,p^A \qquad 3.44$$

where N_A and G_A are isoparametric shape functions, ξ is the vector of natural coordinates, and $\mathbf{x}^A$ and p^A are the nodal coordinates and nodal pressure, respectively.

Weak form of equations 3.39 and 3.40 are generally nonlinear in the unknown displacement field $\mathbf{u}$ and pressure p. They are solved by the Newton-Raphson iterative method, after linearization (of the weak form) based on the first order Taylor's expansion. In matrix form, the governing equations of motion for a finite element is:

$$\begin{bmatrix} \mathbf{K_{UU}} & \mathbf{K_{UP}} \\ \mathbf{K_{PU}} & \mathbf{K_{PP}} \end{bmatrix} : \begin{bmatrix} \Delta\mathbf{u} \\ \Delta\mathbf{p} \end{bmatrix} = \begin{bmatrix} \mathbf{R} \\ 0 \end{bmatrix} - \begin{bmatrix} \mathbf{F_U} \\ \mathbf{F_P} \end{bmatrix}, \qquad 3.45$$

where $\mathbf{R}$ are the nodal point forces (vector of the external forces) corresponding to a given time $t + \Delta t$, $\Delta(\bullet)$ is the linearization operator and $\Delta\mathbf{u}$ and $\Delta\mathbf{p}$ are vectors containing nodal increments in $\mathbf{u}$ and p, respectively.

$\left[\mathbf{F}_{\mathbf{U}} \quad \mathbf{F}_{\mathrm{P}}\right]^T$ is the internal forces vector, which is partitioned into two parts, one part for displacements variations and the other for pressure variations. Similarly, the stiffness matrix is divided in four parts.

After some mathematical manipulations, the following algebraic expression (in indicial notation) of $\mathbf{F}_{\mathbf{U}}$ and $\mathbf{F}_{\mathrm{P}}$ can be determined, respectively:

$$F_{\mathbf{U}i} = \frac{\partial}{\partial u_i}\left(\int_{\Omega_0} W d\Omega_0\right) = \frac{1}{2}\int_{\Omega_0} \Pi_{kl} \frac{\partial C_{kl}}{\partial u_i} d\Omega_0 \qquad 3.46$$

$$F_{\mathbf{P}i} = \frac{\partial}{\partial p_i}\left(\int_{\Omega_0} W d\Omega_0\right) = \int_{V_0} \frac{1}{\lambda_k}\left(\bar{p} - \tilde{p}\right)\frac{\partial \tilde{p}}{\partial p_i} d\Omega_0 \qquad 3.47$$

In addition, $\mathbf{K}_{\mathbf{UU}}$, $\mathbf{K}_{\mathbf{UP}}$, $\mathbf{K}_{\mathbf{PU}}$ and $\mathbf{K}_{\mathrm{PP}}$ are given by:

$$K_{UU\,ij} = \frac{\partial\left(F_{U\,i}\right)}{\partial u_j} = \frac{1}{2}\int_{\Omega_0} C_{UU\,klrs} \frac{\partial C_{kl}}{\partial x_i}\frac{\partial C_{rs}}{\partial x_j} d\Omega_0 + \frac{1}{2}\int_{\Omega_0} \Pi_{kl} \frac{\partial^2 C_{kl}}{\partial x_i \partial x_j} d\Omega_0 \qquad 3.48$$

$$K_{UP\,ij} = \frac{\partial\left(F_{U\,i}\right)}{\partial p_j} = \int_{\Omega_0} \frac{1}{\lambda_k}\frac{\partial \bar{p}}{\partial C_{kl}}\frac{\partial \tilde{p}}{\partial p_j}\frac{\partial C_{kl}}{\partial u_i} d\Omega_0 \qquad 3.49$$

$$K_{PU\,ij} = \frac{\partial\left(F_{P\,i}\right)}{\partial u_j} = \int_{\Omega_0} \frac{1}{\lambda_k}\frac{\partial \bar{p}}{\partial C_{kl}}\frac{\partial \tilde{p}}{\partial p_i}\frac{\partial C_{kl}}{\partial u_j} d\Omega_0 = K_{UP\,ji} \qquad 3.50$$

$$K_{PP\,ij} = \frac{\partial\left(F_{P\,i}\right)}{\partial p_j} = \int_{\Omega_0} -\frac{1}{\lambda_k}\frac{\partial \tilde{p}}{\partial p_j}\frac{\partial \tilde{p}}{\partial p_i} d\Omega_0 \qquad 3.51$$

In the previous set of equations (3.46 to 3.51) the following definitions are used:

$$C_{UU\,klrs} = \frac{\partial \Pi_{kl}}{\partial C_{rs}} = \bar{C}_{klrs} - \frac{2}{\lambda_k}\frac{\partial \bar{p}}{\partial C_{kl}}\frac{\partial \bar{p}}{\partial C_{rs}} - \frac{2}{\lambda_k}\left(\bar{p} - \tilde{p}\right)\frac{\partial^2 \bar{p}}{\partial C_{kl}\partial C_{rs}} \qquad 3.52$$

Where $\bar{C}_{klrs}$ is the 4th order constitutive tensor that derives from the chosen isotropic and/or anisotropic constitutive models and volumetric strain function:

$$\bar{C}_{klrs} = \frac{\partial \bar{\Pi}_{kl}}{\partial C_{rs}} = 2\frac{\partial^2 \bar{W}\left(\bar{\mathbf{C}}\right)}{\partial C_{rs}\partial C_{kl}} + 2\frac{\partial^2 \bar{W}_H\left(J\right)}{\partial C_{rs}\partial C_{kl}}. \qquad 3.53$$

The following set of derivatives with respect to nodal displacements and pressure are also considered:

$$\frac{\partial C_{kl}}{\partial u_{Li}} = F_{il}\ N_{L,k} + F_{ik}\ N_{L,l} \qquad 3.54$$

$$\frac{\partial^2 C_{kl}}{\partial u_{Li} \partial u_{Mj}} = \left(N_{L,k} N_{M,l} + N_{L,l} N_{M,k} \right) \qquad 3.55$$

$$\frac{\partial \tilde{p}}{\partial p} = G_A \qquad 3.56$$

Finally, it is worth noting that the equilibrium of the deformable body is achieved when the following equality is verified:

$$\begin{bmatrix} \mathbf{R} \\ 0 \end{bmatrix} = \begin{bmatrix} \mathbf{F}_{\mathrm{U}} \\ \mathbf{F}_{\mathrm{P}} \end{bmatrix} \quad \text{or} \quad \begin{bmatrix} \mathbf{R} \\ 0 \end{bmatrix} - \begin{bmatrix} \mathbf{F}_{\mathrm{U}} \\ \mathbf{F}_{\mathrm{P}} \end{bmatrix} = \mathbf{0}. \qquad 3.57$$

The equality of equation 3.57 means that when the vector of external forces is equal to the vector of internal ones, the deformable body is in equilibrium.

The Newton-Raphson iterative method for equation 3.56 at each load (time) increment is defined in iteration j by:

$$\begin{bmatrix} \mathbf{K}_{\mathrm{UU}} & \mathbf{K}_{\mathrm{UP}} \\ \mathbf{K}_{\mathrm{PU}} & \mathbf{K}_{\mathrm{PP}} \end{bmatrix}^j : \begin{bmatrix} \Delta\mathbf{u} \\ \Delta\mathbf{p} \end{bmatrix}^j = -\left\{ \begin{bmatrix} \mathbf{R} \\ 0 \end{bmatrix}_{t+\Delta t} - \begin{bmatrix} \mathbf{F}_{\mathrm{U}} \\ \mathbf{F}_{\mathrm{P}} \end{bmatrix}^j \right\}, \qquad 3.58$$

Which is followed by the update:

$$\begin{bmatrix} \mathbf{u} \\ \mathbf{p} \end{bmatrix}^{j+1} = \begin{bmatrix} \mathbf{u} \\ \mathbf{p} \end{bmatrix}^j + \begin{bmatrix} \Delta\mathbf{u} \\ \Delta\mathbf{p} \end{bmatrix}^j. \qquad 3.59$$

$\mathbf{u}$ is the vector of solution of displacement of the nodal values and $\mathbf{p}$ is the vector of solution of pressure nodal values. For a given time increment $[t, t+\Delta t]$, a trial solution is firstly determined using an explicit algorithm.

Starting from the explicit "trial" solution, the equilibrium is iteratively determined until the norm of the total non-equilibrated forces is smaller than a threshold value, which is typically lower than 1% of the norm of the external forces.

3.1.6. Innovative Biphasic Modeling

Biphasic soft-tissues, such as the IVD components, are typically almost incompressible. This feature is taken into account by assuming a multiplicative decomposition of the deformation gradient into volumetric and isochoric parts, and by using a mixed interpolation of the displacement and pressure fields, as previously described.

The biphasic medium is assumed to be homogeneous and continuous, in the macroscopic point of view. It can be simply characterized by the initial fluid (f) and solid (s) volume fractions, n_α, with $\alpha = \{f, s\}$ and $\sum n_\alpha = 1$. The fluid is assumed to fill completely the pores of the solid phase, by flowing through it. The fluid flux relative to the solid matrix is commonly modeled by Darcy's law (Huyghe et al., 1991; Wilson, van Donkelaar, van Rietbergen, et al., 2005), written as:

$$\mathbf{w} = n_f(\mathbf{v}_f - \mathbf{v}_s) = -\mathbf{K}^* \cdot \nabla p^f , \qquad 3.60$$

Where $\mathbf{w}$ is the flux of the fluid relative to the solid matrix, n_f is the current fluid fraction and $(\mathbf{v}_f - \mathbf{v}_s)$ is the relative velocity of the fluid with respect to the solid matrix. $\mathbf{K}^*$ is the hydraulic permeability tensor which, in case of isotropic permeability, is simply defined as $\mathbf{K}^* = K^*(J)\mathbf{I}$. $K^*(J)$ is the strain-dependent permeability, $\mathbf{I}$ the second order unity tensor and ∇p^f is the gradient of the pore (or fluid) pressure (Ehlers et al., 2009; Huyghe et al., 1991; Wilson et al., 2006; Wilson, van Donkelaar, van Rietbergen, et al., 2005). The permeability is strain-dependent and $M > 0$ is the unique material parameter, accordingly to (van der Voet, 1997):

$$K^*(J) = K_0^* \left(\frac{1 - n_{f,0}}{1 - n_f} \right)^M = K_0^* J^M . \qquad 3.61$$

The biphasic formulation here adopted consists of an innovative implementation that couples the strain energy density potential shown in equation 3.21 with Darcy's law (equation 3.60), embedded on the formulation proposed by Huyghe (1986) for a biphasic medium.

As a result of such coupling, the new elemental stiffness matrix and the corresponding elemental system of equations are written as follows:

$$\begin{bmatrix} \mathbf{K}_{UU} & \mathbf{K}_{UP} \\ \mathbf{K}_{PU} & K_{PP} - K_{K^*} \end{bmatrix} : \begin{bmatrix} \Delta \mathbf{u} \\ \Delta p \end{bmatrix} = \left(\begin{bmatrix} \mathbf{R} \\ 0 \end{bmatrix} + \begin{bmatrix} \mathbf{0} \\ U + T_1 + T_2 \end{bmatrix} \right) - \begin{bmatrix} \mathbf{F}_U \\ F_P \end{bmatrix} \qquad 3.62$$

The initial formulation based on the strain energy density potential presented on equation 3.21 was updated to a biphasic formulation, being the major differences the introduction of term K_{K^*} on the stiffness matrix and the dissipative terms U, T_1, T_2 on the right hand side of equation 3.62, defined as follows (Huyghe, 1986):

$$K_{K^*} = \int_{\Omega_0} \nabla_0 G_A{}^T \cdot K^* \cdot \nabla_0 G_A \cdot \Delta t \cdot d\Omega_0 \qquad 3.63$$

$$U = \int_{\Omega_0} G_A \cdot \left(J - J_n \right) \cdot d\Omega_0 \qquad 3.64$$

$$T_1 = \int_{\Omega_0} \left(K^* \cdot \nabla_0 \tilde{p} \right) \cdot \nabla G_A \cdot \Delta t \cdot d\Omega_0 \qquad 3.65$$

$$T_2 = (1 - \theta) \int_{\Omega_0} \left(K^* \cdot \nabla_0 \tilde{p}_n \right) \cdot \nabla G_A \cdot \Delta t \cdot d\Omega_0 \qquad 3.66$$

Indexes n and 0 refer to the beginning of the time increment ($t = t_n$) and to the reference configuration ($t = 0$), respectively. The term U acts as quantifier of the volume variation due to fluid flowing in time increment $[t_n, t_n + \Delta t]$. G_A are the shape functions for pressure field interpolation and K_{K^*} introduces the permeability phenomenon (K^*) in the elemental stiffness matrix, what will allow to take into account fluid flowing.

From equation 3.62, one must pay special attention to the term F_P, which was previously defined on equation 3.47. This term "weights", for a given material point, the non-equilibrated pressure between displacements field and the interpolated pressure, i.e., $\bar{p} - \tilde{p}$. For a monophasic formulation, this non-equilibrated pressure should vanish in the vicinity of the equilibrium configuration, once that $\bar{p} = \tilde{p}$. The introduction of a biphasic formulation in the FE model imposes that this link between the pressures determined from either the displacement fields or the pressure field shall be eliminated from the right-hand side of the stiffness matrix, and thus $F_P = 0$[III].

[III] Validation of formulation is already published, as shown on the fourth annex of the present work ("Publications and Communications").

As shown in equation 3.42, the second Piola-Kirchhoff stress tensor depends only on the interpolated pressure $\tilde{p}$, and not on the displacement based interpolated pressure $\bar{p}$, i.e., this term does not play any role on the final form of the second Piola-Kirchhoff stress tensor, and thus on the effective Cauchy stress tensor. The point is that, while previously the hydrostatic pressure was linked with the displacement field, such connection is eliminated, and now the independent pressure variable results from the deformation history of the biphasic medium, i.e., the contribution to the equilibrium of the pressure-field is now introduced by terms U, T_1, T_2.

Finally, because a totally implicit formulation is here adopted (i.e., $\theta = 1$), also T_2 can be eliminated. Consequently, the right-hand side of equation 3.62 may finally be re-written in the following form:

$$\begin{bmatrix} \mathbf{R} \\ U + T_1 \end{bmatrix} - \begin{bmatrix} \mathbf{F}_U \\ 0 \end{bmatrix} \qquad 3.67$$

3.1.7. Osmotic Swelling Behavior

Several studies have shown the importance of osmotic swelling behavior to the IVD biomechanics, namely for the height recovery during rest periods and for the maintenance of healthy IDP levels (Riches et al., 2002; Huyghe et al., 2003; Schroeder et al., 2010). Therefore, the osmotic swelling pressure gradient must be included in the formulation.

In the standard biphasic theory, the total Cauchy stress ($\boldsymbol{\sigma}_{tot}$), which can be determined the push-forward expression:

$$\boldsymbol{\sigma}_{tot} = \frac{1}{J} \mathbf{F}\, \boldsymbol{\Pi}\, \mathbf{F}^T , \qquad 3.68$$

Which results from the contribution of both solid ($\boldsymbol{\sigma}_s$) and fluid phases ($-p\mathbf{I}$), as stated on equation 3.69 (Huyghe et al., 1991; Wilson, van Donkelaar, van Rietbergen, et al., 2005):

$$\boldsymbol{\sigma}_{tot} = \boldsymbol{\sigma}_s - p\mathbf{I} \qquad 3.69$$

Where p is the pore (or fluid) pressure and $\boldsymbol{\sigma}_s$ the effective solid phase stress tensor. The biphasic osmotic swelling model implemented is the one adopted by Wilson et al. (2005), in the following form:

$$\boldsymbol{\sigma}_{tot} = -\left(\mu^f + \Delta\pi\right)\mathbf{I} + \boldsymbol{\sigma}_s , \qquad 3.70$$

where μ^f is the water chemical potential and $\Delta\pi$ is the osmotic pressure gradient (Wilson, van Donkelaar, van Rietbergen, et al., 2005), as defined by:

$$\Delta\pi = \pi_{int} - \pi_{ext} = \phi_{int} RT\left(\sqrt{c_F^2 + 4c_{ext}^2}\right) - 2\phi_{ext} RTc_{ext} \qquad 3.71$$

On equation 3.71, temperature (T), external salt concentration (c_{ext}) and osmotic coefficients (ϕ_{int} and ϕ_{ext}) were assumed to be constants. The ionic concentrations in all areas of the disc are assumed in equilibrium with the external salt concentration c_{ext} at all times. Hence, ion flow is assumed to be infinitely fast compared to fluid flow. Otherwise, one would have to move for tri- or quadriphasic formulations (Frijns et al., 1997; Huyghe et al., 1991). The fixed charge density (c_F) is strain-dependent, and thus can be expressed as a function of the tissue's deformation (Wilson, van Donkelaar, van Rietbergen, et al., 2005):

$$c_F = c_{F,0} \frac{n_{f,0}}{n_{f,0} - 1 + J} \qquad 3.72$$

Where $n_{f,0}$ is the initial fluid volume fraction and $c_{F,0}$ the initial fixed charge density. It must be highlighted that the osmotic pressure in equilibrium is only function of the deformation tensor $\mathbf{F}$. In depth, the volume variation defined by J (between the initial and current configurations) rules the calculus of the osmotic pressure in the equilibrium state (Wilson et al., 2007). Swelling behavior was considered for both NP and AF (Galbusera et al., 2011; Schmidt et al., 2013).

3.1.8. Viscoelastic Behavior

Viscoelasticity is also important for the biomechanics of the IVD, as previously discussed. Both creep and stress relaxation shall be taken into account when describing the time-dependent behavior of soft tissues. A quasi-linear hyper-viscoelastic model was adopted, with a rheological

model based on the coupling of up to 5 Maxwell elements in parallel with a nonlinear spring. This model is known as generalized non-linear Maxwell model or Maxwell-Wiechert model (Figure 3.3).

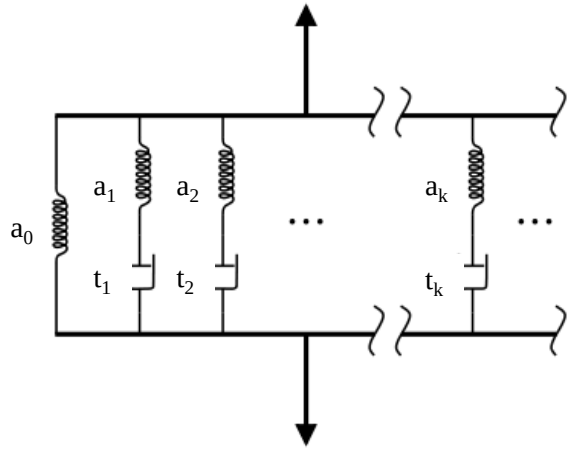

Figure 3.3. Schematic representation of the adopted rheological model, i.e., a generalized Maxwell model, where up to 5 Maxwell elements can be assembled in parallel with a non-linear spring. Adapted from (Jimenez Rios et al., 2007).

The formulation is stated on equation 3.73, as presented by Kaliske et al. (2001):

$$G(t) = 1 + \sum_{n=1}^{N} a_n \exp\left(-\frac{t}{\tau_n}\right) \qquad 3.73$$

Where $G(t)$ is the so-called time relaxation function, τ_n is the damper characteristic time and $a_n = E_n / E_0$ is the ratio between the nonlinear spring a_n introduced by the Maxwell element and the nonlinear spring a_0 (Kaliske et al., 2001).

Viscoelastic behavior was taken into account for the NP matrix (Ehlers et al., 2009; Iatridis et al., 1997). Finally, the long term viscous effect can be determined from the hereditary time integral:

$$\mathbf{\Pi}^{v,long}(\overline{\mathbf{C}}, t) = G(t) \cdot \mathbf{\Pi}^{pas}(\overline{\mathbf{C}}, 0+) + \int_0^{\infty} G(t-\tau) \frac{\partial \mathbf{\Pi}^{pas}(\overline{\mathbf{C}}, \tau)}{\partial \tau} d\tau \,. \qquad 3.74$$

3.1.9. Innovative Annulus Fibrosus Modeling

The AF was modeled with regional differentiation (Cavalcanti et al., 2013). Firstly, the angles of the fibers within the AF evolve circumferentially from ventral to dorsal regions. Being φ the absolute fiber angle[IV], the following evolution law was used (Holzapfel et al., 2005):

$$|\varphi| = 23.2 + 0.130\alpha \,, \qquad 3.75$$

Where α is the polar angle associated with the circumferential position of a given material point, as shown in Figure 3.4.

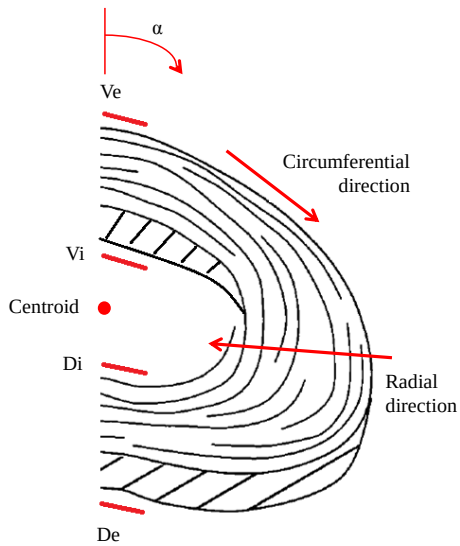

Figure 3.4. Schematic representation of the AF differentiation. "V" stands for "ventral" and "D" stands for "dorsal". In addition, "e" stands for exterior and "i" stands for "interior", in relation to the position of the IVD in the spine. Adapted from Elliott and Setton (2000) and Holzapfel et al. (2005).

The implementation of equation 3.75 means that the fiber angle increases linearly from about 23.2° at ventral region ($\alpha = 0^{o}$) to about 43.6° at dorsal region ($\alpha = 180^{o}$), as function of its initial polarposition within the AF.

In addition, based on the works of Eberlein et al. (2001) and Holzapfel et al. (2005), it was found that the matertial parameters of the Holzapfel model for anisotropic behavior (k_1 and k_2, as shown in equation 3.29) should be reduced to 25% on the circumferential direction (ventral to

[IV] Angle within the axial plane.

dorsal) and to 15% on the radial direction (external to internal), starting from the ventral-external area (Cavalcanti et al., 2013). In other words, this means that the mechanical properties assigned to each material point took into account its relative radial and circumferential positioning within the AF.

3.1.10. Summary

The fundamental mechanical modeling implemented on the home-developed open-source FE solver was briefly described along this section. The implemented features were explicitly oriented to the IVD constitutive modeling, even if the solver already had some of the necessary conditions for the numerical simulation by FE of the soft-tissues' behavior, such as their almost incompressibility and viscoelastic effects.

The innovative biphasic poroelastic formulation here developed intends to take into account the multi-physics phenomena occurring inside the IVD and also the interaction between the IVD and its adjacent structures. The osmotic swelling behavior was coupled to this formulation, in order to account for the osmotic pressure gradients that equilibrate and maintain the viability of the IVD. Finally, the innovative modeling of the AF fibers was included to follow the current knowledge on the AF regional differentiation, i.e., the radial and circumferential evolution of both the AF mechanical properties and the fibers' orientation within the AF were accurately taken into account in order to mimic the anatomical structure of a real IVD.

3.2. Finite Element Model

The development of the MS FE model was based on a model of a Human L4 VB and the two adjacent IVDs previously published by Smit (1996), which is shown in Figure 3.5. This model was available in the Biomechanical Data Resources of the International Society of Biomechanics (ISB), in the section denominated "ISB FEM Mesh Repository"[v], and it was developed with ANSYS software. Other authors, such as Noailly et al. (2005), also used this model as the basis for their spine-related FE studies.

On the one hand, the specifications of Smit's model are very coherent with the particularities of the native Human VB and IVD, i.e., all the relevant components[vi] are included and the dimensions[vii] are compatible with the Human lumbar spine. On the other hand, the mesh was mostly built with 8-node linear hexahedra (Hex8)[viii], which allowed the straightforward conversion for u/P-c 27-node quadratic hexahedra (Hex27).

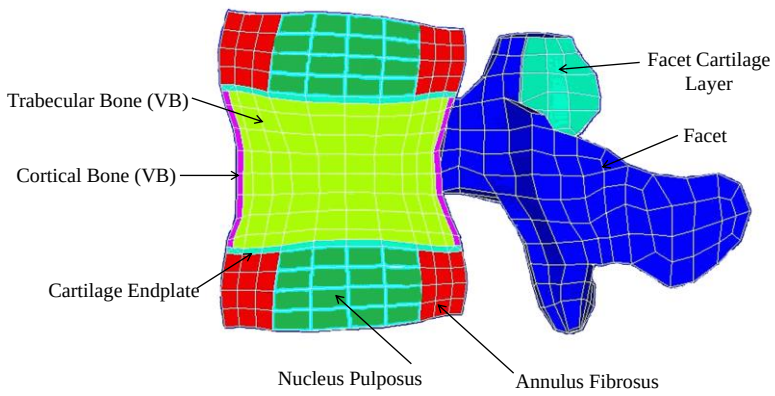

Figure 3.5. Sagittal cut of the original Human L4 VB FE model from Smit (1996).

[v] The main link for the ISB Biomechanical Data Resources is http://isbweb.org/data/. However, these resources are now available at the Data Repository of the Biomed Town Portal, and the main link for it is https://www.biomedtown.org/biomed_town/LHDL/Reception/datarepository/repositories/BelRepWikiPages. The L4 VB model is available at the section "L4 Vertebra For Ansys".

[vi] Despite having some anatomical issues, which will be described later, this model included the three IVD components and the VB with the facet and respective facet cartilage layer.

[vii] The height of the Human native lumbar IVD is 7 to 13mm, while its diameter is around 35 to 55mm, as described in the previous chapter.

[viii] The original mesh had some degenerated hexahedral elements, with 6 nodes.

The other possible strategy for the development of the MS FE model would be the mesh generation from medical images after 3D reconstruction. In general, a FE model can be generated from a solid voxel-based 3D model obtained from 3D reconstruction of a set of 2D medical images. Medical images are usually obtained from X-Ray, CT and MRI. In fact, most of FE models are based on CT images, MRI images or a combination of CT and MRI images. Part of them are even created by algorithms using "standard" dimensions mentioned in literature (Tyndyka et al., 2007).

The resolution of medical images[IX] plays an important role in the accuracy of 3D geometrical reconstruction of anatomical structures from 2D images. In fact, image resolution is directly proportional to the quality of the FE mesh, i.e., the higher is resolution, more accurate is the FE mesh (Kelm et al., 2012). The 3D reconstruction process is somewhat tricky, mostly due to the poor identification of some tissues or extremely complex geometric details. In addition, the NP and the AF have similar densities, which makes 3D reconstruction even more difficult (Li and Wang, 2006; Wang et al., 2012). The imaging segmentation could become a very user-dependent task and the time consumption would increase drastically (Kelm et al., 2012).

This option could be more accurate than using an existent FE model, but it has some major drawbacks, namely the time consumption and the difficulty in gathering high resolution medical images. Such drawbacks reinforced the option for the adaptation of the Smit's full VB FE model.

3.2.1. Model development

The original VB model from Smit (1996) was converted on a full MS, including the two facets and its respective facet cartilage layers, as shown in Figure 3.6. The conversion process involved the removal of the top IVD and the replication of the VB (with its respective facet), in order to create a model of the L3-L4 MS. The original mesh was discretized with Hex8 and some 6-node degenerated elements, which were all updated to Hex27, by dividing each 8-node initial element in eight elements. After this procedure, a Hex27 FE element mesh was obtained. It must also be highlighted that the degenerated elements were arranged in groups of three, in order to create

[IX] The image resolution is determined by pixel size and slice thickness (Li and Wang, 2006).

regular 8-node elements, by eliminating the internal nodes and thus maintaining the external boundaries of the model. All the modifications on the FE mesh were performed using the mesh-edition features of the open-source FE solver.

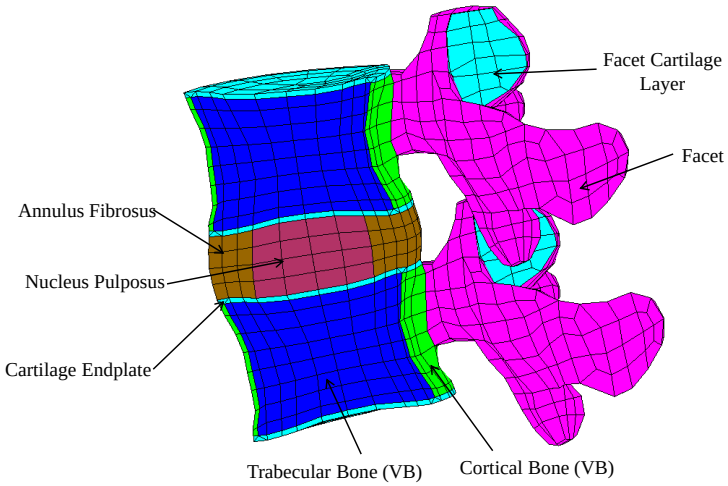

Figure 3.6. Sagittal cuts of the original FE models: a) The model developed by Smit (1996), with one VB and two IVDs; b) The first stage of the full MS model, with the two facets and its respective facet cartilage layers.

The first stage of the full MS model (Figure 3.6) had some anatomical issues, namely the absence of the VEP and the exaggerated length of the CEP on the axial plane. Figure 3.7 shows a sagittal cut of the FE mesh used in this study. It comprises a full MS, including all relevant features of one IVD and two VBs.

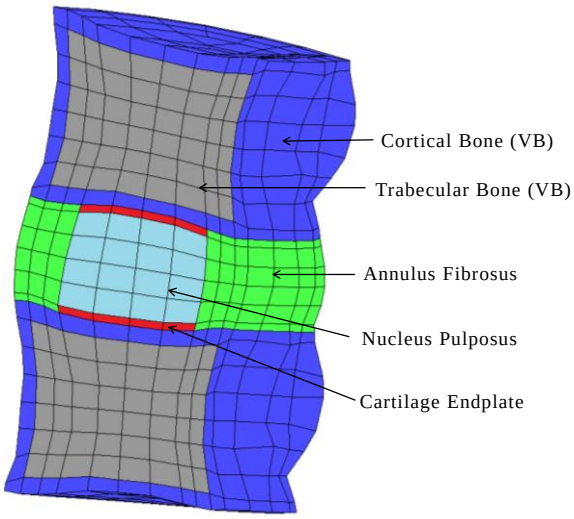

Figure 3.7. Sagittal cut of the L3-L4 FE model.

This second stage model had the mentioned anatomical issues solved, namely in what concerns to the VB and to the CEP. The two components of the VB, i.e., the TB and the CB, have a more accurate distribution, as the CB layer is larger in this model. However, the most relevant alteration on the VB is the inclusion of the VEP, i.e., the layer of CB which is adjacent to the IVD, through the AF and the CEP. The VEP-CEP interaction is one of the most debated topics in the literature (Adams et al., 2009; Ebraheim et al., 2004; Swider et al., 2010), as discussed in the previous chapter. The CEP is also shorter, which is a more realistic configuration, i.e., the AF is now in direct contact with the VEP, as described in the literature (Adams et al., 2009; Raj, 2008). The most accurate representation would be the CEP covering the NP and one-third of the AF (Raj, 2008). However, the current configuration was more compatible with the chosen fibrillar model.

The facets were removed, in order to reduce the computational weight of the model, as they were not essential for the forthcoming simulations. The IVD has an average height of 12.8mm and an axial cross section of 1555.3mm^2, while the full MS has an average height of 60.9mm. The FE mesh is discretized with 1 892 27-node u/P-c quadratic hexahedra and 16 425 nodes. For the sake of simplicity, only vertex nodes are visualized in Figure 3.7.

3.2.2. Material Parameters

The constitutive modeling of the IVD FE model was fully described in the previous section of this chapter and the L3-L4 FE model components were defined in the previous sub-section of this chapter. This section intends to enunciate the constitutive material parameters of each one of the MS FE model components.

The five MS ground substances (NP, AF, CEP, TB and CB) were considered to be isotropic (Mooney-Rivlin model, as presented by Bonet and Wood (1997)) and permeable (strain-dependent permeability model from (van der Voet, 1997)). The AF fibers were anisotropic (Holzapfel model, as presented by Holzapfel et al. (2005)), while the NP was considered to be viscoelastic (Maxwell model, as presented by Kaliske et al. (2001)). Swelling properties were considered for both NP and AF (strain-dependent osmotic swelling pressure model from Wilson et al. (2005)). The components of the VB were considered to be very stiff and highly permeable. Regarding these characteristics, the material parameters selected for the standard numerical simulations are shown in Table 3.1. These parameters were based on multiple literature sources

and numerical optimization, i.e., some parameters were taken from the literature and then adjusted throughout the development of the work to allow a more realistic behavior of the model.

Table 3.1. Material properties of the MS components. Multiple data sources were assessed, as stated on each entry of the table. Numerical optimization was also performed throughout the choice of these parameters.

		NP	AF	CEP	TB	CB
Isotropy[X]	C_{10} [MPa]	0.15	0.18	1.00	41.67	3846.15
	C_{01} [MPa]	0.03	0.045	0.00	0.00	0.00
Permeability[XI]	K_0^* [mm^4.N^{-1}.s^{-1}]	7.50e-4	7.50e-4	7.50e-3	0.10	0.10
	M	8.50	8.50	8.50	18.00	22.00
Anisotropy[XII]	k_2	-	300.00	-		
	k_1 [MPa]	-	12.00	-		
Viscoelasticity[XIII]	a_1	1.70	-	-		
	τ_1 [s]	11.765	-	-		
	a_2	1.20	-	-		
	τ_2 [s]	1.100	-	-		
	a_3	2.00	-	-		
	τ_3 [s]	0.132	-	-		
Swelling[XIV]	R [N.mm.mmol^{-1}.K^{-1}]	8.31450	8.31450	-		
	T [K]	298.00	298.00	-		
	ϕ_{int}	0.83	0.83	-		
	ϕ_{ext}	0.92	0.92	-		
	c_{ext} [mmol.mm^{-3}]	0.00015	0.00015	-		
	$c_{F,0}$ [mmol.mm^{-3}]	0.00030	0.00018	-		
	$n_{f,0}$	0.80	0.70	-		

[X] (Schmidt et al., 2007; Smit, 1996)
[XI] (Argoubi and Shirazi-Adl, 1996; Ferguson et al., 2004)
[XII] (Cavalcanti et al., 2013; Holzapfel et al., 2005)
[XIII] (Ehlers et al., 2009; Iatridis et al., 1997)
[XIV] (Galbusera et al., 2011)

3.3. Mesh Convergence Study

Starting from the initial 3D MS FE model presented on Figure 3.7, five other FE models were developed, as shown in Figure 3.8. The geometrical and anatomical features are shared between the six models and are identified in Figure 3.8a). Material properties were also kept unchanged, i.e., all the models used the material parameters listed on Table 3.1.

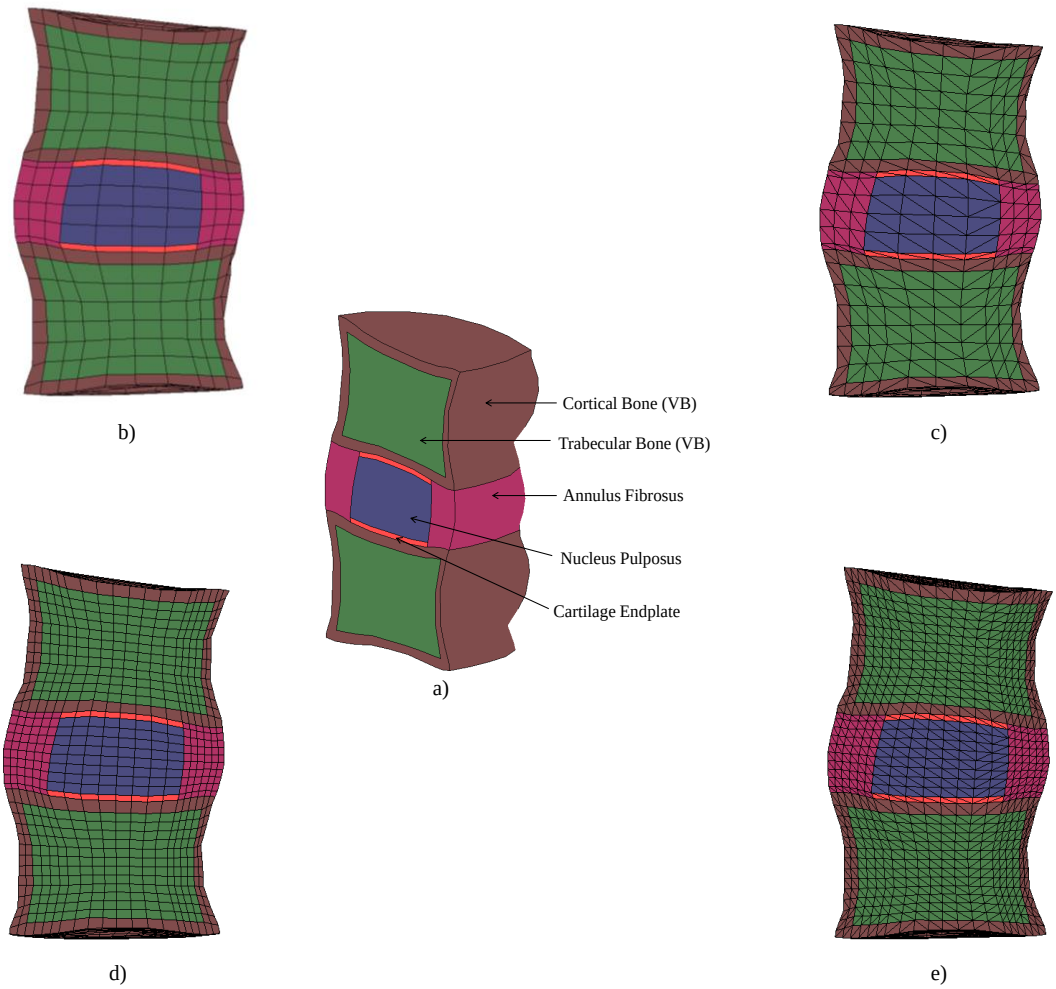

Figure 3.8. The geometrical MS model (a)) derived in six different FE models. b) and c) are the non-refined models, while d) and e) ate the refined ones. b) and d) were built with 27-node hexahedrons. As only the vertex nodes are shown, the visualization of 4-node and 10-node tetrahedra is the same (c) and e)).

A sagittal cut is shown for all the models.

These six models are divided in two groups, the non-refined and the refined models. For each group, the three types of u/P-c quadratic elements were used (4-node and 10-node tetrahedra and 27-node quadratic hexahedron). Figure 3.8b) and Figure 3.8c) show the primary models, i.e., the models with a coarse FE mesh refinement. The refined FE meshes are shown in Figure 3.8d) and Figure 3.8e). For the sake of simplicity, only vertex nodes are shown. Consequently, the visualization of the 4-node and 10-node tetrahedra is the same (Figure 3.8c) and Figure 3.8e)). Table 3.2 contains the number of nodes and number of elements of each FE mesh.

Table 3.2. List of characteristics of each 3D FE MS model.

Mesh		Number of nodes	Number of elements
Non-refined	Tet4	26 827	22 704
	Tet10	31 561	22 704
	Hex27	16 425	1 892
Refined	Tet4	184 171	156 864
	Tet10	213 685	156 864
	Hex27	109 109	13 072

The main goal for the development of these six different FE meshes with the same geometry was to perform a convergence study, i.e., to compare the outcomes of the different FE meshes for the same geometrical model, in order to ensure the validity of the forthcoming results and to eliminate possible mesh-related inaccuracies. The simulations and results related to this convergence study will be presented and discussed in the "Validation" chapter.

The procedures of alteration between the different finite elements and mesh refinement were executed using the mesh-edition features of the open-source FE solver, but the selected visualization software was GiD 7.4.6b®. In other words, the mesh pre-processing procedures were accomplished with custom-made FORTRAN code, being the mesh files[xv] compatible with GiD 7.4.6b®, as well the numerical output files[xvi].

[xv] The available mesh format files are ".msh" and ".unv".
[xvi] The output files concerning the resultant mesh are expressed in ".res" format.

3.4. References

Adams, M.A., Dolan, P., McNally, D.S., 2009. The internal mechanical functioning of intervertebral discs and articular cartilage, and its relevance to matrix biology. Matrix Biol. 28, 384–9.

Alves, J.L., 2003. Simulação Numérica do Processo de Estampagem de Chapas Metálicas - Modelação Mecânica e Métodos Numéricos.

Alves, J.L., Yamamura, N., Oda, T., Teodosiu, C., 2010. Numerical simulation of musculo-skeletal systems by V-Biomech. In: CMBBE2010.

Argoubi, M., Shirazi-Adl, A., 1996. Poroelastic creep response analysis of a lumbar motion segment in compression. J. Biomech. 29, 1331–9.

Bonet, J., Wood, R.D., 1997. Nonlinear Continuum Mechanics for Finite Element Analysis. Cambridge University Press, Cambridge.

Cavalcanti, C., Correia, H., Castro, A.P.G., Alves, J.L., 2013. Constituive modelling of the annulus fibrosus: Numerical implementation and numerical analysis. In: 2013 IEEE 3rd Portuguese Meeting in Bioengineering (ENBENG). IEEE, pp. 1–4.

Eberlein, R., Holzapfel, G.A., Schulze-Bauer, C.A.J., 2001. An Anisotropic Model for Annulus Tissue and Enhanced Finite Element Analyses of Intact Lumbar Disc Bodies. Comput. Methods Biomech. Biomed. Engin. 4, 209–229.

Ebraheim, N., Hassan, A., Lee, M., Xu, R., 2004. Functional anatomy of the lumbar spine. Semin. Pain Med. 2, 131–137.

Ehlers, W., Karajan, N., Markert, B., 2009. An extended biphasic model for charged hydrated tissues with application to the intervertebral disc. Biomech. Model. Mechanobiol. 8, 233–51.

Elliott, D., Setton, L., 2000. A linear material model for fiber-induced anisotropy of the anulus fibrosus. J. Biomech. Eng. 122, 173–179.

Ferguson, S.J., Ito, K., Nolte, L.-P., 2004. Fluid flow and convective transport of solutes within the intervertebral disc. J. Biomech. 37, 213–221.

Frijns, A.J.H., Huyghe, J.M., Janssen, J.D., 1997. A validation of the quadriphasic mixture theory for intervertebral disc tissue. Int. J. Eng. Sci. 35, 1419–1429.

Galbusera, F., Schmidt, H., Noailly, J., Malandrino, A., Lacroix, D., Wilke, H.-J., Shirazi-Adl, A., 2011. Comparison of four methods to simulate swelling in poroelastic finite element models of intervertebral discs. J. Mech. Behav. Biomed. Mater. 4, 1234–41.

Holzapfel, G., Gasser, T.C., 2001. A viscoelastic model for fiber-reinforced composites at finite strains: Continuum basis, computational aspects and applications. Comput. Methods Appl. Mech. Eng. 190, 4379–4403.

Holzapfel, G.A., Schulze-Bauer, C.A.J., Feigl, G., Regitnig, P., 2005. Single lamellar mechanics of the human lumbar anulus fibrosus. Biomech. Model. Mechanobiol. 3, 125–40.

Huyghe, J.M., 1986. Non-linear finite element models for the beating left ventricle and the intramyocardial coronary circulation.

Huyghe, J.M., Houben, G.B., Drost, M.R., van Donkelaar, C.C., 2003. An ionised/non-ionised dual porosity model of intervertebral disc tissue. Biomech. Model. Mechanobiol. 2, 3–19.

Huyghe, J.M., van Campen, D.H., Arts, T., Heethaar, R.M., 1991. A two-phase finite element model of the diastolic left ventricle. J. Biomech. 24, 527–38.

Iatridis, J., Setton, L., Weidenbaum, M., Mow, V., 1997. The viscoelastic behavior of the non-degenerate human lumbar nucleus pulposus in shear. J. Biomech. 30, 1005–1013.

Jimenez Rios, J.L., Steif, P.S., Rabin, Y., 2007. Stress-strain measurements and viscoelastic response of blood vessels cryopreserved by vitrification. Ann. Biomed. Eng. 35, 2077–86.

Kaliske, M., Nasdala, L., Rothert, H., 2001. On damage modelling for elastic and viscoelastic materials at large strain. Comput. Struct. 79, 2133–2141.

Kelm, B.M., Wels, M., Zhou, S.K., Seifert, S., Suehling, M., Zheng, Y., Comaniciu, D., 2012. Spine detection in CT and MR using iterated marginal space learning. Med. Image Anal.

Li, H., Wang, Z., 2006. Intervertebral disc biomechanical analysis using the finite element modeling based on medical images. Comput. Med. imaging Graph. 30, 363–70.

Noailly, J., Lacroix, D., Planell, J., 2005. Finite element study of a novel intervertebral disc substitute. Spine (Phila. Pa. 1976). 30, 2257–64.

Raj, P., 2008. Intervertebral Disc: Anatomy Physiology Pathophysiology Treatment. Pain Pract. 8, 18–44.

Riches, P.E., Dhillon, N., Lotz, J., Woods, a W., McNally, D.S., 2002. The internal mechanics of the intervertebral disc under cyclic loading. J. Biomech. 35, 1263–71.

Schmidt, H., Bashkuev, M., Galbusera, F., Wilke, H.-J., Shirazi-Adl, A., 2013. Finite element study of human lumbar disc nucleus replacements. Comput. Methods Biomech. Biomed. Engin.

Schmidt, H., Kettler, A., Rohlmann, A., Claes, L., Wilke, H.-J., 2007. The risk of disc prolapses with complex loading in different degrees of disc degeneration - a finite element analysis. Clin. Biomech. (Bristol, Avon) 22, 988–98.

Schroeder, Y., Huyghe, J.M., van Donkelaar, C.C., Ito, K., 2010. A biochemical/biophysical 3D FE intervertebral disc model. Biomech. Model. Mechanobiol. 9, 641–50.

Simo, J.C., Taylor, R.L., 1991. Quasi-incompressible finite elasticity in principal stretches. continuum basis and numerical algorithms. Comput. Methods Appl. Mech. Eng. 85, 273–310.

Smit, T.H., 1996. The mechanical significance of the trabecular bone architecture in a human vertebra.

Sussman, T., Bathe, K., 1987. A finite element formulation for nonlinear incompressible elastic and inelastic analysis. Comput. Struct. 26, 357–409.

Swider, P., Pédrono, A., Ambard, D., Accadbled, F., Sales de Gauzy, J., 2010. Substructuring and poroelastic modelling of the intervertebral disc. J. Biomech. 43, 1287–91.

Tyndyka, M. a, Barron, V., McHugh, P.E., O'Mahoney, D., 2007. Generation of a finite element model of the thoracolumbar spine. Acta Bioeng. Biomech. 9, 35–46.

Van der Voet, A., 1997. A comparison of finite element codes for the solution of biphasic poroelastic problems. Proc. Inst. Mech. Eng. H. 211, 209–11.

Wang, S., Park, W.M., Gadikota, H.R., Miao, J., Kim, Y.H., Wood, K.B., Li, G., 2012. A combined numerical and experimental technique for estimation of the forces and moments in the lumbar intervertebral disc. Comput. Methods Biomech. Biomed. Engin.

Wilson, W., Huyghe, J.M., van Donkelaar, C.C., 2006. A composition-based cartilage model for the assessment of compositional changes during cartilage damage and adaptation. Osteoarthritis Cartilage 14, 554–60.

Wilson, W., Huyghe, J.M., van Donkelaar, C.C., 2007. Depth-dependent compressive equilibrium properties of articular cartilage explained by its composition. Biomech. Model. Mechanobiol. 6, 43–53.

Wilson, W., van Donkelaar, C.C., Huyghe, J.M., 2005. A Comparison Between Mechano-Electrochemical and Biphasic Swelling Theories for Soft Hydrated Tissues. J. Biomech. Eng. 127, 158.

Wilson, W., van Donkelaar, C.C., van Rietbergen, B., Huiskes, R., 2005. A fibril-reinforced poroviscoelastic swelling model for articular cartilage. J. Biomech. 38, 1195–204.

4. VALIDATION

This chapter presents the validation of the innovative biphasic poroelastic formulation and also of the lumbar IVD FE model. Firstly, the validation of the through Terzaghi's 1D test is presented. Then, several tests are described, in order to evaluate the IVD FE model. The swelling periods, the comparison with benchmark literature data and the outcomes of the mesh convergence study are included in this chapter.

4.1. Terzaghi's 1D Test

The first step on the numerical analysis of the current work is to validate the innovative biphasic formulation. This task was based on Terzaghi's uniaxial compression test for 1D consolidation (Terzaghi, 1943, 1925).

The theoretical model developed by Terzaghi is based on the relationship between Relative Pressure (P_T), Relative Depth (Z_T), Relative Consolidation time (T_T) and also a cumulative parameter (M_T). The analytical solution is given by:

$$P_T = \sum_{n=0}^{\infty} \left(\frac{2}{M_T} \right) \left(\sin\left(M_T Z_T \right) \right) \left(e^{-M_T{}^2 T_T} \right) \qquad 4.1$$

This model is valid for confined compression tests and was originally developed to analyze soil consolidation problems, i.e., it was first devoted to answer geomechanical questions. Later on, Terzaghi's model started being applied to bioporomechanics, in order to evaluate the behavior of biological mixtures, as performed by (Huyghe, 1986; Oomens et al., 1987a, 1987b).

The parameters on equation 4.1 are defined by the following expressions:

$$P_T = \frac{\tilde{p}}{\tilde{p}_0} \qquad 4.2$$

$$Z_T = \frac{z}{h} \qquad 4.3$$

$$T_T = \frac{K^* H t^*}{h^2} \qquad 4.4$$

$$M_T = \frac{\pi}{2}(2n+1) \qquad 4.5$$

From equations 4.3 and 4.4, z is the consolidation depth, h is the thickness of the layer and H is the compressive modulus. For the sake of simplicity, in equation 4.5, $n = [1,5]$, given that M_T is merely slightly influenced by values of n higher than 5. The pressure-related variables of equation 4.2 stand for the initially applied pressure ($\tilde{p}_0$) and the current pressure ($\tilde{p}$)[1]. The objective of this test is to evaluate the consolidation process of a given material, as the fluid outflow takes place. It must be highlighted that for $T \geq 1$ the consolidation process of the specimen should be largely completed (Huyghe, 1986; Terzaghi, 1943).

The testing scheme included a clay layer and a consolidation layer (with height = h). The load is applied on the top surface of the clay layer. The example for the 27-node hexahedral mesh (Hex27) is shown in Figure 4.1, but the testing model was built with each one of the three types of u/p-c elements available on the open source FE solver, i.e., the linear 4-node tetrahedron (linear tetrahedron enriched with a bubble function at the center of the element, Tet4) and the quadratic 10-node tetrahedron (Tet10) were also tested, in order to prove the validity of the developed formulation.

The clay layer is much more permeable than the consolidation layer, in order to allow the fluid to flow from top to bottom. The primary layers of elements of the consolidation layer are more refined then the bottom ones, to facilitate the fluid flowing and achieve better description of the pressure gradients. The first layers of elements are critical for the consolidation process, i.e., the probability of occurrence of numerical instabilities is higher on the first layers. The fluid flow is steadier on the bottom layers, so the mesh refinement can be dismissed for those layers (Huyghe, 1986).

[1] These pressure variables were already detailed in Chapter 3.

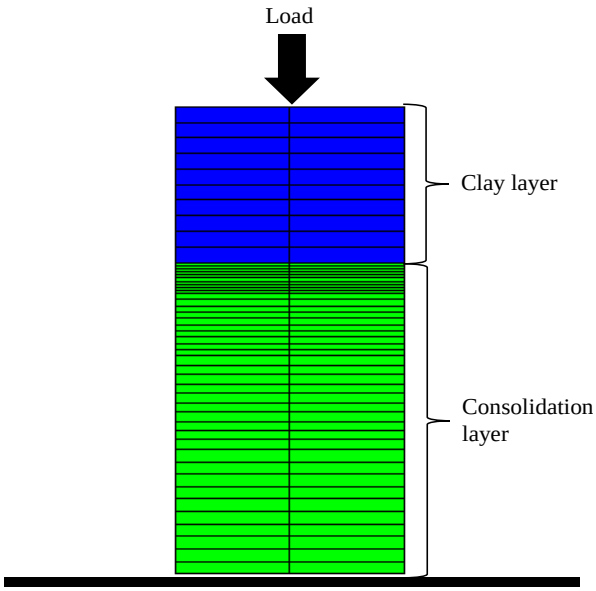

Figure 4.1. Testing scheme for Terzaghi's test, for the 27-node hexahedral mesh. The same scheme was adopted for the 4 and 10-node tetrahedral meshes. Only vertex nodes are shown.

The absolute stiffness properties are not relevant at this point. However, the two layers were considered to be isotropic and linear elastic, with the same value of compressive modulus for both of them.

The applied load was uniaxial compression, while all the other degrees of freedom were fully constrained. Fluid flow was only allowed on the top of the clay layer, being blocked on the rest of the model, i.e., the fluid could not flow through the other boundaries. The bottom of the model (ground) is rigid and impermeable.

Each test was performed with the same boundary conditions, having T as the only non-constant parameter. Therefore, the results for each type of element were compared with the analytical solution correspondent to the following four Relative Consolidation Time values, i.e., $T_T \in \{0.0105, \quad 0.0901, \quad 0.540, \quad 1.112\}$, as shown in Figure 4.2.

The results from the comparison between the numerical simulations and the analytical solution of Terzaghi's model are quite satisfactory, as the consolidation process is taking place as it should (Huyghe, 1986; Oomens et al., 1987a, 1987b; Terzaghi, 1943, 1925). Minor differences between the P_T vs. Z_T curves are perceived along the four different time values. Therefore, each model shows good agreement with the analytical solution, for the used range of values of T_T.

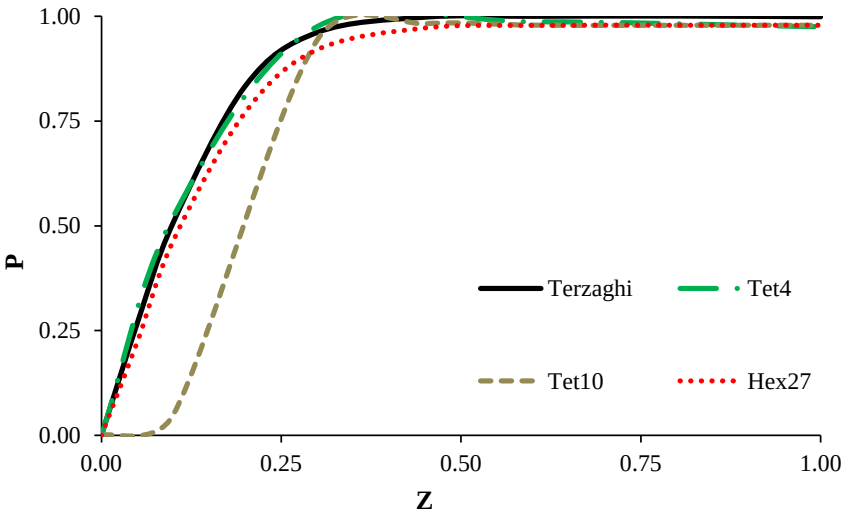
1.00
0.75
0.50
0.25
0.00
P
0.00
0.25
0.50
0.75
1.00
Z
Terzaghi
Tet4
Tet10
Hex27

a)

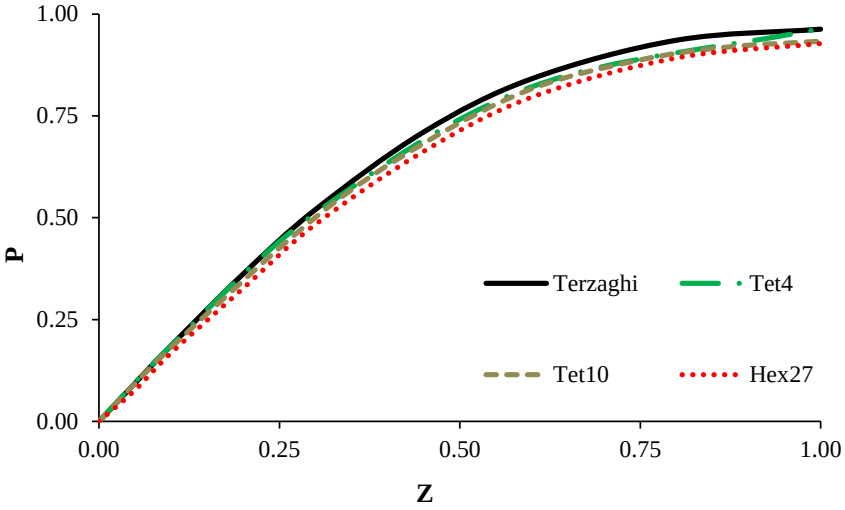
1.00
0.75
0.50
0.25
0.00
P
0.00
0.25
0.50
0.75
1.00
Z
Terzaghi
Tet4
Tet10
Hex27

b)

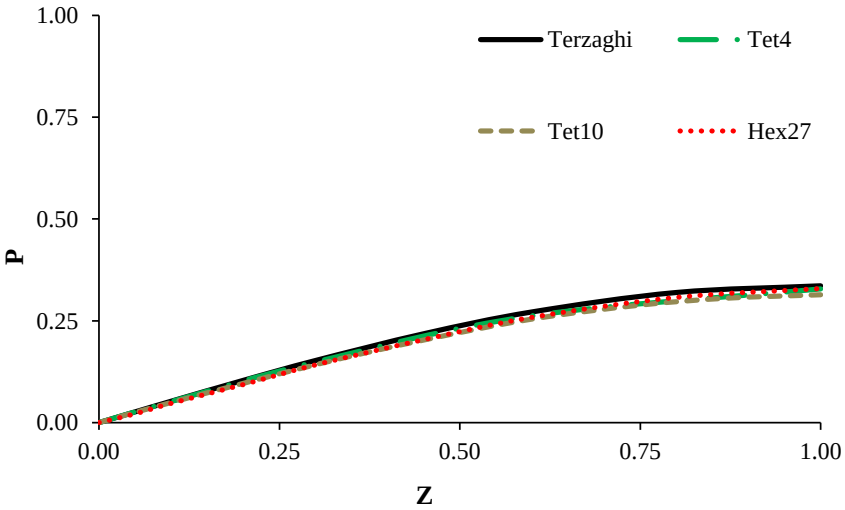
1.00
0.75
0.50
0.25
0.00
P
0.00
0.25
0.50
0.75
1.00
Z
Terzaghi
Tet4
Tet10
Hex27

c)

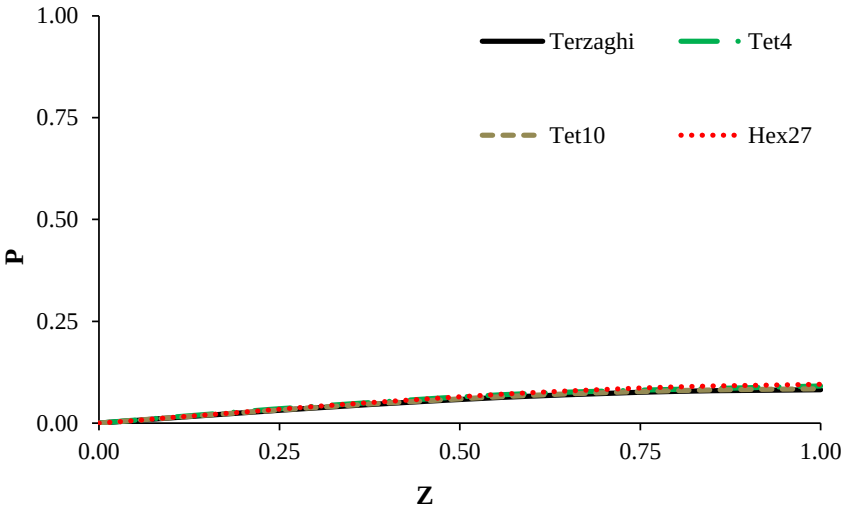

d)

Figure 4.2. Comparison between the results of Relative Pressure vs. Relative Depth predicted by the analytical solution of Terzaghi's model and the results obtained with different types of elements, namely the linear 4-node tetrahedron enriched with a bubble function at the center of the element (Tet4), the quadratic 10-node tetrahedron (Tet10) and the quadratic 27-node hexahedra (Hex27). The Relative Consolidation Time varied between four values: a) $T_T = 0.0105$; b) $T_T = 0.0901$; c) $T_T = 0.540$; d) $T_T = 1.112$.

Nevertheless, Figure 4.2a) shows a noticeable difference between the 10-node tetrahedron and the other three curves, which may be justified by the relationship between the configuration of the element (tetrahedron with quadratic interpolation) and the reduced consolidation time. In fact, with larger consolidation times, significant differences were no longer verified.

This simple test was the first stage for the validation of the developed biphasic formulation, as the fluid flow seems to be ensured in correct conditions, which means that the present results may be extrapolated for more complex 2D and 3D situations. The three types of elements, i.e., Tet4, Tet10 and Hex27 were proved as reliable to be applied in the following simulation tasks of the current work.

4.2. Swelling Periods

Physiologically, the swelling periods are the time intervals which usually correspond to the rest periods. These periods are considered to averagely last for one-third of the day (8h) and are usually denominated by rest or recovery phases (Schmidt et al., 2010). The activity periods are characterized by loading profiles with multiple combination of efforts and positions. In fact, axial compression, rotation and flexion-extension efforts occur along the regular day period, during diverse positions, such as normal walking, climbing stairs or carrying objects. The load magnitudes are usually above 500N (Galbusera et al., 2011). The rest periods are characterized by a reduction of the load to the minimum and steady positions, which usually correspond to sleeping. This combination allows the IVD to recover height, mostly due to its swelling properties, which means that the IVD regains the fluid content lost during the activity periods. However, it must be highlighted that the swelling properties also play an important role on the activity periods, i.e., it was proved that the loading equilibrium is greatly influenced by the osmotic swelling pressure gradient (Schmidt et al., 2013).

In what concerns to numerical simulations, the initial swelling period is somewhat different from the functional swelling periods. The condition of the IVD FE model shall be approximated to the physiological condition of the *in vivo* IVD, before the "real" simulation starts. Therefore, the initial swelling period may be understood as a numerical pre-conditioning. Several loading levels for the pre-conditioning and recovery periods can be found in the literature. Four different loadcases were considered for the simulation of the initial swelling periods, namely free swelling (Galbusera et al., 2011) and loaded swelling with 200N (idem), 250N (Sato et al., 1999) and 350N (Schmidt et al., 2010).

Regarding the four tests, the bottom VB was fully constrained, while lateral and sagittal movements of the MS were allowed. Unconstrained fluid flow was allowed in all external boundaries of the MS model. The loading profiles were necessarily different, as per the free swelling test no load was applied and the top VB was left unconstrained. For the three loaded swelling cases, uniaxial compression was performed, being the load applied on the top VB for 60s and then held until the end of the test. The total duration of the tests was 8h.

First, the disc height variation (DHV) of the four loadcases was compared (Figure 4.3). DHV expresses the difference in time between the initial IVD height and current IVD height. Secondly, three different pressure variables were assessed, for each loadcase. NP average pressure (NP AveP) denotes the pressure of the NP, i.e., the pressure of the biphasic mixture that constitutes the NP. IDP represents the pressure of the fluid in the center of the IVD, i.e., inside the NP[ii]. Osmotic pressure (OsmP) is the osmotic swelling pressure gradient measured for the NP. These quantities are evaluated in Figure 4.4.

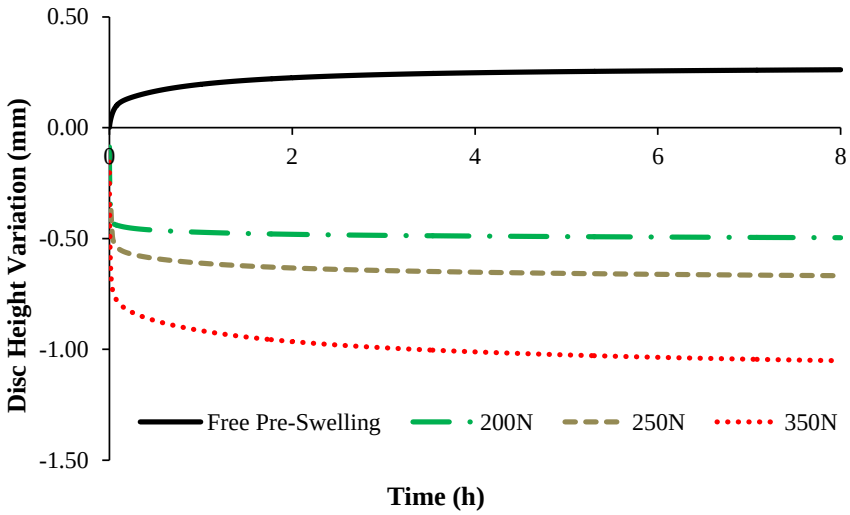

Figure 4.3. Comparison between the DHV results of the four possibilities for the initial swelling period, along the 8h of the present (Free Pre-Swelling, 200N, 250N and 350N).

In what concerns the loaded swelling, the AveP results for the 200N load seem to be well-balanced with the OsmP component, as both present an average value of 0.182MPa and a very similar evolution throughout the test. This finding is solid evidence that the average pressure of the IVD is provided by the swelling equilibrium. The IDP is slightly lower (average of 0.144MPa), but the curve of IDP versus time is similar to the curves of the other two components of the pressure, along the 8h of the test, as visible in Figure 4.4b)). The DHV also seems to be stable around -0.50mm, which is consistent with the available data (Galbusera et al., 2011). When the load was slightly increased to 250N, the OsmP did not changed significantly, as its average value was 0.184MPa. The final values for both IDP and AveP increased marginally, to 0.172MPa and 0.215MPa, respectively. However, those components started to reveal a slight creep effect, i.e.,

[ii] In some cases, this pressure variable is denominated simply as "fluid pressure".

the initial pressure value (just after the application of the load) is higher than the final one, for the same load (Figure 4.4c)). In addition, the DHV increased to -0.67mm and also denoted a creep effect, given that a DHV value of -0.50mm was measured immediately after the application of the load (Figure 4.3). In the 350N loadcase, the AveP is consistently above the OsmP, meaning that real compression is occurring on the IVD. This finding is reinforced by the DHV results, i.e., the IVD height loss is increasing along the test (Figure 4.3). The final value of -1.05mm, after a noticeable creep effect, is in accordance with literature data (Schmidt et al., 2010). However, the OsmP and the IDP come to equilibrium around the 6th hour of test, which was also theoretically expected (Galbusera et al., 2011) (Figure 4.4d)).

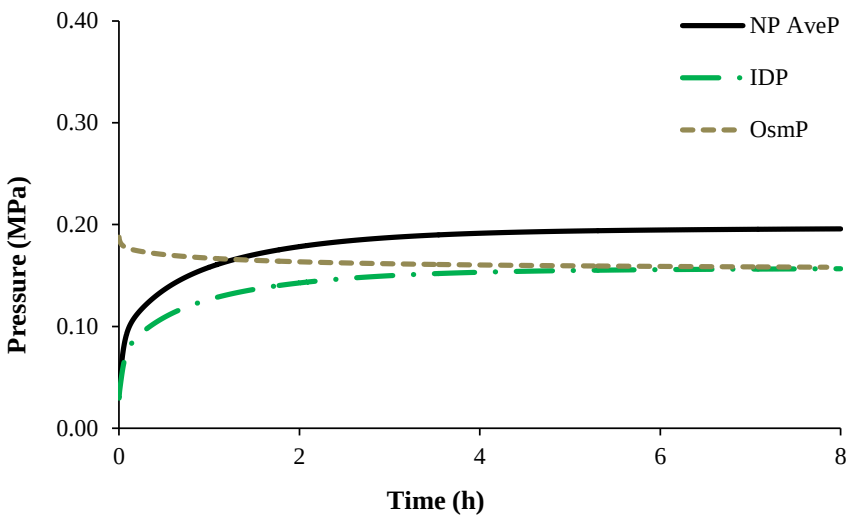

a)

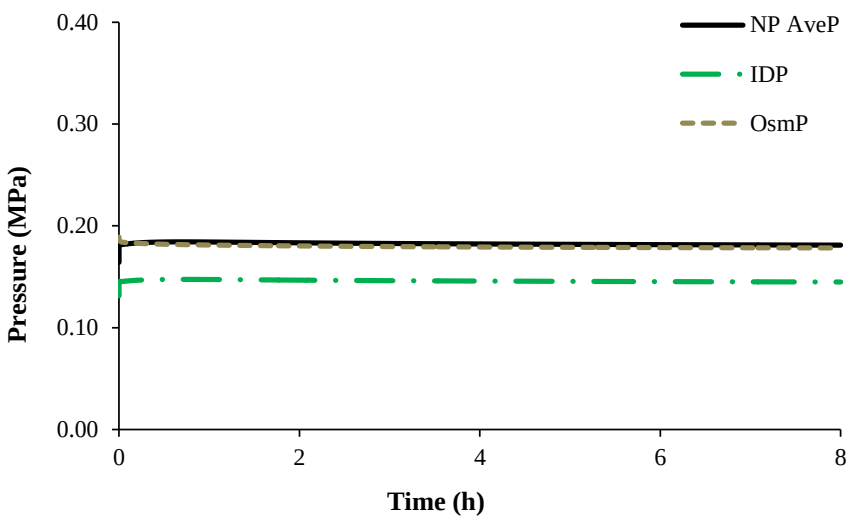

b)

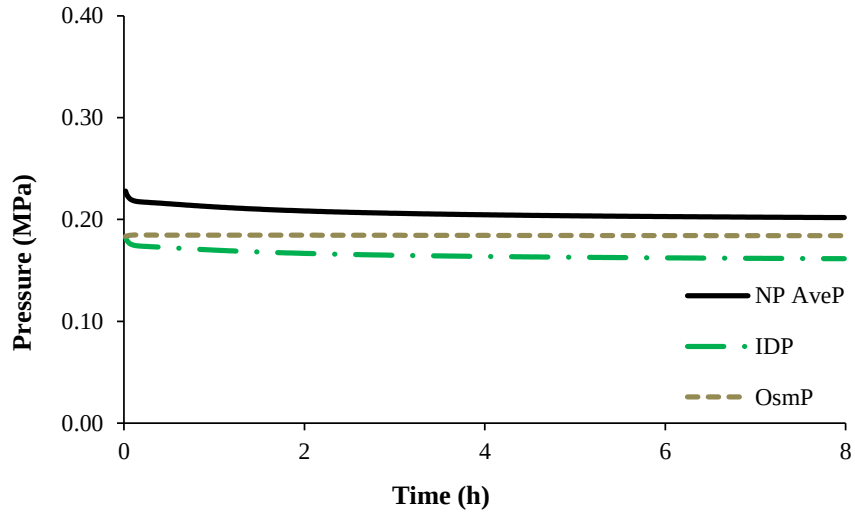

c)

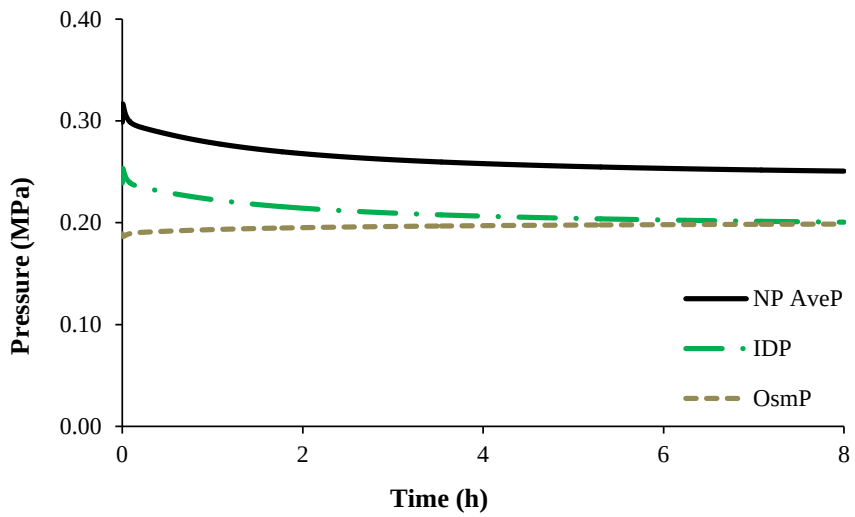

d)

Figure 4.4. Pressure results of the four possibilities for the initial swelling period: a) Free Pre-Swelling; b) 200N; c) 250N and d) 350N. NP AveP, IDP and OsmP were assessed and compared between each other, along the 8h of the test.

To summarize, the 200N load seems to be the most appropriated to simulate the resting period. The 250N load might also be considered to such purposes, due to the presented displacement and pressure equilibrium. Finally, the 350N load seems to be exaggerated and the results seem to show that this load magnitude will not allow the average lumbar IVD to recover from the activity periods. Free swelling allows the disc to increase in height, as theoretically expected (Galbusera et al., 2011; Johannessen and Elliott, 2005), i.e., Figure 4.3 shows positive

DHV for this case, which means that the IVD slightly increased in height. Table 4.1 summarizes the pressure and displacement measurements along the 8h of that test.

Table 4.1. Pressure and displacement measurements over time, for the free swelling test.

Time (h)	DHV (mm)	IDP (MPa)	OsmP (MPa)
0	0.00	0.00	0.188
1	0.196	0.126	0.167
2	0.226	0.143	0.163
4	0.248	0.153	0.160
6	0.257	0.156	0.159
8	0.262	0.158	0.158

After the fourth hour, IDP and OsmP become almost equilibrated, and their value at the end of the test is the same (0.158MPa), which was also theoretically expected, as no load is being applied on the MS. However, the most important part of the free swelling phenomena occurs in the first two hours of test. As a matter of fact, 75% of the final DHV and 80% of the final IDP are measured at the first hour of test. At the second hour, 86% of the final DHV and 90% of the final IDP are already obtained.

This is probably the best approximation for the simulation of the pre-conditioning period because it replicates the *in vivo* condition of the IVD. The equilibrium between the IDP and OsmP shows that the pressurization of the IVD comes directly from the strain-dependent osmotic swelling pressure gradient (Wilson et al., 2005). The DHV relative increase of only 14% after the second hour is a direct consequence of such equilibrium. In addition, the IVD height increase of 0.262mm only represents 2% of the total initial IVD height, which is negligible.

4.2.1. Comparison of swelling simulation methods

The described procedure for simulating the pre-conditioning period using free swelling was also applied by Galbusera et al. (2011) on ABAQUS®. In that work, strain-dependent and fixed swelling methods were considered. On the one hand, strain-dependent osmotic pressure gradient

is the same approach that was previously described, i.e, the osmotic pressure gradient is also calculated through Wilson's model[iii]. This approach will be further denominated as "BS", which stands for "Biphasic Swelling".

On the other hand, the osmotic pressure gradient in the center of the NP was a given input parameter. This condition will be further denominated as "FOP", which stands for "fixed osmotic pressure". Galbusera and co-workers used the result of the strain-dependent osmotic pressure gradient at the end of the 8h of free swelling as the fixed osmotic pressure value (0.165 MPa). In the present work, two different situations were considered, as the fixed osmotic pressure gradient was tested with the result of the strain-dependent osmotic pressure gradient at the beginning of the test ("FOP (1)", 0.188 MPa) and then with the result of the strain-dependent osmotic pressure gradient at the end of the test ("FOP (2)", 0.158 MPa). The material properties of both AF and CEP remained unaltered.

Figure 4.5 shows the comparison between the three hypotheses of the present work (BS, FOP (1) and FOP (2)) and the two hypotheses (BS and FOP) from Galbusera et al., in terms of DHV (Figure 4.5a)), IDP (Figure 4.5b)), NP volume variation (Figure 4.5c)) and AF volume variation (Figure 4.5d)). DHV and AF volume variation were very similar for the strain-dependent approaches of both works, at the end of the 8 hours (around 0.26mm and 1.8%, respectively). However, both IDP and NP volume variation are slightly lower on Galbusera's work (4.9% versus 6.2% and 0.136MPa versus 0.158MPa, respectively). On the one hand, as the DHV is similar, this correlation between lower NP volume variation and higher IDP is probably associated with the existing differences on material properties and geometrical features, which alter the stress distribution inside the NP. On the other hand, as both works use Wilson's model for strain-dependent osmotic swelling, Figure 4.6 compares the evolution of IDP and OsmP along the 8 hours of the test.

The OsmP curves present a different evolution, but the starting and ending values (around 0.19 and 0.16MPa, respectively) are close, as expected. The first two hours are the most significant for the behavior of Galbusera's model. This finding was already listed and discussed, in what concerns the present work. As a matter of fact, the major part of the behavioral changes seems to happen during the first hour of free swelling. However, IDP and OsmP seem to need more time to reach the equilibrium on Galbusera's model.

[iii] Using a user-subroutine integrated on ABAQUS®, as first implemented by Wilson et al. (2005).

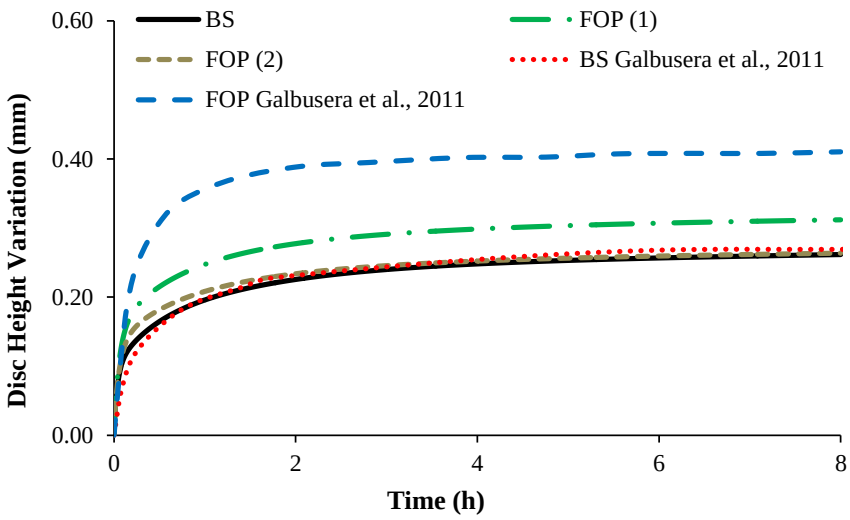
BS
FOP (1)
FOP (2)
BS Galbusera et al., 2011
FOP Galbusera et al., 2011
Disc Height Variation (mm)
0.60
0.40
0.20
0.00
0
2
4
6
8
Time (h)

a)

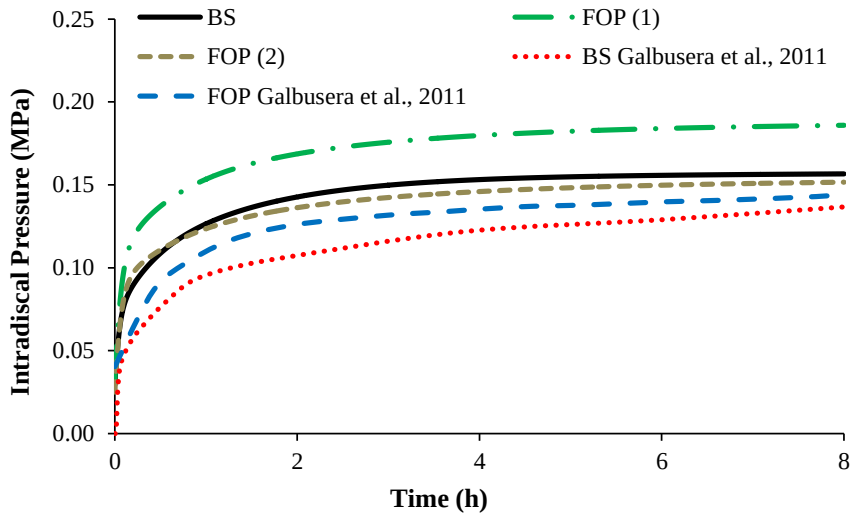
BS
FOP (1)
FOP (2)
BS Galbusera et al., 2011
FOP Galbusera et al., 2011
Intradiscal Pressure (MPa)
0.25
0.20
0.15
0.10
0.05
0.00
0
2
4
6
8
Time (h)

b)

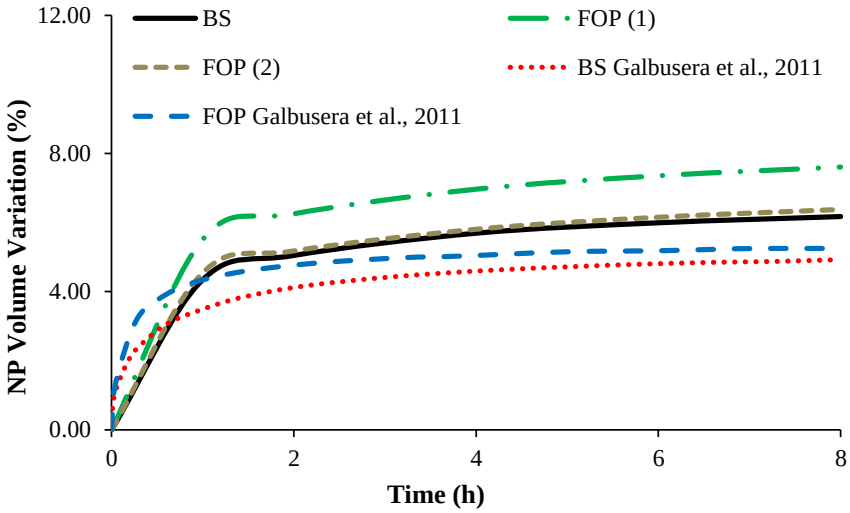
BS
FOP (1)
FOP (2)
BS Galbusera et al., 2011
FOP Galbusera et al., 2011
NP Volume Variation (%)
12.00
8.00
4.00
0.00
0
2
4
6
8
Time (h)

c)

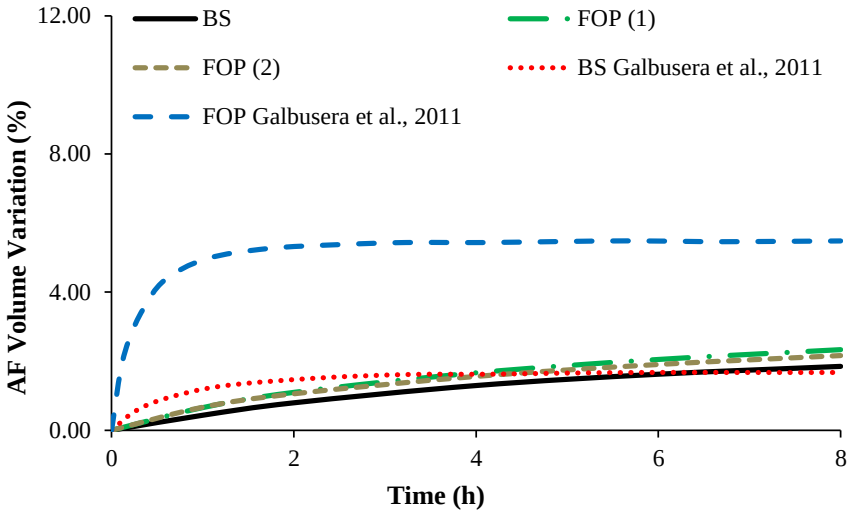

d)

Figure 4.5. Comparison between the present model and Galbusera and co-workers model: a) DHV; b) IDP; c) NP volume variation and d) AF volume variation.

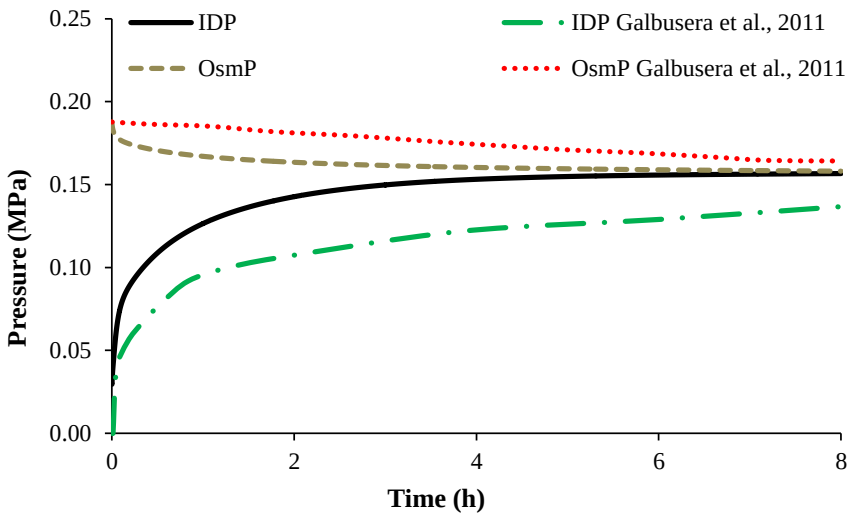

Figure 4.6. Comparison between the evolution of IDP and OsmP of the BS models from the present work and the work of Galbusera et al. (2011).

The FOP (2) model seems to be very similar to the current BS model, probably meaning that the open source FE solver allowed more flexibility to the calculus of the strain-stress conditions of the IVD than the commercially available FEM package here evaluated[IV], even when the osmotic swelling pressure gradient is constant and not strain-dependent.

[IV] It must be reminded that Galbusera and co-workers implemented the same osmotic swelling formulation on ABAQUS®.

The slight differences noticed between BS and FOP (2) models still give the impression that the BS approach is the most accurate one. Fixed osmotic pressure gradient will not be suitable for more complex loadcases, as it would not track the larger deformations. The FOP (1) presents significant differences to both FOP (2) and BS models, showing that the model is sensitive to the higher osmotic pressure gradient. The Galbusera's FOP model also presents significant differences to the correspondent BS model, in all measured quantities.

In fact, the top values for Galbusera's FOP model are higher than the equivalent values for the BS model. This finding is more evident on the DHV and AF volume variation results, which are interconnected: the IVD height increase is greater, due to the higher and constant OsmP, so the stretching effect on the AF fibers is harsher.

4.2.2. Summary

To go over the main points of the swelling periods simulation, one has to start by distinguishing between the initial swelling period and the following functional swelling periods. The purpose of the initial swelling period is to approximate the condition of the IVD FE model to the physiological condition of the *in vivo* IVD, before the start of the realistic simulation. This may be understood as a numerical pre-conditioning. The obtained results have shown that the idealistic free swelling condition is the fastest and most accurate method to simulate the initial swelling period.

The other swelling periods are associated with the recovery periods, also known as night periods, as they usually occur during the night, in order to allow the spine to recover from the occurrences of the activity routines. Loads higher than 250N were proved to be over the limits that allow the recovery of the IVD, as they caused increasing height reduction, instead of maintaining a given height diminution[v]. This finding is in accordance with the works of (Eijkelkamp et al., 2001; Galbusera et al., 2011; Goins et al., 2005).

This recovery process takes place through the imbibition of the fluid that is lost during the activity routines, which results on the regain of IVD height. These results provided a valuable insight on the daily mechanisms of fluid flowing in the spine, which will be detailed in the "Long Creep" and "Bioreactor Data Analysis" sections of the "Results and Discussion" chapter.

[v] In other words, creep effect was noticed, but it is not supposed to occur during the resting period.

4.3. Short Creep Validation

The following set of tests intended to evaluate the response of the MS FE model under short loading periods, i.e., loadcases that do not last more than 3h. It must be highlighted that this premise does not account for duration of the pre-conditioning periods. The creep behavior of healthy human IVD is then assessed and compared with experimental and numerical literature sources, particularly Heuer et al. (2007) and Schroeder et al. (2010).

The benchmark of short creep test for this work is the experiment performed by Heuer et al. (2007). This test helped to understand the significance of the osmotic swelling behavior. Then, a convergence study was performed, in order to ensure that the quality of the results is not significantly influenced by the configuration of the FE mesh neither by mesh refinements. Alternative material configurations were also tested, in order to validate the selected set of material parameters.

4.3.1. 500N, 15mins

This first set of tests aimed to reproduce the experimental protocol of Heuer et al. (2007). For that purpose, 500 N were applied on the upper VB during 5min (slow loading to allow proper stabilization of the model) and then held for 15min. The load was applied through the vertical axis of the MS model, with the bottom VB fully constrained. Lateral and sagittal movements were allowed, in order to follow all the requirements described by Heuer's protocol. The importance of the osmotic swelling behavior for the IVD biomechanics was also evaluated, as this test was performed with three different swelling conditions: without osmotic swelling ("No Swelling"), with a pre-conditioning period of 1h of free swelling ("Pre-Swelling") and also with osmotic swelling, but without that pre-conditioning period ("No Pre-Swelling"). This pre-conditioning period represents the minimum required interval to reach swelling equilibrium, as described in the previous section of the present chapter. Figure 4.7 shows comparison between the experimental

results and the numerical ones, considering the different swelling modes. DHV and NP average pressure (NP AveP)[vi] were assessed.

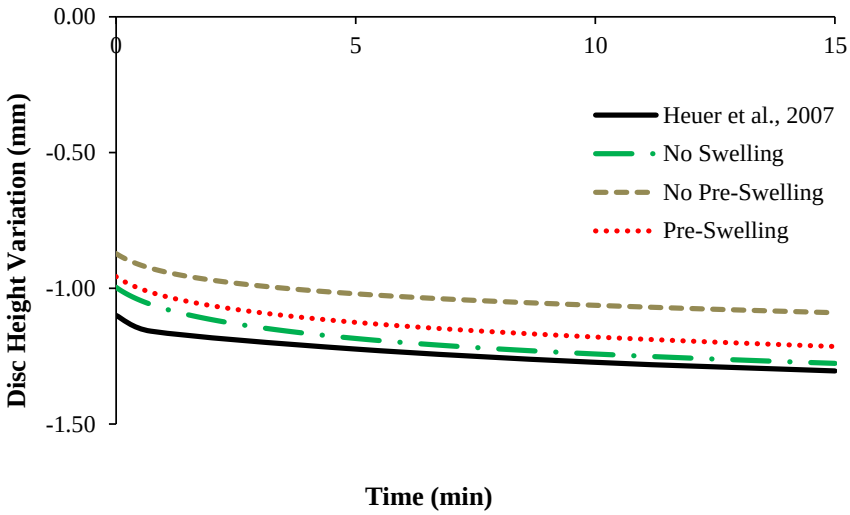

a)

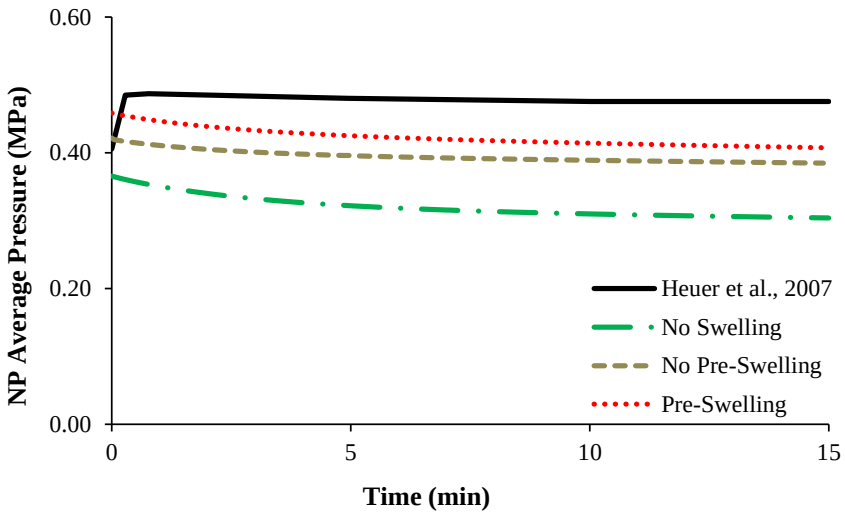

b)

Figure 4.7. Results of a 15min creep test at 500N of compression: a) DHV; b) NP AveP. The three options for the swelling behavior of the numerical model are compared with the experimental work of Heuer et al. (2007).

Heuer et al. (2007) experimentally measured a range of -1.08 to -1.57mm of DHV (average of -1.32mm), at the end of the 15 min. At the same time, the range of the NP AveP was between 0.36 and 0.52MPa (average of 0.44MPa). From the three numerical situations, the best

[vi] Average pressure on the NP, which considers both solid and fluid phases.

fit between numerical and experimental data seems to be obtained by the test which included a pre-conditioning period of 1h of free swelling ("Pre-Swelling"), the simulated DHV for these testing conditions is -1.21mm and the NP AveP is 0.41MPa. When the osmotic swelling is not considered ("No Swelling"), the DHV is in agreement with the experimental data (-1.28mm), but the NP AveP is outside the measured range (0.30MPa). The last situation, with osmotic swelling, but no pre-conditioning period ("No Pre-Swelling"), presents good fit for the NP AveP (0.39MPa), but a poor agreement for the DHV measurements (-1.09mm).

These findings emphasize the importance of the osmotic swelling for IVD biomechanics. Without osmotic swelling, the pressure gradients[VII] do not reach the expected levels. Therefore, the expected fluid imbibition and exudation cannot be simulated.

The differences between the values obtained with that setup and those from Heuer et al. (2007) are probably related to specimen-to-specimen variability and material properties (Johannessen and Elliott, 2005; Périé et al., 2005).

In addition, the pre-conditioning period is apparently important for the numerical reproduction of the experimental tests. The literature states that the pre-conditioning periods should be related with the recovery times, which are usually between 1 and 8h, as already described in the previous section of the present chapter. The results here obtained seem to follow these statements. This period is essential to simulate some of the effect of the loading history, since the IVD is naturally under an initial stress condition (Schmidt et al., 2010). To sum up, the setup with pre-conditioning period ("Pre-Swelling") was considered to be the standard for the forthcoming simulations.

4.3.2. Convergence study outcomes

In order to ensure the validity of the results, the six different MS FE models[VIII] were submitted to the same test. The previously described protocol for uniaxial compression based on Heuer's experiment (500N load during 15mins) was applied, and the pre-conditioning period of 1h of free swelling was also considered. The experimental data was compared with the results from the six FE models. Figure 4.8 shows the comparison between Heuer's data and the non-refined and

[VII] Pressure distribution inside the IVD.
[VIII] Described in the "Mesh Convergence Study" section of the 3rd Chapter.

refined mesh models, respectively. Figure 4.10 shows the comparison between the non-refined and refined mesh models. DHV and NP AveP were assessed.

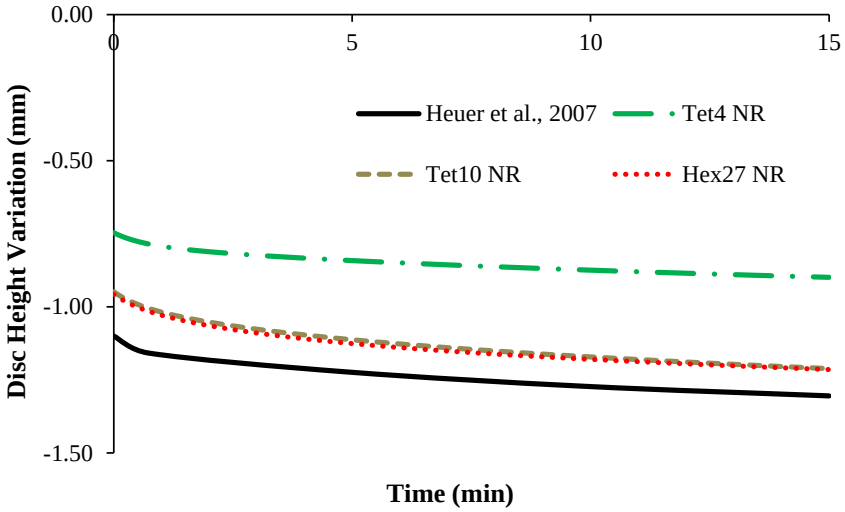

a)

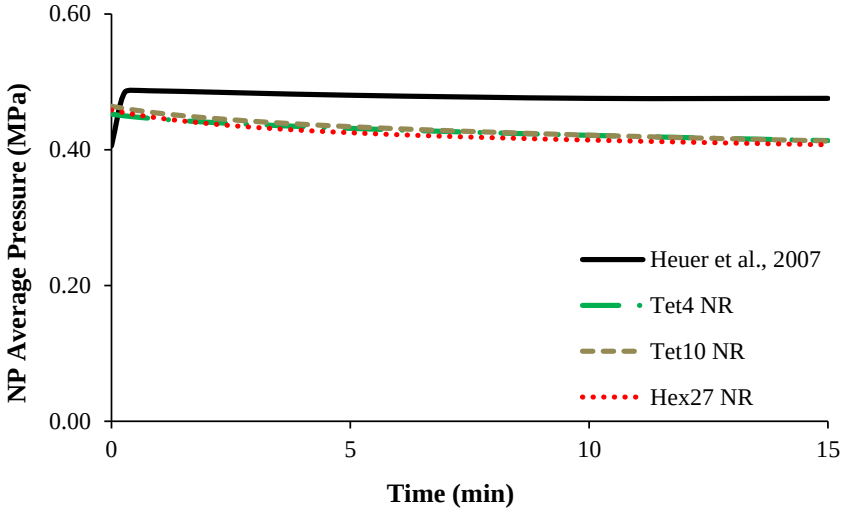

b)

Figure 4.8. Comparison between the experimental results of Heuer et al. (2007) and the numerical results obtained with different types of elements, for the non-refined meshes ("NR"): a) DHV; b) NP AveP.

On the one hand, the numerical DHV values are inside the experimental range, for both primary and refined Tet10 and Hex27 models, as shown on Figure 4.8a). Both configurations present an average DHV of -1.18mm at the end of the 15mins. The results for the Tet4 models are slightly outside that range, which may be explained by the unique configuration of the linear 4-node tetrahedra (enriched with a bubble function at the center of each element). It is likely that

such FE configuration would not be appropriate to predict DHV, at least with this low number of nodes. In fact, the refined Tet4 model (final DHV of -1.02mm) is closer to the other models than the non-refined model (final DHV of -0.90mm), as shown on Figure 4.10a). This combination of outcomes probably means that higher number of nodes means less deviation on the numerical results, when one is using the Tet4 elements. On the other hand, in what concerns the NP AveP measurements, minor differences are perceived between the three types of elements, for the cases of both primary and refined model, as shown on Figure 4.8b), Figure 4.9b) and Figure 4.10b).

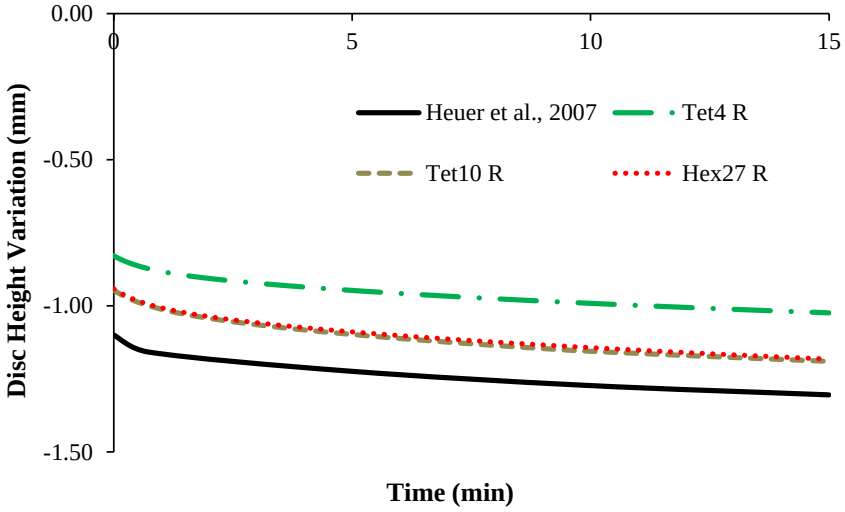

a)

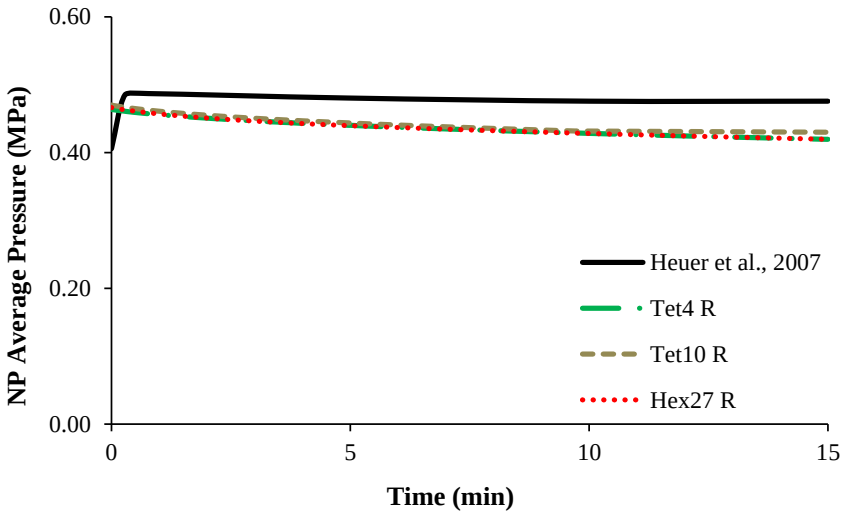

b)

Figure 4.9. Comparison between the experimental results of Heuer et al. (2007) and the numerical results obtained with different types of elements, for the refined meshes ("R"): a) DHV; b) NP AveP.

The referred values are inside the experimental range, as the average NP AveP is 0.43MPa. Such findings point out that the new biphasic formulation here implemented is sufficiently accurate to describe the fluid exchanges and pressure gradients that occur within the IVD and adjacent structures, independently of the topology of the FE mesh, i.e., the quality of the results was not significantly affected by the type of element, which means that one can choose any of the three types of element. However, the lower number of nodes and elements of the non-refined Hex27 model means lower simulation time, in comparison with the other possibilities. For this reason, it was demonstrated that the non-refined "Hex27" model is the appropriated choice for the numerical simulations.

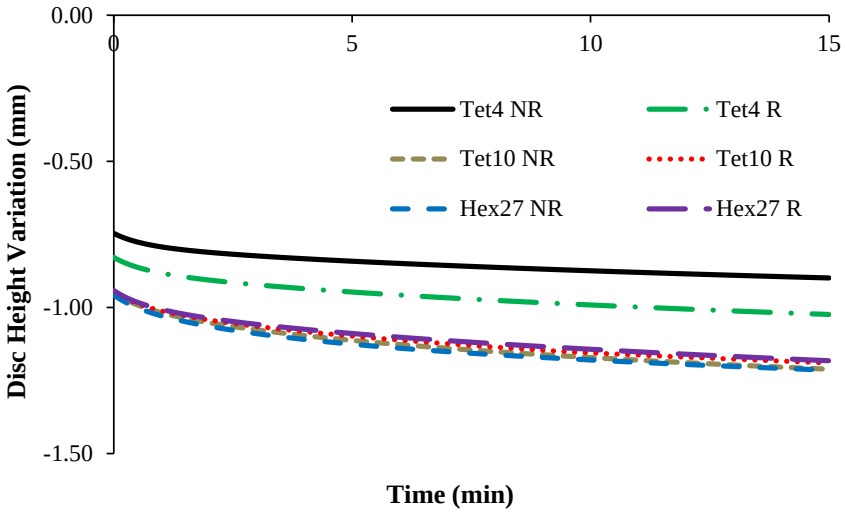

a)

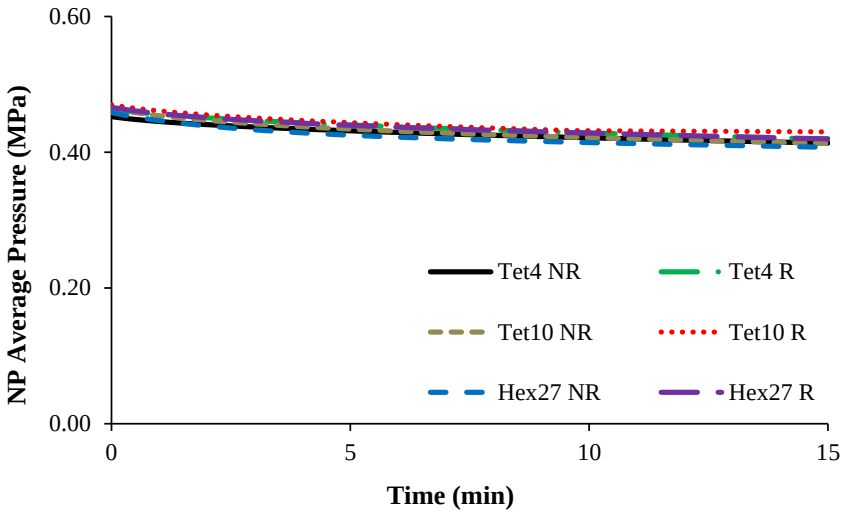

b)

Figure 4.10. Comparison between the non-refined ("NR") and the refined ("R") models: a) DHV; b) NP AveP.

4.3.3. Increasing loads, 15mins

The second set of short creep tests intended to match the conclusions of the works of O'Connell et al. (2011) and Wilke et al. (1999). The test settings were the same of the first tests, only with different load magnitudes, namely 1000N, 1500N and 2000 N. These load magnitudes are in the scope of moderate to harsh daily activities[IX] (McMillan et al., 1996; Pollintine et al., 2010; Wilke et al., 1999). The loads were applied during 5 min and then held for 15 min. The pre-conditioning period of 1h of free swelling was considered for all the loadcases. NP AveP and DHV were assessed and compared between the loadcases (Figure 4.11). The outcomes of the 500N loadcase were also included in that comparison.

Another possible approach to understand the behavior of the IVD under different compressive loadings is the calculus of the spine height reduction (SHR). SHR is based on the assumption that the lumbar, thoracic and cervical spine will undergo the same deformation (Krag et al., 1990; Williams et al., 2007). If one also assumes that each lumbar IVD deforms equally, one third of the total stature loss is in the lumbar spine and then each one of the five lumbar IVDs will be responsible for one fifteenth of the total stature loss. Therefore, SHR is calculated through the ratio of DHV in relation to the initial disc height (DHi), as shown on the following expression:

$$SHR = \frac{1 - \left(\frac{DHi - DHV}{DHi} \right)}{15} \qquad 4.6$$

The relative variations of the disc height (RDHV) and NP AveP (RPV) may also be considered. Both of these quantities are calculated through the ratio of the difference between the initial and final values, in relation to the final value:

$$RDHV = \frac{DHVi - DHVf}{DHVf} \qquad 4.7$$

$$RPV = \frac{NPAvePi - NPAvePf}{NPAvePf} \qquad 4.8$$

[IX] These loads may represent activities such as manual labor, car driving or lifting/carrying an object.

The values of SHR and RDHV are presented on Table 4.2, while the RPV values are presented in Table 4.3. The results presented on Figure 4.11a) and Table 4.2 seem to be in good agreement with the experimental data available in the literature. Before the creep period, the DHV is about -1.40mm for 1000N, -1.74mm for 1500N and -1.98mm for 2000N. These results are inside the range of the studies of Joshi et al. (2009) and O'Connell et al. (2011), as both groups measured an average DHV of about -1.40mm for 1000N, -1.60mm for 1500N and -1.85mm for 2000N. It must be highlighted that these values were obtained in in-vitro axial compression tests of non-degenerated human IVD.

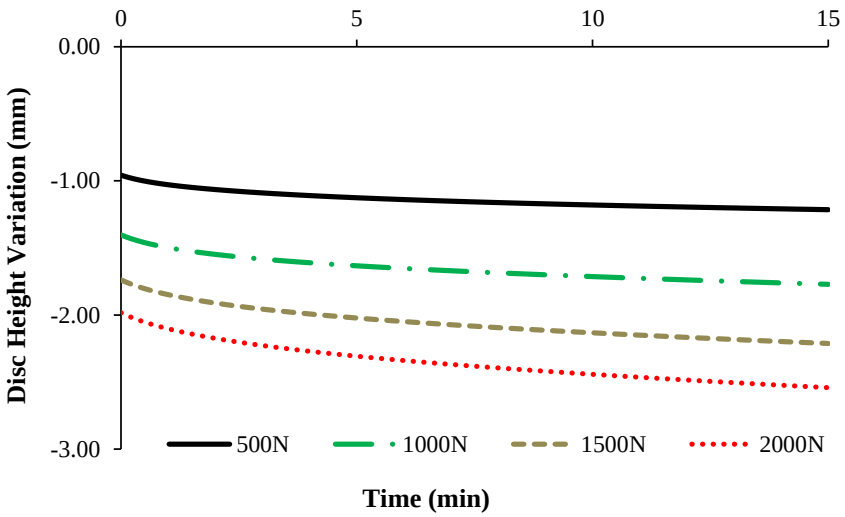

a)

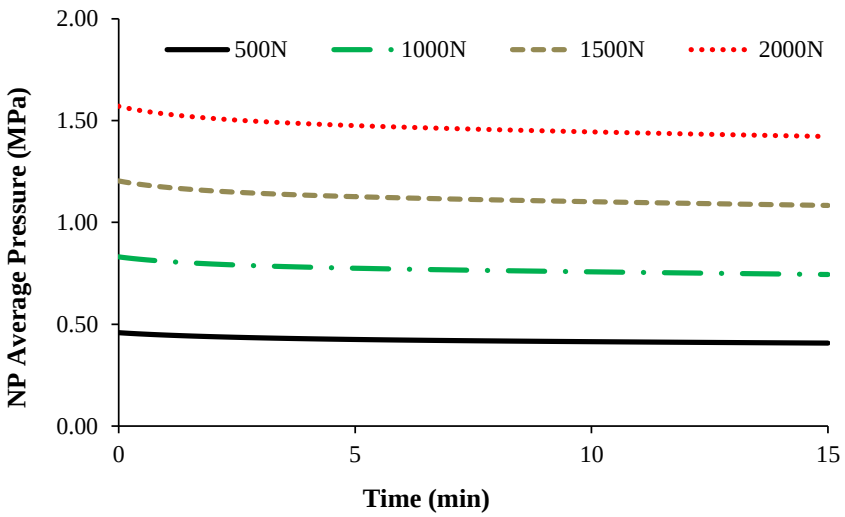

b)

Figure 4.11. Simulated creep test during 15min at different load magnitudes of uniaxial compression, namely 500, 1000, 1500 and 2000N: a) DHV; b) NP AveP.

Figure 4.11a) reveals that the different loads yield a relative increase of the DHV in the same average level, as the outlines of the DHV versus time curves are very similar. In addition, Table 4.2 shows that the creep response of the IVD model to the different loadcases is effectively consistent with the work of Heuer et al. (2007).

Table 4.2. Displacement measurements for the different load magnitudes of uniaxial compression, namely 500N, 1000N, 1500N and 2000N.

Loadcase [N]	DHVi [mm]	DHVf [mm]	SHR [%]	RDHV [%]
500	-0.96	-1.21	0.63	21.17
1000	-1.40	-1.77	0.92	20.84
1500	-1.74	-2.21	1.15	21.43
2000	-1.98	-2.54	1.32	22.00

Table 4.3. NP AveP measurements for the different load magnitudes of uniaxial compression, namely 500N, 1000N, 1500N and 2000N.

Loadcase [N]	NP AvePi [MPa]	NP AvePf [MPa]	RPV [%]
500	0.46	0.41	11.14
1000	0.83	0.74	10.47
1500	1.20	1.08	10.05
2000	1.57	1.42	9.48

The relative increase of the DHV (positive RDHV) for 500N is about 21% (from -0.96 to -1.21mm, which means progressive loss of IVD height), which is also verified for the other three loadcases. The evolution of the SHR values reveals that the relative difference between each loadcase is inversely proportional to the increase of the load, i.e., the difference between the 500N and 1000N loadcases is 0.29% and the difference between the 1500N and 2000N loadcases is 0.17%. One might have predicted that the SHR value for 2000N would be four times the SHR value for 500N (2.53% instead of 1.32%), but when the load becomes exaggerated, the IVD starts to reach its physiological and anatomical limits. The osmotic component of the native IVD is an important feature for this type of regulatory and protective effect, as well as the AF fibers. In what concerns the NP AveP results (presented in Figure 4.11b) and Table 4.3), the applied loads are in agreement with the load profiles of the daily activities studied by Wilke et al.

(1999). The curves of NP AveP versus time have similar evolutions, varying from 0.83MPa to 0.74MPa for 1000N, 1.20MPa to 1.08MPa for 1500N and 1.57 to 1.42MPa for 2000N. Consequently, the relative decrease of the NP AveP in 15mins is averagely 10% (negative RPV) for the four loadcases, which is consistent with the model's response to the aforementioned 500N load. In fact, these outcomes are in agreement with the work of Schmidt et al. (2010) whose numerical model was also validated by in vivo and in vitro data. In addition, the similarity in the evolution of NP AveP as a function of load is aligned with the previously discussed consistency on the RDHV values.

4.3.4. Other configurations

In order to consolidate the validation of the current model, other two material configurations were tested, following the protocol of holding a 500N load during 15mins. The pre-conditioning and the load application periods were also unaltered. Firstly, only the permeability parameters (K_0^* and M) for the IVD components were altered. The new values are the ones provided by Argoubi and Shirazi-Adl (1996). Secondly, the Neo-Hookean model[x] was chosen to describe the isotropic part of the IVD ground substances. The characteristic Neo-Hookean parameters (μ and K) and the permeability parameters were updated based on the work of Schmidt et al. (2013). Table 4.4 shows the values of the parameters for these two different configurations. All the other parameters, such as the osmotic swelling or viscoelastic properties, were unaltered[xi].

In addition, the numerical test of Schroeder et al. (2010) was also included in this comparison. The main differences between the current model and the one from Schroeder and co-workers are the applied FE solver and the material properties. This group used ABAQUS FE-package with user-defined materials[xii] and a composition-based material model, i.e., they used the measurable tissue composition from in-house experimental studies directly as an input for the numerical simulations.

The comparison between the experimental outcomes from Heuer et al. (2007), the outcomes from the current MS model, the alternative configurations and the numerical outcomes

[x] The Neo-Hookean model is properly described in the 3rd chapter.
[xi] The material properties are listed on Table 3.1.
[xii] Which included the osmotic swelling model of Wilson et al. (2005).

from Schroeder et al. (2010) is shown in Figure 4.12. DHV (Figure 4.12a)) and NP AveP (Figure 4.12b)) were assessed.

Table 4.4. Alternative material configurations.

			NP	AF	CEP
Argoubi and Shirazi-Adl (1996)	Permeability	K_0^* [mm^4.N^{-1}.s^{-1}]	3.0e-4	3.0e-4	7.0e-3
		M	10.00	12.00	10.00
Schmidt et al. (2013)	Isotropy	G [MPa]	1.34	2.46	2.14
		K [MPa]	0.81	2.91	2.53
	Permeability	K_0^* [mm^4.N^{-1}.s^{-1}]	2.13e-3	3.0e-4	7.0e-3
		M	10.00	12.00	10.00

Figure 4.12 shows that some important differences may occur if the material properties are changed. The standard simulation achieved -1.21mm of DHV and 0.41MPa of NP AveP. On the one hand, the slight differences between the "original" permeability parameters and the ones of Argoubi and Shirazi-Adl (1996) have little effect on the behavior of the model. For this case, the final DHV is -1.15mm and the final NP AveP is 0.41MPa. On the other hand, the parameters provided by Schmidt et al. (2013) resulted on largely different outcomes, in comparison with the standard simulations. The IVD model is clearly stiffer in this situation, which is perceptible on the DHV final value of -0.43mm and also on the NP AveP final value of 0.34MPa.

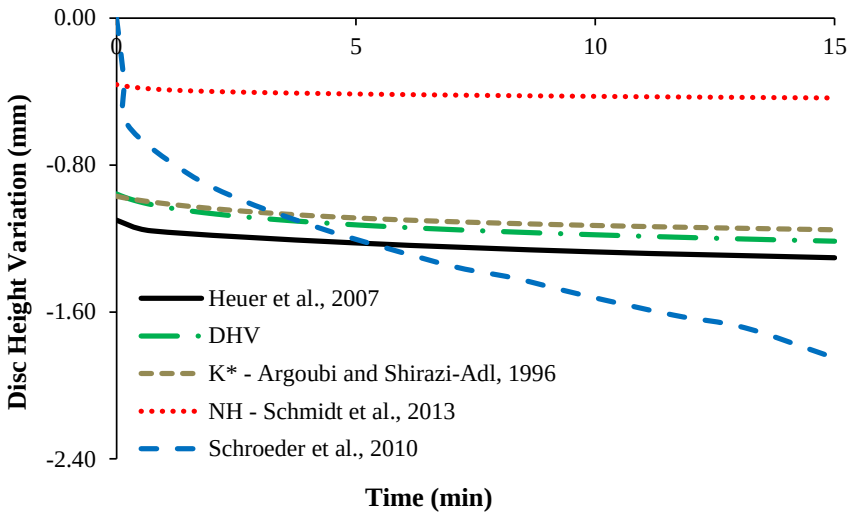

a)

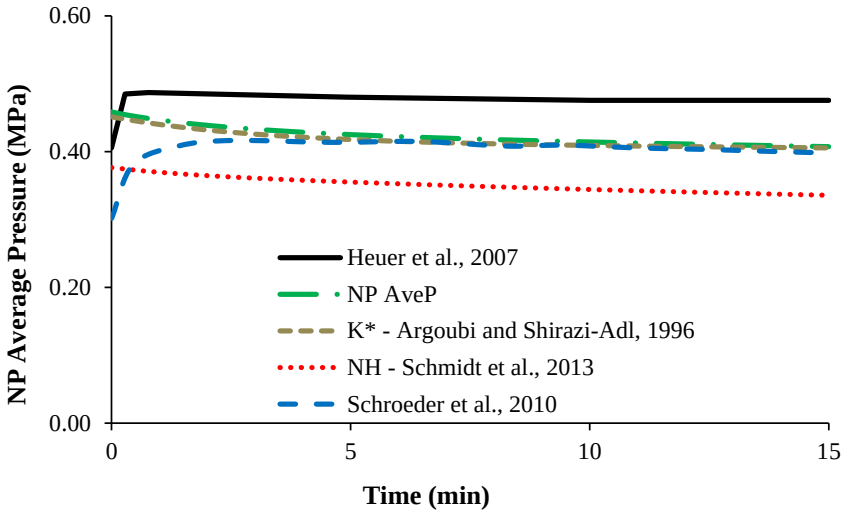

b)

Figure 4.12. Simulated creep test during 15min at 500N of uniaxial compression. The FE model was configured with three different sets of material properties (standard parameters, permeability parameters from Argoubi and Shirazi-Adl (1996) and material parameters from Schmidt et al. (2013)) and the outcomes were compared with the experimental results of Heuer et al. (2007) and also with the numerical results of Schroeder et al. (2010). Assessed outcomes: a) DHV; b) NP AveP.

The Neo-Hookean parameters probably have major influence in the analyzed outcomes, in comparison with the permeability properties. Regarding the outcomes of the two alternative configurations, one may assume that the standard material parameters deliver the best approximation to the experiment of Heuer and co-workers.

Finally, Schroeder et al. (2010) numerically achieved -1.85mm of DHV and 0.40MPa of IDP in the end of the 15mins. The NP AveP curve presented on that work (Figure 4.12b)) presents a similar evolution and a close final value (0.40MPa), but the evolution of the DHV (Figure 4.12a)) poles apart. The present MS model presents DHV curves with analogous evolution for the analyzed situations, regardless of the material properties.

The same analogous evolution is verified on Figure 4.7a) and Figure 4.11a), with different osmotic swelling approaches and varying loading profiles, respectively. The curve presented by Schroeder and co-workers has a very significant increase rate (RDHV of 82.12%, against 21.17% of the current standard simulation), which means that their IVD model is not capable of reaching stabilization after 15mins as it should. The osmotic swelling formulation is the same, but its implementation on ABAQUS® is inevitably different. In addition, their composition-based material model may also be contributing for the disclosed behavioral discrepancies.

4.3.5. Summary

The pressure and displacement outcomes are consistent among the different loading profiles, i.e., variables like NP AveP or (absolute) DHV increased when the load was also increased. This proves that the FE model has the ability of responding to harsh loading levels, but it also means that the numerical outcomes have to be carefully analyzed if one wants to identify the risk of overloading, as no damage laws were implemented.

The mesh convergence study proved that the innovative biphasic formulation implemented in the open-source home-developed FE solver is sufficiently accurate to describe the fluid exchanges and pressure gradients that occur within the IVD, with any of the three types of elements tested, i.e., Tet4, Tet10 and Hex27. The non-refined version of the mesh with these last elements is the most appropriate choice for the remaining work, as it means less computational effort, without prejudice for the numerical results.

Finally, the comparison with the work of Schroeder et al. (2010) shows that the present model is even capable of producing more realistic outcomes than other models, which used commercial FE packages. Therefore, this section provided very satisfactory outcomes concerning the advantages of using the open-source home-developed FE solver.

4.4. References

Argoubi, M., Shirazi-Adl, A., 1996. Poroelastic creep response analysis of a lumbar motion segment in compression. J. Biomech. 29, 1331–9.

Eijkelkamp, M.F., van Donkelaar, C.C., Veldhuizen, A.G., van Horn, J.R., Huyghe, J.M., Verkerke, G.J., 2001. Requirements for an artificial intervertebral disc. Int. J. Artif. Organs 24, 311–21.

Galbusera, F., Schmidt, H., Noailly, J., Malandrino, A., Lacroix, D., Wilke, H.-J., Shirazi-Adl, A., 2011. Comparison of four methods to simulate swelling in poroelastic finite element models of intervertebral discs. J. Mech. Behav. Biomed. Mater. 4, 1234–41.

Goins, M.L., Wimberley, D.W., Yuan, P.S., Fitzhenry, L.N., Vaccaro, A.R., 2005. Nucleus pulposus replacement: an emerging technology. Spine J. 5, 317S–324S.

Heuer, F., Schmitt, H., Schmidt, H., Claes, L., Wilke, H.-J., 2007. Creep associated changes in intervertebral disc bulging obtained with a laser scanning device. Clin. Biomech. (Bristol, Avon) 22, 737–44.

Huyghe, J.M., 1986. Non-linear finite element models for the beating left ventricle and the intramyocardial coronary circulation.

Johannessen, W., Elliott, D.M., 2005. Effects of degeneration on the biphasic material properties of human nucleus pulposus in confined compression. Spine (Phila. Pa. 1976). 30, E724–9.

Joshi, A., Massey, C.J., Karduna, A., Vresilovic, E., Marcolongo, M., 2009. The effect of nucleus implant parameters on the compressive mechanics of the lumbar intervertebral disc: a finite element study. J. Biomed. Mater. Res. B. Appl. Biomater. 90, 596–607.

Krag, M.H., Cohen, M.C., Haugh, L.D., Pope, M.H., 1990. Body Height Change During Upright and Recumbent Posture. Spine (Phila. Pa. 1976). 15.

McMillan, D.W., Garbutt, G., Adams, M.A., 1996. Effect of sustained loading on the water content of intervertebral discs: implications for disc metabolism. Ann. Rheum. Dis. 55, 880–7.

O'Connell, G.D., Jacobs, N.T., Sen, S., Vresilovic, E.J., Elliott, D.M., 2011. Axial creep loading and unloaded recovery of the human intervertebral disc and the effect of degeneration. J. Mech. Behav. Biomed. Mater. 4, 933–42.

Oomens, C., van Campen, D.H., Grootenboer, H.J., 1987a. A mixture approach to the mechanics of skin. J. Biomech. 20, 877–885.

Oomens, C.W., van Campen, D.H., Grootenboer, H.J., 1987b. In vitro compression of a soft tissue layer on a rigid foundation. J. Biomech. 20, 923–35.

Périé, D., Korda, D., Iatridis, J.C., 2005. Confined compression experiments on bovine nucleus pulposus and annulus fibrosus: sensitivity of the experiment in the determination of compressive modulus and hydraulic permeability. J. Biomech. 38, 2164–71.

Pollintine, P., van Tunen, M., Luo, J., Brown, M., Dolan, P., Adams, M.A., 2010. Time-dependent compressive deformation of the ageing spine: relevance to spinal stenosis. Spine (Phila. Pa. 1976). 35, 386–94.

Sato, K., Kikuchi, S., Yonezawa, T., 1999. In vivo intradiscal pressure measurement in healthy individuals and in patients with ongoing back problems. Spine (Phila. Pa. 1976). 24, 2468–74.

Schmidt, H., Bashkuev, M., Galbusera, F., Wilke, H.-J., Shirazi-Adl, A., 2013. Finite element study of human lumbar disc nucleus replacements. Comput. Methods Biomech. Biomed. Engin.

Schmidt, H., Shirazi-Adl, A., Galbusera, F., Wilke, H.-J., 2010. Response analysis of the lumbar spine during regular daily activities–a finite element analysis. J. Biomech. 43, 1849–56.

Schroeder, Y., Huyghe, J.M., van Donkelaar, C.C., Ito, K., 2010. A biochemical/biophysical 3D FE intervertebral disc model. Biomech. Model. Mechanobiol. 9, 641–50.

Terzaghi, K., 1925. Principle of soil mechanics. Liepzig: Eng. News Record.

Terzaghi, K., 1943. Theoretical soil mechanics. John Wiley & Sons.

Wilke, H.-J., Neef, P., Caimi, M., Hoogland, T., Claes, L.E., 1999. New in vivo measurements of pressures in the intervertebral disc in daily life. Spine (Phila. Pa. 1976). 24, 755–62.

Williams, J.R., Natarajan, R.N., Andersson, G.B.J., 2007. Inclusion of regional poroelastic material properties better predicts biomechanical behavior of lumbar discs subjected to dynamic loading. J. Biomech. 40, 1981–7.

Wilson, W., van Donkelaar, C.C., Huyghe, J.M., 2005. A Comparison Between Mechano-Electrochemical and Biphasic Swelling Theories for Soft Hydrated Tissues. J. Biomech. Eng. 127, 158.

5. RESULTS AND DISCUSSION

This chapter presents the outcomes of the FE study. The lumbar IVD FE model was tested under several loading profiles, and the outcomes are here presented. These loading profiles are divided in pre-conditioning swelling periods and short and long creep tests. The last section also deals with the evaluation of previously unreleased experimental data from VUmc's bioreactor. The central purpose is to characterize the biomechanical behavior and functionality of the lumbar IVD, both in healthy and pathological conditions. The results are analyzed and discussed at the light of the current knowledge on IVD biomechanics.

5.1. Short Creep

The creep behavior of healthy Human IVD is here assessed and compared with experimental and numerical literature sources (Heuer et al., 2007; Joshi et al., 2009; O'Connell, Jacobs, et al., 2011; Schroeder et al., 2010; Tyrrell et al., 1985; Wilke et al., 1999; Williams et al., 2007), corresponding to short term tests[1]. Nonetheless, other studies regarding the non-degenerated behavior of the Human lumbar spine could also be in the scope of the current analysis, namely the works of Adams et al., (1990), Ferguson et al. (2004), Frei et al. (2002), Johannessen and Elliott (2005), Keller et al. (1987), McMillan et al. (1996), Pollintine et al. (2010), Sato et al. (1999), Schmidt et al. (2010) and Sivan et al. (2006).

As this chapter is devoted to the creep behavior evaluation, only (uni)axial compression loads are taken into consideration. However, compressive strain tests and the subsequent stress relaxation effects are also described by several sources in the literature (Ellingson and Nuckley, 2012; Iatridis et al., 1999; Périé et al., 2005; Yao and Gu, 2007).

[1] It must be reminded that short creep tests stand for loadcases that do not last more than 3h.

5.1.1. 800N, 20mins

The experimental test for *in-vivo* short creep evaluation of Human IVD performed by Tyrrell et al. (1985) was numerically reproduced by Williams et al. (2007). This test consisted on two steps of uniaxial unconfined compression, i.e., an 800N load was applied and held during 20mins and then reduced (and held) to 400N during 10mins. The referred protocol does not contain any reference to a pre-conditioning period, but the need for IVD pressurization before the actual numerical simulation starts was already defined in this work. Three different pre-conditioning situations were applied, for 1h: i) free swelling; ii) 200N loading and iii) 400N loading. Firstly, free swelling is the benchmark choice of the present work. Secondly, the 200N load was chosen due to the association with the native osmotic swelling pressure, also as described in the previous chapter. Finally, the 400N load is aligned with the experimental protocol, namely with the last 10mins of the test.

In addition, two different load protocols were tested: i) reduced load of 400N (1), as described originally by Tyrrell et al. (1985) and Williams et al. (2007), and ii) reduced load of 200N (2). This last option was also related to the native osmotic swelling pressure and native loading profiles for the recovery periods.

Therefore, six numerical simulations were performed and the percentage of SHR was compared with the results of SHR versus time obtained by Tyrrell et al. (1985) and Williams et al. (2007), first with the original protocol (Figure 5.1a)) and then with the reduced load of 200N (Figure 5.1b)). The numerical results obtained with the two reduced load protocols were compared in terms of SHR, NP AveP and OsmP, and presented in Figure 5.2. Figure 5.3 shows the comparison between NP AveP and OsmP of each pre-conditioning option, considering both reduced load protocols.

The numerical work of Williams et al. (2007) lead to noteworthy agreement with the experimental data from Tyrrell et al. (1985), on both stages of the present test. The current model showed good agreement with the experimental work on the first stage, but satisfactory results on the second stage were obtained only when the reduced load was 200N, instead of the original 400N reduced load. This fact is probably related with the differences on the initial osmotic pressure considered for the two models. In fact, the initial osmotic pressure considered by Williams' model is 0.36MPa, while the initial osmotic pressure considered in the current

model is 0.19MPa. The choice of the parameters for the calculus of the strain-dependent osmotic pressure gradient was based on the work of Galbusera et al. (2011), as defined in the previous chapter[ii]. In simple terms, the described adjustment of the reduced load in accordance with the osmotic properties allowed a good adjustment with both experimental and numerical references, which means that the current model is functioning as expected.

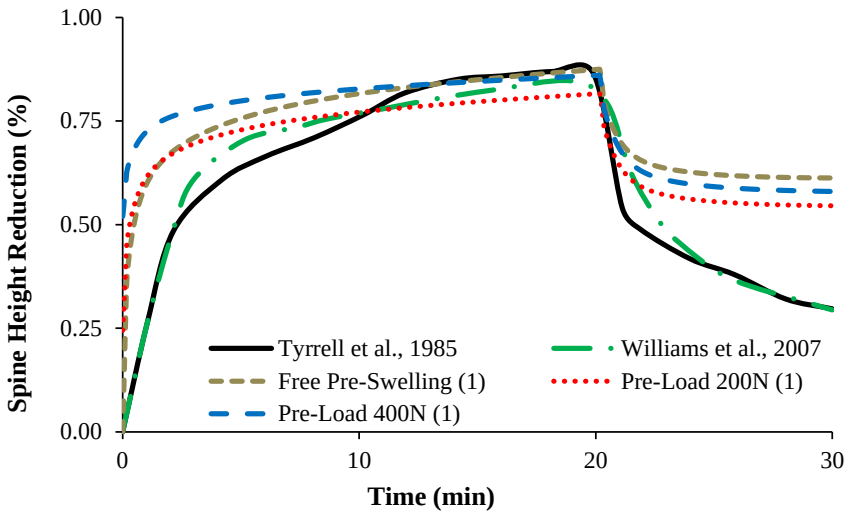

a)

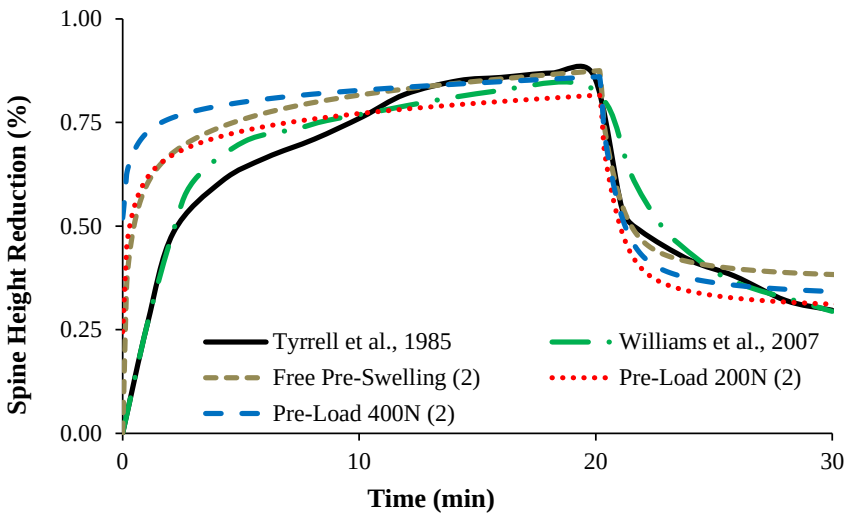

b)

Figure 5.1. Curves of SHR versus time: a) Comparison of the literature data (Tyrrell et al. (1985) and Williams et al. (2007)) with the numerical results of the three pre-conditioning options, applying the original protocol; b) Comparison of the literature data with the numerical results of the three pre-conditioning options, applying the adapted protocol with reduced load of 200N.

[ii] Other literature sources, such as Ferguson et al. (2004), Schroeder et al. (2006) or Urban and McMullin, (1988) also pointed out an OsmP value of approximately 0.20MPa for the healthy NP.

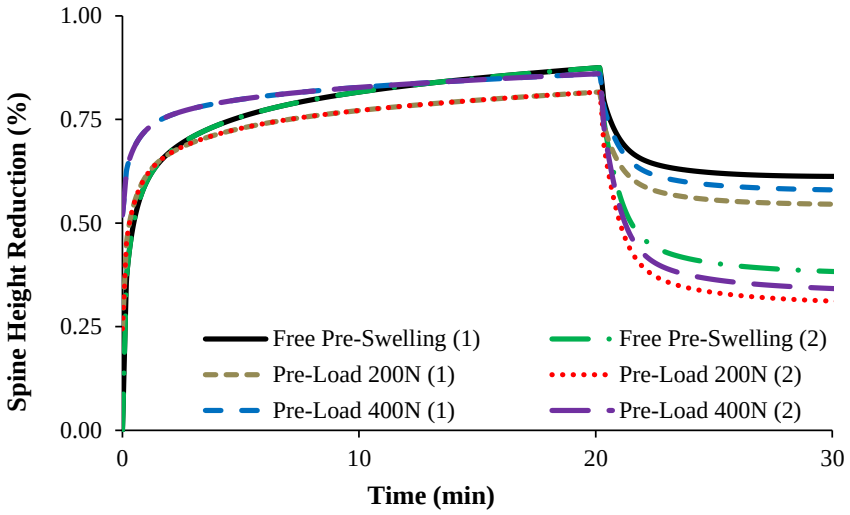

a)

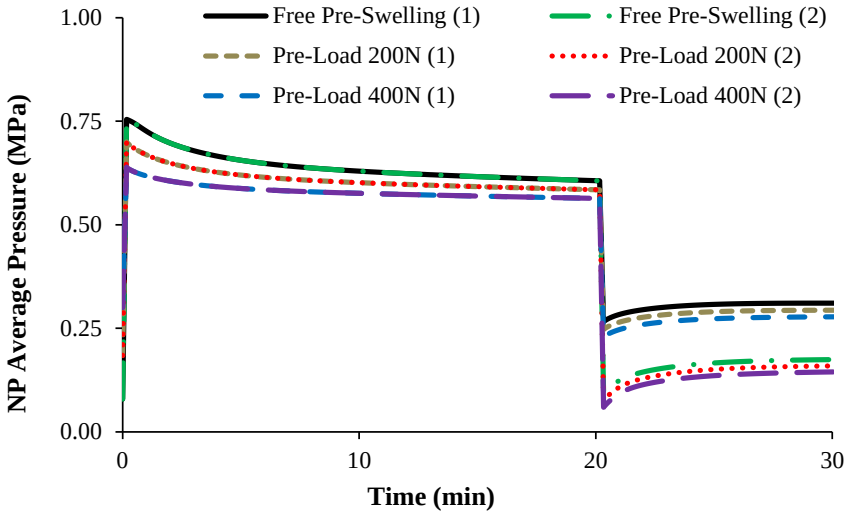

b)

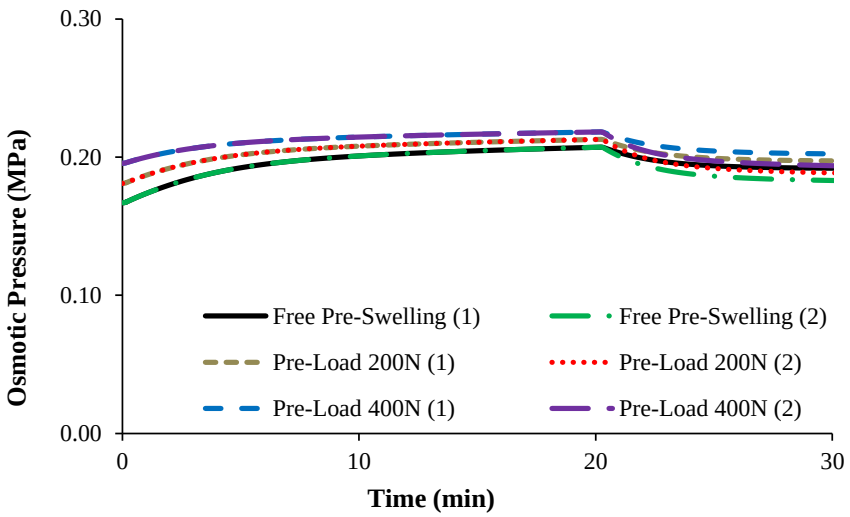

c)

Figure 5.2. Comparison between the outcomes of the six numerical simulations: a) SHR; b) NP AveP; c) OsmP.

The results of the modified protocol (2) are the ones to be compared with the works of Tyrrel and co-workers and Williams and co-workers. The top SHR calculated by Tyrrell et al. was 0.87%, while Williams et al. obtained 0.85%. Both free swelling and 400N pre-load situations presented good results (0.87% and 0.86%, respectively), while the 200N pre-loadcase presented a slightly inferior SHR value of 0.82%. In what concerns the final SHR values, Tyrrell et al. calculated 0.30%, while Williams et al. obtained 0.29%. The current model registered 0.38% for the free swelling case, 0.31% for the 200N pre-loadcase and, lastly, 0.34% for the 400N pre-loadcase. However, the SHR evolution of the 400N pre-loadcase is quite far from the references, particularly in the first 10mins of the test. The SHR initial value of this loadcase is different from 0% (0.52%), which was also registered for the 200N pre-loadcase (0.24%).

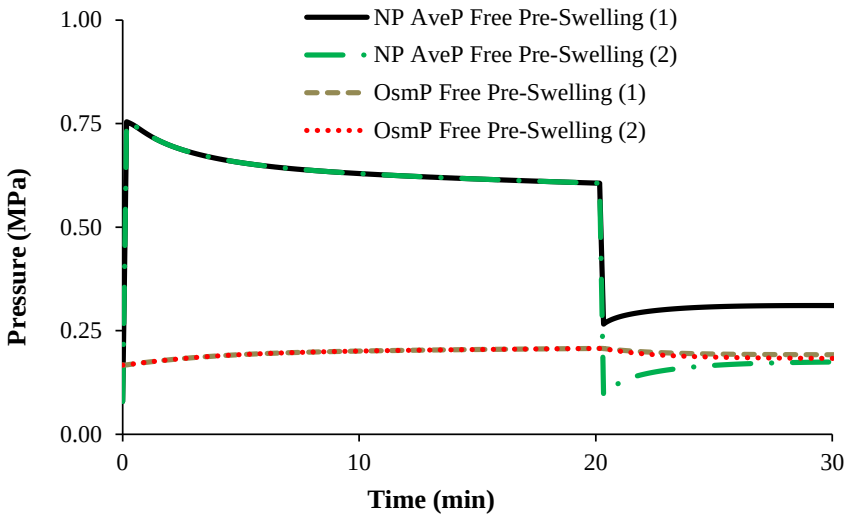

a)

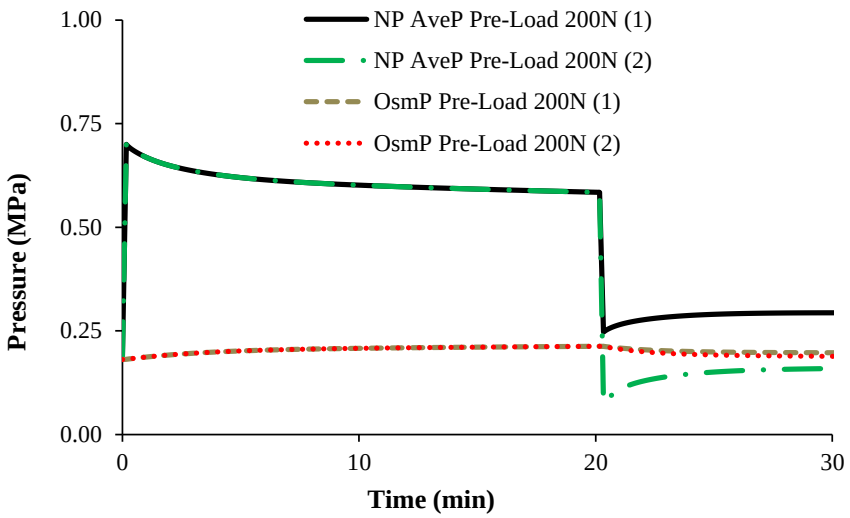

b)

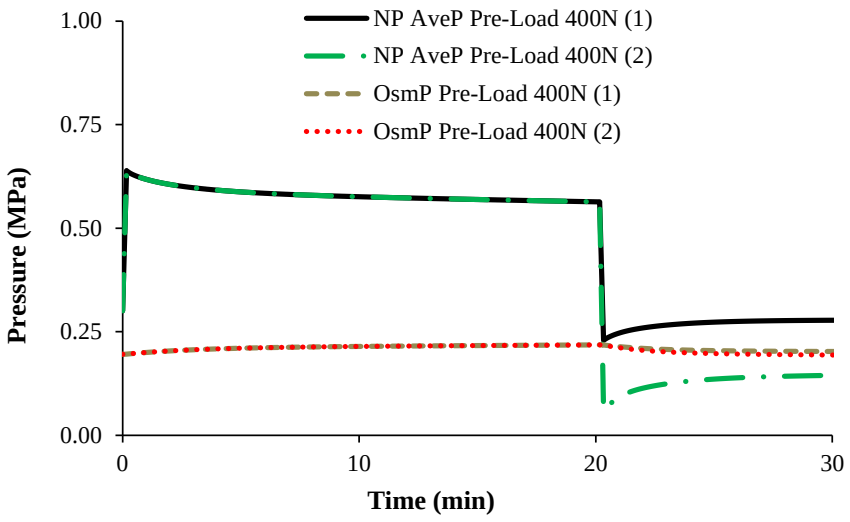

c)

Figure 5.3. Comparison between the pressure variables (NP AveP and OsmP) of the numerical simulations: a) Free Pre-Swelling; b) Pre-Load 200N; c) Pre-Load 400N.

The evolution of the free swelling case throughout the whole test is the closest to the references, as it starts from 0% of SHR, despite of having the most distant final value. These facts indicate that the two situations of loaded pre-conditioning produced slightly worse results than the free swelling option, which is coherent with previous findings.

The comparisons held on Figure 5.2 show the responsiveness of the model to the different loading profiles. Figure 5.2a) highlights the differences between the original and the modified protocols, which were previously discussed. Figure 5.2b) shows that the free swelling options present the highest value of NP AveP in the first stage (0.75MPa) and also the highest values in the end of both protocols (0.31 and 0.18MPa for the original and modified protocols, respectively). In what concerns the OsmP measurements (Figure 5.2c)), little differences are noticed between the different loading profiles. Nevertheless, the loading profile of free pre-swelling with reduced load of 200N ("Free Pre-Swelling (2)") presents an equilibrium between both analyzed pressure variables at the end of the test (Figure 5.3a)), which reinforces the indication that the modified protocol is well-matched with the IVD FE model properties and also that free swelling is the correct choice for the pre-conditioning period (as discussed earlier in this work). In fact, Figure 5.3b) and c) show a noticeable lag between NP AveP and OsmP for the "Pre-Load 200N (2)" and "Pre-Load 400N (2)" loading profiles, at the end of the test.

Figure 5.4 shows the average pressure distribution inside the MS FE model, at the end of the first stage (Figure 5.4a)) and the at the end of the test (Figure 5.4b)), for the "Free Pre-

Swelling (2)" loading profile. This profile was chosen because it represents the best fit with the literature data, as already discussed.

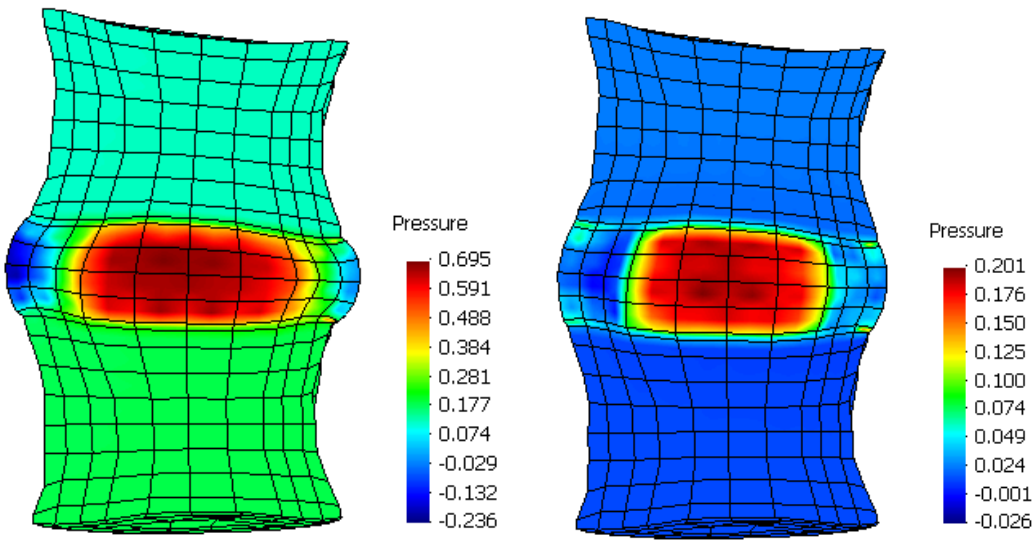

a) b)

Figure 5.4. Sagittal cut of the MS FE model, with the visualization of the (average) pressure distribution correspondent to the "Free Pre-Swelling (2)" loading profile: a) After the first stage; b) At the end of the test. The scale is presented on the images, and the pressure unit is MPa.

Figure 5.4 only represents the "Free Pre-Swelling (2)" loading profile, but the pressure distribution inside the MS FE model is similar on the six numerical simulations. A clear compressive effective (positive AveP) is noticed inside the NP. The other components of the MS present lower average pressure and a slight traction effect can be occurring on the inferior VB. The boundaries between the NP and the AF are well distinguishable, which means that the AF is stiffer than the NP and thus the pressure is lower in that area. Therefore, seems like the AF fibers are working efficaciously to the AF reinforcement and pressure control.

5.1.2. 2000N, at 1N/s

The final short creep test was performed in agreement with the experimental test of (O'Connell, Jacobs, et al., 2011), through a loading test with three stages, i.e., this test included a pre-

conditioning period of 1h (i), a ramp loading period (compressive uniaxial load) of 2000N at 1 N/s (ii) and a creep period (holding of the 2000N load) of 1h (iii). Figure 5.5a) shows the evolution of the IVD height versus the applied load. Figure 5.5b) shows the evolution of both intradiscal and osmotic pressures in the center of the NP. Figure 5.5c) shows the relative evolution of the volume of the three IVD components. Lastly, Figure 5.5d) shows the percentage of AF fibers on each level of stretch. These values were assessed at the end of the test. The stretch (λ) is defined as follows:

$$\lambda = \frac{l}{L} \qquad 5.1$$

Where l is the final length of the fiber and L is its initial length. Stretch values lower than 1 mean that the fibers are under compression, while stretch values higher than 1 mean that the fibers are under traction. In addition, Figure 5.6 shows the average pressure distribution inside the MS FE model, at the end of each of the three stages. This information is complementary to the "Time vs. NP AveP" curve of Figure 5.5b).

This final test also showed the expected IVD behavior. After the ramp loading period, the DHV is 2.55mm and the NP AveP is 1.45MPa (Figure 5.5a) and b)). The comparison of these values with the results of the previous tests indicates that the loading rate influences the stress-state of the IVD, but only in what concerns to the pressure measurements. It must be highlighted that the NP AveP is lower than the OsmP during the first hour of the test (Figure 5.5b)), due to the free swelling conditions.

On the one hand, this "initial" NP AveP is lower than the NP AveP measured after loading for the loadcase of 2000N during 15mins (1.57MPa). The final NP AveP is 1.32MPa, which is in agreement with the data from Wilke et al. (1999). The evolution of both intradiscal and osmotic pressures reveals a straight response to the applied load, from the pre-conditioning to the creep period. On the other hand, the presented DHV signifies an average reduction of 20% of the initial IVD height and 1.33% of SHR, which are similar outcomes to the ones of the loadcase of 2000N during 15mins. Nevertheless, at the end of the extended creep period, the DHV is 3.29mm or 26% of the initial IVD height. These measurements are in good agreement with the 23% of average axial compression experimentally determined by O'Connell et al. (2011), but they probably represent an overloading effect (Paul et al., 2013).

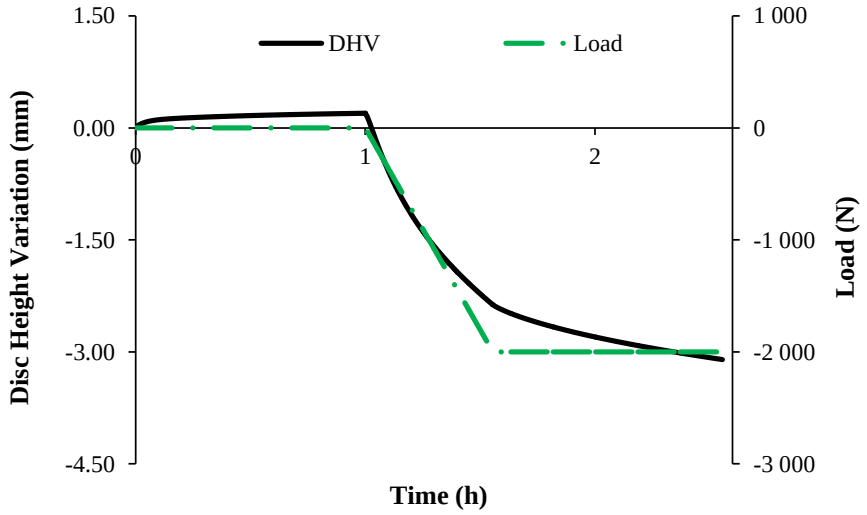
1.50
0.00
-1.50
-3.00
-4.50
Disc Height Variation (mm)
DHV
Load
1 000
0
-1 000
-2 000
-3 000
Load (N)
0
1
2
Time (h)

a)

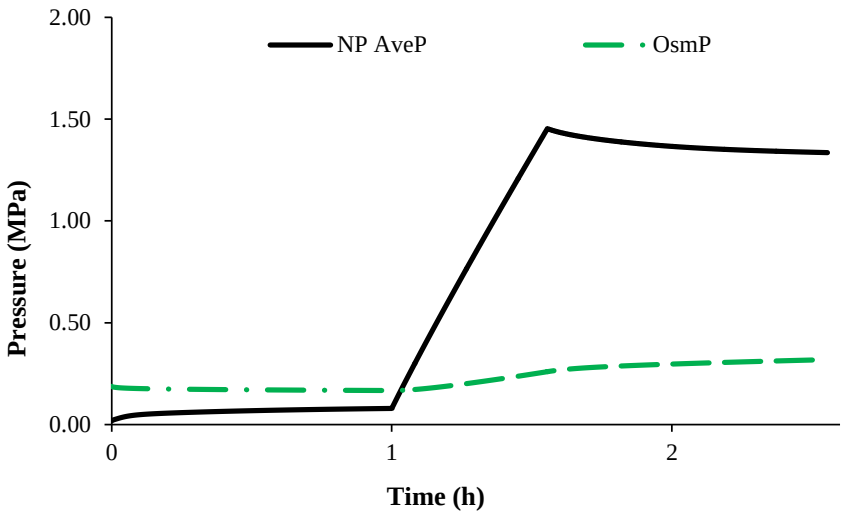
2.00
1.50
1.00
0.50
0.00
Pressure (MPa)
NP AveP
OsmP
0
1
2
Time (h)

b)

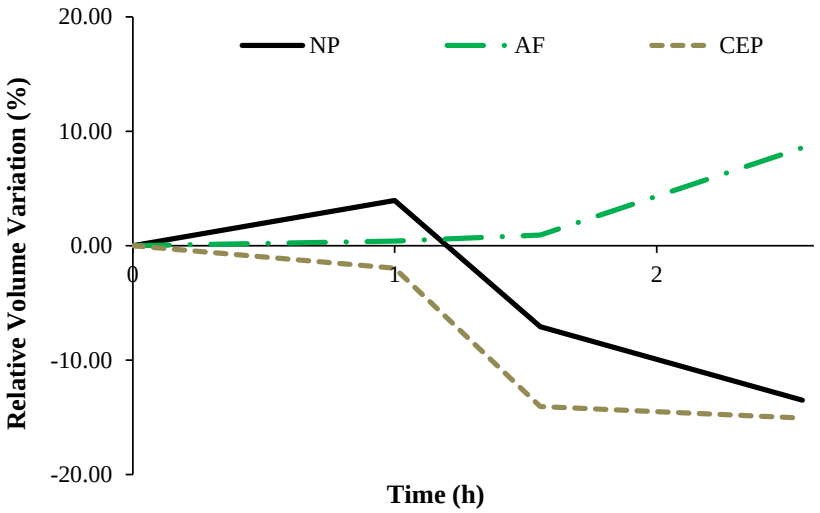
20.00
10.00
0.00
-10.00
-20.00
Relative Volume Variation (%)
NP
AF
CEP
0
1
2
Time (h)

c)

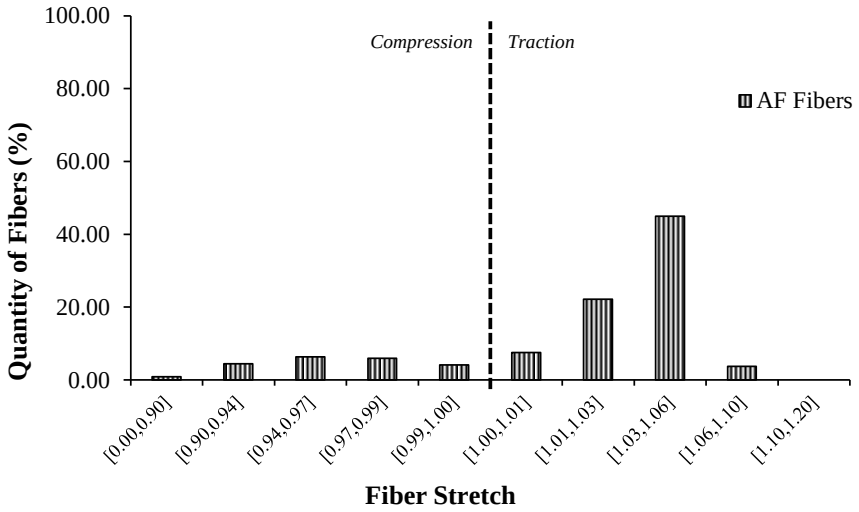

d)

Figure 5.5. Three stages loading test, involving: i) a pre-conditioning period, ii) a loading period of 2000N at 1 N/s and, finally, iii) a creep stage. The following parameters were assessed, considering the full length of the test: a) DHV versus loading scheme; b) NP AveP and Osmotic Pressure of the NP (OsmP); c) Volume variation of the three IVD components (NP, AF and CEP); d) Relative distribution of AF fibers by its stretch, at the end of the test. The distinction between the compression and traction zones is signaled.

Figure 5.5c) shows that both NP and CEP were losing volume during the loading phases of this test. The final relative volume variation values were -13.5% and- 15.1%, respectively. In contrast, the volume of the AF is increasing throughout the test (8.6% of relative volume variation). This volume increase is due to the fluid flow and pressure gradients within the IVD.

The physiological direction of the flow is from the CEP into the inner structures of the IVD, so volume variations outcomes are most likely in accordance with the literature (Ferguson et al., 2004). The same explanation may be valid to justify the high percentage of AF fibers under tension (stretch values higher than 1), as seen in Figure 5.5d). In fact, the AF is bulging and its fibers are stretched, which gives the impression that the axial compression of the FE model is occurring as expected (Eberlein et al., 2004; Holzapfel et al., 2005).

Figure 5.6 confirms that the 2000N compression is excessive for the MS. Figure 5.6b) shows a clear bulging effect after the ramp loading, even if it does not seem exaggerated. However, after 1h of sustained 2000N loading (Figure 5.6c)), the bulging is visibly non healthy, as the IVD becomes highly deformed. Nevertheless, the NP still contains most of the pressure, in comparison with the other MS components. The combined analysis of these outcomes (Figure

5.5 and Figure 5.6) shows that the IVD may be able to bear up the ramp loading of 2000N at 1N/s. In that period, the numerical outcomes are inside the range of the results from the work of O'Connell et al. (2011), even if the overloading effect is already noticeable. Moreover, the sustainment of those 2000N for 1h is noticeably out of the physiological range.

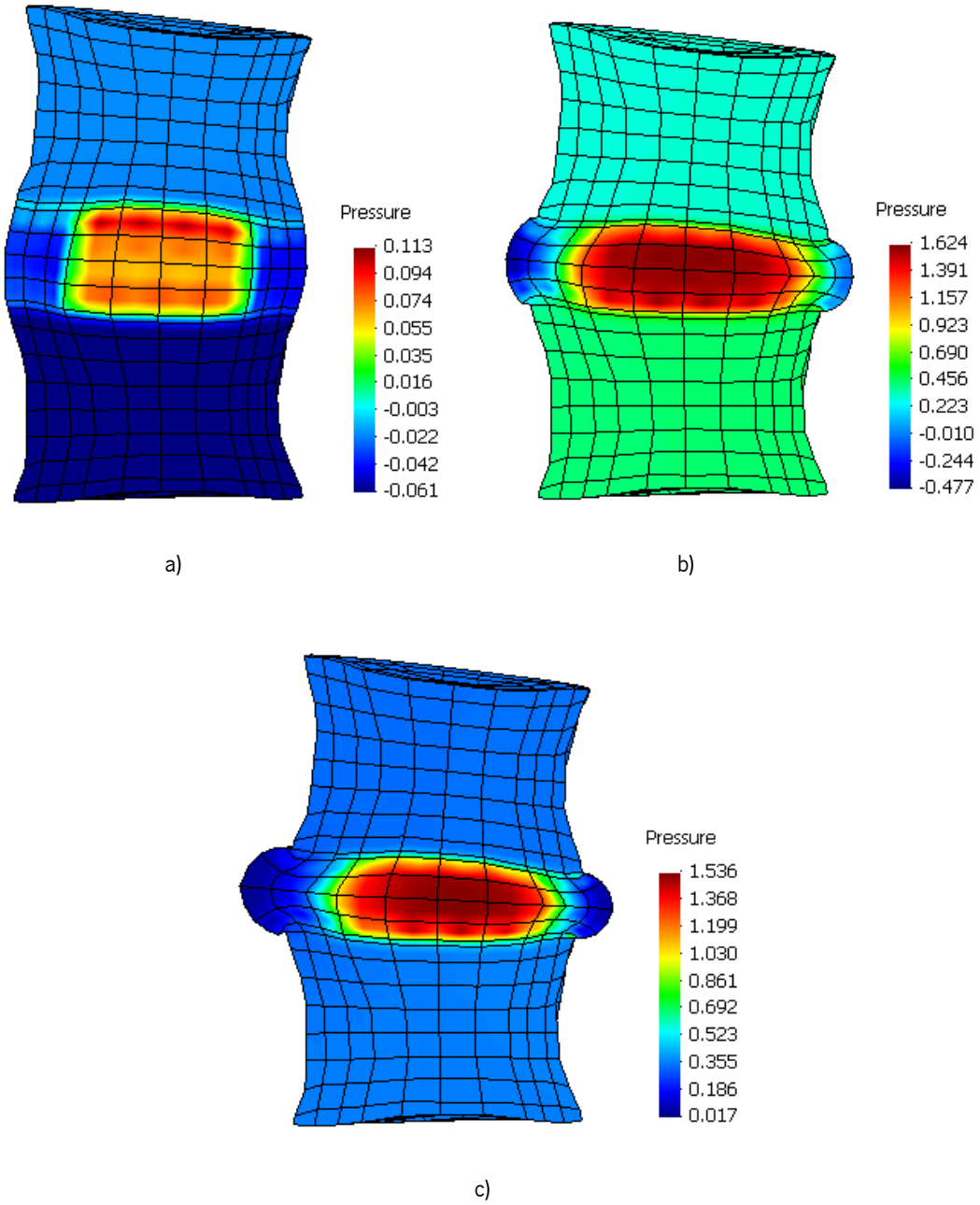

Figure 5.6. Sagittal cuts of the MS FE model, at the end of each one of the three stages: a) After the pre-conditioning; b) After the ramp loading; c) At the end of the test, after the creep phase. The average pressure distribution inside the model is shown. The scale is presented on the images, and the pressure unit is MPa.

5.1.3. Summary

The short creep tests here presented show that the behavior of the native MS FE model is aligned with experimental and numerical literature data, which means that the selected material parameters and the innovative biphasic formulation and the models implemented for the description of strain-dependent permeability, biphasic osmotic swelling, fibers anisotropy and viscoelasticity have proved to be valid for the FE simulation of the physiological IVD behavior.

The comparison with the work of (O'Connell, Jacobs, et al., 2011) and the tests with increasing load magnitude allowed to conclude that loads higher than 1000N are potentially harmful for the IVD, particularly when these efforts are prolonged on time[III]. Some tests with loadcases over 2000N can still be found in the literature (Eijkelkamp et al., 2001; Li and Wang, 2006; White and Panjabi, 1990)[IV], but such efforts are clearly exaggerated and do not reflect the loading range of the native Human IVD.

The next step is to perform longer tests, which can express the circadian variations of the IVD behavior.

[III] For very harsh loadcases, even a few seconds may be enough to cause damages on the spine.

[IV] Natarajan et al. (2007) pointed out that the Human spine is probably capable of bearing 4000N loads, for acute/extreme efforts.

5.2. Long Creep

Several loading profiles were tested and compared, in order to understand the physiological and biomechanical behavior of the IVD during 48h, in which two recovery periods (8h each) and two activity periods (16h each) were included. This section also includes comparisons of the numerical outcomes with selected literature data.

The first recovery period also serves the purpose of pre-conditioning or adaptation to the load, as described on the "Swelling Periods" section of the previous chapter. The loads were applied during 60s and then held through the duration of the period. Four resting loads were considered, namely 200N, 250N, 350N and 500N. In what concerns the activity periods, 500N, 600N, 700N, 850N and 1000N loads were tested. The denomination of the loadcase is given by the magnitude of the loads, i.e., "200-500N" means that the resting load is 200N (for 8h) and the activity load is 500N (16h), repeated twice.

5.2.1. 200-500N

This loading profile partially reproduces the test implemented by Galbusera et al. (2011). Figure 5.7 shows the outcomes of the current model and the comparison with the reference work, whenever data is available[v]. DHV (Figure 5.7a)), pressure variables (IDP, OsmP and NP AveP - Figure 5.7b)) and volume variation (Figure 5.7c)) are presented.

The DHV results suggest that the current model is working analogously to the model of Galbusera and co-workers, even if the comparison may only be held for the second day. The maximum axial displacement of -1.53mm is also inside the range of the studies of Schmidt et al. (2013, 2011), correspondent to 16h of 500N of axial compression. However, in what concerns the pressure measurements, the current model seems to be more accurate on the prediction of the osmotic component. Firstly, as described earlier, the 200N rest load seems to be adjusted to

[v] The work of Galbusera et al. (2011) considers a different approach for the first day, so the comparison may only be held for the second day of the test.

the period of IVD recovery, as demonstrated by the pressure results for the initial 8h: the evolution of both NP AveP and the OsmP is very similar. Secondly, on the second resting period, between the 24th and 32th hours, the NP AveP and the OsmP components tend to the equilibrium and their final values are almost equal (around 0.175MPa), as expected. Then, as was also expected, the IDP gets equilibrated with the OsmP. The top value of 0.43MPa and the creep effect during the activity period are consistent with the studies of (Frei et al., 2002; Heuer et al., 2007; Schmidt et al., 2011; Schroeder et al., 2010) on NP internal pressure evaluation. In what concerns the volume variation, the volume of the NP increases during the resting periods and diminishes during the activity periods, associated with the variations on the IVD height, which seems to be mostly caused by the fluid flow.

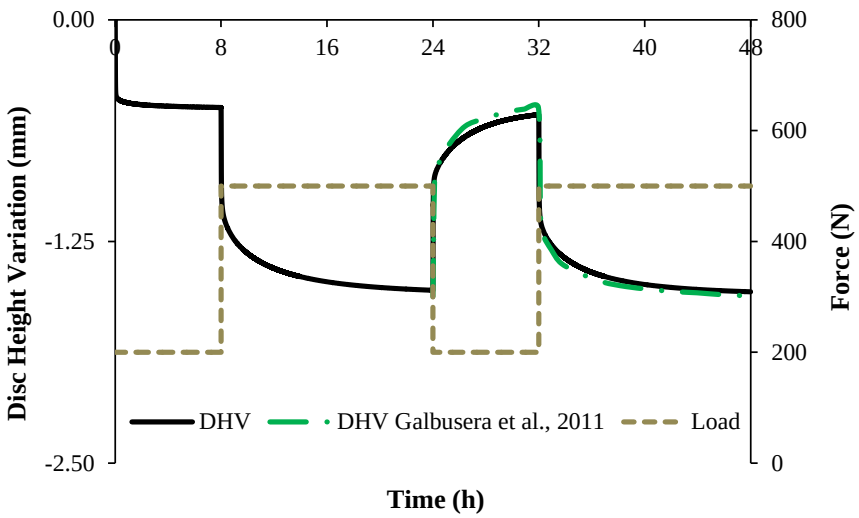

a)

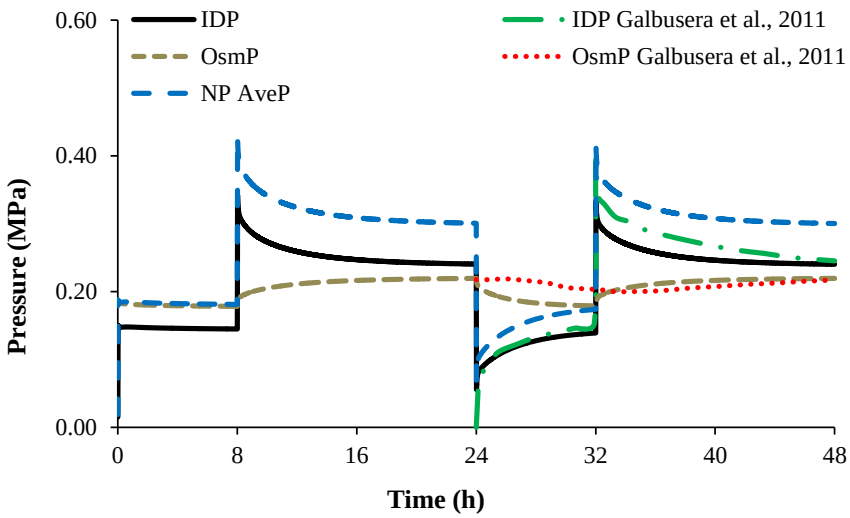

b)

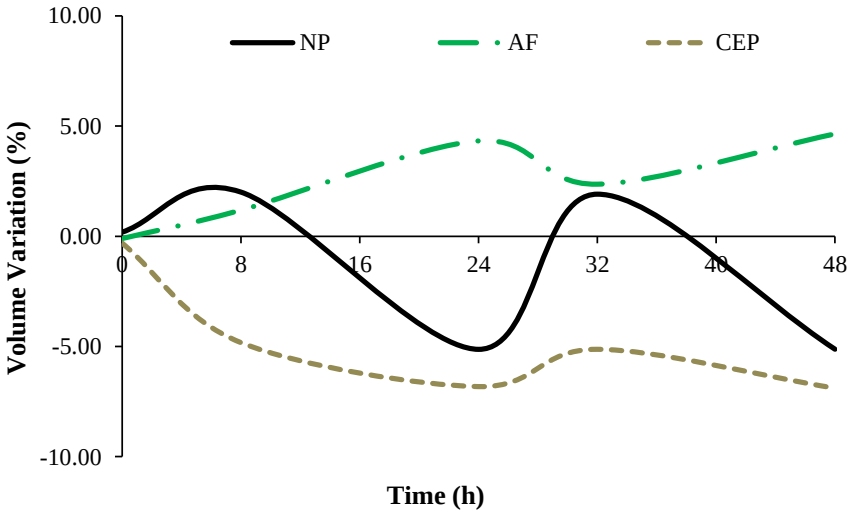

c)

Figure 5.7. Results of the 200-500N loading profile, along 48h: a) DHV vs. Load; c) Pressure variables (IDP, OsmP and NP AveP); c) Volume variation. The comparison with the work of Galbusera et al. (2011) is held between 24 and 48h, for the DHV, IDP and OsmP variables.

The volume of the AF increases on the first 8h (pre-conditioning period), correspondingly to the bulging effect (Heuer et al., 2008). On the following 36h, the evolution of AF volume is related to the volume variation of the NP, as it increases on the activity periods and diminishes in the resting periods, i.e., the volume variation of the AF is inversely proportional to the volume variation of the NP, as theoretically expected (Ferguson et al., 2004; O'Connell, Jacobs, et al., 2011). Such proportionality may be explained by the fluid exchanges between these two components and also by the characteristic traction response of the AF fibers to the compressive loading, which cause AF bulging. Finally, the volume of the CEP diminishes along the test, probably due to the effects of the compressive load.

5.2.2. 200-600N

The literature points out that the non-harmless average activity load[vi] should be between 500 and 1000N (Galbusera et al., 2011; Schmidt et al., 2013; Tyrrell et al., 1985; Zander et al., 2010). The lowest end of this physiological range should probably between 500 and 600N, for low to

[vi] The activity load may also be referred to as the day-time load.

moderate activity days. In what concerns the resting load, 200 and 250N loads were already justified on the "Swelling Periods" section of the previous chapter. These loads are associated with the native osmotic pressure gradient, and thus are the most indicated for the simulation of the recovery periods. This statement was discussed and confirmed in the mentioned section. Figure 5.8 shows the outcomes of the 200-600N loading profile. In detail, DHV (Figure 5.8a)), pressure variables (IDP, OsmP and NP AveP - Figure 5.8b)) and volume variation (Figure 5.8c)) are presented. The global discussion on these outcomes will be held in the "Comparison #1" sub-section, where the present loadcase is compared with 200-500N and 250-600N loadcases, i.e., the other low to moderate circadian loading profiles.

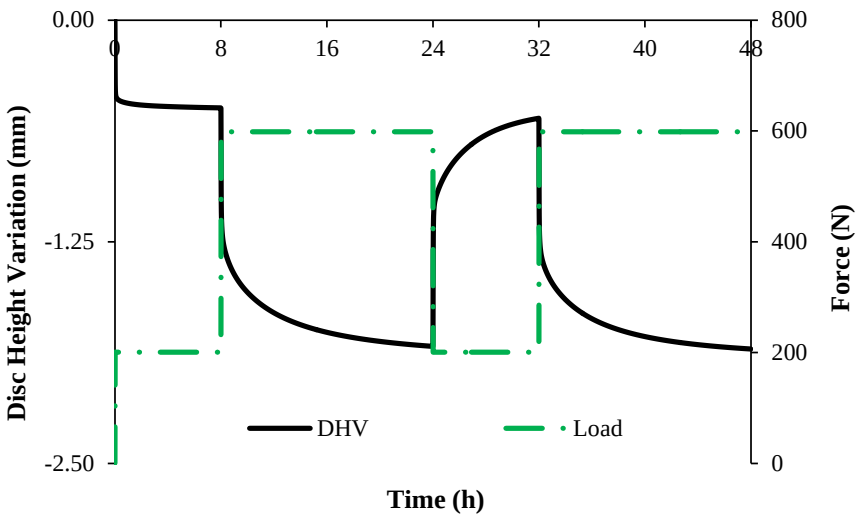

a)

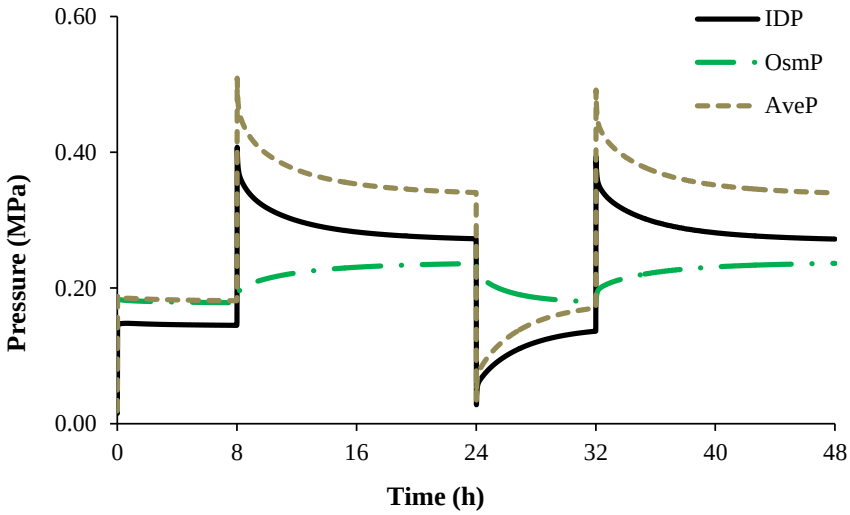

b)

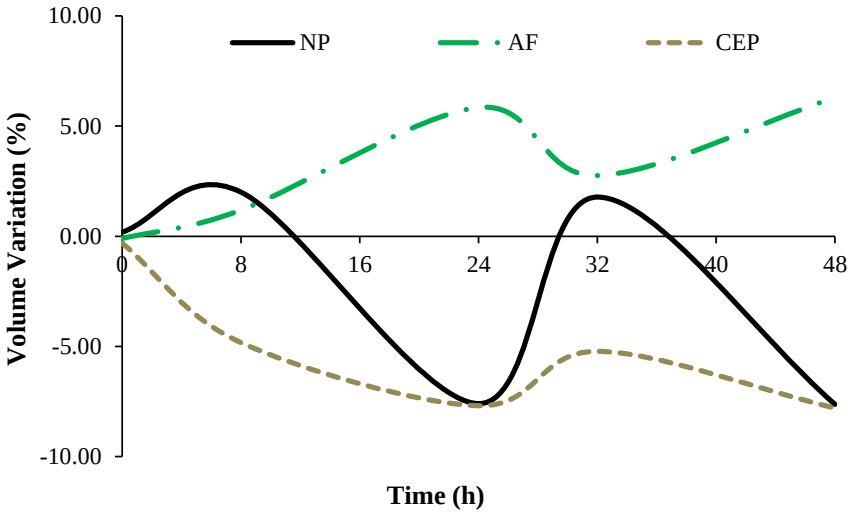

c)

Figure 5.8. Results of the 200-600N loading profile, along 48h: a) DHV vs. Load; c) Pressure variables (IDP, OsmP and NP AveP); c) Volume variation.

5.2.3. 250-600N

This loadcase is the last of the three low activity daily cycles. Therefore, Figure 5.9 shows the outcomes of the 250-600N loading profile, namely DHV (Figure 5.9a)), pressure variables (IDP, OsmP and NP AveP - Figure 5.9b)) and volume variation (Figure 5.9c)). The discussion on these outcomes will be held in the "Comparison #1" sub-section.

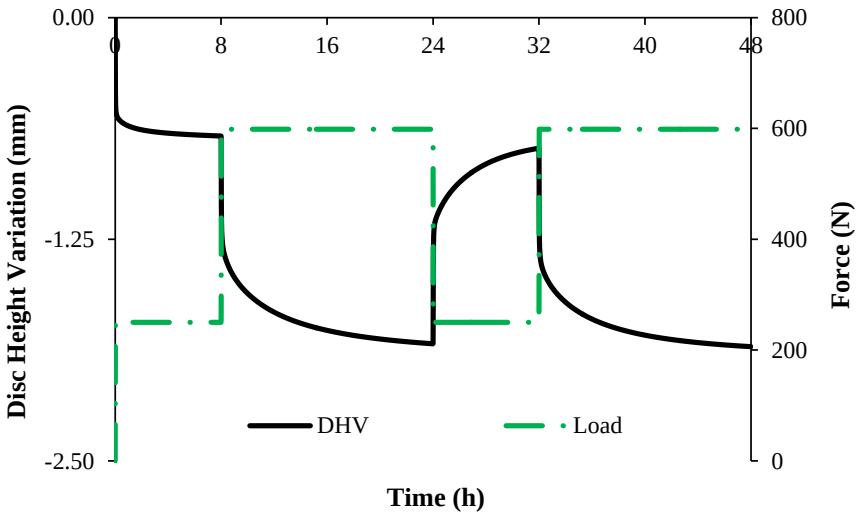

a)

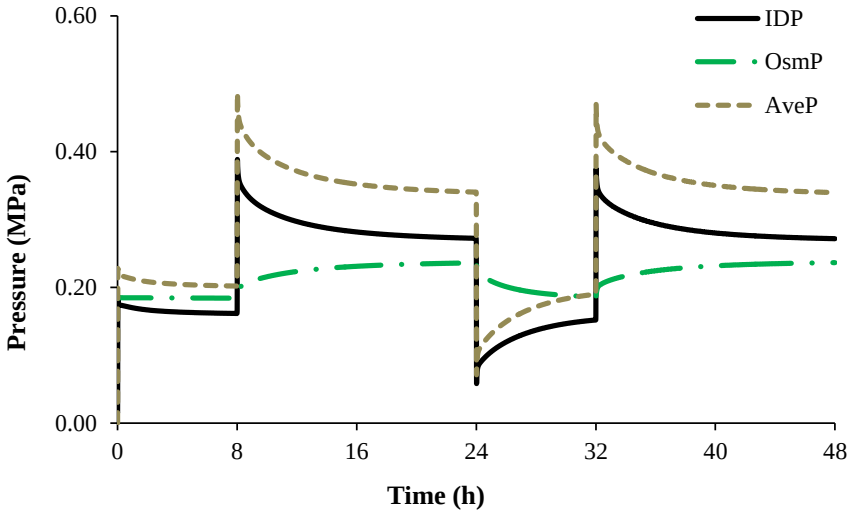

b)

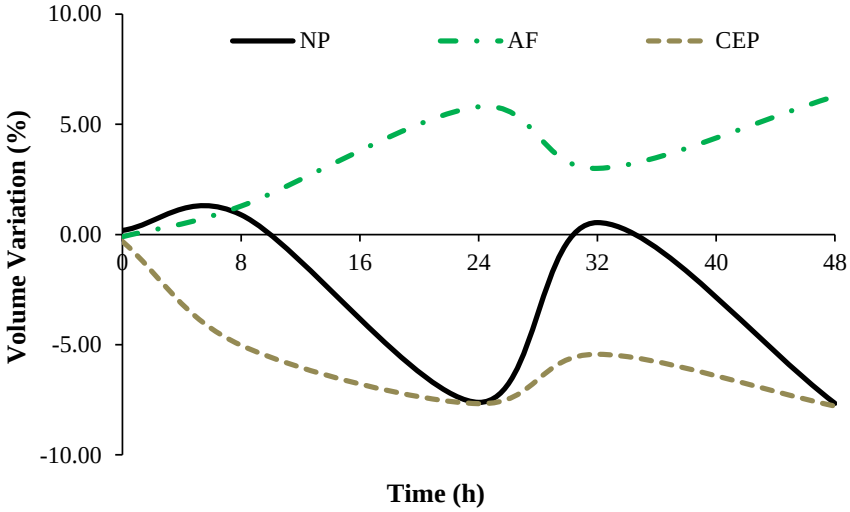

c)

Figure 5.9. Results of the 250-600N loading profile, along 48h: a) DHV vs. Load; c) Pressure variables (IDP, OsmP and NP AveP); c) Volume variation.

5.2.4. Comparison #1

Figure 5.10 shows the comparison between the outcomes of the three low to moderate daily cycles (200-500N, 200-600N and 250-600N), namely DHV (Figure 5.10a)), IDP (Figure 5.10b)), OsmP (Figure 5.10c)) and NP AveP (Figure 5.10d)). These three circadian loading profiles intended to simulate the physiological stimulation on the Human spine during a regular day, without promoting any overloading or IVD degeneration.

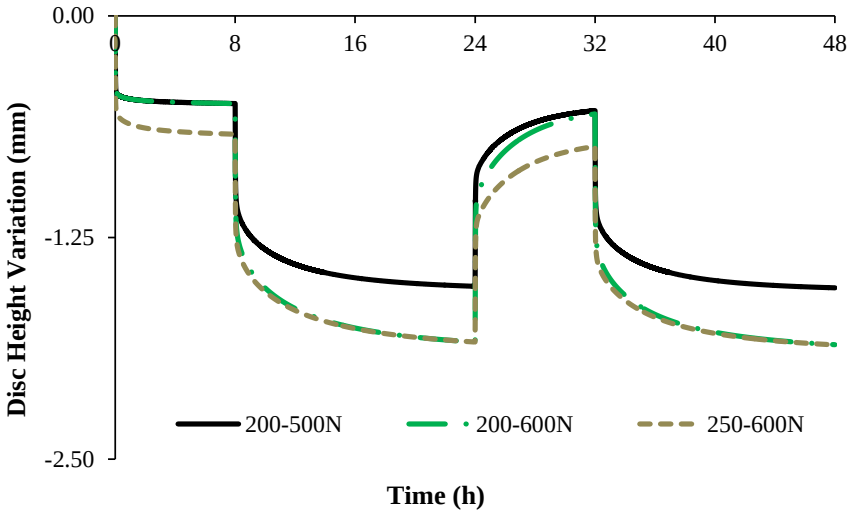
0.00
-1.25
-2.50
0
8
16
24
32
40
48
Disc Height Variation (mm)
200-500N
200-600N
250-600N
Time (h)

a)

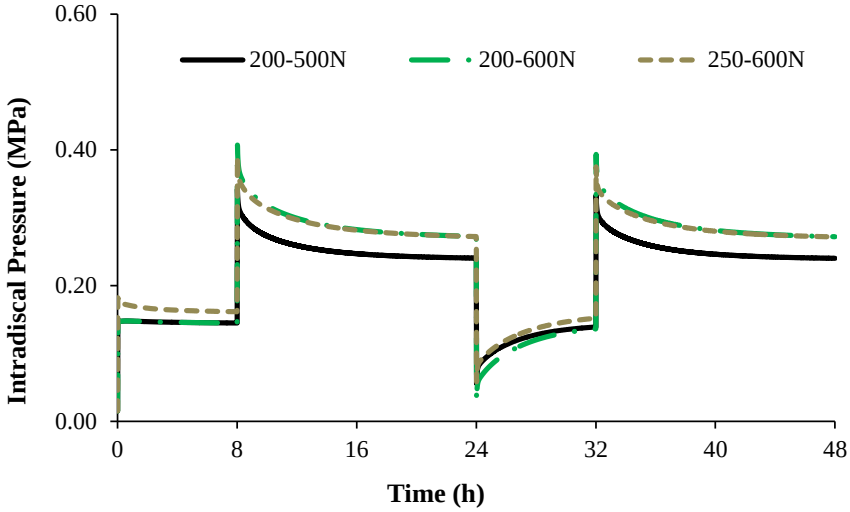
0.60
0.40
0.20
0.00
0
8
16
24
32
40
48
Intradiscal Pressure (MPa)
200-500N
200-600N
250-600N
Time (h)

b)

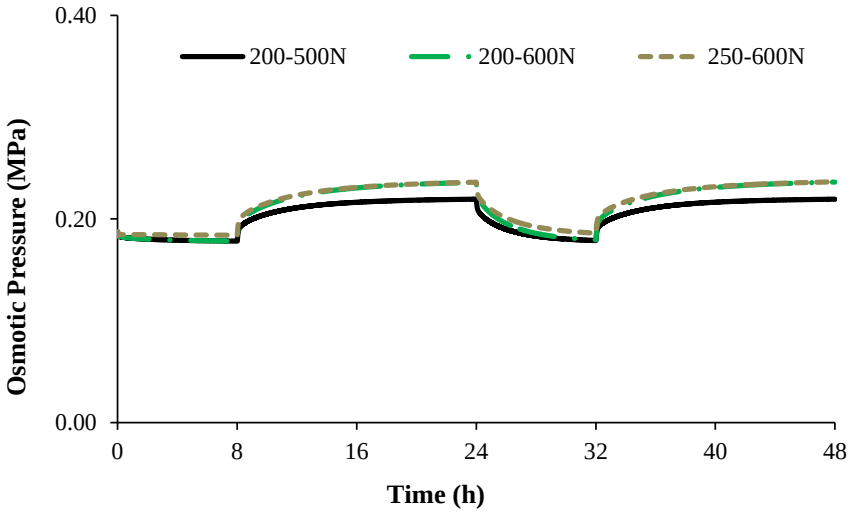
0.40
0.20
0.00
0
8
16
24
32
40
48
Osmotic Pressure (MPa)
200-500N
200-600N
250-600N
Time (h)

c)

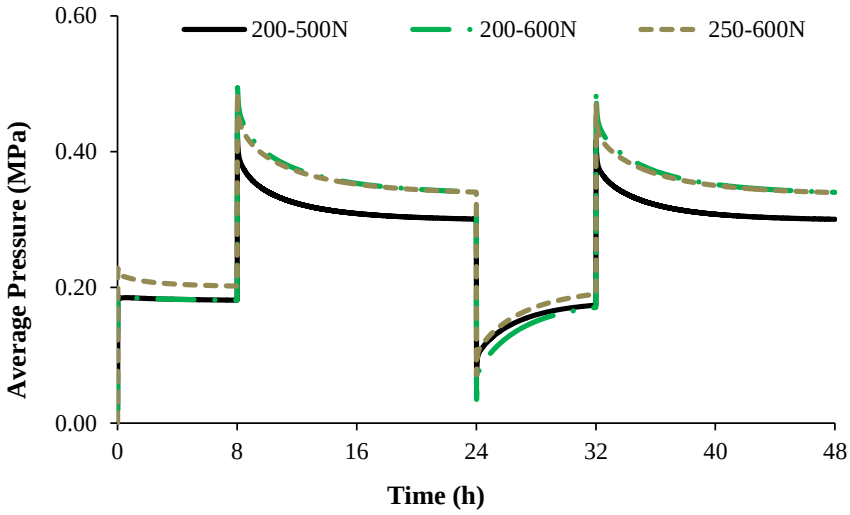

d)

Figure 5.10. Comparison between the three low activity daily cycles, namely 200-500N, 200-600N and 250-600N loadcases. a) DHV; b) IDP; c) OsmP; d) NP AveP.

From the results shown in Figure 5.7, Figure 5.8 and Figure 5.9, one may assume that the three low activity loading profiles seem to properly describe the daily routine of the Human lumbar spine, without any noticeable overloading effect.

The two loadcases with resting load of 200N present almost exactly the same DHV, IDP, OsmP and NP AveP values in the end of the 32th hour (approximately -0.53mm, 0.14MPa, 0.18MPa and 0.17MPa, respectively), while values of -0.74mm, 0.15MPa, 0.185MPa and 0.19MPa were measured for the 250-600N loadcase, for the same variables. The 200-600N loadcase has the highest load variation (400N), but the recovery velocity of the DHV curve is only slightly lower, in comparison with the 200-500N loadcase (300N of load variation). Due to this higher load variation, the pressure variation is also higher, which is noticeable in the end of the 24th hour, on the IDP and NP AveP curves. The two loadcases with activity load of 600N show similar behavior in the end of the 24th and 48th hours, which supports the non-overloading assumption. The NP AveP for these two loadcases is approximately 0.33MPa in the end of the 24th hour and 0.34MPa in the end of the test, while a value of 0.30MPa was measured on both time periods for the 200-500N loadcase.

Altogether, the relative increase in the resting load was solely 25% and the analogous increase on the activity load was even lower (20%). The described outcomes indicate that the MS FE model is highly sensitive to the changes on the load's magnitude. At the same time, the

loading history seems to influence the velocity of stabilization of the IVD model, but not the displacement and pressure measurements after stabilization. This postulation is only valid for non-overloading situations.

5.2.5. 250-700N

As abovementioned, literature sources suggested other loadcases to describe the loading daily routine. Crossing such references with the previous obtained data[VII], three other situations were tested, using the resting load of 250N and three higher levels of activity load (700, 850 and 1000N). These three situations were analyzed individually and then compared between each other. The 250-600N loadcase was also compared with the abovementioned loadcases. The objective for such comparison is to understand the IVD response to different top loads, while applying the same physiological recovery conditions.

Figure 5.11 shows the outcomes of the 250-700N loading profile, namely DHV (Figure 5.11a)), pressure variables (IDP, OsmP and NP AveP - Figure 5.11b)) and volume variation (Figure 5.11c)). The discussion on these outcomes will be held in the "Comparison #2" sub-section, which will aggregate these moderate to harsh loadcases. The 700N load was selected based on the works of (Adams et al., 1990; Sato et al., 1999).

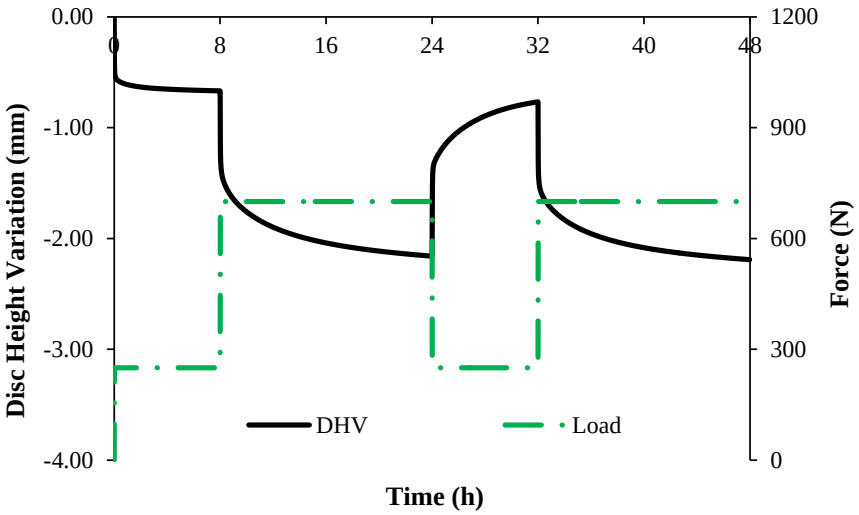

a)

[VII] From the "Swelling Periods" section and also from "Comparison #1" sub-section.

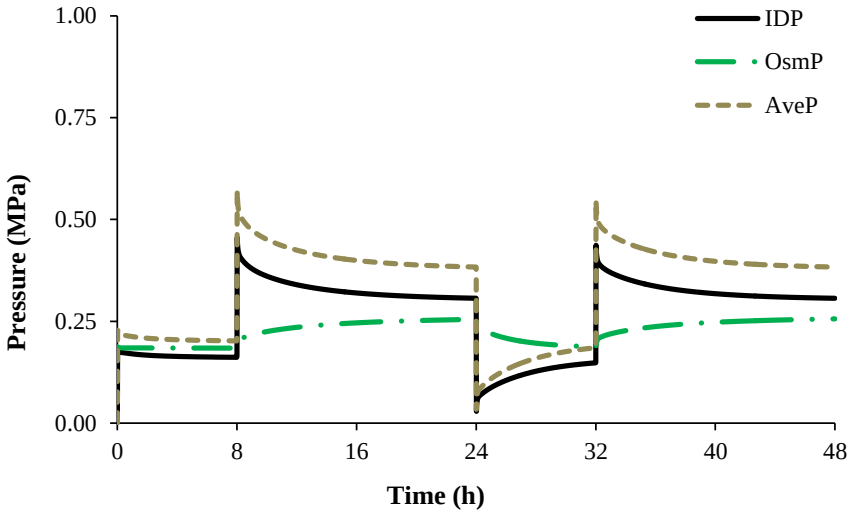

b)

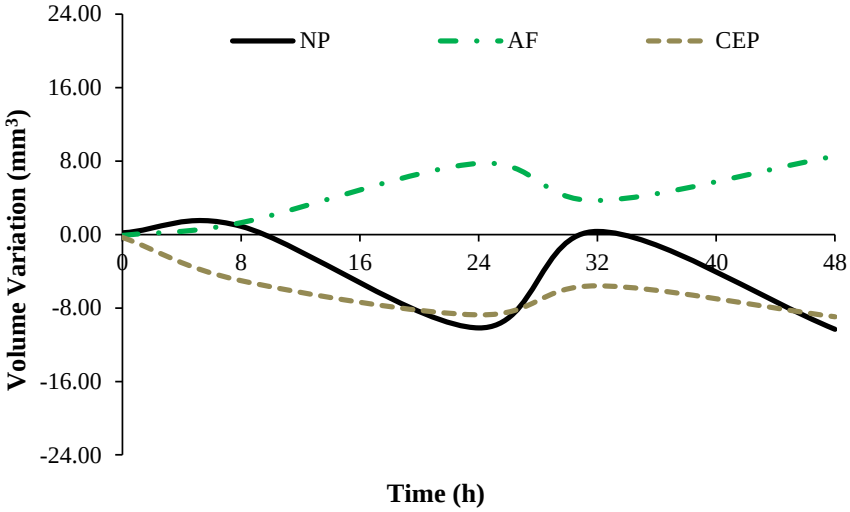

c)

Figure 5.11. Results of the 250-700N loading profile, along 48h: a) DHV vs. Load; c) Pressure variables (IDP, OsmP and NP AveP); c) Volume variation.

5.2.6. 250-850N

Figure 5.12 shows the outcomes of the 250-850N loading profile, namely DHV (Figure 5.12a)), pressure variables (IDP, OsmP and NP AveP - Figure 5.12b)) and volume variation (Figure 5.12c)). As abovementioned, since this is a moderate circadian loading profile, the discussion on its outcomes will be held in the "Comparison #2" sub-section. The 850N load was selected based on the work of (Tyrrell et al., 1985).

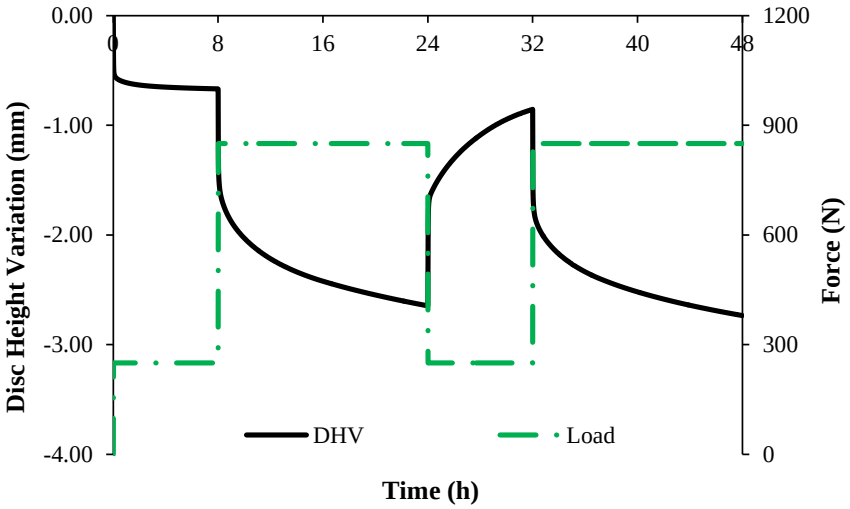

a)

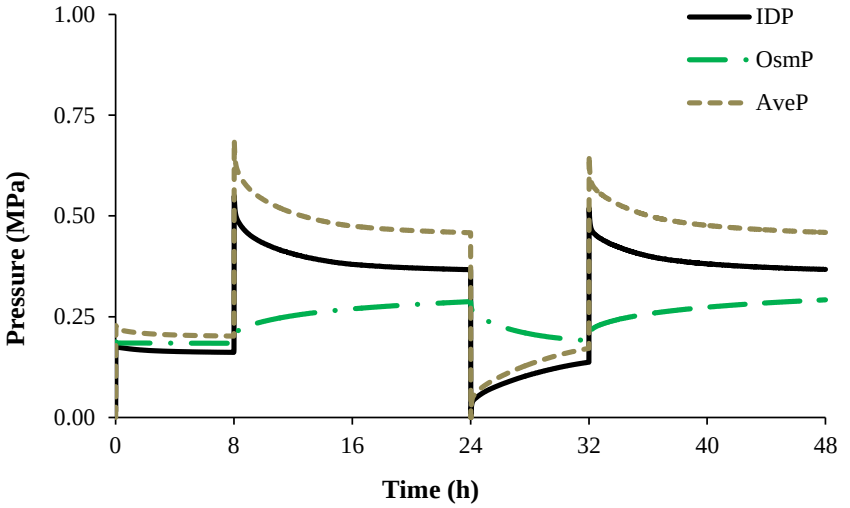

b)

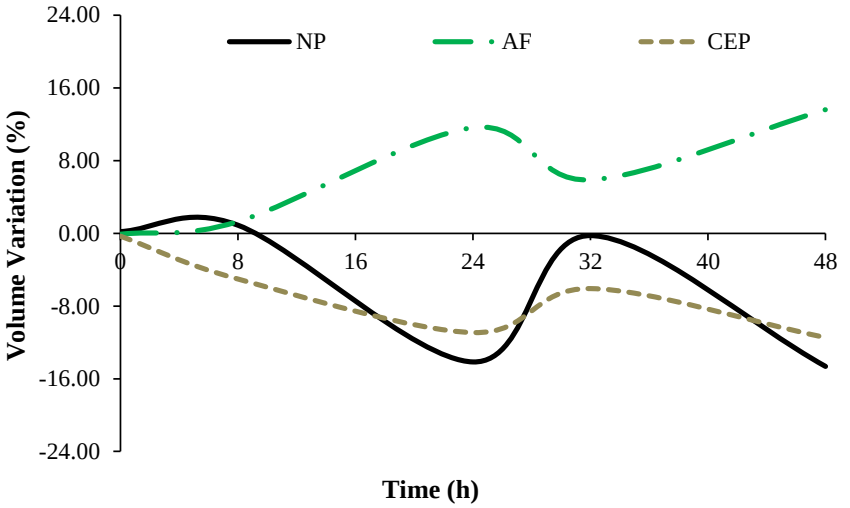

c)

Figure 5.12. Results of the 250-850N loading profile, along 48h: a) DHV vs. Load; c) Pressure variables (IDP, OsmP and NP AveP); c) Volume variation.

5.2.7. 250-1000N

Figure 5.13 shows the outcomes of the 250-1000N loading profile, namely DHV (Figure 5.13a)), pressure variables (IDP, OsmP and NP AveP - Figure 5.13b)) and volume variation (Figure 5.13c)). The discussion on these outcomes will be held in the "Comparison #2" sub-section.

This loadcase represents the border line between the moderate to the harsh circadian loading profiles, even if several contemporary works pointed out this 1000N load as the regular activity load (Galbusera et al., 2011; Joshi et al., 2009; Malandrino et al., 2009; O'Connell, Jacobs, et al., 2011; Schmidt et al., 2013; van den Broek et al., 2012).

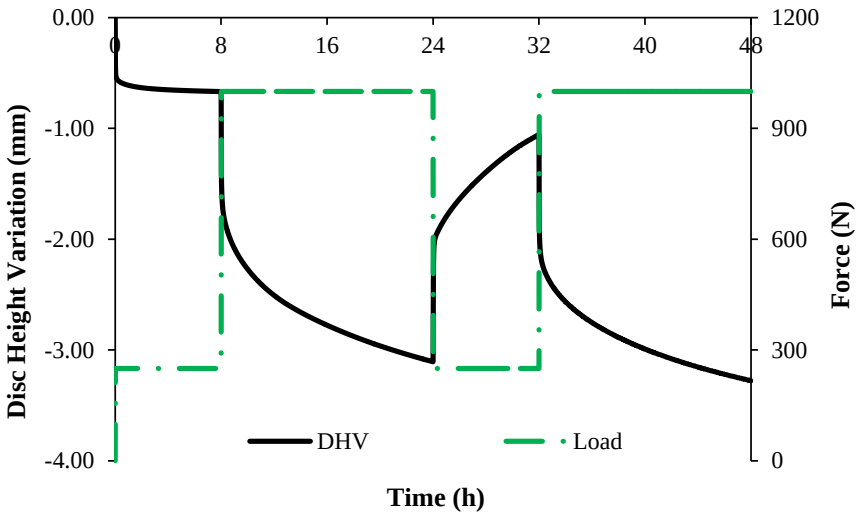

a)

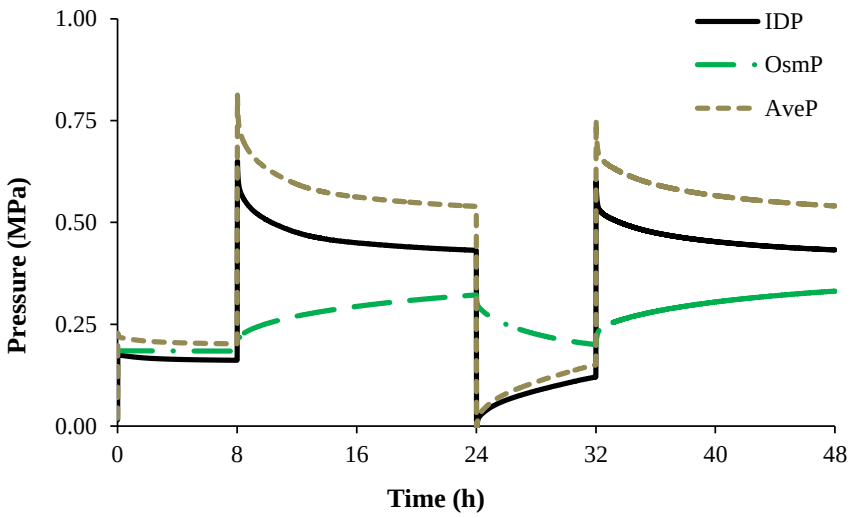

b)

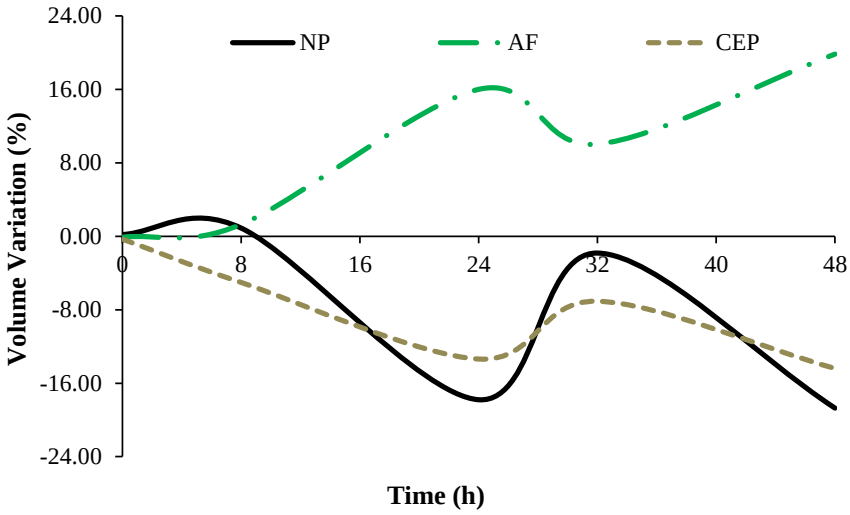

c)

Figure 5.13. Results of the 250-1000N loading profile, along 48h: a) DHV vs. Load; c) Pressure variables (IDP, OsmP and NP AveP); c) Volume variation.

5.2.8. Comparison #2

Figure 5.14 contains the global comparison between the four loading profiles with resting load of 250N, from 600 to 1000N of activity load. DHV (Figure 5.14a)), IDP (Figure 5.14b)), OsmP (Figure 5.14c)) and NP AveP (Figure 5.14d)) are evaluated. Table 5.1 summarizes the maximum values of DHV and IDP for each loadcase.

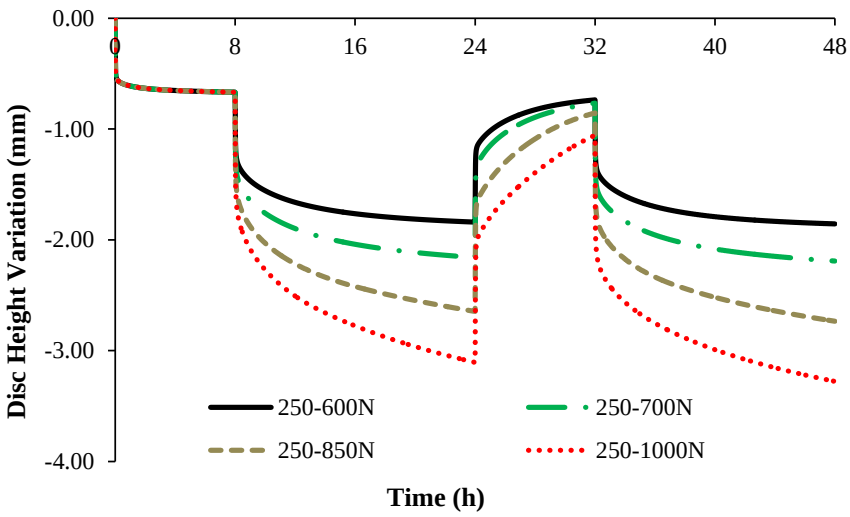

a)

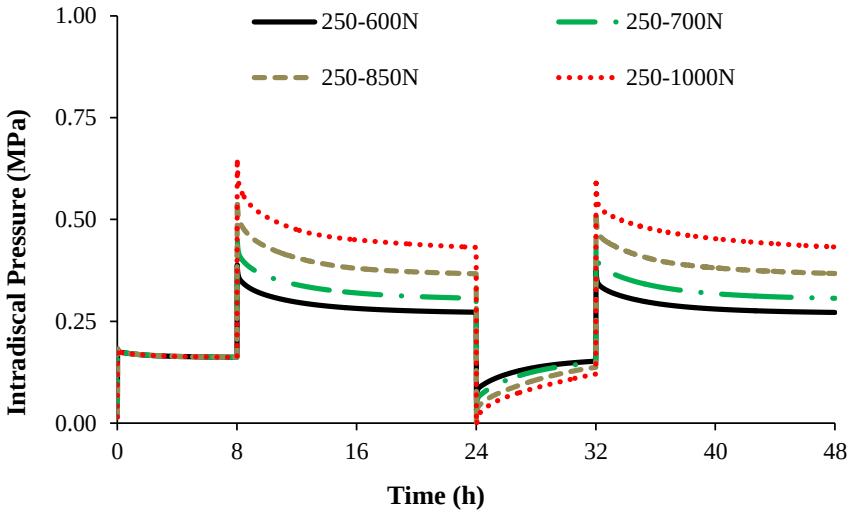

b)

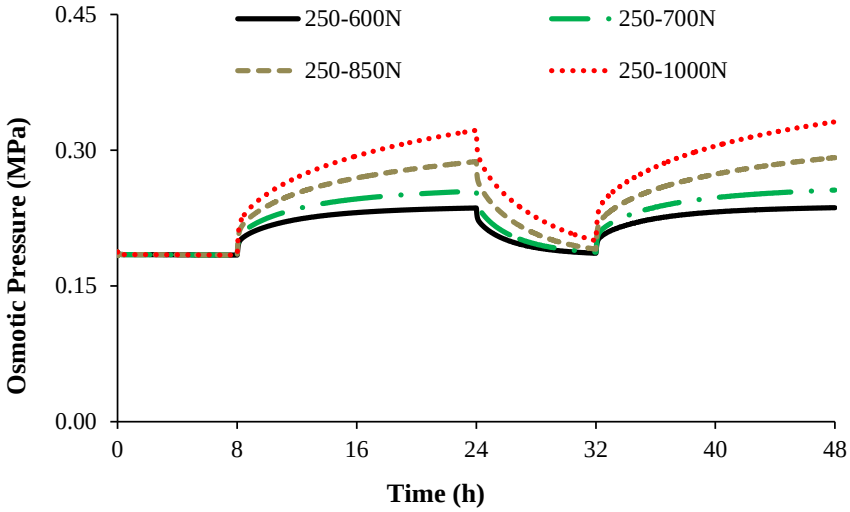

c)

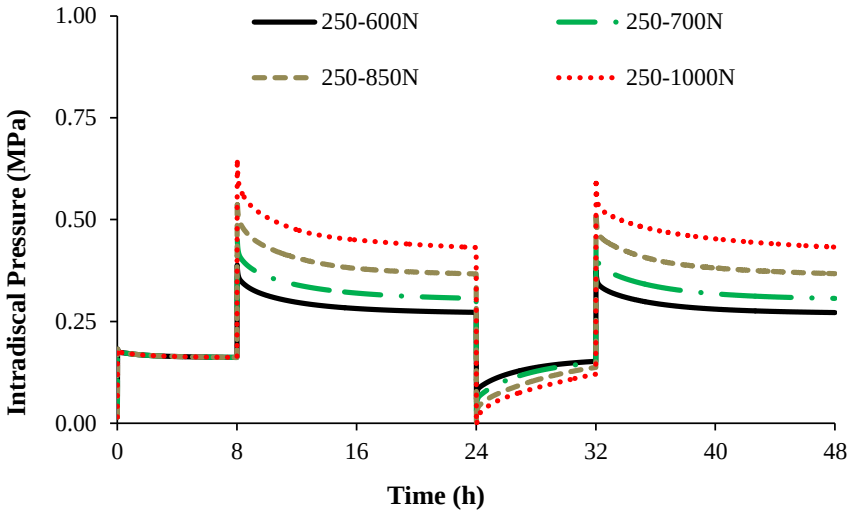

d)

Figure 5.14. Comparison between the four moderate to harsh activity daily cycles, namely 250-{600, 700, 850, 1000}N loadcases. a) DHV; b) IDP; c) OsmP; d) NP AveP.

Table 5.1. Maximum values of DHV and IDP, for the four moderate to harsh activity daily cycles, namely 250-{600, 700, 850, 1000}N loadcases.

Loadcase [N]	DHVmax [mm]	IDPmax [MPa]
250-600	-1.85	0.39
250-700	-2.19	0.46
250-850	-2.73	0.55
250-1000	-3.28	0.65

The comparison between these four loading conditions seems to demonstrate that the IVD responds differently to different activity loads. The top values of DHV and IDP, shown on Table 5.1, are directly proportional to the magnitude of the load[VIII], which means that the model is very sensitive to loading variations, as theoretically expected (Natarajan et al., 2004). These values are also inside the range of literature data (Ferguson et al., 2004; Galbusera et al., 2011; Schmidt et al., 2013). However, as the recovery load was the same, the DHV and pressure behavior of the four tests is very similar on the final stage of the resting period, which means that the IVD is also responding properly to the load adjustment. It must be highlighted that the evolution of the OsmP, during the initial 8h, is not exactly adjusted to the evolution of the analogous NP AveP and IDP, which means that the 250N load is probably slightly exceeding the natural resting load for a lumbar IVD with this characteristics[IX]. However, in the end of the 32th hour, the IDP and OsmP converged to the same value (around 0.19MPa), for the four tests, which gives good indications about the accuracy of the recovery process.

Nevertheless, the two higher top loads (850 and 1000N) produce some overloading effect. The analyzed time period (two days) is not enough to evaluate long-term damage, but the analysis of DHV and volume variation gives the indication that the repetition of such loading profiles over time would trigger IVD degeneration through mechanical factors. The analysis of the pressure variables also reveal some tendency to non-healthy values, in accordance with the works of (Massey et al., 2012; Sato et al., 1999). The 1000N load is described by multiple authors (Galbusera et al., 2011; Noailly et al., 2011; O'Connell, Jacobs, et al., 2011; Ruiz et al., 2013; Schmidt et al., 2013) as related to moderate daily activities, but the healthy levels of

[VIII] This observation is also valid for the NP AveP and OsmP.

[IX] This situation was already revealed in the 2nd section of the present chapter.

average loading for 16h are exceeded. Loading levels of 600 to 700N seem to be much more appropriate for the good functioning of the MS in the Human spine, as already discussed.

5.2.9. 350-1000N

Figure 5.15 shows the outcomes of the 350-1000N loading profile, namely DHV (Figure 5.15a)), pressure variables (IDP, OsmP and NP AveP - Figure 5.15b)) and volume variation (Figure 5.15c)). The purpose of this loadcase was to establish a comparison with the analogous numerical test presented by (Schmidt et al., 2010).

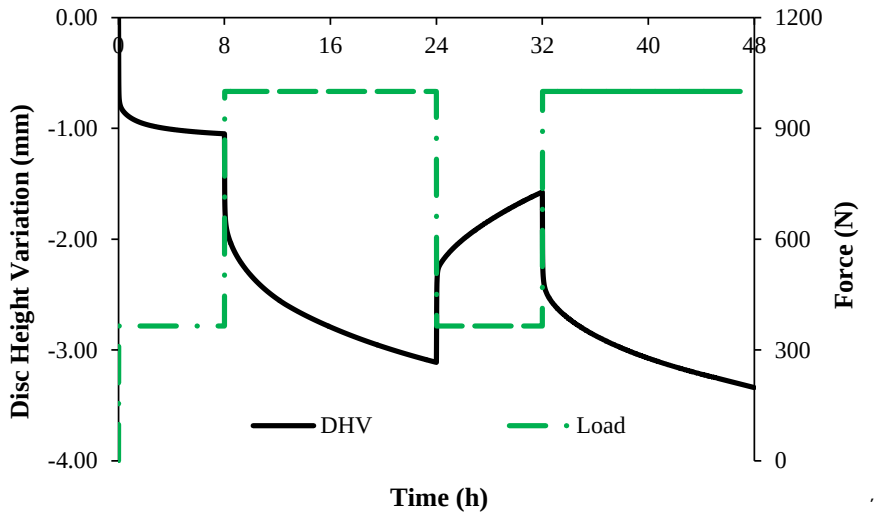

a)

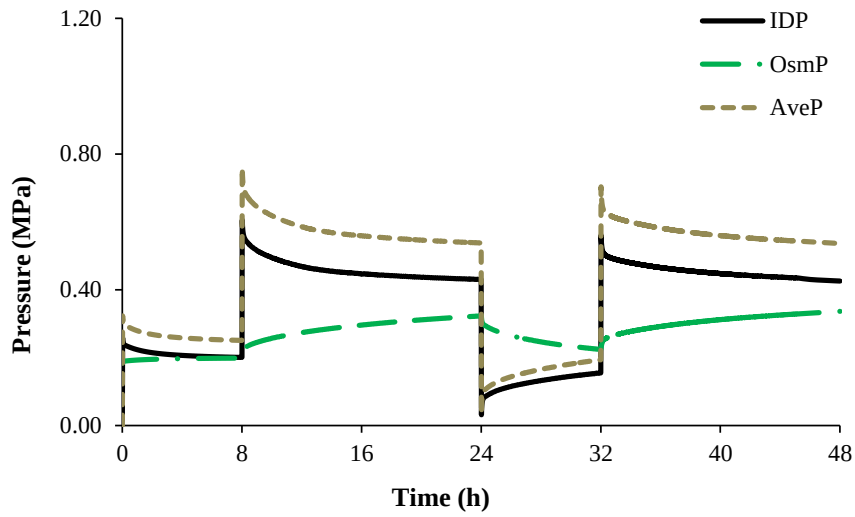

b)

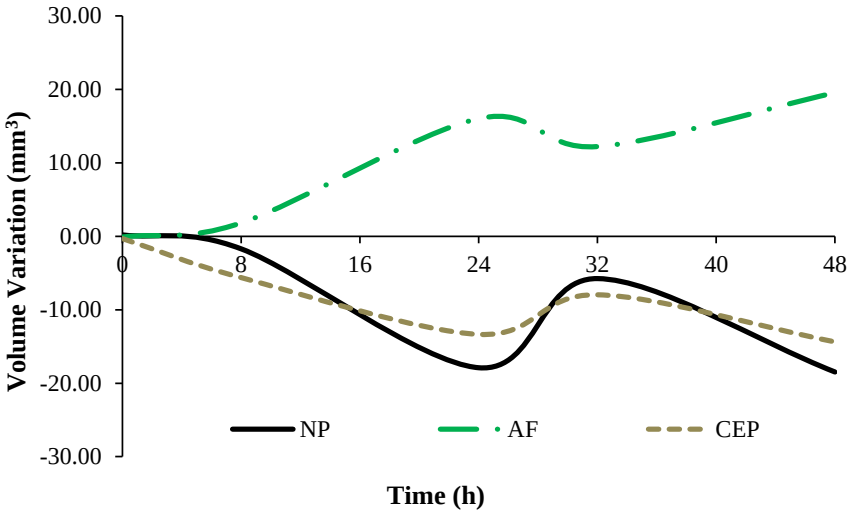

c)

Figure 5.15. Results of the 350-1000N loading profile, along 48h: a) DHV vs. Load; c) Pressure variables (IDP, OsmP and NP AveP); c) Volume variation.

On the one hand, the 350N load seems to create an overloading effect since the beginning of the test, as the NP AveP, IDP and OsmP values are misadjusted on the initial 8h[x]. This discrepancy also occurs in the end of the 32th hour. On the other hand, the 1000N load associated with the activity period also seems to contribute for the overloading effect, as was already revealed in the previous sub-section. In the present test, the initial disc height is also not recovered on the second resting period and the volume variation of the NP is negative all along the test. The top IDP of 0.61MPa is lined up with the experimental work of (McMillan et al., 1996), but the top DHV value (-3.34mm) is about 25% of the initial disc height.

In comparison with the 250-1000N loadcase, the lower load variation of this loading profile (650N against 750N) caused lower top IDP, but higher top DHV. On the one hand, this situation indicates that harsh loading variations may cause acute damage, namely AF disruption, as described by (Adams and Green, 1993; Hollingsworth and Wagner, 2011). On the other hand, it also reveals that the higher load levels along the daily cycles cause sustained IVD height reduction, which may not be recovered if the activity period is regularly too severe or if the recovery period is not well established.

These results were then compared with the two hypotheses considered on the numerical work of (Schmidt et al., 2010), which was validated with experimental data. They simulated the

[x] This situation was already discussed in the 2nd section of the present chapter.

IVD osmotic swelling behavior by imposing a 0.25MPa pressure on the MS external boundaries[XI], which is an alternative approach to the abovementioned BS and FOP methods. The differences between the two hypotheses considered are solely the permeability properties. The first hypothesis (1) is based on the same source of the current model (Ferguson et al., 2004) and the second hypothesis (2) uses a hybrid approach[XII] with permeability parameters that were also assessed in this work[XIII] (Schmidt et al., 2010).

The initial OsmP of the current model is 0.187MPa, and the initial IDP is 0.26MPa, while the initial IDP of both models from Schmidt and co-workers is around 0.39MPa. This higher initial IDP is probably explained by the fixed boundary pressure. The higher slope of both IDP curves seems to be caused by the lack of the strain-dependent osmotic swelling behavior, as the OsmP gradient contributes to the equilibrium of the IDP.

In what concerns the DHV, the fixed boundary pressure of 0.25 MPa is also the most likely cause for the lower maximum displacement of both models from Schmidt and co-workers and for the full recovery of the initial disc height at the 32th hour (second resting period)[XIV].

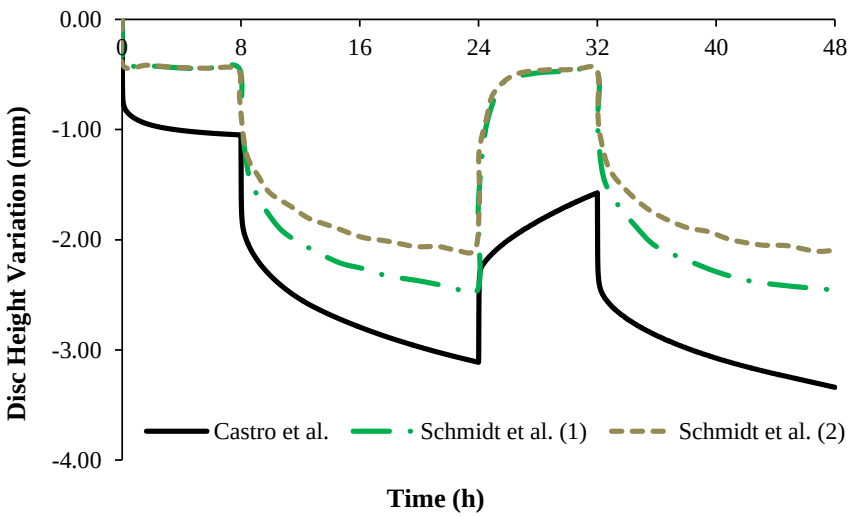

a)

[XI] Schmidt and co-workers didn't consider any specific osmotic swelling algorithm.

[XII] The permeability parameters from Argoubi and Shirazi-Adl (1996) were applied for the activity periods and the parameters from Ferguson et al. (2004) were applied for the recovery periods.

[XIII] This situation is described on the "Alternative Configurations" sub-section of the "Short Creep" section of the present chapter, even if there was no variation of parameters along the test, as performed by Schmidt and co-workers.

[XIV] Similar assumptions were reached on the analysis of the "800N, 20mins" sub-section of the "Short Creep" section of the present chapter, based on the works of (Tyrrell et al., 1985; Williams et al., 2007).

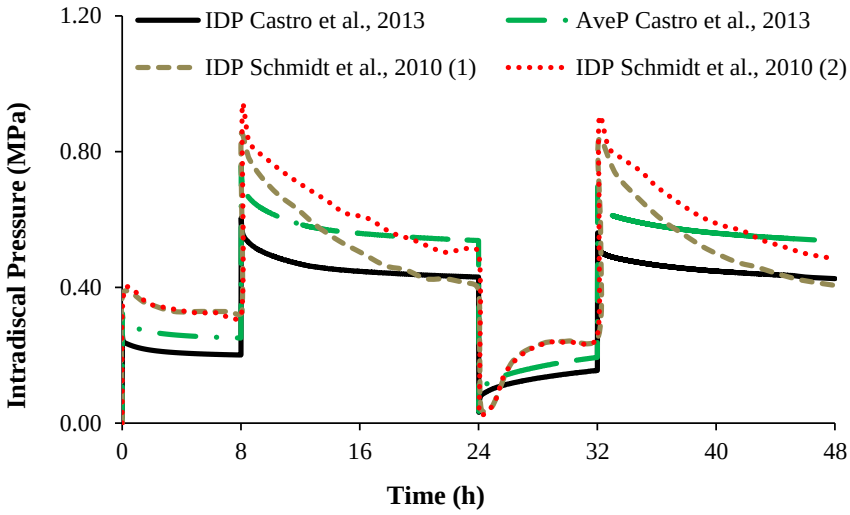

b)

Figure 5.16. Comparison between the numerical outcomes of the MS FE model and the analogous outcomes of the work of Schmidt et al. (2010): a) DHV; b) Pressure (IDP and NP AveP). The first situation (Schmidt et al., 2010 (1)) considered the permeability parameters from Ferguson et al. (2004) and the second situation (Schmidt et al., 2010 (2)) considered a hybrid set of parameters.

As abovementioned, the two configurations for the permeability applied by Schmidt and co-workers are not significantly different from the ones of the current MS model, so one may assume that the permeability properties shall not be a cause for the discrepancy on the results of both works. Nevertheless, they proved that the choice of different permeability parameters clearly produces different outcomes of the numerical model, for long periods of time. The specific geometrical features of the IVD FE model of Schmidt and co-workers are most likely to have a role on that discrepancy.

5.2.10. 500-1000N

Figure 5.17 shows the outcomes of the 500-1000N loading profile, namely DHV (Figure 5.17a)), pressure variables (IDP, OsmP and NP AveP - Figure 5.17b)) and volume variation (Figure 5.17c)). The application of the 500N load for the resting period was not previously explored, but this loadcase was based on the numerical test presented by (Galbusera et al., 2011). The outcomes of that work are included in Figure 5.17a) and Figure 5.17b), between the 24th and the 48th hours.

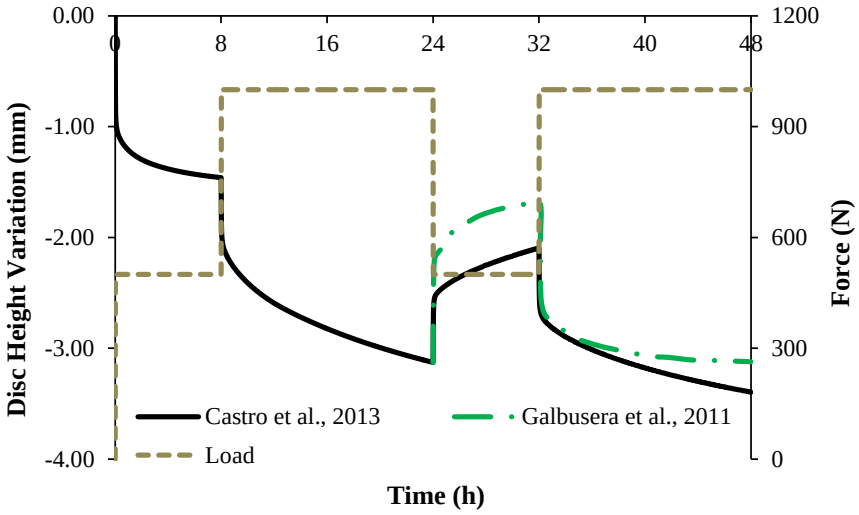

a)

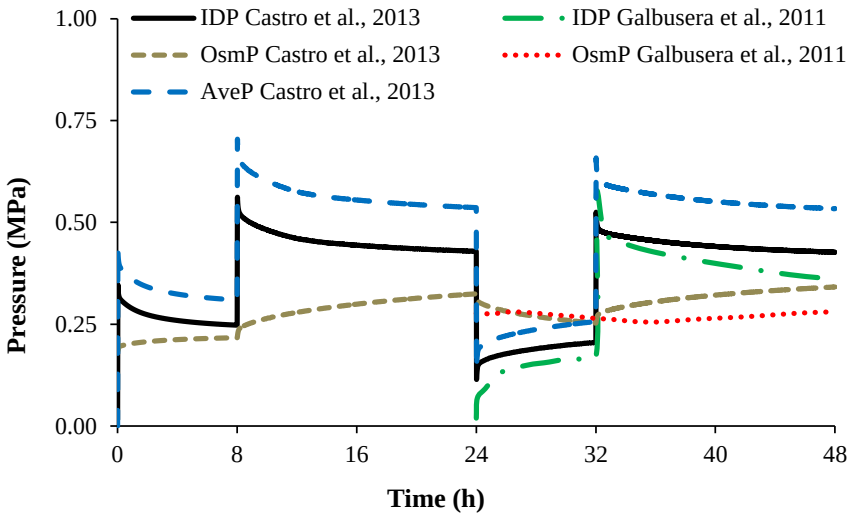

b)

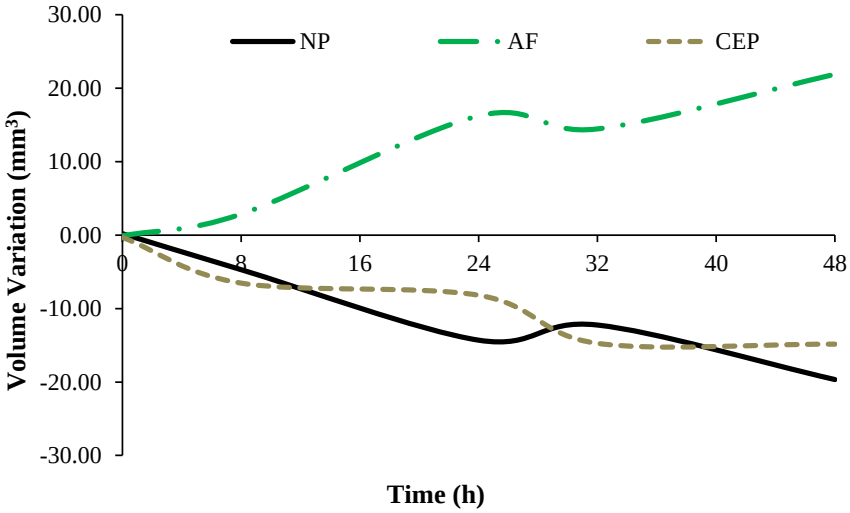

c)

Figure 5.17. Results of the 500-1000N loading profile, along 48h: a) DHV vs. Load; c) Pressure variables (IDP, OsmP and NP AveP); c) Volume variation. The comparison with the work of Galbusera et al. (2011) is held between 24 and 48h, for the DHV, IDP and OsmP variables.

The present work uses the same osmotic swelling pressure model (and constitutive parameters[xv]) applied on the study of Galbusera and co-workers. However, the stiffness properties are not the same. This situation was not evident on the comparison for the 200-500N loading profile, but is probably the main reason for the discrepancy on the DHV values. In fact, while the current MS model denotes a clear overloading effect (visible on the DHV and volume variation curves, Figure 5.17a) and c), respectively), the model from Galbusera and co-workers seems to be able to handle with the 500 and 1000N loads. This situation may not be favorable for that model, because the risk of damage is probably being masked. The chosen recovery load of 500N is not aligned with the majority of the literature, as previously discussed.

In what concerns the pressure variables, the top IDP value measured by Galbusera and co-workers is 0.57MPa. At the same time, the current model registered 0.53MPa[xvi]. However, Figure 5.17b) shows that, at the end of the test, Galbusera and co-workers measured IDP and OsmP values of 0.36 and 0.28MPa, respectively, while the present model registered 0.43 and 0.34MPa for the same variables. The ending difference between these two pressure components is similar for both models (around 0.08MPa). The main difference between the two models is visible on the evolution of each component, as the OsmP measured by Galbusera and co-workers is steadier along the test than the OsmP registered by the present model. On the contrary, the IDP component of the present model stabilizes faster than the analogous component of the other model. The higher sensitivity of the osmotic component, on the current model, seems to indicate that the integration of the strain-dependent osmotic swelling algorithm on the home-developed solver produces better results than the integration of the same algorithm on a commercial FE-package, i.e., the present model seems to be more accurate, as already described on the 200-500N loadcase.

5.2.11. Comparison #3

Figure 5.18 shows the comparison between the three loading profiles with activity load of 1000N. DHV (Figure 5.18a)), IDP (Figure 5.18b)), OsmP (Figure 5.18c)) and NP AveP (Figure 5.18d)) are evaluated.

[xv] Presented on the previous chapter.

[xvi] The top IDP value registered by the current simulation is 0.56MPa, but it occurs at the 8th hour, which cannot be compared with the work of Galbusera and co-workers.

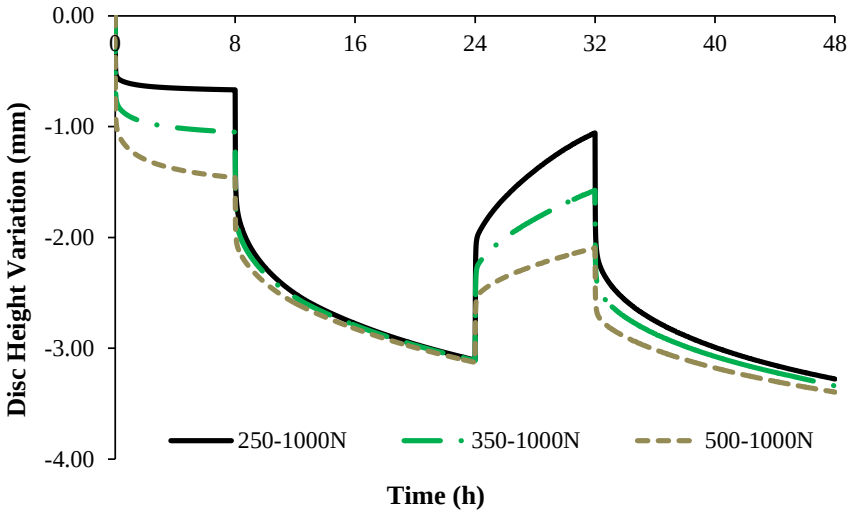
0.00
-1.00
-2.00
-3.00
-4.00
0
8
16
24
32
40
48
Disc Height Variation (mm)
250-1000N
350-1000N
500-1000N
Time (h)

a)

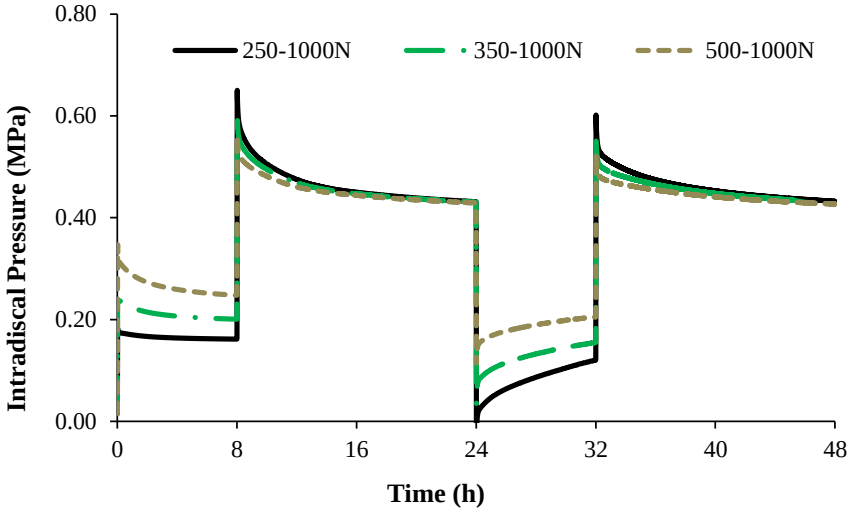
0.80
0.60
0.40
0.20
0.00
0
8
16
24
32
40
48
Intradiscal Pressure (MPa)
250-1000N
350-1000N
500-1000N
Time (h)

b)

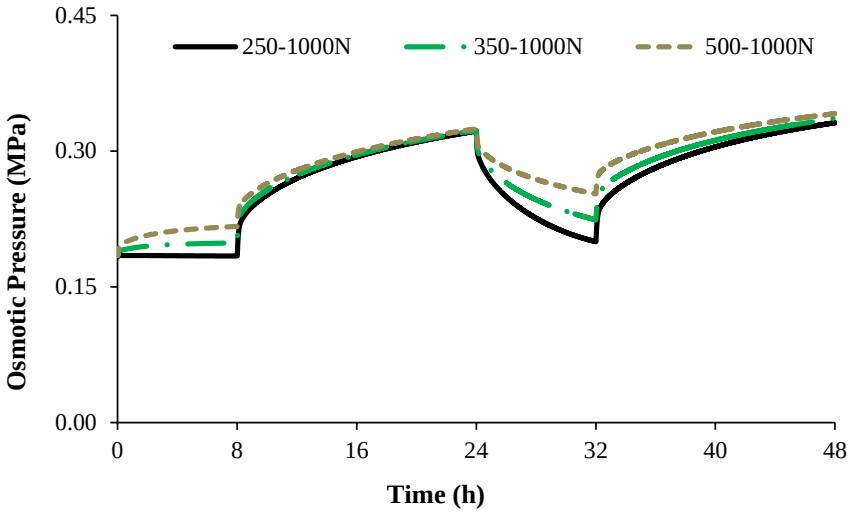
0.45
0.30
0.15
0.00
0
8
16
24
32
40
48
Osmotic Pressure (MPa)
250-1000N
350-1000N
500-1000N
Time (h)

c)

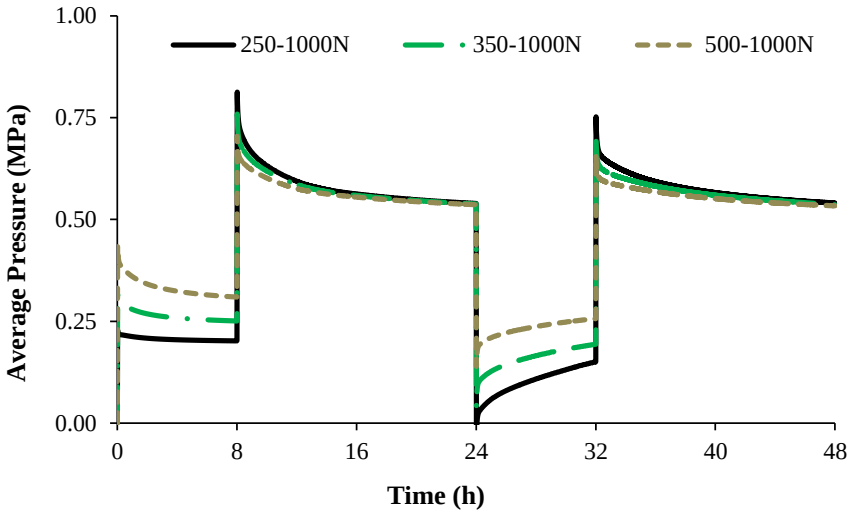

d)

Figure 5.18. Comparison between the three loadcases with the top activity load, namely {250, 350, 500}-1000N loadcases. a) DHV; b) IDP; c) OsmP; d) NP AveP.

The comparative revision presented on Figure 5.18 demonstrates the different responses of the IVD to the different loading profiles, following the consistency of the previous tests[XVII]. When the equilibrium is reached, the displacement and pressure values for the three tests are similar, which means that the different resting loads have little influence on the activity periods.

However, the larger load variation on the 250-1000N test is the most probable cause for the IDP to be the highest of this set (0.65MPa, against 0.61MPa from the 350-1000N loadcase and 0.56MPa from the 500-1000N loadcase), as already discussed.

One already reached the conclusion that the 1000N load is almost certainly exaggerated for the 16h of the physiological activity period, but the focus of the present comparison is on the resting loads. The model's response to the different values for the resting load confirms the previous finding that the natural resting load is about 200-250N, for the healthy lumbar Human IVD, which is firmly associated with the average value of 0.20MPa for the native OsmP (in the equilibrium). The 350 and 500N resting loads cause a visible overloading effect since the beginning of the test, i.e., the maintenance of these loads during these 8h do not allow the IVD to recover from the activity period. Nevertheless, the abovementioned severe load variation of the 250-1000N loadcase is also a possible cause for the mechanical failure of the IVD.

[XVII] This consistency of the numerical outcomes was also demonstrated on "Comparison #1" and "Comparison #2" sub-sections.

5.2.12. Summary

The outcomes of displacement, pressure and volume variation allowed the evaluation of the biomechanical behavior of the IVD FE osmo-poro-visco-elastic model (with fiber-reinforcement), under different loadcases of uniaxial unconfined compression.

The activity load was described as three or four times averagely larger than the recovery load. The initial swelling essays[XVIII] gave the clue that the recovery load should be around 200N, for a healthy lumbar disc. In what concerns to the activity load, it should have an average magnitude of 700N, which was also indicated by (Adams et al., 1990; Helfenstein, 2011; Sato et al., 1999). Moderate daily activities can be represented by a 1000N load, as described by (Galbusera et al., 2011; Noailly et al., 2011; Ruiz et al., 2013; Schmidt et al., 2013, 2010). However, the recovery process of the IVD is impaired for loads higher than 850N, which means that higher loads will probably accelerate IVD degeneration.

[XVIII] "Swelling Periods" section.

5.3. Bioreactor Data Analysis

This section deals with the analysis of the bioreactor data from the Department of Orthopedic Surgery of VUmc (Amsterdam, The Netherlands). The *ex vivo* bioreactor system was developed within this group, and is denominated as Loaded Disc Culture System (LDCS). In short, this system is capable of maintaining an IVD alive for at least 3 weeks after extraction[xix], without losing its biomechanical and physiological properties. A schematic representation of this system is shown in Figure 5.19.

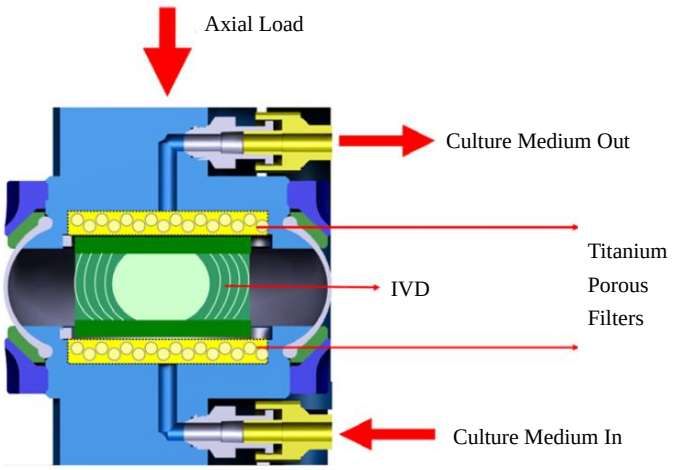

Figure 5.19. Schematic representation of the LCDS. Adapted from (Paul et al., 2012).

Other IVD-oriented bioreactors are described in the literature (Chan et al., 2013; Gantenbein et al., 2006; Korecki et al., 2007)[xx], but the LDCS reports the longest period of IVD viability. This system reproduces the IVD native environment, by enabling the close monitoring of oxygen and nutrient supply levels, through the introduction of a culture medium, along with providing static or dynamic mechanical axial loading, as seen in Figure 5.19. Up to twelve IVDs may be simultaneously under experiment in this equipment. The LDCS-related publications from Paul and co-workers reported experiments with several loading profiles, varying not only the load

[xix] The IVDs are extracted after the sacrifice of the animal, which is usually a goat.

[xx] This type of bioreactor was already mentioned in the second chapter. Each system may use IVDs from different animals.

magnitude, but also the loading regime, which could be static or dynamic[xxi] (Paul et al., 2013, 2012). The LDCS data to be analyzed in this section was not previously explored nor published, so the first step is to discuss the displacement outcomes from the experimental loading tests, and then compare them with the results of analogous numerical simulations.

Three test-groups were considered for the present analysis, organized as follows: i) test-group 1 includes four IVDs from goats 1 and 2, which were kept alive for 22 days, ii) test-group 2 includes four IVDs from goats 3 and 4, which were kept alive for 24 days and iii) test-group 3, which includes an IVD from goat 5, which was kept alive for 16 days. It must be highlighted that the viability of the IVD on the LDCS is related with the magnitude of the loading profile. In order to compare these three test-groups, the duration of the test-groups 1 and 2 was limited to 16 days.

Test-groups 1 and 2 included two native ("Nat") and two injected ("Inj") IVDs, i.e., each goat from these groups had one IVD left intact and the adjacent IVD injected with 0.5U/ml 100uL of chondroitinase ABC (CABC) on PBS solution[xxii]. These IVDs were tested under physiological loading conditions, which means that this loading profile is comparative to activities such as lying down and walking in goats and relaxed standing and unsupported sitting in Humans. It consists of a sinusoidal load (1Hz) of 150N average and 100N amplitude for 16h (activity period), followed by other sinusoidal load (1Hz) of 50N average and 10N amplitude for 8h (resting period)[xxiii]. However, the transition between the activity and resting periods is performed with 1h of triangular loading (0.25Hz) of 200N average and 100N amplitude. Slight adjustments on the system's functioning[xxiv] explain the extra two days of duration of test-group 2.

The IVD from the fifth goat was maintained intact, but it was Overloaded ("Ove"), i.e., the activity period loading profile was increased, in comparison with the other two test-groups. The resting period and the transitions between the major periods are the same, but the activity loading profile consists of a sinusoidal load (1Hz) of 300N average and 100N amplitude for 16h. This loading profile simulates jumping on a haystack in goats or lifting objects in Humans.

The maximum displacement from each one of the 16 days was analyzed, after filtering of the LDCS output data. A custom-made FORTRAN filter was developed and applied to reduce the

[xxi] The authors stated that, from the physiological point of view, the dynamic regimes cause large dynamic displacement, while the static regimes induced a prolonged creep effect.

[xxii] The CABC is an enzyme that cleaves proteoglycans, i.e., this PBS-CABC compound (further denominated only as CABC) is injected on the goat IVD with the aim of triggering degeneration (Detiger et al., 2013).

[xxiii] Sinusoidal loadings are associated with dynamic loading regimes.

[xxiv] For example, the buffering period when the loads are altered was optimized.

computational weight of the raw experimental data, since these were sampled at 10Hz[xxv]. The comparison was first held between the four non-degenerated IVDs (Figure 5.20a)) and then between the four injected IVDs, plus the overloaded one (Figure 5.20b)). Secondly, the test-groups 1 and 2 were internally compared, i.e., the native IVDs from goats 1 and 2 were compared with the injected IVDs from the same goats (Figure 5.21a)). The same procedure was followed for goats 3 and 4 (Figure 5.21b)).

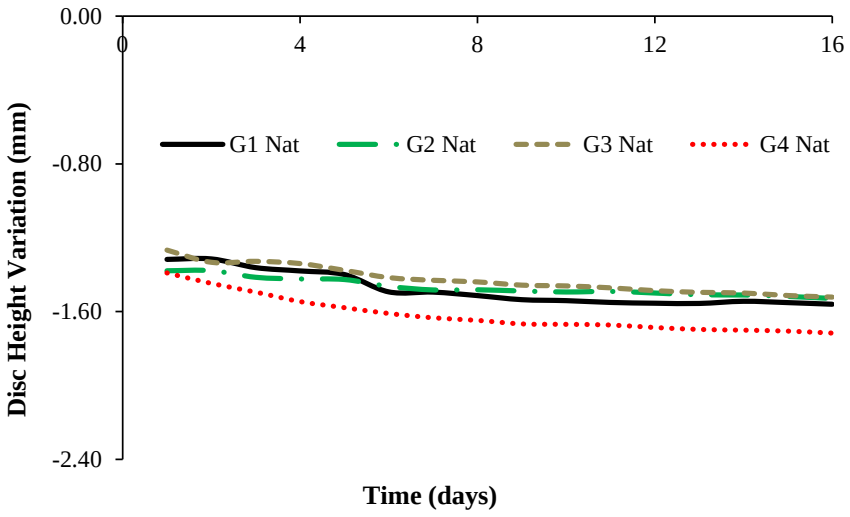

a)

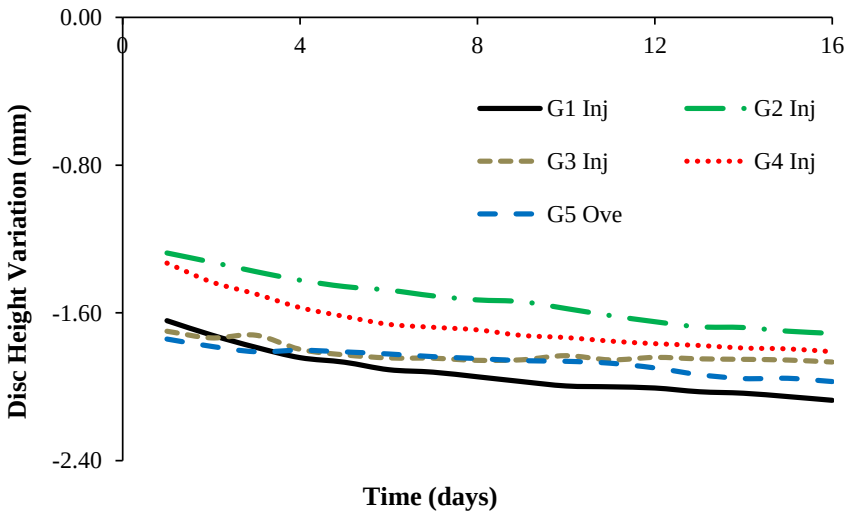

b)

Figure 5.20. Comparison of the overall displacement outcomes of the LDCS test-groups, for 16 days. a) DHV of the native IVDs, from test-groups 1 and 2; b) DHV of the injected IVDs, from test-groups 1 and 2 and overloaded IVD from test-group 3.

[xxv] This sampling rate corresponds to 10 samples per second, which ultimately resulted in 36000 values per hour. The developed filter was adjusted to 0.1Hz, i.e., a maximum of 360 values per hour.

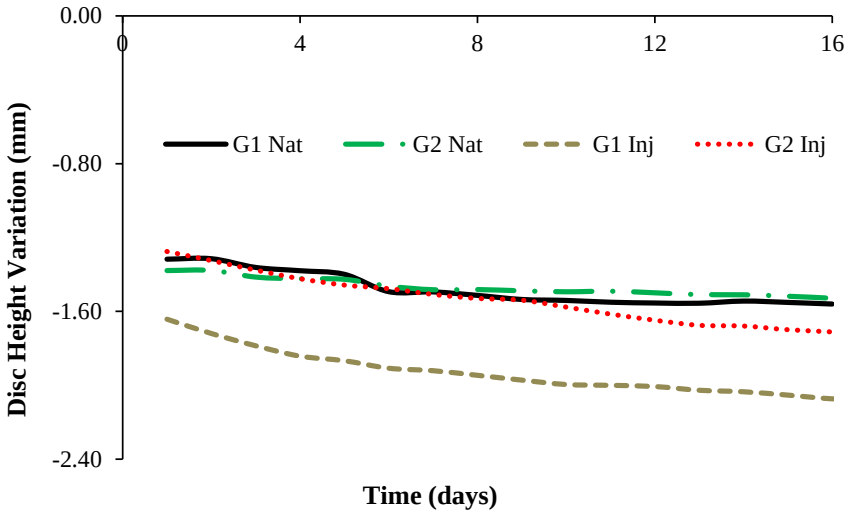

a)

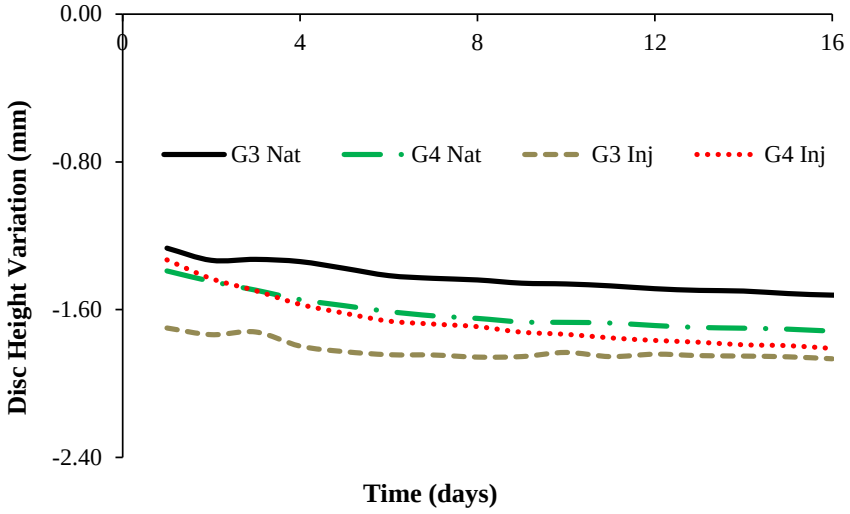

b)

Figure 5.21. Comparison of the DHV outcomes within each test-group, for 16 days. a) Test-group 1; b) Test-group 2.

In order to help on the analysis of Figure 5.20 and Figure 5.21, Table 5.2 summarizes all the displacement measurements, in terms of ending DHV (DHVf) and relative variation of the DHV, from the first to the 16th day.

The four native IVDs present similar DHVf, with only 0.20mm of difference between the lowest and the highest DHVf, i.e., the IVD from goat 3 reached -1.52mm and the IVD from goat 4 obtained -1.72mm. The IVDs from test-group 1 reached almost the same DHVf, with -1.57mm and -1.58mm, for goats 1 and 2, respectively. In what concerns to the injected IVDs, the difference between the lowest and the highest DHVf is 0.36mm, which means higher dispersion

of results. The lowest DHVf corresponds to the second goat (-1.77mm), while the top value corresponds to the first goat (-2.13mm). The IVDs from test-group 2 reached close DHVf values, with -1.87mm and -1.81mm, for goats 3 and 4, respectively. The overloaded IVD (goat 5) reached -1.97mm on the 16th day, which is inside the range of the DHVf measurements from the injected IVDs.

Table 5.2. Relative displacement measurements of the nine IVDs, from the five goats.

Goat	Condition	DHVf (mm)	RDHV (%)
1	Native	-1.57	16.10
	Injected	-2.13	22.88
2	Native	-1.56	11.75
	Injected	-1.77	27.80
3	Native	-1.52	16.72
	Injected	-1.87	8.93
4	Native	-1.72	18.99
	Injected	-1.81	26.49
5	Overloaded	-1.97	11.67

However, the analysis of the DHVf values is not enough to understand the overall behavior of the IVDs on the LDCS. The assessment of the RDHV shows that the evolution of native IVDs along the 16 days is similar for three of them, with 18.99% for the IVD of the fourth goat, 16.72% for the third and 16.10% for the first. The native IVD of the second goat is somewhat out of scope, as it registered a lower difference between the first and the 16th day, with a RDHV value of 11.75%. The injected IVDs presented higher dispersion of results, as was also noticed on the DHVf analysis, with 27.80% for the IVD of the second goat, 26.49% for the fourth and 22.88% for the first. The injected IVD of goat 3 presented a RDHV value of 8.93%, which is the lowest RDHV value of the nine analyzed IVDs. In the current analysis, the overloaded IVD is closer to the native IVDs, as it registered 11.67% of RDHV.

After analyzing all the presented daily displacement outcomes (DHV vs. time, DHVf and RDHV), one may say that the native IVDs present analogous behavior over the 16 days, as visible in Figure 5.20a), even considering the enumerated slight differences.

In what concerns to the injected IVDs, one may admit that the injection of the CABC compound can produce different effects, which is probably related with individual particularities of each goat and each IVD. The injected IVD from goat 3 showed regular DHVf and low RDHV, which probably means that the influence of the compound on the IVD was effective since the first day, while the other injected IVDs suffered from a more gradual degeneration effect. However, the two IVDs from the fourth goat showed close evolution of the DHV over time, thereby the injection of the CABC solution on the IVD of this goat was presumably not as significant as expected. The overloaded IVD presented low RDHV combined with high DHVf, meaning that the overloading was noticed since day 1 and also that the global behavior was not significantly altered during the test[xxvi].

Regardless of the mentioned exceptions, both injected and overloaded IVDs show higher DHVf and RDHV values, in comparison with the native ones, meaning that degeneration is probably occurring on those IVDs. The overloading effect is noticed since the first application of the exaggerated activity load, but the influence of the CABC compound is slower.

After the analysis of the overall displacement outcomes, the DHV of the first two days of test-groups 1 and 2 were exhaustively analyzed. Therefore, two activity periods, two recovery periods and three transitions stages were highlighted. Figure 5.22a) shows the described outcomes from the first test-group, while Figure 5.22b) shows the analogous outcomes from the second test-group. As the intention here was to compare the behavior of the native IVD versus the injected IVD of the same goat, for the two goats of each test-group, the overloaded IVD from test-group 3 was not included.

Regarding the first test-group (Figure 5.22a)), it is visible that the two native IVDs present similar behavior. Further, the DHV evolution of the injected IVD from goat 2 is close to the analogous evolution of the native IVDs. However, the progressive degenerative effect can be observed on the second recovery period, as the minimum DHV (-0.72mm) is higher than the DHV of the first recovery period (-0.68mm), meaning that the IVD is consistently losing height. This height loss is not perceived on the native IVDs. The injected IVD from goat 1 lost more height than the other three IVDs of this test-group since the beginning of the test. The DHV difference between of first and the second recovery periods is also larger (measured DHV values of -0.96mm and -1.05mm, respectively).

[xxvi] This particular situation is comprehensively analyzed on the third section of the Annexes.

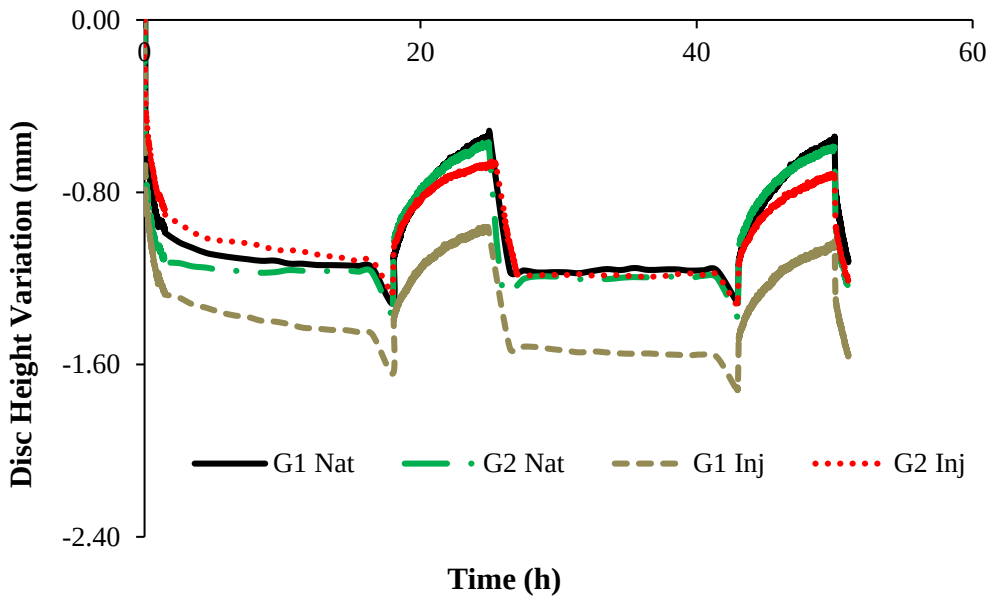

a)

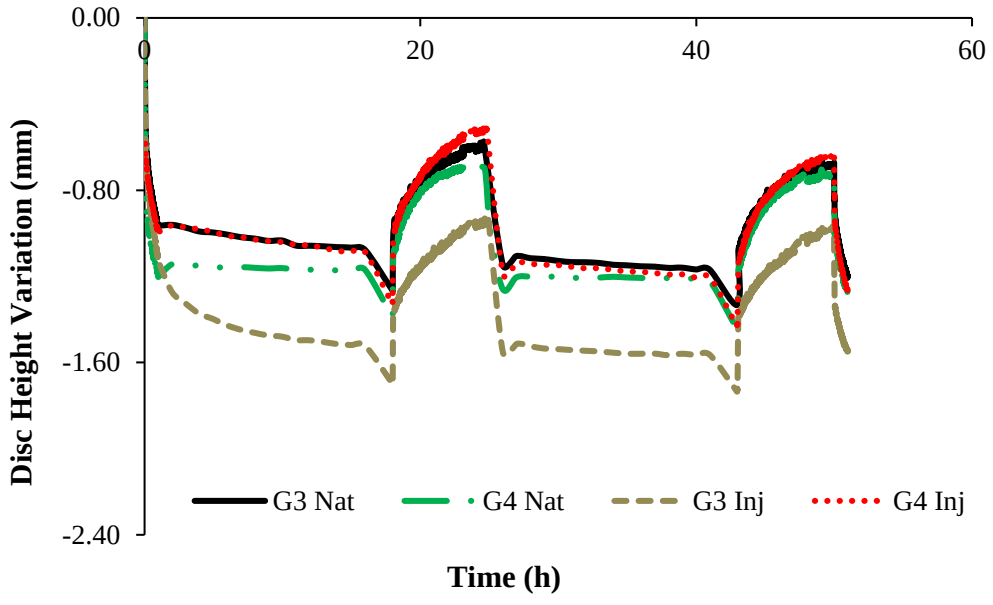

b)

Figure 5.22. DHV evolution over the first two days of the LDCS experiment. a) First test-group; b) Second test-group. Two native and two injected IVDs are considered in each test-group.

The outcomes from the second test-group (Figure 5.22b)) are not so clear, due to the DHV evolution of the IVDs from the fourth goat. The native IVD presents the same final DHV value than the correspondent injected IVD (approximately -1.26mm), without presenting a progressive height loss. In other words, the injected IVD diminished in height from the first recovery period to the

second one (measured DHV values of -0.49mm versus -0.63mm, respectively), which is the sign of progressive degenerative effect, but it ended losing the same height than the native IVD[xxvii]. This finding probably means that the initial height of the IVDs should have been taken into consideration, in order to normalize the DHV measurements. Nevertheless, it must be highlighted that this height difference may be related with the cutting of the VB[xxviii] and not directly with the IVD, since the studied IVDs belonged to adjacent levels and their height should not be significantly different.

The DHV evolution of the IVDs from the third goat was also not straightforward, as the native IVD presented similar behavior to the injected IVD of the fourth goat, i.e., the IVD was not injected, but it disclosed some progressive degenerative effect. In what concerns to the injected IVD of the third goat, this one obeyed to what was initially expected, i.e., it diminished in height more significantly than the other IVDs since the first activity period. In addition, the DHV measured after the first recovery period was lower than the analogous value of the second recovery period (-0.92mm versus -0.98mm, respectively).

In agreement with the findings of the DHV outcomes after 16 days, the DHV detailed measurements during the first two days of the experiments allow the identification of some degeneration signs on the injected IVDs. Detiger and co-workers (2013) also found consistent evidence of IVD height reduction after the injection of the CABC compound, even if their analysis was performed using different methods.

The native IVDs tend to maintain their height along the experiment, while the injected IVDs tend to lose height progressively. This systematic height reduction is mostly noticed on the loss of the ability to return to the same height level after the recovery period. However, some discrepancies were noticed between the two analyzed test-groups (1 and 2) and also between the IVDs of the same test-group, which can be justified by the adjustments on the equipment and on the testing procedures[xxix], but also by the inter-specimen variability of the goats.

On the one hand, one can conceive that some goats have genetic predisposition to degeneration, which may have promoted the unexpected behavior of the native IVD of the third goat, under physiological loading. On the other hand, the injection of the CABC compound on the

[xxvii] The DHV variation of the native IVD in the same time steps was limited to -0.02mm, i.e., -0.70mm at the end of the first recovery period and -0.72mm after the second recovery period.

[xxviii] This refers to the preparation of the IVDs prior to the LDCS experiments.

[xxix] The already mentioned differences on the VB cutting may influence the height measurements significantly.

adjacent level may have stimulated the degeneration of the IVD that was supposed to be kept under native conditions.

The next step is to compare these first two daily cycles of the experimental tests with analogous numerical simulations, using the developed MS FE model.

5.3.1. Comparison with the MS FE model

In order to have better understanding over the LDCS outcomes, and also to continue the evaluation of the MS FE model, the experimental tests were numerically reproduced. However, some important assumptions had to be held, since the experiments were performed with goat IVDs and the FE model correspond to a full Human MS. The average axial cross section of the goat IVD is around 300-400mm^2, accordingly to the VUmc experimental data, while the average axial cross section of the Human IVD stands between 1200 to 1600mm^2. The IVD FE model has an axial cross section of 1555.3mm^2, as described in the previous chapter.

Consequently, the Human IVD is averagely four times larger than the goat IVD, so one could assume that the loads to be applied on the MS FE model should be four times greater than the loads experimentally applied on the goat IVDs, on the LDCS. The sinusoidal loadings were also simplified to linear loadings, given that the sinusoidal wave would meant an extra computational effort, without significant improvements on the numerical outcomes. Linear loadings may also be denominated as static loadings, at the light of the available loadings regimes of the LDCS. Computationally, at the hourly time-scale, it was verified that the sinusoidal and the linear loading regimes produce similar outcomes. If one was working with shorter tests[xxx], the two regimes probably caused different behavior of the FE model, due to the viscoelastic effects. Therefore, the numerical physiological loading profile consists of 600N for 16h (activity period), followed by 200N for 8h (resting period). This model is known as "Native". The transition between the activity and resting periods is performed with 800N for 1h, in order to maintain a similar timeline with the experimental tests. The overloading profile, which will be ahead denominated as "Overload", had the same resting and transition periods, but the activity load was increased to 1200N.

[xxx] Shorter tests, in this context, mean tests with duration inferior than one minute.

The effect of the CABC compound was reproduced on the numerical modeling through the reduction of the osmotic pressure gradient. As aforementioned, CABC cleaves proteoglycans, which are involved on the osmotic pressure mechanisms, through the regulation of the fixed charged density (c_F). In detail, proteoglycans have an essential role on fluid attraction and detainment, which allows the IVD to maintain its internal pressure, namely due to the "vessel-wall"-like behavior of the AF fibers. Hence, if the proteoglycan content is reduced, the hydration of the IVD is also reduced and the osmotic pressure gradient is lower (Massey et al., 2012; Wognum et al., 2006). The initial fixed charge density ($c_{F,0}$) of the NP was then reduced, in two levels, as presented on Table 5.3. The objective was to reduce the native NP $c_{F,0}$ (0.00030mmol.mm^{-3}) step by step until it reaches the native $c_{F,0}$ value of the AF (0.00018mmol.mm^{-3}). The model with the first $c_{F,0}$ reduction is entitled "Low OsmP 1" and the model with the second $c_{F,0}$ reduction is denominated "Low OsmP 2"[xxxi]. In order to evaluate an extreme situation of proteoglycans cleavage, i.e., total split, a model without osmotic swelling was also tested ("No Swelling").

Table 5.3. Osmotic swelling material properties of the native FE model and reduced OsmP models.

Model	NP $c_{F,0}$ [mmol.mm^{-3}]
Native	0.00030
Low OsmP 1	0.00024
Low OsmP 2	0.00018

The other core hypothesis to simulate degeneration was the modification of the tissues' permeability, but this mechanism is highly dependent on the degeneration grade[xxxii]. Low to mild degeneration are probably related to a decrease of CEP permeability, due to the calcification of this component, while mild to severe degeneration are more likely associated with an increase of CEP permeability, as a result of probable crack openings (Adams and Dolan, 2012; Urban et al., 2000). The permeability behavior of the degenerated NP and AF remains uncertain, but some studies pointed out that it could increase (Iatridis et al., 1998; Johannessen and Elliott, 2005;

[xxxi] These two reduced osmotic pressure models will also be analyzed on the first section of the Annexes.
[xxxii] Mild degeneration, as reported by Detiger et al. (2013), stands for grades III to IV on Thompson's scale.

O'Connell, Vresilovic, et al., 2011; Urban et al., 2000). Some of these studies tried to implement these permeability changes on their numerical models, but those parameters are also diffuse. The proteoglycans might be related to the permeability variations, but the association is also unclear. The IVD components are also described to increase in stiffness, as modeled by (Natarajan et al., 2006) and (Schmidt et al., 2007), but this variation was not previously described in the literature as having a direct link to the injection of CABC compound (Detiger et al., 2013).

Figure 5.23 shows the behavior of the five numerical approaches, namely "Native", "Low OsmP 1", "Low OsmP 2", "No Swelling" and "Overload" models. Figure 5.24 shows the comparison between the native and non-physiological DHV outcomes of the experimental and numerical tests.

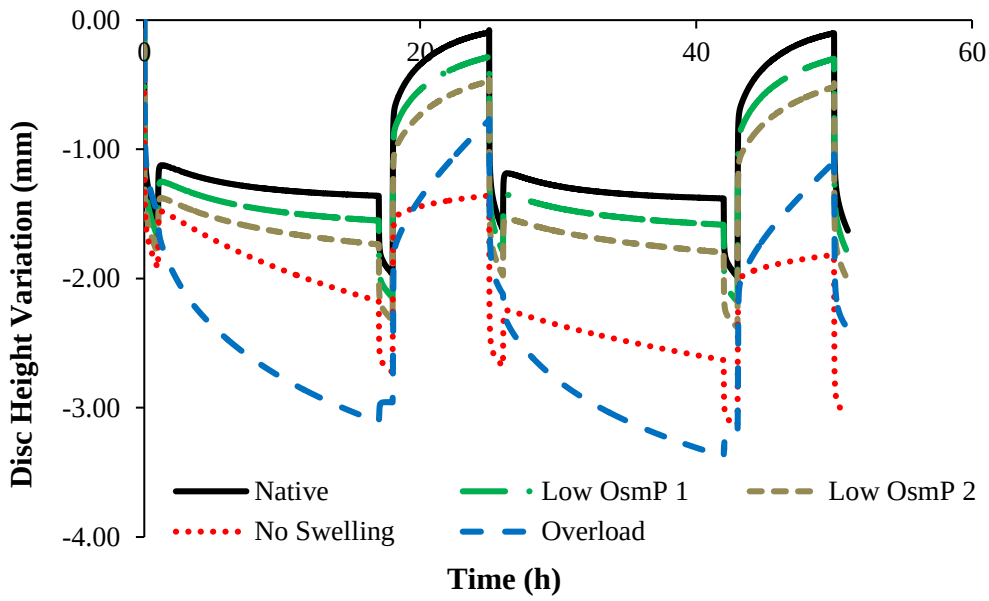

Figure 5.23. DHV outcomes of the five numerical approaches to the experimental data, namely "Native", "Low OsmP 1", "Low OsmP 2", "No Swelling" and "Overload" models.

The behavior of the numerical model corresponds to what was theoretically expected[xxxiii]. Firstly, the "Native" model is able to fully recover the initial height on the resting periods, and the maximum DHV is inside the physiological displacement range. Secondly, the reduced OsmP

[xxxiii] The transition periods will be excluded from the analysis of the maximum and minimum displacement measurements, as their purpose was just to establish the transition between the activity and recovery periods, on the experimental apparatus.

models show some signs of degeneration, as the fluid flow seems to be diminished, and thus the initial height is not recovered. This effect is progressive, as the "Low OsmP 1" model is less affected than the "Low OsmP 2" model. The maximum displacement also progressively increased[xxxiv], in comparison with the "Native" model. In addition, the "No Swelling" model shows clear signs of degeneration, as the maximum displacement is significantly increased and this increase is progressive throughout the daily cycles, without any sign of recovery. Finally, the "Overload" model shows the highest top displacement, but not the lowest recovery rate[xxxv], i.e., the overloading origins severe DHV levels, but the native constitutive properties allow this model to maintain some capacity to recapture the lost fluid, when the load is decreased. These differences between the five numerical models are visible on Figure 5.23.

The comparison of the first two daily cycles of the native IVDs with the equivalent period of the "Native" model (Figure 5.24a)) shows that the numerical model is able to reproduce the physiological behavior of the goat IVD, particularly during the activity period. Numerically, the maximum DHV was -1.36mm, while the average experimental measurement was -1.20mm[xxxvi].

In what concerns to the resting periods, an important difference is noticed, as the numerical model is able to regain all the fluid lost during the activity period. The goat IVDs do not reach that DHV value of approximately 0.00mm, as their average DHV value on the resting period is -0.58mm.

Nonetheless, these four IVDs maintain the same DHV recovery level from the first to the second daily cycle, which was previously described as a sign of no degeneration. In other words, the DHV results indicate no degeneration, but incomplete recovery. This fact is probably related with the intrinsic behavioral differences between the goat and Human IVDs, namely the specific biomechanical stimuli[xxxvii]. The numerical model helped to understand that the ideal situation is to fully recover the fluid on the resting periods. However, the action of AF fibers may also be limiting the range of DHV, and this limit situation[xxxviii] is not predicted in the FE solver. This action shall not be considerably different in Human and goat spines.

[xxxiv] From the first to the second daily cycle.

[xxxv] The recovery rate shall be understood as the difference between the DHV after the activity period and the DHV after the recovery period. The lowest recovery was registered by the "No Swelling" model.

[xxxvi] Considering the four native goat IVDs.

[xxxvii] The nutrition pathways included in the LDCS functioning and the ion-influenced fluid retention may also have a role in this situation.

[xxxviii] The limit situation shall be understood as the maximum extension of the fibers.

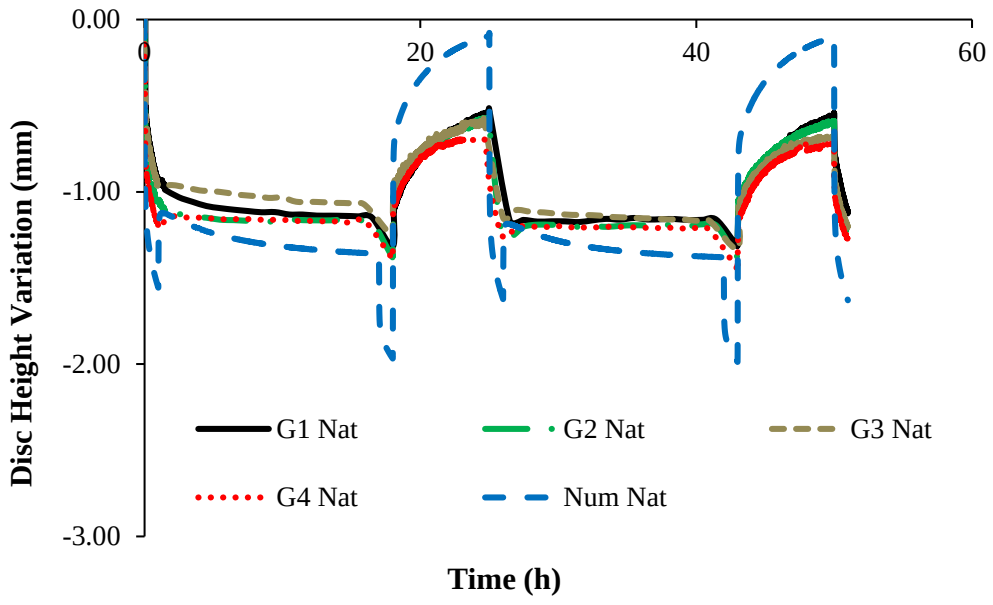

a)

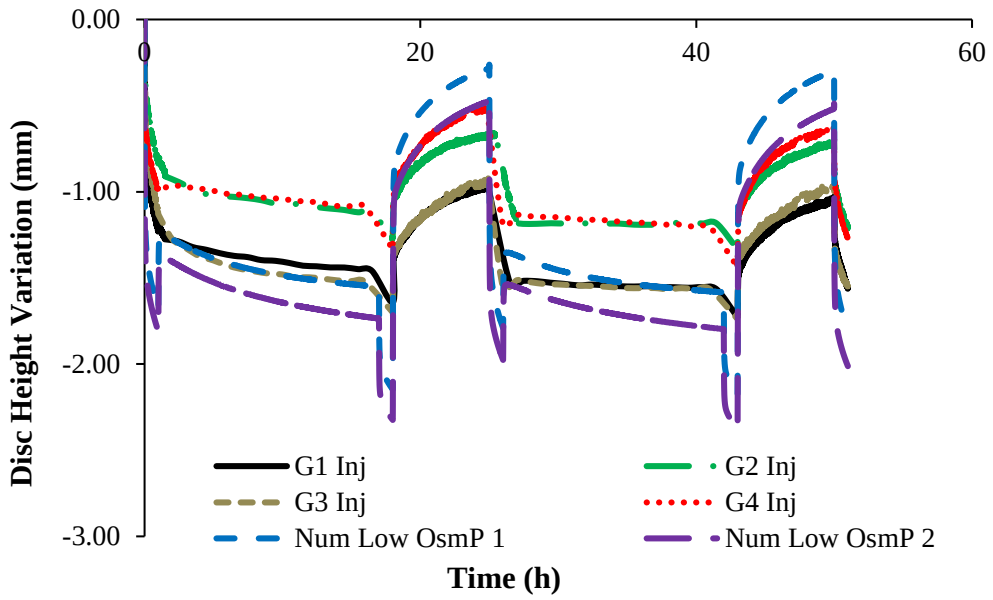

b)

Figure 5.24. Native and non-physiological DHV outcomes of the experimental and numerical tests, for two daily cycles. a) The four native IVDs compared with the native numerical model; b) The four injected IVDs compared with the two reduced OsmP models.

The comparison of the first two daily cycles of the injected IVDs with the equivalent period of the reduced OsmP models (Figure 5.24b)) shows that the behavior of both numerical models may be associated with the IVDs from goats 1 and 3, but not so much with the IVDs from goats 2 and 4. Subsequently, Figure 5.25 shows selective comparisons between the non-physiological

DHV results of the experimental and numerical tests. The analysis of Figure 5.24b) suggested that the injected IVDs from goats 1 and 3 should be grouped in one graphic (Figure 5.25a)), while the injected IVDs from goats 2 and 4 should be compiled in other graphic (Figure 5.25b)).

These two groups of injected IVDs were compared with the two reduced OsmP models and, additionally, with the "No Swelling" model. Table 5.4 summarizes the DHV values of these six DHV curves, and it helps to demonstrate the abovementioned differences between the four experimental tests, and also between the experimental tests and the numerical ones.

The "Low OsmP 1" model shows only slight signs of degeneration[xxxix], while the "Low OsmP 2" model is closer to the injected IVDs from goats 1 and 3. The native IVDs presented a DHV difference of averagely 0.58mm after the recovery periods, when compared with the "Native" model. The average difference between "G1 Inj" and "G3 Inj" and the "Low OsmP 2" model, after the recovery periods, is 0.50mm, i.e., the distance between these two injected IVDs and the numerical model is close to what was measured for the native condition, which denotes consistency of the outcomes. In addition, the analogous difference for the maximum displacement is averagely 0.25mm, which is in agreement with the 0.16mm difference found for the native condition.

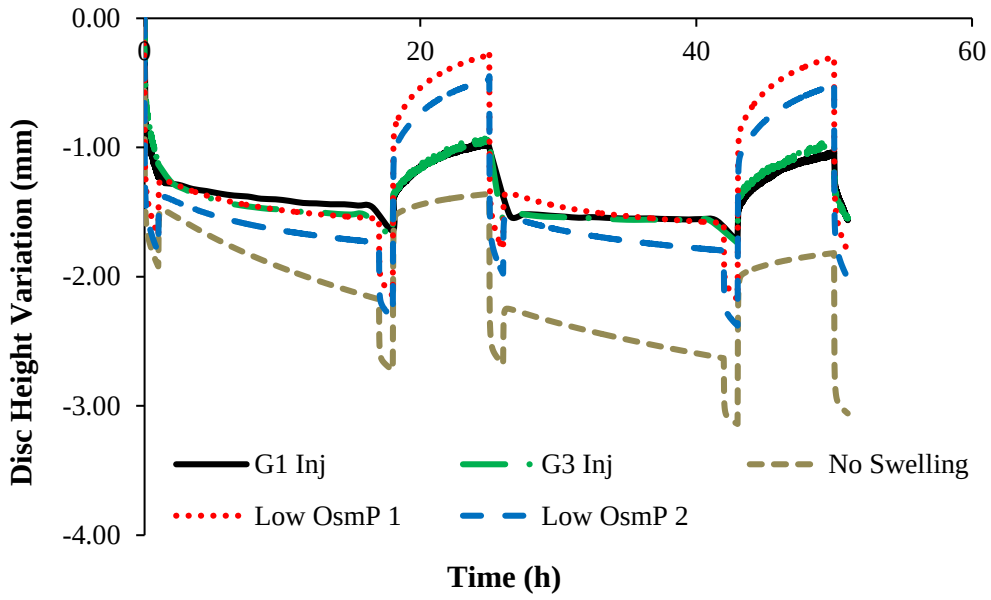

a)

[xxxix] Both maximum DHV and DHV after recovery are not significantly distant, when one is comparing the first daily cycle with the second one.

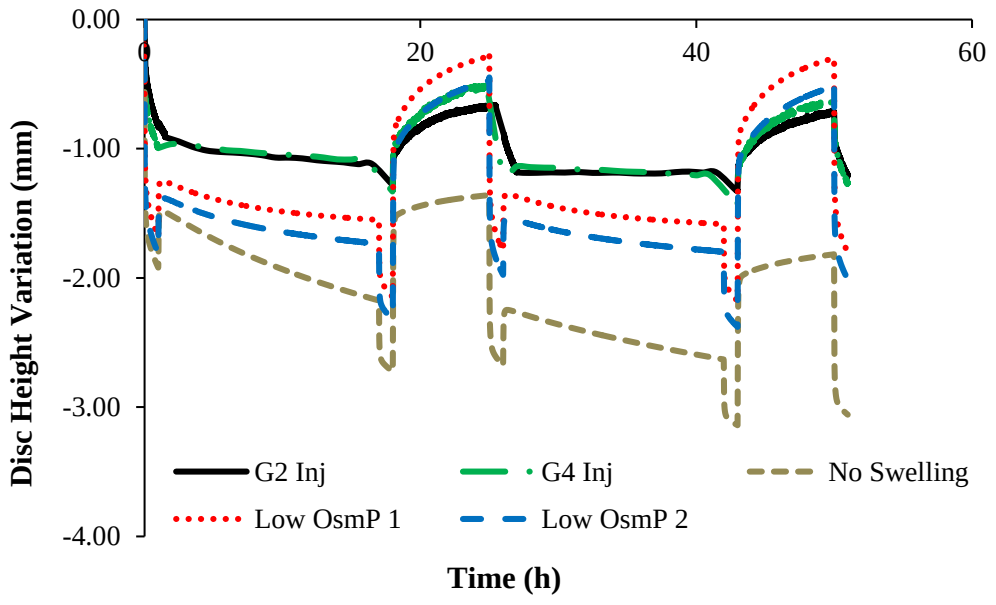

b)

Figure 5.25. Non-physiological DHV outcomes of the experimental and numerical tests, for two daily cycles. a) The injected IVDs from goats 1 and 3 compared with the two reduced OsmP and the "No Swelling" models; b) The injected IVDs from goats 2 and 4 compared with the two reduced OsmP and the "No Swelling" models.

Table 5.4. Summary of the DHV values of the four injected IVDs and the reduced OsmP models, after each activity and recovery period, obtained by numerical simulation.

IVD		DHV [mm]			
		1st Activity Period	1st Recovery Period	2nd Activity Period	2nd Recovery Period
Experimental	G1 Inj	-1.46	-0.96	-1.57	-1.05
	G2 Inj	-1.12	-0.68	-1.18	-0.72
	G3 Inj	-1.52	-0.92	-1.56	-0.97
	G4 Inj	-1.09	-0.49	-1.21	-0.63
Numerical	Low OsmP 1	-1.56	-0.29	-1.59	-0.30
	Low OsmP 2	-1.74	-0.47	-1.80	-0.49
	No Swelling	-2.17	-1.36	-2.63	-1.82

However, none of these injected IVDs is by chance near to the behavior of the "No Swelling" model. The recovery rate of this model is approximately 0.80mm for the two daily cycles, meaning that this is the model with less capacity for regaining fluid content, as already referred.

At the light of the experimental tests, the behavior of the "No Swelling" model probably means that the proteoglycan cleavage promoted by the injected quantity of CABC compound is only enough to cause mild degeneration, as expected. Considering the described outcomes, the situation of an IVD without any osmotic pressure gradient is certainly related to severe degeneration.

The DHV measurements from the injected IVDs of goats 2 and 4 shall not be directly compared with these numerical outcomes, as their maximum displacement is significantly lower than the analogous measurement of the other two injected IVDs. Therefore, the DHV measured after each recovery period is nearer to the numerical models, but the recovery rate is considerably uneven. The unexpected behavior of these IVDs, particularly the behavior of "G2 Inj", was previously discussed. Nevertheless, the average recovery rate of "G4 Inj" is inside the [0.50-0.60]mm range of the other two injected IVDs.

Finally, the five non-physiological IVDs were compared with the overloaded model, as shown in Figure 5.26. As already discussed, there are clear dissimilarities between the injected IVDs, so the behavior of "G5 Ove" is unsurprisingly closer to the behavior of "G1 Inj" and "G3 Inj". However, the DHV measured from the "Overload" model is unexpectedly distant from the experimental outcomes.

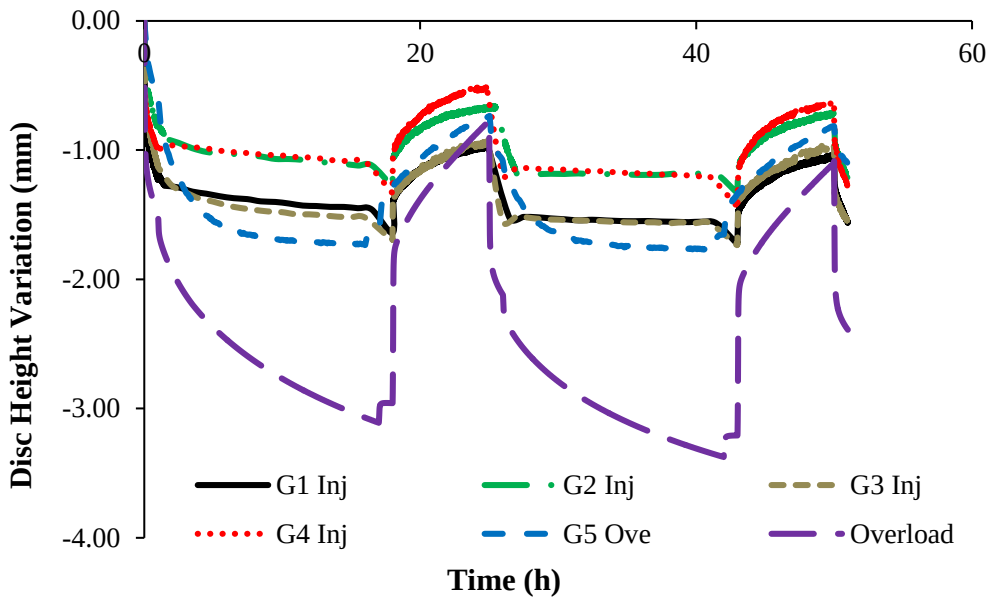

Figure 5.26. DHV outcomes from the five non-physiological goat IVDs compared with the overloaded model.

This finding probably means that the MS FE model is excessively sensitive to the applied loads, having that the goat IVDs present a much more limited range of height variation. If these experimental tests were performed *in vivo*, one might argued about the great influence of the ligaments, but these structures were removed before the IVDs are tested in the LDCS. Therefore, this noticeable behavioral difference is almost certainly related to the intrinsic biochemical and biomechanical properties of the goat IVDs. One may also argue that the Human IVDs would have a larger range of height variation, due to their greater cross-sections and initial height. In addition, the action of AF fibers shall not be neglected. As abovementioned, the response of the fibers to the compressive loadings may restrict the range of DHV.

5.3.2. Summary

The LDCS outcomes were exhaustively analyzed, but such analysis was only possible after filtering, as the amount of data was too large to work with. Globally, it was possible to notice that the injection of the CABC compound on the goats caused degeneration on the targeted IVDs, but it could affect the adjacent levels similarly. In addition, the overloading mode also resulted on a pathological IVD, even if the biomechanical behavior was different, i.e., the overloaded IVD starting being degraded right after the application of the load, while the injected IVDs revealed a gradual degenerated behavior.

The comparison with the MS FE model was successful, particularly for the physiological situations. The degenerated behavior of the IVD is extremely complex, particularly because of the undisclosed physiological preventing criteria related to the diverse loading and environmental stimuli. However, the numerical model was able to reproduce the general behavioral lines of the goat IVDs from the three test-groups.

5.4. References

Adams, M.A., Dolan, P., 2012. Intervertebral disc degeneration: evidence for two distinct phenotypes. J. Anat. 221, 497–506.

Adams, M.A., Dolan, P., Hutton, W.C., Porter, R.W., 1990. Diurnal changes in spinal mechanics and their clinical significance. J. Bone Joint Surg. Br. 72, 266–70.

Adams, M.A., Green, T.P., 1993. Tensile properties of the annulus fibrosus. Eur. Spine J. 203–208.

Argoubi, M., Shirazi-Adl, A., 1996. Poroelastic creep response analysis of a lumbar motion segment in compression. J. Biomech. 29, 1331–9.

Chan, S.C.W., Walser, J., Käppeli, P., Shamsollahi, M.J., Ferguson, S., Gantenbein-Ritter, B., 2013. Region specific response of intervertebral disc cells to complex dynamic loading: an organ culture study using a dynamic torsion-compression bioreactor. PLoS One 8, e72489.

Detiger, S.E.L., Hoogendoorn, R.J.W., van der Veen, A.J., van Royen, B.J., Helder, M.N., Koenderink, G.H., Smit, T.H., 2013. Biomechanical and rheological characterization of mild intervertebral disc degeneration in a large animal model. J. Orthop. Res. 31, 703–9.

Eberlein, R., Holzapfel, G.A., Frolich, M., 2004. Multi-segment FEA of the human lumbar spine including the heterogeneity of the annulus fibrosus. Comput. Mech. 34, 147–163.

Eijkelkamp, M.F., van Donkelaar, C.C., Veldhuizen, A.G., van Horn, J.R., Huyghe, J.M., Verkerke, G.J., 2001. Requirements for an artificial intervertebral disc. Int. J. Artif. Organs 24, 311–21.

Ellingson, A.M., Nuckley, D.J., 2012. Intervertebral disc viscoelastic parameters and residual mechanics spatially quantified using a hybrid confined/in situ indentation method. J. Biomech. 45, 491–6.

Ferguson, S.J., Ito, K., Nolte, L.-P., 2004. Fluid flow and convective transport of solutes within the intervertebral disc. J. Biomech. 37, 213–221.

Frei, H., Oxland, T.R., Nolte, L.P., 2002. Thoracolumbar spine mechanics contrasted under compression and shear loading. J. Orthop. Res. 20, 1333–8.

Galbusera, F., Schmidt, H., Noailly, J., Malandrino, A., Lacroix, D., Wilke, H.-J., Shirazi-Adl, A., 2011. Comparison of four methods to simulate swelling in poroelastic finite element models of intervertebral discs. J. Mech. Behav. Biomed. Mater. 4, 1234–41.

Gantenbein, B., Grünhagen, T., Lee, C.R., van Donkelaar, C.C., Alini, M., Ito, K., 2006. An in vitro organ culturing system for intervertebral disc explants with vertebral endplates: a feasibility study with ovine caudal discs. Spine (Phila. Pa. 1976). 31, 2665–73.

Helfenstein, J., 2011. Continuum Mechanical Investigations of the Intervertebral Disc.

Heuer, F., Schmidt, H., Wilke, H.-J., 2008. The relation between intervertebral disc bulging and annular fiber associated strains for simple and complex loading. J. Biomech. 41, 1086–94.

Heuer, F., Schmitt, H., Schmidt, H., Claes, L., Wilke, H.-J., 2007. Creep associated changes in intervertebral disc bulging obtained with a laser scanning device. Clin. Biomech. (Bristol, Avon) 22, 737–44.

Hollingsworth, N.T., Wagner, D.R., 2011. Modeling shear behavior of the annulus fibrosus. J. Mech. Behav. Biomed. Mater. 4, 1103–14.

Holzapfel, G.A., Schulze-Bauer, C.A.J., Feigl, G., Regitnig, P., 2005. Single lamellar mechanics of the human lumbar anulus fibrosus. Biomech. Model. Mechanobiol. 3, 125–40.

Iatridis, J., Kumar, S., Foster, R.J., Weidenbaum, M., Mow, V.C., 1999. Shear mechanical properties of human lumbar annulus fibrosus. J. Orthop. Res. 17, 732–7.

Iatridis, J., Setton, L., Foster, R.J., Rawlins, B., Weidenbaum, M., Mow, V.C., 1998. Degeneration affects the anisotropic and nonlinear behaviors of human anulus fibrosus in compression. J. Biomech. 31, 535–44.

Johannessen, W., Elliott, D.M., 2005. Effects of degeneration on the biphasic material properties of human nucleus pulposus in confined compression. Spine (Phila. Pa. 1976). 30, E724–9.

Joshi, A., Massey, C.J., Karduna, A., Vresilovic, E., Marcolongo, M., 2009. The effect of nucleus implant parameters on the compressive mechanics of the lumbar intervertebral disc: a finite element study. J. Biomed. Mater. Res. B. Appl. Biomater. 90, 596–607.

Keller, T.S., Spengler, D.M., Hansson, T.H., 1987. Mechanical behavior of the human lumbar spine. I. Creep analysis during static compressive loading. J. Orthop. Res. 5, 467–78.

Korecki, C.L., MacLean, J.J., Iatridis, J.C., 2007. Characterization of an in vitro intervertebral disc organ culture system. Eur. Spine J. 16, 1029–37.

Li, H., Wang, Z., 2006. Intervertebral disc biomechanical analysis using the finite element modeling based on medical images. Comput. Med. imaging Graph. 30, 363–70.

Malandrino, A., Planell, J., Lacroix, D., 2009. Statistical factorial analysis on the poroelastic material properties sensitivity of the lumbar intervertebral disc under compression, flexion and axial rotation. J. Biomech. 42, 2780–8.

Massey, C.J., van Donkelaar, C.C., Vresilovic, E., Zavaliangos, A., Marcolongo, M., 2012. Effects of aging and degeneration on the human intervertebral disc during the diurnal cycle: a finite element study. J. Orthop. Res. 30, 122–8.

McMillan, D.W., Garbutt, G., Adams, M.A., 1996. Effect of sustained loading on the water content of intervertebral discs: implications for disc metabolism. Ann. Rheum. Dis. 55, 880–7.

Natarajan, R.N., Williams, J.R., Andersson, G.B.J., 2004. Recent advances in analytical modeling of lumbar disc degeneration. Spine (Phila. Pa. 1976). 29, 2733–41.

Natarajan, R.N., Williams, J.R., Andersson, G.B.J., 2006. Modeling changes in intervertebral disc mechanics with degeneration. J. Bone Joint Surg. Am. 88 Suppl 2, 36–40.

Natarajan, R.N., Williams, J.R., Lavender, S. a., Andersson, G.B.J., 2007. Poro-elastic finite element model to predict the failure progression in a lumbar disc due to cyclic loading. Comput. Struct. 85, 1142–1151.

Noailly, J., Planell, J., Lacroix, D., 2011. On the collagen criss-cross angles in the annuli fibrosi of lumbar spine finite element models. Biomech. Model. Mechanobiol. 10, 203–19.

O'Connell, G.D., Jacobs, N.T., Sen, S., Vresilovic, E.J., Elliott, D.M., 2011. Axial creep loading and unloaded recovery of the human intervertebral disc and the effect of degeneration. J. Mech. Behav. Biomed. Mater. 4, 933–42.

O'Connell, G.D., Vresilovic, E.J., Elliott, D.M., 2011. Human intervertebral disc internal strain in compression: The effect of disc region, loading position, and degeneration. J. Orthop. Res. 29, 547–555.

Paul, C., Schoorl, T., Zuiderbaan, H., Zandieh Doulabi, B., van der Veen, A., van de Ven, P., Smit, T., van Royen, B., Helder, M., Mullender, M., 2013. Dynamic and Static Overloading Induce Early Degenerative Processes in Caprine Lumbar Intervertebral Discs. PLoS One 8, e62411.

Paul, C., Zuiderbaan, Zandieh Doulabi, B., van der Veen, A.J., van de Ven, P.M., Smit, T.H., Helder, M.N., van Royen, B.J., Mullender, M.G., 2012. Simulated-physiological loading conditions preserve biological and mechanical properties of caprine lumbar intervertebral discs in ex vivo culture. PLoS One 7, e33147.

Périé, D., Korda, D., Iatridis, J.C., 2005. Confined compression experiments on bovine nucleus pulposus and annulus fibrosus: sensitivity of the experiment in the determination of compressive modulus and hydraulic permeability. J. Biomech. 38, 2164–71.

Pollintine, P., van Tunen, M., Luo, J., Brown, M., Dolan, P., Adams, M.A., 2010. Time-dependent compressive deformation of the ageing spine: relevance to spinal stenosis. Spine (Phila. Pa. 1976). 35, 386–94.

Ruiz, C., Noailly, J., Lacroix, D., 2013. Material property discontinuities in intervertebral disc porohyperelastic finite element models generate numerical instabilities due to volumetric strain variations. J. Mech. Behav. Biomed. Mater. 26, 1–10.

Sato, K., Kikuchi, S., Yonezawa, T., 1999. In vivo intradiscal pressure measurement in healthy individuals and in patients with ongoing back problems. Spine (Phila. Pa. 1976). 24, 2468–74.

Schmidt, H., Bashkuev, M., Galbusera, F., Wilke, H.-J., Shirazi-Adl, A., 2013. Finite element study of human lumbar disc nucleus replacements. Comput. Methods Biomech. Biomed. Engin.

Schmidt, H., Galbusera, F., Wilke, H.-J., Shirazi-Adl, A., 2011. Remedy for fictive negative pressures in biphasic finite element models of the intervertebral disc during unloading. Comput. Methods Biomech. Biomed. Engin. 14, 293–303.

Schmidt, H., Kettler, A., Rohlmann, A., Claes, L., Wilke, H.-J., 2007. The risk of disc prolapses with complex loading in different degrees of disc degeneration - a finite element analysis. Clin. Biomech. (Bristol, Avon) 22, 988–98.

Schmidt, H., Shirazi-Adl, A., Galbusera, F., Wilke, H.-J., 2010. Response analysis of the lumbar spine during regular daily activities–a finite element analysis. J. Biomech. 43, 1849–56.

Schroeder, Y., Huyghe, J.M., van Donkelaar, C.C., Ito, K., 2010. A biochemical/biophysical 3D FE intervertebral disc model. Biomech. Model. Mechanobiol. 9, 641–50.

Schroeder, Y., Wilson, W., Huyghe, J.M., Baaijens, F.P.T., 2006. Osmoviscoelastic finite element model of the intervertebral disc. Eur. Spine J. 15 Suppl 3, S361–71.

Sivan, S., Merkher, Y., Wachtel, E., Ehrlich, S., Maroudas, A., 2006. Correlation of swelling pressure and intrafibrillar water in young and aged human intervertebral discs. J. Orthop. Res. 24, 1292–8.

Tyrrell, A.R., Reilly, T., Troup, J.D., 1985. Circadian variation in stature and the effects of spinal loading. Spine (Phila. Pa. 1976). 10, 161–164.

Urban, J., Roberts, S., Ralphs, J., 2000. The nucleus of the intervertebral disc from development to degeneration. Am. Zool. 40, 53–61.

Urban, J.P.G., McMullin, J.F., 1988. Swelling pressure of the lumbar intervertebral discs: influence of age, spinal level, composition, and degeneration. Spine (Phila. Pa. 1976). 13, 179–187.

Van den Broek, P.R., Huyghe, J.M., Ito, K., 2012. Biomechanical behavior of a biomimetic artificial intervertebral disc. Spine (Phila. Pa. 1976). 37, E367–73.

White, A., Panjabi, M., 1990. Clinical biomechanics of the spine.

Wilke, H.-J., Neef, P., Caimi, M., Hoogland, T., Claes, L.E., 1999. New in vivo measurements of pressures in the intervertebral disc in daily life. Spine (Phila. Pa. 1976). 24, 755–62.

Williams, J.R., Natarajan, R.N., Andersson, G.B.J., 2007. Inclusion of regional poroelastic material properties better predicts biomechanical behavior of lumbar discs subjected to dynamic loading. J. Biomech. 40, 1981–7.

Wognum, S., Huyghe, J.M., Baaijens, F.P.T., 2006. Influence of osmotic pressure changes on the opening of existing cracks in 2 intervertebral disc models. Spine (Phila. Pa. 1976). 31, 1783–8.

Yao, H., Gu, W.Y., 2007. Three-dimensional inhomogeneous triphasic finite-element analysis of physical signals and solute transport in human intervertebral disc under axial compression. J. Biomech. 40, 2071–7.

Zander, T., Krishnakanth, P., Bergmann, G., Rohlmann, A., 2010. Diurnal variations in intervertebral disc height affect spine flexibility, intradiscal pressure and contact compressive forces in the facet joints. Comput. Methods Biomech. Biomed. Engin. 13, 551–7.

"Science never solves a problem without creating ten more."

George Bernard Shaw

6. CONCLUSIONS

This chapter conceals the wide-ranging description of the essential outcomes of the present work. Therefore, a critical review of the whole work is presented. In addition, suggestions for further improvements and future work are also enumerated.

6.1. Concluding Remarks

The literature review endorsed the IVD as an inhomogeneous porous tissue, which contains solid and fluid materials. Its main components are the NP, the AF and the CEP. The NP is a gel-like-structure with high proteoglycan content and embedded collagen fibers, which results on a tissue that is mostly isotropic, hyper-viscoelastic and incompressible. The AF consists of a porous skeleton with high density of interconnected collagen fibers, which support the NP content and confers noticeable anisotropic behavior. Finally, the CEP is a layer of hyaline cartilage that handles the nutrients exchange with the VB, the major bony components of the spine[1].

The IVDs provide six degrees of freedom to each spinal MS, serving as central axial cushions for the diverse loading efforts. *In vivo* studies are problematic and potentially harmful, mostly due to the proximity of the spinal canals. Therefore, the major part of the information about the IVD biochemistry and biomechanical behavior comes from *in vitro* studies. Despite of the advances on the experimental techniques, which are essential to the description of the

[1] The other bony components of the spine are the facets, which are attached to the VBs.

biomechanical features of the tissues, the numerical methods are an essential tool to analyze and dissect the IVD behavior, as they allow unlimited repetitions and complete control over the testing conditions. The FE method was the selected numerical tool for the analysis of the micro and macro biomechanical behavior of the Human IVD.

In order to achieve valid numerical studies, the IVD must be accurately modeled. The researcher shall first choose between using commercial or open-source FE packages, and then construct the FE model. The commercial solvers are powerful tools, with multiple solutions and a large community of users. However, the outcomes here presented proved the ability of a home-developed open-source FE solver to equal and even overcome the performance of commercial FE packages, regardless of the aggregation of user-defined materials and behavior laws to such solvers. This is the primary conclusion of this work.

The current lumbar MS FE model included an IVD with osmo-hyper-poro-visco-elastic behavior and with noteworthy influence of the anisotropic AF fibers as well. The key basis was the development and implementation of an innovative biphasic poroelastic formulation, which included the strain-dependent permeability model of van der Voet (1997) and the osmotic swelling model of Wilson, van Donkelaar, van Rietbergen, et al. (2005). The generalized non-linear Maxwell model (Kaliske et al., 2001) was selected for the hyper-viscoelastic behavior, while the Mooney-Rivlin model (Bonet and Wood, 1997) was chosen for the isotropic matrix behavior. The other novelty was the implementation of the regional differentiation of the AF fibers, based on the anisotropic model of Holzapfel et al. (2005) and also on the findings of Eberlein et al. (2001). These formulations were implemented on the home-developed open-source FE solver, which means that the described choices and developments on the constitutive modeling were determinant for the remarkable performance of the MS FE model.

The other significant branch for the presented good outcomes was the FE mesh, which was constructed with Hex27 elements. The geometrical accuracy of this model and the appropriate choice of finite elements and mesh refinement allowed valid comparisons with literature data[ii] and with outcomes from the VUmc's LDCS. Nevertheless, the Terzaghi's test for 1D consolidation and the convergence study proved that the Tet4 elements (linear tetrahedron enriched with a bubble function at the center of the element) and the Tet10 elements were also valid choices for the numerical simulations, as their behavior on those tests was very satisfactory

[ii] Experimental (Heuer et al., 2007; O'Connell et al., 2011; Tyrrell et al., 1985; Wilke et al., 1999) and numerical data (Galbusera et al., 2011; Williams et al., 2007).

and generally similar to the behavior of the Hex27 elements. This flexibility on the finite element's configuration was one of the relevant points for the validation of the innovative biphasic formulation.

The comparison with experimental and numerical data was the other relevant point for validation of the innovative biphasic formulation, as well as for the evaluation of the home-developed open-source FE solver. The lumbar MS FE model was tested under several loading profiles, from the pre-conditioning periods to the circadian variations. The major outcomes were displacement and pressure (NP AveP, OsmP and IDP), but volume variation or fiber stretch were also discussed. The stress-strain condition of the IVD was thus analyzed at the macromechanical point of view, i.e., internal variables as stress and strain were not discussed, since they are not measurable in the experimental studies.

The swelling tests have shown that the free swelling condition is the fastest and most accurate method to simulate the pre-conditioning, even if this is a non-realistic condition. However, this stage is essential to induce the physiological stressed condition of the IVD. The recovery periods are best simulated with loads until 250N, as higher loads were proved to cause increasing height reduction, instead of allowing the IVD to regain the fluid lost during the activity periods.

The short and long creep tests have shown that the behavior of the native MS FE model is aligned with experimental and numerical literature data. The comparisons with the works of Schroeder et al. (2010) and (Galbusera et al., 2011) were determinant for the evaluation of the performance of the home-developed open-source FE solver and the associated MS FE model. It was proved that the MS model here developed is able of reproducing experimental studies and theoretical predictions, equally or better than the referred studies, which used ABAQUS® with user-defined material laws. It was also concluded that loads higher than 1000N are potentially harmful for the IVD, despite of several studies indicating otherwise. The creep response of the MS model denoted a clear overload effect when loads of that magnitude were applied, both on displacement and pressure outcomes.

The LDCS analysis involved exploration of both experimental and numerical data. Globally, the IVDs injected with the CABC compound were more vulnerable to degeneration than the other IVDs, even if some exceptions were detected. The overloading mode also caused IVD degeneration, but the observed biomechanical degenerative behavior was different, i.e., the

overloaded IVD starting being degraded right after the application of the load, while the injected IVDs revealed a gradual degenerated behavior. After the analysis of the experimental outcomes, analogous numerical simulations were performed and their behavior was compared. The comparison with the MS FE model was fruitful, particularly for the physiological situations. However, some discrepancies were noticed on the simulations of degenerated IVDs is extremely complex, probably due to the undisclosed physiological damage-prevention mechanism. Nevertheless, the general behavior of the non-physiological numerical models was also satisfactorily simulated, which proved the broadness of the MS model.

In resume, the numerical simulations with the MS FE model, using the home-developed open-source FE solver, showed its validity and potential to contribute to the understanding on the IVD biomechanics. This shall be the *take-home message* associated with this work.

Finally and in a nutshell, a very personal comment from the author: spine biomechanics is a fascinating and promising subject, and I do feel that we are still very far from a complete understanding of the biomechanics and the biomechanisms playing a paramount role on the IVD in particular and spine in general. Future will bring us, certainly, fascinating new achievements on this area of science.

6.2. Future Work

The present work could be improved with a list of additional tasks, which were not performed mostly due to lack of time.

First of all, different types of loading profiles could be applied, such as multi-axial translational loadings or rotation, flexion and extension efforts. These possibilities are already enclosed on the home-developed open-source FE solver, but the current option was to not explore them in this work. The option was to exhaustively explore the available data on uniaxial compression, but the other loading profiles could be explored later on.

The FE model could be extended to the full extension of the lumbar spine and include the adjacent structures to the VB and IVD, namely the facets, ligaments and muscles. These structures would be particularly helpful for the rotation, flexion and extension efforts. In what concerns to the other lumbar IVDs, the larger model could possibly be more accurate on the macro-scale behavioral predictions.

The macromechanical behavior, namely the calculus of the global loads acting on the spine, could also benefit from a hybrid numerical approach, i.e., integration of both FE and MBS techniques with retro-feedback between the outcomes of each technique. The advantage of the simulation through MBS is its fastness, as this method uses lower amount of computational memory and processing capability. Therefore, the hybrid approach would be based on using the FE method to simulate the local behavior of the MS and the MBS to predict the global behavior of the spine.

In what concerns to the local behavior of the IVD, quadriphasic modeling could be implemented. The biphasic approach was proved to be effective, but the consideration of the ionic fluxes could bring extra accuracy to the current model. The disadvantage of the quadriphasic modeling is the augmented number of variables, which could be hard to quantify. In addition, the computational weight time could also increase exponentially.

To sum up, these tasks could be performed to increase the accuracy and also to expand the outcomes of the present work, if the time was not a limitation.

6.3. References

Bonet, J., Wood, R.D., 1997. Nonlinear Continuum Mechanics for Finite Element Analysis. Cambridge University Press, Cambridge.

Eberlein, R., Holzapfel, G.A., Schulze-Bauer, C.A.J., 2001. An Anisotropic Model for Annulus Tissue and Enhanced Finite Element Analyses of Intact Lumbar Disc Bodies. Comput. Methods Biomech. Biomed. Engin. 4, 209–229.

Galbusera, F., Schmidt, H., Noailly, J., Malandrino, A., Lacroix, D., Wilke, H.-J., Shirazi-Adl, A., 2011. Comparison of four methods to simulate swelling in poroelastic finite element models of intervertebral discs. J. Mech. Behav. Biomed. Mater. 4, 1234–41.

Heuer, F., Schmitt, H., Schmidt, H., Claes, L., Wilke, H.-J., 2007. Creep associated changes in intervertebral disc bulging obtained with a laser scanning device. Clin. Biomech. (Bristol, Avon) 22, 737–44.

Holzapfel, G.A., Schulze-Bauer, C.A.J., Feigl, G., Regitnig, P., 2005. Single lamellar mechanics of the human lumbar anulus fibrosus. Biomech. Model. Mechanobiol. 3, 125–40.

Kaliske, M., Nasdala, L., Rothert, H., 2001. On damage modelling for elastic and viscoelastic materials at large strain. Comput. Struct. 79, 2133–2141.

O'Connell, G.D., Jacobs, N.T., Sen, S., Vresilovic, E.J., Elliott, D.M., 2011. Axial creep loading and unloaded recovery of the human intervertebral disc and the effect of degeneration. J. Mech. Behav. Biomed. Mater. 4, 933–42.

Schroeder, Y., Huyghe, J.M., van Donkelaar, C.C., Ito, K., 2010. A biochemical/biophysical 3D FE intervertebral disc model. Biomech. Model. Mechanobiol. 9, 641–50.

Tyrrell, A.R., Reilly, T., Troup, J.D., 1985. Circadian variation in stature and the effects of spinal loading. Spine (Phila. Pa. 1976). 10, 161–164.

Van der Voet, A., 1997. A comparison of finite element codes for the solution of biphasic poroelastic problems. Proc. Inst. Mech. Eng. H. 211, 209–11.

Wilke, H.-J., Neef, P., Caimi, M., Hoogland, T., Claes, L.E., 1999. New in vivo measurements of pressures in the intervertebral disc in daily life. Spine (Phila. Pa. 1976). 24, 755–62.

Williams, J.R., Natarajan, R.N., Andersson, G.B.J., 2007. Inclusion of regional poroelastic material properties better predicts biomechanical behavior of lumbar discs subjected to dynamic loading. J. Biomech. 40, 1981–7.

Wilson, W., van Donkelaar, C.C., van Rietbergen, B., Huiskes, R., 2005. A fibril-reinforced poroviscoelastic swelling model for articular cartilage. J. Biomech. 38, 1195–204.

7. ANNEXES

7.1. 500N, 15mins, different osmotic properties

The loading protocol of 500N during 15mins[i], as performed experimentally by Heuer et al. (2007), was used in this work as a benchmark for short creep analyzes. The importance of the osmotic swelling for the natural behavior of the IVD was also previously examined, as well as the influence of different stiffness properties[ii]. One has also registered that the reduction of the osmotic swelling pressure gradient[iii] played a major role on the long term IVD behavior.

Therefore, the described short creep loading protocol was applied to find out the influence of the osmotic swelling material properties on the short term[iv]. This task was not included neither on the "Validation" chapter, nor on the "Results and Discussion" chapter because it was not directly associated with the remaining simulation tasks.

Figure 7.1 shows the displacement (Figure 7.1a)) and pressure (Figure 7.1b)) outcomes of four numerical variations, namely "No Swelling", "Pre-Swelling" (standard $c_{F,0}$[v]), "Low OsmP 1" and "Low OsmP 2", which were compared with the work of Heuer and co-workers.

As theoretically expected, the osmotic swelling material properties, namely the fixed charge (c_F)[vi], do not play a significant role on the short term response of the IVD. On the one hand, the pressure (NP AveP, Figure 7.1b)) naturally dropped, from the standard model to the "No Swelling" case, i.e., the two reduced osmotic pressure models and the model without any osmotic pressure gradient were gradually more distant from the reference situation, in

[i] Uniaxial compressive load.

[ii] Chapter 4, "Short Creep Validation" section, "500N, 15mins" and "Other configurations" sub-sections, respectively.

[iii] Through the alteration of the initial fixed charge density ($c_{F,0}$).

[iv] Chapter 5, "Bioreactor Data Analysis" section, "Comparison with the MS FE model" sub-section.

[v] As stated in Chapter 3, "Finite Element Model" section, "Material Parameters" sub-section.

[vi] Which is dependent on the initial fixed charge density ($c_{F,0}$)

comparison with the standard model. On the other hand, the displacement outcomes of the four numerical models (DHV, Figure 7.1a)) are not very apart from each other, which means that the reduction of the osmotic pressure is only noticeable for longer test periods. One may thus assume that the extrapolation of the outcomes from the short creep tests may not be enough to establish solid conclusions about the circadian variations of the IVD biomechanical behavior. As already discussed, poroelasticity and osmolality are essentially noticed on the long term, so the variation of the material properties associated with these constitutive features can only be evaluated on long term simulations.

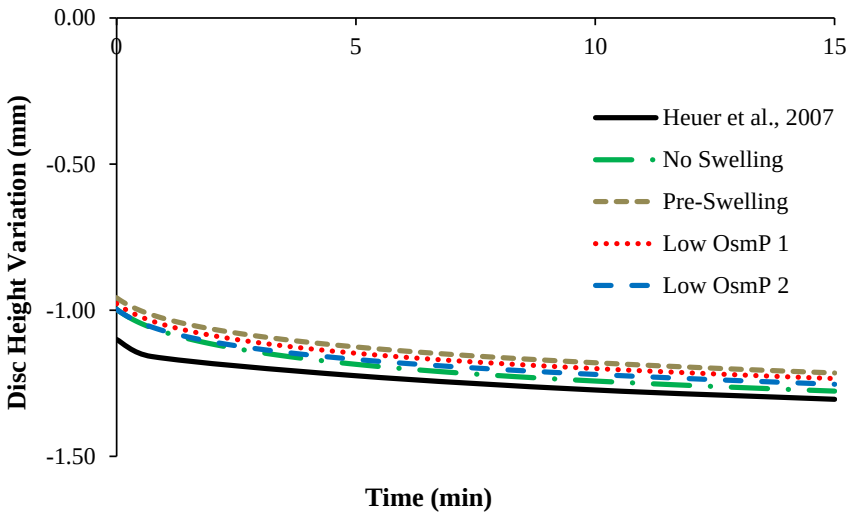

a)

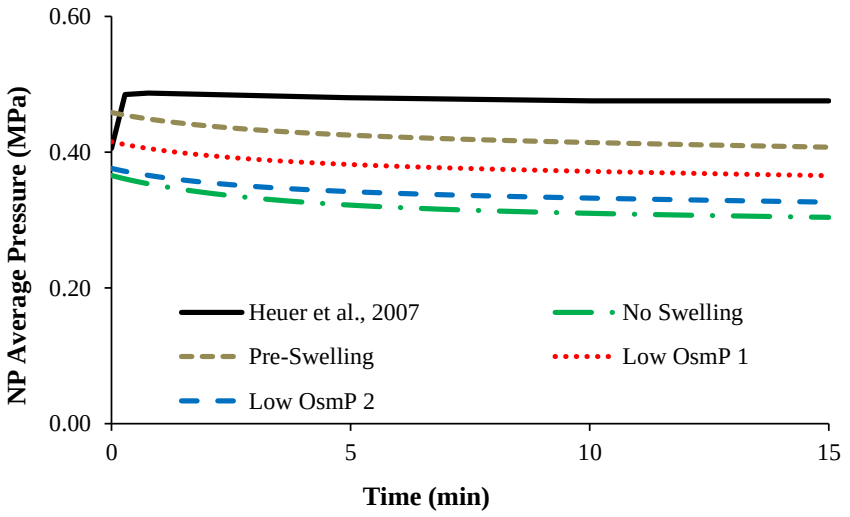

b)

Figure 7.1. Simulated creep test during 15min at 500N of uniaxial compression. The FE model was configured with four different sets of osmotic swelling material properties, namely "No Swelling", "Pre-Swelling" (standard parameters), "Low OsmP 1" and "Low OsmP 2". Assessed outcomes: a) DHV; b) NP AveP.

7.2. Detailed analysis of Overloaded LDCS Data

On the "Bioreactor Data Analysis" section of the "Results and Discussion" chapter, the general LDCS outcomes were analyzed. At this stage, a different approach for the analysis of the behavior of the overloaded IVD is discussed. Only the activity periods were here considered, along the 16 days of the experiment. Figure 7.2 shows the comparison between the DHV of the days 1, 2, 8 and 16, during the referred period. "Exp" stands for "experimental values".

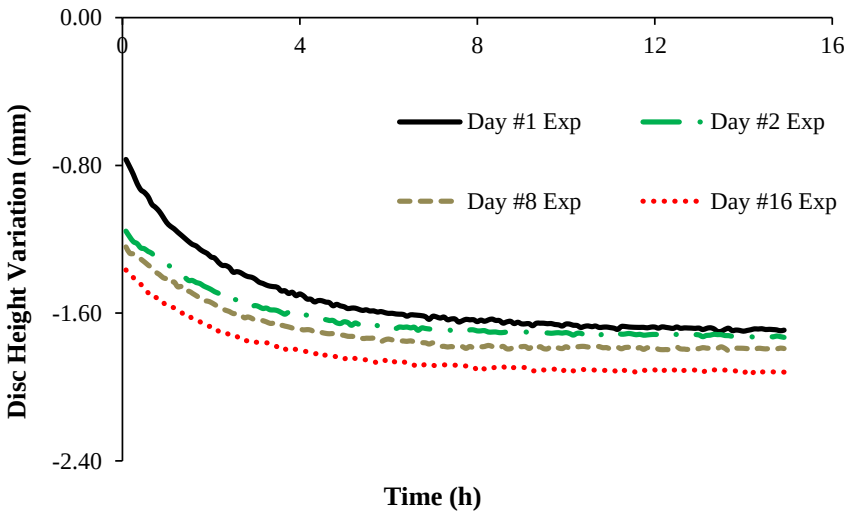

Figure 7.2. Comparison between the experimental displacement outcomes ("Exp") during the activity periods, for the overloaded IVD. The presented outcomes are from days 1, 2, 8 and 16.

On the one hand, Figure 7.2 confirms that the maximum displacement is increasing along the experiment, as a consequence of the overloading mode. On the other hand, this graphic also shows that the evolution of the displacement is not significantly different along the days. The exception is the first day, but this situation can be explained by the initial adaptation of the IVD to the LDCS and the respective stimuli. In other words, the first day is the experimental pre-conditioning. On the succeeding selected days, the global DHV of the activity period is considerably lower, which may be explained by a daily load accumulation effect. In order to demonstrate the similarity between the behavior of this IVD on the different days, an adjustment of an exponential curve was taken into consideration. The expressions for this curve and for the

calculus of the mean absolute error (MAE) between the theoretical and experimental results are the following:

$$d^c = d_0 + d_{sat}\left[1 - e^{(-c_d(t-t_0))}\right] \qquad 7.1$$

$$MAE = \frac{\sum_1^n (d^c - \text{"Exp"})}{n} \qquad 7.2$$

Regarding equation 7.1, d_0 is the DHV measured for the first time step, d_{sat} and c_d are adjustable parameters, t is the current time step and t_0 is initial time step. d^c is the resultant adjusted value, which will be ahead denominated as "Adj". On equation 7.2, n is the number of samples of the experimental data. The results of this adjustment are shown on Figure 7.3. The comparison between the exponential adjustment and the experimental curves from the first and sixteenth days is shown on Figure 7.4. Table 7.1 contains the parameters obtained from the adjustment of the exponential curve.

On the one hand, the adjustment of the exponential curve was quite satisfactory, as the experimental and theoretical curves are very close and the generic MAE is meaningfully low. On the other hand, the contents of Table 7.1 confirm that the overloaded IVD maintains regular behavior along the 16 days of the experiment. In fact, the adjustable parameters d_{sat} and c_d are very similar, on the four days analyzed. The MAE values are also near between each other. The exception is the already discussed adaptation on the first day, which is noticeable on the largest d_{sat} and MAE parameters of this analysis.

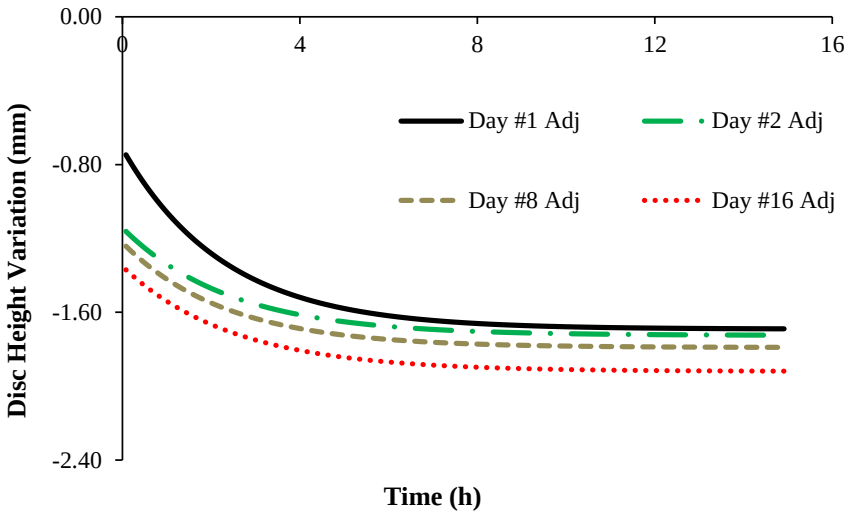

Figure 7.3. Comparison between the adjusted exponential curves ("Adj") related to the displacement outcomes of the activity periods, for the overloaded IVD. The presented outcomes are from days 1, 2, 8 and 16.

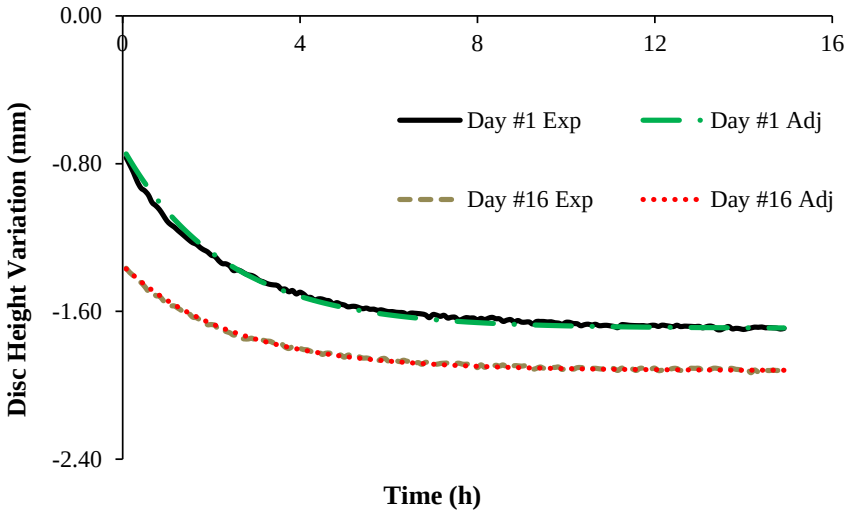

Figure 7.4. Comparison between the exponential and the experimental curves. The presented DHV curves are from days 1 and 16.

Table 7.1. Characteristic parameters of the exponential curve adjustment, for days 1, 2, 8 and 16.

Day	d_{sat}	c_d	n	MAE
#1	-0.977	0.434	5381	0.036%
#2	-0.582	0.413	5379	0.004%
#8	-0.568	0.428	5377	0.005%
#16	-0.568	0.402	5374	0.005%

From the current analysis, concerning the DHV outcomes of the activity periods, it may be concluded that the growing maximum displacement is a result of the gradual degradation of the IVD under overloading conditions. In addition, the evolution of the DHV is similar during the extension of the experiment, i.e., the DHV curves are almost equal for the four studied days, which means that the displacement increase rate does not vary significantly throughout these 16 days. This is probably the most important conclusion that may be drawn from the exponential adjustment of the experimental data, i.e., the degeneration caused by the overloading mode is clearly distinguishable from the degenerative cascade promoted by the CABC compound.

7.3. General aspects of the open-source FE solver

7.3.1. Input Files

VBIO_ivdnr.bio - Bloco de notas

Ficheiro Editar Formatar Ver Ajuda

```
500000                | NSTMAX    .Maximum number of steps
50                    | IEQMAX    .Maximum number of implicit iterative steps
0.001                 | CRIT      .Convergence Criterion ( critF+critP < CRIT )
0.1                   | RSAFE     .Maximum increment for iterations ( >0.001 )
10.0                  | dTIMEmax    .Maximum TIME increment
                      |
1                     | REPEAT      .number of executions of this "bio" file
bio1                  | NEXTbio     .extension of the next "bio" file to be read
                      |
                      |
==============================================================================
OUTPUT strategy of saving data (saving data once every N times)
------------------------------+-----------------------------------------------
0                     | Universal file
0                     | VTK file
10                    | GID file
                      |
==============================================================================
TIME history of loading and muscle activation
------------------------------+-----------------------------------------------
 11      0.        0.       2 | BOUNDARYCONDITION
 11    300.        0.       2 | BOUNDARYCONDITION
------------------------------+-----------------------------------------------
 22      0.        0.       2 | BOUNDARYCONDITION
 22    300.        0.       2 | BOUNDARYCONDITION
------------------------------+-----------------------------------------------
 33      0.        0.       2 | BOUNDARYCONDITION
 33    300.        0.       2 | BOUNDARYCONDITION
------------------------------+-----------------------------------------------
 44      0.        0.       2 | BOUNDARYCONDITION
 44    300.        0.       2 | BOUNDARYCONDITION
------------------------------+-----------------------------------------------
 55      0.        0.       2 | BOUNDARYCONDITION
 55    300.        0.       2 | BOUNDARYCONDITION
------------------------------+-----------------------------------------------
 77      0.        0.       0 | BOUNDARYCONDITION
 77   3600.        0.       0 | BOUNDARYCONDITION
------------------------------+-----------------------------------------------
 88      0.        0.       0 | BOUNDARYCONDITION
 88   3600.        0.       0 | BOUNDARYCONDITION
------------------------------+-----------------------------------------------
 66      0.        0.       0 | BOUNDARYCONDITION
 66   3600.        0.       0 | BOUNDARYCONDITION
------------------------------+-----------------------------------------------
125      0.        0.       0 | BOUNDARYCONDITION
125   3600.        0.       0 | BOUNDARYCONDITION
------------------------------+-----------------------------------------------
- definition of the piecewise linear evolution functions of:
- MUSCLE activation, 3 values (materialID, time, activation value)
- BOUNDARYCONDITION, time-evolution of BC, 4 values (BCID, time, BCval, NCRval)
==============================================================================
```

a)

VBIO_ivdnr.bio1 - Bloco de notas

Ficheiro Editar Formatar Ver Ajuda

```
500000                | NSTMAX    .Maximum number of steps
50                    | IEQMAX    .Maximum number of implicit iterative steps
0.001                 | CRIT      .Convergence Criterion ( critF+critP < CRIT )
0.1                   | RSAFE     .Maximum increment for iterations ( >0.001 )
5.0                   | dTIMEmax    .Maximum TIME increment
                      |
1                     | REPEAT      .number of executions of this "bio" file
                      | NEXTbio     .extension of the next "bio" file to be read
                      |
                      |
================================================================================
OUTPUT strategy of saving data (saving data once every N times)
------------------------------+-------------------------------------------------
0                     | Universal file
0                     | VTK file
5                     | GID file
                      |
================================================================================
TIME history of loading and muscle activation
------------------------------+-------------------------------------------------
 11      0.        0.       2 | BOUNDARYCONDITION
 11    600.        0.       2 | BOUNDARYCONDITION
------------------------------+-------------------------------------------------
 22      0.        0.       2 | BOUNDARYCONDITION
 22    600.        0.       2 | BOUNDARYCONDITION
------------------------------+-------------------------------------------------
 33      0.        0.       2 | BOUNDARYCONDITION
 33    600.        0.       2 | BOUNDARYCONDITION
------------------------------+-------------------------------------------------
 44      0.        0.       2 | BOUNDARYCONDITION
 44    600.        0.       2 | BOUNDARYCONDITION
------------------------------+-------------------------------------------------
 55      0.        0.       2 | BOUNDARYCONDITION
 55    600.        0.       2 | BOUNDARYCONDITION
------------------------------+-------------------------------------------------
 77      0.        0.       0 | BOUNDARYCONDITION
 77   1200.        0.       0 | BOUNDARYCONDITION
------------------------------+-------------------------------------------------
 88      0.        0.       0 | BOUNDARYCONDITION
 88   1200.        0.       0 | BOUNDARYCONDITION
------------------------------+-------------------------------------------------
 66      0.        0.       1 | BOUNDARYCONDITION
 66    300.       -1.37     1 | BOUNDARYCONDITION
 66   1200.       -1.37     1 | BOUNDARYCONDITION
------------------------------+-------------------------------------------------
125      0.        0.       0 | BOUNDARYCONDITION
125   1200.        0.       0 | BOUNDARYCONDITION
------------------------------+-------------------------------------------------
- definition of the piecewise linear evolution functions of:
- MUSCLE activation, 3 values (materialID, time, activation value)
- BOUNDARYCONDITION, time-evolution of BC, 4 values (BCID, time, BCval, NCRval)
================================================================================
```

b)

Figure 7.5. Example of an input file for the assignment of the boundary conditions. The FE solver has the capacity of reading sequential boundary conditions files. a) First input file (".bio"); b) Second input file (".bio1").

```
VBIO_ivdnr.bcid - Bloco de notas
Ficheiro  Editar  Formatar  Ver  Ajuda
Parametric definition for V-Biomech V2.002
of BCIDs for each dof
================================================================================
11            |  BCID                          ( 1-99 )
1             |  Coordinate                    ( 1->"x";  2->"y";  3->"z";  4->"p" )
B             |  Nodes pre-selection           ( A-> all nodes; B-> Boundary nodes )
0             |  Material                      ( 0-> all matID; matID-> matID only )
--------------------------------------------------------------------------------
Seeding node  | numNO,{x,y,z}          iNN          x           y           z
              |                          C          M           M           L
Normal        | @numNO,{nx,ny,nz}     @iNN         nx          ny          nz
              |                            0       0.0         0.0        -1.0
--------------------------------------------------------------------------------
N             |  Check     (S or N - Seed or Normal)
20.0          |  error     (S, [length units], N [degrees]
A             |  A/R       (Absolute or Relative error
================================================================================
22            |  BCID                          ( 1-99 )
2             |  Coordinate                    ( 1->"x";  2->"y";  3->"z";  4->"p" )
B             |  Nodes pre-selection           ( A-> all nodes; B-> Boundary nodes )
0             |  Material                      ( 0-> all matID; matID-> matID only )
--------------------------------------------------------------------------------
Seeding node  | numNO,{x,y,z}          iNN          x           y           z
              |                          C          M           M           L
Normal        | @numNO,{nx,ny,nz}     @iNN         nx          ny          nz
              |                            0       0.0         0.0        -1.0
--------------------------------------------------------------------------------
N             |  Check     (S or N - Seed or Normal)
20.0          |  error     (S, [length units], N [degrees]
A             |  A/R       (Absolute or Relative error
```

Figure 7.6. Example of a section of an input file for the identification of each degree-of-freedom where the boundary conditions will be assigned. ".bcid" stand for "Boundary Conditions Identification".

```
VBIO_ivdnr_mater1.dat - Bloco de notas
Ficheiro  Editar  Formatar  Ver  Ajuda
matID           | 1
Name            | NP
Desc            | NP
================+=================================================================
CMisotropic     | 1
  N             | 1
  Values        | 0.15    0.03
CManisotropic   | 0
  N             | 2
  Values        | 5.0        10.0     0.0    10.0  0.0   0.0   0.0   0.0
----------------
bulkM           | 0.0
----------------
HPermeability   | 7.5e-4
M (+)           | 8.5
----------------
Swelling        | 2
  Fixed DePi    | 0.20
  R             | 8.31450
  T             | 298.0
  phi(i)        | 0.83
  phi(e)        | 0.92
  ce            | 0.00015
  cf0           | 0.00030
  nf0           | 0.8
----------------
viscous         | 1
  N             | 3
  aki(1-5)      | 1.7      1.2   2.0     6.0
  tki(1-5)      | 11.765   1.1   0.132   0.01
================+=================================================================
```

Figure 7.7. Example of an input file for the assignment of the constitutive parameters of a given material. This example refers to the standard NP.

7.3.2. Output Files

ivdnr.lst - Bloco de notas

Ficheiro Editar Formatar Ver Ajuda

```
*** Number of surface nodes                    2450

*** BCID    11, number of DOFs assigned:      365
*** BCID    22, number of DOFs assigned:      365
*** BCID    33, number of DOFs assigned:      365
*** BCID    44, number of DOFs assigned:      365
*** BCID    55, number of DOFs assigned:      365
*** BCID    66, number of DOFs assigned:      365
*** BCID    77, number of DOFs assigned:      575
*** BCID    77, number of DOFs assigned:      765
*** BCID    77, number of DOFs assigned:      315
*** BCID    77, number of DOFs assigned:      311
*** BCID    88, number of DOFs assigned:      575
*** BCID    88, number of DOFs assigned:      765
*** BCID    88, number of DOFs assigned:      311
*** BCID    88, number of DOFs assigned:      315
*** BCID   125, number of DOFs assigned:      403
*** BCID   125, number of DOFs assigned:      741
*** BCID   125, number of DOFs assigned:      307
*** BCID   125, number of DOFs assigned:      311
*** BCID   125, number of DOFs assigned:      365
*** BCID   125, number of DOFs assigned:      365

          Problem name: ivdnr
Number of elements            - NE    =      1892
Number of nodes               - NN    =     16425
Dof/node                      - NDEG  =         4
Number of degrees of freedom - NTDF   =     65700

          Implicit Parameters
Max. steps                  - NSTMAX   =    500000
Max. iterations             - IEQMAX   =        50
Convergence Criterion       - CRIT     =    0.0010
Max. increments             - RSAFE    =    0.1000
Max. TIME increment         - dTIMEmax =   10.0000


Material Data
NMAT =      5
 1  NP       CM: 1- ANI: 0, MSL: 0, VSH: 0, VLG: 1, MEM: 0
    - Isotropic model Mooney-Rivlin (N = 1)
       Bulk Modulus:  0.36E+03
       IsoParas:  0.15E+00  0.30E-01
    - Viscous effect LONG (Relax. Factor - Charact. Time)
        1  0.17E+01  0.12E+02
        2  0.12E+01  0.11E+01
        3  0.20E+01  0.13E+00
    - Poroelasticity
       K0 =   0.75E-03, M =   0.85E+01
    - Osmotic Swelling =   Variable
```

a)

ivdnr.lst - Bloco de notas

Ficheiro Editar Formatar Ver Ajuda

```
        2  AF       CM:11- ANI: 1, MSL: 0, VSH: 0, VLG: 1, MEM: 0
           - Isotropic model Mooney-Rivlin (N = 1)
              Bulk Modulus:  0.45E+03
              IsoParas:  0.18E+00  0.45E-01
           - Anisotropic model Holzapfel  (N = 2)
              ANIparas: 0.30E+03 0.12E+02 0.00E+00 0.12E+02
              ANIparas: 0.00E+00 0.00E+00 0.00E+00
              ratioCompTens:   0.0000
           - Viscous effect LONG (Relax. Factor - Charact. Time)
               1  0.17E+01  0.12E+02
               2  0.12E+01  0.11E+01
               3  0.20E+01  0.13E+00
           - Poroelasticity
              K0 =   0.75E-03, M =   0.85E+01
           - Osmotic Swelling =   Variable
        3  CEP      CM: 1- ANI: 0, MSL: 0, VSH: 0, VLG: 1, MEM: 0
           - Isotropic model Mooney-Rivlin (N = 1)
              Bulk Modulus:  0.20E+04
              IsoParas:  0.10E+01  0.00E+00
           - Viscous effect LONG (Relax. Factor - Charact. Time)
               1  0.17E+01  0.12E+02
               2  0.12E+01  0.11E+01
               3  0.20E+01  0.13E+00
           - Poroelasticity
              K0 =   0.75E-02, M =   0.85E+01
           - Osmotic Swelling =   Variable
        4  CortB    CM: 1- ANI: 0, MSL: 0, VSH: 0, VLG: 0, MEM: 0
           - Isotropic model Mooney-Rivlin (N = 1)
              Bulk Modulus:  0.77E+07
              IsoParas:  0.38E+04  0.00E+00
           - Poroelasticity
              K0 =   0.10E+00, M =   0.22E+02
           - Osmotic Swelling =       Off
        5  CancB    CM: 1- ANI: 0, MSL: 0, VSH: 0, VLG: 0, MEM: 0
           - Isotropic model Mooney-Rivlin (N = 1)
              Bulk Modulus:  0.83E+05
              IsoParas:  0.42E+02  0.00E+00
           - Poroelasticity
              K0 =   0.10E+00, M =   0.18E+02
           - Osmotic Swelling =       Off

 it       critF       critP          totF         noneqF         noneqP
  1   0.198E+02   0.000E+00      0.103E-09      0.198E+02      0.000E+00
  2   0.410E+01   0.100E+01      0.126E+01      0.517E+01      0.236E+01
  3   0.258E+00   0.841E-01      0.190E+01      0.489E+00      0.198E+00
  4   0.487E-01   0.774E-02      0.202E+01      0.985E-01      0.182E-01
  5   0.337E-02   0.774E-03      0.202E+01      0.679E-02      0.182E-02
  6   0.193E-03   0.833E-04      0.202E+01      0.389E-03      0.196E-03
+++ NST=      1   RSUM=   0.000  RMIN= 4.400E-04  TIME t=     0.132 secs
+++ CYCLE     1  of      1 from VBIO_ivdnr.bio
+++ Iteration time =   40.81 s  --   6steps
```

b)

Figure 7.8. Example of the generic output file, which contains the evolution of the simulation. This information is also visualized in real time through command line environment. a) First section of the file, containing the generic information from the mesh, from the simulation and also from the materials; b) Continuation, with the information from the other materials and also with the numerical characteristics of the first time step of the simulation.

OUT_ivdnr_FORCES.txt - Bloco de notas

Ficheiro Editar Formatar Ver Ajuda

NST	IEQUI	TIME	TIME(min.)	TF_11_x	NCR	X-Xinit	TF_22_y	NCR	X-Xinit
1	6	0.13200	0.00220	0.000045	Displ	0.000000	-0.397635	Displ	0.000000
2	5	0.39600	0.00660	0.000002	Displ	0.000000	-0.362199	Displ	0.000000
3	4	0.92400	0.01540	0.000029	Displ	0.000000	-0.352893	Displ	0.000000
4	4	1.98000	0.03300	0.000034	Displ	0.000000	-0.360680	Displ	0.000000
5	4	4.09200	0.06820	0.000123	Displ	0.000000	-0.387850	Displ	0.000000
6	5	8.31600	0.13860	0.000068	Displ	0.000000	-0.436285	Displ	0.000000
7	5	16.76400	0.27940	0.000080	Displ	0.000000	-0.508153	Displ	0.000000
8	5	26.76400	0.44607	0.000109	Displ	0.000000	-0.585266	Displ	0.000000
9	5	36.76400	0.61273	0.000143	Displ	0.000000	-0.661427	Displ	0.000000
10	5	46.76400	0.77940	0.000140	Displ	0.000000	-0.738437	Displ	0.000000
11	4	56.76400	0.94607	0.000207	Displ	0.000000	-0.817600	Displ	0.000000
12	4	66.76400	1.11273	0.000154	Displ	0.000000	-0.897343	Displ	0.000000
13	4	76.76400	1.27940	0.000183	Displ	0.000000	-0.978665	Displ	0.000000
14	4	86.76400	1.44607	0.000154	Displ	0.000000	-1.058916	Displ	0.000000
15	4	96.76400	1.61273	0.000149	Displ	0.000000	-1.139130	Displ	0.000000
16	4	106.76400	1.77940	0.000145	Displ	0.000000	-1.215932	Displ	0.000000
17	4	116.76400	1.94607	0.000164	Displ	0.000000	-1.288539	Displ	0.000000
18	4	126.76400	2.11273	0.000168	Displ	0.000000	-1.357407	Displ	0.000000
19	4	136.76400	2.27940	0.000164	Displ	0.000000	-1.422412	Displ	0.000000
20	4	146.76400	2.44607	0.000167	Displ	0.000000	-1.482175	Displ	0.000000
21	4	156.76400	2.61273	0.000163	Displ	0.000000	-1.535762	Displ	0.000000
22	4	166.76400	2.77940	0.000194	Displ	0.000000	-1.583957	Displ	0.000000
23	4	176.76400	2.94607	0.000245	Displ	0.000000	-1.628884	Displ	0.000000
24	4	186.76400	3.11273	0.000256	Displ	0.000000	-1.670378	Displ	0.000000
25	4	196.76400	3.27940	0.000234	Displ	0.000000	-1.707940	Displ	0.000000
26	4	206.76400	3.44607	0.000237	Displ	0.000000	-1.743071	Displ	0.000000
27	4	216.76400	3.61273	0.000251	Displ	0.000000	-1.775480	Displ	0.000000
28	4	226.76400	3.77940	0.000248	Displ	0.000000	-1.804642	Displ	0.000000
29	4	236.76400	3.94607	0.000241	Displ	0.000000	-1.831900	Displ	0.000000
30	4	246.76400	4.11273	0.000228	Displ	0.000000	-1.857516	Displ	0.000000

Figure 7.9. Example of a section of an output file containing force and displacement information, along the duration of the simulation. This file is divided per each "bcid". It also provides additional information on whether force or displacement boundary conditions were applied to that "bcid".

OUT_ivdnr_PRESSUREaverage.txt - Bloco de notas

Ficheiro Editar Formatar Ver Ajuda

NST	TIMEt(sec.)	Average pressure for each material		
1	0.132000000000000	1.861101696105939E-002	-1.268650199941309E-002	-3.246132793916641E-002
2	0.396000000000000	1.847296545396038E-002	-1.233171592567794E-002	-3.718456392784533E-002
3	0.924000000000000	1.846199770738238E-002	-1.196837348590898E-002	-4.170199500730794E-002
4	1.98000000000000	1.862542133630366E-002	-1.158555760163118E-002	-4.537930573480013E-002
5	4.09200000000000	1.912066159673299E-002	-1.127207919432642E-002	-4.726907683931372E-002
6	8.31600000000000	2.018427817375084E-002	-1.117018277733129E-002	-4.647842657413981E-002
7	16.7640000000000	2.185425286965990E-002	-1.135426402855062E-002	-4.231516818975478E-002
8	26.7640000000000	2.331783018719547E-002	-1.162911915588257E-002	-3.786514995016547E-002
9	36.7640000000000	2.456291482078510E-002	-1.191230102893297E-002	-3.414354692353772E-002
10	46.7640000000000	2.573669474754064E-002	-1.221696654378751E-002	-3.091825592024627E-002
11	56.7640000000000	2.689524661087494E-002	-1.254968279439067E-002	-2.804158254085689E-002
12	66.7640000000000	2.805237950869936E-002	-1.291007571839826E-002	-2.540634684720929E-002
13	76.7640000000000	2.919516204575314E-002	-1.328777578587897E-002	-2.298107479577075E-002
14	86.7640000000000	3.032216093281170E-002	-1.367861900176621E-002	-2.073341881038402E-002
15	96.7640000000000	3.143605027863141E-002	-1.408440363138686E-002	-1.863727340323161E-002
16	106.764000000000	3.252042104449031E-002	-1.449127712909751E-002	-1.668773814434370E-002
17	116.764000000000	3.355931462546278E-002	-1.488593150524091E-002	-1.488123879872776E-002
18	126.764000000000	3.455753316469296E-002	-1.527162838453471E-002	-1.320203683648491E-002
19	136.764000000000	3.553283642506908E-002	-1.566112291658485E-002	-1.162879973270712E-002
20	146.764000000000	3.647162074221404E-002	-1.604310872354371E-002	-1.016215864353532E-002
21	156.764000000000	3.736528056925905E-002	-1.640929408489601E-002	-8.800702909507114E-003
22	166.764000000000	3.821242613605159E-002	-1.675718918379699E-002	-7.538808943986734E-003
23	176.764000000000	3.901070099936225E-002	-1.708301207320021E-002	-6.371997738494802E-003
24	186.764000000000	3.976519421642909E-002	-1.739022661975069E-002	-5.291212289142179E-003
25	196.764000000000	4.048267717940079E-002	-1.768276981592341E-002	-4.287760557760388E-003
26	206.764000000000	4.116632365478694E-002	-1.796195024460371E-002	-3.356332330744540E-003
27	216.764000000000	4.181613609547038E-002	-1.822737531525514E-002	-2.492637793333926E-003
28	226.764000000000	4.243755792082236E-002	-1.848247268811646E-002	-1.690116036628886E-003
29	236.764000000000	4.302722503219829E-002	-1.872340733052396E-002	-9.474475476032617E-004
30	246.764000000000	4.358680480028386E-002	-1.895072870565820E-002	-2.603335632803054E-004

Figure 7.10. Example of a section of an output file containing the results for average pressure, divided per material, for each time step of the simulation.

OUT_ivdnr_FIBERS.txt - Bloco de notas

Ficheiro Editar Formatar Ver Ajuda

FIBER stretch statistics (% of fibers within the following intervals)

stretch	>	0.00	0.90	0.94	0.97	0.99	1.00	1.01	1.03	1.06	1.10
	<=	0.90	0.94	0.97	0.99	1.00	1.01	1.03	1.06	1.10	2.00
NST	iMAT										
1	2	0.0	0.0	0.0	0.0	50.0	50.0	0.0	0.0	0.0	0.0
2	2	0.0	0.0	0.0	0.0	50.4	49.6	0.0	0.0	0.0	0.0
3	2	0.0	0.0	0.0	0.0	50.7	49.3	0.0	0.0	0.0	0.0
4	2	0.0	0.0	0.0	0.0	50.6	49.3	0.1	0.0	0.0	0.0
5	2	0.0	0.0	0.0	0.0	49.8	49.7	0.5	0.0	0.0	0.0
6	2	0.0	0.0	0.0	0.0	48.2	50.0	1.9	0.0	0.0	0.0
7	2	0.0	0.0	0.0	0.0	45.7	50.8	3.5	0.0	0.0	0.0
8	2	0.0	0.0	0.0	0.0	43.2	52.4	4.4	0.0	0.0	0.0
9	2	0.0	0.0	0.0	0.0	40.7	54.1	5.2	0.0	0.0	0.0
10	2	0.0	0.0	0.0	0.0	38.2	56.1	5.7	0.0	0.0	0.0
11	2	0.0	0.0	0.0	0.0	35.6	58.4	6.1	0.0	0.0	0.0
12	2	0.0	0.0	0.0	0.0	32.8	60.8	6.3	0.0	0.0	0.0
13	2	0.0	0.0	0.0	0.0	30.1	63.4	6.5	0.0	0.0	0.0
14	2	0.0	0.0	0.0	0.0	27.6	65.8	6.6	0.0	0.0	0.0
15	2	0.0	0.0	0.0	0.0	25.2	68.1	6.8	0.0	0.0	0.0
16	2	0.0	0.0	0.0	0.0	22.9	70.2	6.9	0.0	0.0	0.0
17	2	0.0	0.0	0.0	0.0	21.2	71.8	6.9	0.0	0.0	0.0
18	2	0.0	0.0	0.0	0.0	19.5	73.5	7.0	0.0	0.0	0.0
19	2	0.0	0.0	0.0	0.0	17.5	75.3	7.1	0.0	0.0	0.0
20	2	0.0	0.0	0.0	0.0	15.8	77.0	7.2	0.0	0.0	0.0
21	2	0.0	0.0	0.0	0.0	14.6	78.2	7.2	0.0	0.0	0.0
22	2	0.0	0.0	0.0	0.0	13.6	79.1	7.3	0.0	0.0	0.0
23	2	0.0	0.0	0.0	0.0	12.8	79.8	7.4	0.0	0.0	0.0
24	2	0.0	0.0	0.0	0.0	11.9	80.6	7.4	0.0	0.0	0.0
25	2	0.0	0.0	0.0	0.0	11.2	81.4	7.5	0.0	0.0	0.0
26	2	0.0	0.0	0.0	0.0	10.6	81.9	7.5	0.0	0.0	0.0
27	2	0.0	0.0	0.0	0.0	10.1	82.3	7.6	0.0	0.0	0.0
28	2	0.0	0.0	0.0	0.0	9.5	82.8	7.7	0.0	0.0	0.0
29	2	0.0	0.0	0.0	0.0	9.2	83.1	7.8	0.0	0.0	0.0
30	2	0.0	0.0	0.0	0.0	8.8	83.4	7.8	0.0	0.0	0.0

Figure 7.11. Example of a section of an output file containing the results of the fiber stretch, along the simulation.

OUT_ivdnr_Volume.txt - Bloco de notas

Ficheiro Editar Formatar Ver Ajuda

DVol% = ((Current Volume-Initial Volume) /Initial Volume) *100
RVol = Current Volume/Initial Volume

NST	Time	Time(h)		
matID	InitialVol	CurrentVol	DVol%	RVol
1	0.1320	0.0000		
1	8153.601	8168.847	0.187	1.002
2	11080.474	11069.133	-0.102	0.999
3	1149.989	1146.413	-0.311	0.997
4	25149.195	25148.948	-0.001	1.000
5	34330.651	34330.568	0.000	1.000
2	0.3960	0.0001		
1	8153.601	8173.590	0.245	1.002
2	11080.474	11066.438	-0.127	0.999
3	1149.989	1144.907	-0.442	0.996
4	25149.195	25148.642	-0.002	1.000
5	34330.651	34330.333	-0.001	1.000
3	0.9240	0.0003		
1	8153.601	8177.825	0.297	1.003
2	11080.474	11064.746	-0.142	0.999
3	1149.989	1143.421	-0.571	0.994
4	25149.195	25148.158	-0.004	1.000
5	34330.651	34329.760	-0.003	1.000

Figure 7.12. Example of a section of an output file containing the information on the volume variation of the each one of the materials, along the simulation.

7.4. Publications and Communications

Castro, A.P.G., Completo, A., Flores, P., Alves, J.L., 2011. Overview on the modeling of the biomechanical behavior of the intervertebral disc. In: 4º Congresso Nacional de Biomecânica.

The present work draws an overview on the numerical modeling and numerical simulation of the biomechanical behavior of the Intervertebral Discs (IVD). Since 1974 that several research groups around the world have been devoting attention to this subject and several examples of the application of the Finite Element Analysis (FEA) to study the biomechanics of the IVD can be found. The authors of the present work are presently working under the scope of a wider European project which main expected achievements are: 1) to investigate the biomechanisms of disc degeneration; 2) to develop a biomimetic strategy for the IVD regeneration; 3) the development of several numerical tools, with a special emphasis on a spine-oriented FEA solver, in order to contribute to the investigation of new strategies for treatment and/or rehabilitation of the Degenerative Disc Diseases. The presented overview aims to establish the starting point of such research work.

Castro, A.P.G., Wilson, W., Huyghe, J.M., Ito, K., Alves, J.L., 2012. A poroelastic approach for an open source finite element model of the intervertebral disc. In: CMMBE2012.

Degenerative Disc Disease (DDD) is one of the largest health problems faced worldwide, based on lost working time and associated costs. This works deals with the development of a biomimetic Finite Element (FE) model of the Intervertebral Disc (IVD). Several recent studies have emphasized the importance of an accurate biomechanical modeling of the IVD. Thus, a hyper-visco-poro-elastic formulation is briefly addressed throughout this paper. The FE implementation and numerical simulations are being carried out on a home-developed open source FE solver. The validation of the newly implemented biphasic formulation was performed through Terzaghi's test for confined compression, and some preliminary simulations of a poro-viscoelastic IVD FE model were carried out, being their results briefly discussed. The next step is to include the poroelastic swelling behavior.

Castro, A.P.G., Completo, A., Flores, P., Alves, J.L., 2013. Overview on the modeling of the biomechanical behavior of the intervertebral disc. In: 5º Congresso Nacional de Biomecânica.

The major goal for the present work is to evaluate a biomimetic Finite Element (FE) model of the Intervertebral Disc (IVD). Recent studies have emphasized the importance of an accurate

biomechanical modeling of the IVD, which is a highly complex biphasic medium. A novel biphasic poroelastic model was implemented and coupled with Wilson's model (2005) for biphasic osmotic swelling behavior. Numerical tests were devoted to the analysis of the time-dependent behavior of the IVD. The results show good agreement with literature experimental data (Heuer et al., 2007 or O'Connell et al., 2011) and also with other numerical studies (Galbusera et al., 2011). In brief, this in-development IVD FE model aims to be a valuable tool to study the biomechanics of the IVD and its pathways for degeneration.

Castro, A.P.G., Wilson, W., Huyghe, J.M., Ito, K., Alves, J.L., 2013. Validation of an Open Source Finite Element Biphasic Poroelastic Model. Application to the Intervertebral Disc Biomechanics. In: Poromechanics V. American Society of Civil Engineers, Reston, VA, pp. 2131–2139.

A great amount of experimental and numerical studies have studied the Intervertebral Disc (IVD) and proven that it presents hyper-visco-poro-elastic behavior. However, the accessibility and flexibility of the software used in numerical studies is often hampered by the proprietary nature of the FEM-packages used. A novel biphasic poroelastic formulation was implemented on a home-developed open source FE solver, in order to approach to the biomechanical behavior of the IVD in the Human Spine. Firstly, a simple consolidation test with three different u/p-c elements was compared with Terzaghi's model. Secondly, three IVD FE models were built with the same three types of elements and tested through Heuer's experimental protocol. Terzaghi's test was important to validate the innovative biphasic poroelastic formulation. Such verdict was confirmed by the application of this formulation to the IVD FE model. Therefore, the in-development open source FE solver shall become an appropriate to the description of IVD.

Castro, A.P.G., Wilson, W., Huyghe, J.M., Ito, K., Alves, J.L., 2013. Intervertebral Disc Creep Behavior Assessment Through An Open Source Finite Element Solver. J. Biomech. (http://dx.doi.org/10.1016/j.jbiomech.2013.10.014)

Degenerative Disc Disease (DDD) is one of the largest health problems faced worldwide, based on lost working time and associated costs. By means of this motivation, this work aims to evaluate a biomimetic Finite Element (FE) model of the Intervertebral Disc (IVD). Recent studies have emphasized the importance of an accurate biomechanical modeling of the IVD, as it is a highly complex multiphasic medium. Poroelastic models of the disc are mostly implemented in commercial finite element packages with limited access to the algorithms. Therefore, a novel poroelastic formulation implemented on a home-developed open source FE solver is briefly addressed throughout this paper. The combination of this formulation with biphasic osmotic swelling behavior is also taken into account. Numerical simulations were devoted to the analysis of the non-degenerated Human lumbar IVD time-dependent behavior. The results of the tests performed for creep assessment were inside the scope of the experimental data, with a remarkable improvement of the numerical accuracy when compared with previously published results obtained with ABAQUS®. In brief, this in-development open-source FE solver was validated with literature experimental data and aims to be a valuable tool to study the IVD biomechanics and DDD mechanisms.